For Reference

NOT TO BE TAKEN FROM THIS ROOM

Ex libris
Universitatis
Albertaensis

QUAECUMQUE VERA

Digitized by the Internet Archive
in 2022 with funding from
University of Alberta Library

https://archive.org/details/Santiago1978

THE UNIVERSITY OF ALBERTA

A STUDY OF CO_2 LASER INDUCED BREAKDOWN IN PREIONIZED ARGON

by

© JAIME P. SANTIAGO

A THESIS
SUBMITTED TO THE FACULTY OF GRADUATE STUDIES AND RESEARCH
IN PARTIAL FULFILMENT OF THE REQUIREMENTS FOR THE DEGREE
DOCTOR OF PHILOSOPHY

DEPARTMENT OF ELECTRICAL ENGINEERING

EDMONTON, ALBERTA

SPRING 1978

ABSTRACT

The CO_2 laser induced breakdown of Ar under the influence of an arc discharge is investigated. The laser beam is focused inside and outside the discharge. Inside the discharge the changing electron density and the reduced neutral density modify the breakdown thresholds. Outside the discharge, the effects of uv preionization and shock wave expansion on the breakdown thresholds are investigated.

The pulsed CO_2 laser system, the electric discharge, and the breakdown chamber are described. Langmuir probes, interferometric and CO_2 absorption measurements are performed on the discharge plasma which yield information on the electron and neutral atom concentrations. Rotating Langmuir probes are used to measure uv photoion densities outside the discharge. Shock wave strength measurements using piezoelectric probes are also reported.

A cascade model of the breakdown process is developed. Numerical calculations of the plasma build up in the laser focus are reported.

The experimental thresholds are compared with the results of the calculations. Good agreement is obtained. This leads to the possibility of using the breakdown phenomenon as a diagnostic for electron and neutral atom components of a plasma. The feasibility of this idea is discussed.

ABSTRACT

The CO_2 laser induced breakdown of Ar under the influence of an arc discharge is investigated. The laser beam is focused inside and outside the discharge. Inside the discharge the changing electron density and the reduced neutral density modify the breakdown threshold. Outside the discharge, the effects of UV preionization and shock wave enhancement of the breakdown threshold are investigated.

The pulsed CO_2 laser system, the electric discharge, and the breakdown chamber are described. Langmuir probes (electrostatic) and CO_2 absorption measurements are performed on the discharge plasma which yield information on the electron and neutral atom concentrations. Electric Langmuir probes are used in regions of particular interest outside the discharge. Shock wave schlieren measurements using piezo-electric probes are also reported.

A computer model of the breakdown process is developed. Numerical calculations of the plasma build up in the laser focus are reported.

The experimental breakdown data are compared with the results of the calculations. Good agreement is obtained. This leads to the possibility of using the breakdown phenomenon as a diagnostic for electron and neutral atom components of a plasma. The feasibility of this idea is discussed.

ACKNOWLEDGMENTS

I would like to give special thanks to my supervisor, Dr. A.M. Robinson, for giving me the opportunity to work on this subject. His belief in giving me freedom to explore ideas yet providing firm guidance was most conducive for research work.

I wish to acknowledge the help extended by Dr. Peter Smy especially for the enlightening discussions on discharges and Langmuir probes.

This work would not have been accomplished without the assistance of the technical staff. I would like to take this opportunity to express my thanks to: Doug Way-Nee, Brian Hadley, Barry Haverstock, and Phil Haswell for their patience and forbearance while assisting me with laboratory equipment and for their invaluable help in building electronic apparatus; Konrad Doerrbecker, Herb Gans, and the Electrical Engineering Machine Shop staff for excellent and prompt machine work; Barry Arnold for superb optical components.

Special mention is due to Barbara J. Gallaiford for speedy and excellent typing of the manuscript. The drawings and figures were expertly done by Linda Haswell. The photographs were prepared by Jim George.

The financial assistance of the National Research Council of Canada and the University of Alberta is gratefully acknowledged.

TABLE OF CONTENTS

CHAPTER PAGE

I INTRODUCTION 1

II REVIEW OF PREVIOUS LASER INDUCED GAS BREAKDOWN WORK 4

2.1 Outline 4

2.2 Stages of Gas Breakdown 4

2.3 Multiphoton Ionization 5

2.4 Cascade Ionization 6

2.5 Experimental Results 8

2.6 Expansion and Extinction Stages 11

2.7 Summary 11

III DEFINITION OF GAS BREAKDOWN THRESHOLDS 15

3.1 Outline 15

3.2 The Breakdown Threshold 15

3.3 Dependence of ϕ on Experimental Conditions 17

3.4 Breakdown Threshold in Numerical Calculations 19

CHAPTER PAGE

IV CO_2 LASER SYSTEM AND ELECTRIC DISCHARGE PREIONIZER 22
4.1 Outline 22
4.2 Description of Experimental Setup 22
4.3 Pulsed Laser-Amplifier System 23
4.4 Electric Discharge Preionizer 25

V ELECTRON, ION, AND NEUTRAL ATOM DENSITY: THE REGION OUTSIDE THE DISCHARGE 40
5.1 Outline 40
5.2 Introduction 40
5.3 Probe Theory 41
    5.3.1 Derivation of Formulae 42
    5.3.2 Asymptotic Solutions 45
    5.3.3 Transition Region 46
5.4 UV Photoion Measurements 49
    5.4.1 Experimental Setup 49
    5.4.2 Probe Design 49
    5.4.3 UV Photoion Density in Ar 50
    5.4.4 Curve Fitting and Extrapolation 53
    5.4.5 Error in $n_{ave}(t)$ 55
    5.4.6 UV Photoionization Mechanism 55
5.5 Pressure Probe Measurement of Shock Wave Strength 57

CHAPTER PAGE

5.5.1 Pressure Probe Characteristics 57
5.5.2 Measurement of Shock Strength 58
5.5.3 Discussion 61

VI ELECTRON, ION, AND NEUTRAL DENSITY: IN THE DISCHARGE 83
6.1 Outline 83
6.2 Interferometer Principles 83
6.3 Interferometric Measurement of Electron Density 84
6.3.1 Optical Refractivity of an Ar Plasma 84
6.3.2 Mach-Zehnder Interferometer 85
6.3.3 Cylindrical Geometry 85
6.3.4 Electron Density Distributions 86
6.4 Absorption of 10.6μm Radiation 87
6.5 Probe Measurements 88
6.5.1 Probe Theory 88
6.5.2 Probe Circuit 89
6.5.3 Results of Measurements 90
6.5.4 Plasma Decay Mechanisms 92
6.6 Jamin Interferometer 93

CHAPTER PAGE

VII A CASCADE MODEL OF LASER INDUCED GAS BREAKDOWN 117

7.1 Outline 117

7.2 Introduction 117

7.3 Breakdown Condition 119

7.4 Charge Collection Results 123

7.5 Boltzmann Equation 128

7.5.1 Integral Term 129

7.5.2 Conservation Laws 131

7.5.3 Density and Temperature Equations 132

7.5.4 Maxwellian Distributions 134

7.5.5 Numerical Solution 136

VIII BREAKDOWN THRESHOLD MEASUREMENTS: COMPARISON WITH CASCADE THEORY PREDICTIONS 155

8.1 Outline 155

8.2 Experimental Setup 155

8.3 Breakdown Measurements Outside the Discharge 156

8.4 Breakdown Measurements Inside the Discharge 158

8.5 Discussion 160

IX SUMMARY AND CONCLUSIONS 187

REFERENCES 191

APPENDIX 198

LIST OF TABLES

TABLE	DESCRIPTION	PAGE
6.1	Average Electron Temperature	88
7.1	Summary of Cross-Sections	138

LIST OF FIGURES

FIGURE PAGE

2-1 Typical Transmitted Laser Pulse Shapes With and Without Breakdown 13

2-2 Pressure Dependence of CO_2 Laser Induced Breakdown Threshold for Various Gases 14

3-1 Dependence of Transmitted Laser Energy on the Incident Laser Energy 20

3-2 Dependence of Laser Energy on the Probability of Breakdown 21

4-1 Experimental Setup Used in Breakdown Measurements 28

4-2 CO_2 Laser Output Pulse Shapes 29

4-3 Stability of Laser System Output 30

4-4(a) Beam Profile of Laser Oscillator 31

4-4(b) Beam Profile of Laser Oscillator-Amplifier System 32

4-5 Electric Discharge Circuit Diagram 33

4-6(a) Electric Discharge Current 34

4-6(b) Electric Discharge Voltage 35

4-7(a) Dependence of Discharge Voltage on Electrode Separation 36

4-7(b) Dependence of Discharge Voltage on Electrode Separation 37

4-7(c) Dependence of Discharge Voltage on Electrode Separation 38

5-1 Ion Orbits in Plasma Sheath 62

FIGURE PAGE

5-2 Radius of Plasma Sheath Around Cylindrical Probe 63

5-3 Impact Parameter Y_{01} and θ_{01} as a Function of ρ_0^{-2} 64

5-4 Ion Density as a Function of Probe Current 65

5-5(a) Probe Current Versus Probe Bias Voltage 66

5-5(b) Probe Current per Unit Length as a Function of Bias Voltage 67

5-6 Experimental Setup Used in Probe Measurement 68

5-7 Probe Design and Circuit 69

5-8 Photoplasma Probe Currents 70

5-9 Schematic Diagram Showing ℓ_{eff} at Various Times 71

5-10 Plasma Radius, $\ell_{eff}/2$ Versus Time 72

5-11(a) Photoplasma Density Versus Time 73

5-11(b) Photoplasma Density Versus Time 74

5-11(c) Photoplasma Density Versus Time 75

5-11(d) Photoplasma Density Versus Time 76

5-12 Variation of Photoplasma Density with Distance from UV Source 77

5-13 Pressure Transducer Signal 78

5-14 Linearity of Piezoelectric Pressure Transducer Response 79

5-15(a) Shock Strength as a Function of Distance 80

5-15(b) Shock Strength Versus Distance 81

5-15(c) Shock Strength Versus Distance 82

6-1 Mach-Zehnder Interferometer 95

6-2 Diagram Used in Abel Transformation 96

6-3 Mach-Zehnder Interferometer Signal 97

FIGURE PAGE

6-4(a) Observed Fringe Shifts at Various Times 98

6-4(b) Observed Fringe Shifts at Various Times 99

6-4(c) Observed Fringe Shifts at Various Times 100

6-4(d) Electron Density as a Function of Radius 101

6-4(e) Electron Density as a Function of Radius 102

6-4(f) Electron Density as a Function of Radius 103

6-5 CO_2 Absorption By Discharge Plasma 104

6-6(a) Discharge Plasma Transmittance of 10.6μm Radiation 105

6-6(b) Discharge Plasma Transmittance of 10.6μm Radiation 106

6-6(c) Discharge Plasma Transmittance of 10.6μm Radiation 107

6-7 Langmuir Probe Current 108

6-8 Probe Current Versus Probe Bias Voltage 109

6-9(a) Radial Electron Distribution 110

6-9(b) Radial Electron Distribution 111

6-9(c) Radial Electron Distribution 112

6-10 Decay of Discharge Electron Density 113

6-11 Jamin Interferometer 114

6-12 Jamin Interferometer Fringe Shifts 115

6-13 Neutral Density in the Discharge Versus Time 116

7-1 Electron Density in the Focus at the End of the Laser Pulse as a Function of $(\nu_g - \nu_\ell)\tau$ 141

7-2 Charge Collector Input Circuit 142

7-3(a) Charge Collector Characteristic 143

7-3(b) Charge Collector Characteristic 144

7-4(a) Number of Electron-Ion Pairs Collected When a Spark is Formed 145

FIGURE		PAGE
7-4(b)	Number of Electron-Ion Pairs Collected When a Spark is Not Formed	146
7-5(a)	Laser Heating Rate as a Function of Electron Temperature	147
7-5(b)	Ionization, Excitation and Elastic Collision Loss Rates	148
7-5(c)	Diffusion Loss Rates	149
7-6	Effective Diffusion Coefficient	150
7-7	Laser Pulse Shape Used in Numerical Calculations	151
7-8	Measured and Calculated Thresholds Without Pre-ionization	152
7-9	Peak Electron Temperature and Time at Breakdown as a Function of Gas Pressure	153
7-10	Charge Buildup in Laser Focus for Various Laser Energies and Gas Pressures	154
8-1	Experimental Setup Used in Breakdown Measurements	163
8-2(a)	Breakdown Threshold Outside the Discharge	164
8-2(b)	Breakdown Threshold Outside the Discharge	165
8-2(c)	Breakdown Threshold Outside the Discharge	166
8-2(d)	Breakdown Threshold Outside the Discharge	167
8-3	Laser Peak Power at Threshold Versus Initial Electron Density at the Focus	168
8-4(a)	Breakdown Threshold Outside the Discharge	169
8-4(b)	Breakdown Threshold Outside the Discharge	170
8-4(c)	Breakdown Threshold Outside the Discharge	171

FIGURE PAGE

8-4(d) Breakdown Threshold Outside the Discharge 172

8-4(e) Breakdown Threshold Outside the Discharge 173

8-4(f) Breakdown Threshold Outside the Discharge 174

8-5 Computed Laser Peak Power at Threshold as a Function of the Initial Electron Density 175

8-6(a) Neutral Atom Density in the Shock as a Function of Distance 176

8-6(b) Neutral Atom Density in the Shock as a Function of Distance 177

8-6(c) Neutral Atom Density in the Shock as a Function of Distance 178

8-7 Breakdown Thresholds Inside the Discharge Versus Time for Various Pressures 179

8-8(a) Neutral Density in the Discharge Versus Time 180

8-8(b) Neutral Density in the Discharge Versus Time 181

8-8(c) Neutral Density in the Discharge Versus Time 182

8-9 Breakdown Threshold 8 mm from the Discharge 183

8-10(a) Electron Density as a Function of Time at a Distance of 8 mm from the Discharge 184

8-10(b) Variation of Neutral Density with Time 8 mm from the Center of the Discharge 185

8-11 Variation of Photoplasma Density with Distance from UV Source 186

CHAPTER I

INTRODUCTION

One of the most interesting aspects of the interaction of intense electromagnetic fields with matter is the breakdown of gases under the influence of a strong laser light. Gases which are normally transparent to light at low laser intensity become strongly ionized at some value of the intensity called the breakdown threshold ,resulting in strong absorption of the incident laser light and breakdown of the gas. The plasma produced expands rapidly and emits light and, hence, it is called a "spark". A brief review of the literature on laser induced gas breakdown with emphasis on CO_2 laser breakdown can be found in Chapter II.

Laser induced breakdown has attracted considerable attention in recent years. Numerous investigations have been performed both experimentally and theoretically which have provided much information on the nature of the phenomenon. The dependence of the breakdown threshold on gas pressure, focal length, ionization potential, pulse length and other parameters have already been investigated. In the case of moderate to high pressures,the breakdown thresholds have been explained by the cascade theory of laser induced gas breakdown which says that the electon-ion density produced by a focused laser beam increases exponentially through an avalanche process, i.e., each electron present in the focal volume gains energy from the laser field via inverse bremsstrahlung and creates another electron through an ionizing collision with a gas atom or molecule. The two electrons then repeat the above process until a sufficiently high electron density is reached at the focus.

The cascade theory assumes the existence of initial or priming electrons at the focal volume to start the avalanche at the start of the laser pulse. The more electrons there are at the focus, the fewer generations of electrons needed for breakdown to occur and hence, the smaller the required laser power. Breakdown measurements with deliberate preionization of the gas have been performed and indeed, a lowering of the threshold has been observed.

The primary motivation for doing this project is to determine the dependence of the breakdown threshold on the initial preionization and attempt to explain the results using cascade theory. Although cascade theory has adequately explained breakdown threshold measurements at high pressures, all experiments so far have only been "global" verifications of the theory and there are still some who doubt its validity. A successful cascade theory prediction of the dependence of the threshold on the initial electron density would be strong evidence in its favor. To this end, a CO_2 laser is focused in Ar which has been preionized by an electric discharge. The laser is focused not only in the region filled by the discharge but also in the uv preionized volume away from it. This provides a broad range of initial conditions needed in the study. The effect of temperature on the breakdown threshold can also be studied in this system.

The dependence of the threshold on gas pressure or equivalently, the neutral density, is well known. Hence, if the electron density of a partially ionized gas is known, it may be possible to use the breakdown phenomenon to measure neutral gas density. Gas breakdown as a diagnostic tool would be very useful because it could provide a very high degree of space and time resolution, these being determined by the focal spot size and

the laser pulse length, respectively. At the same time, it would be a very convenient diagnostic tool because we would not need very sophisticated detection systems. This work will investigate the possibilities of gas breakdown being employed as a diagnostic tool.

The exact conditions in the focus at breakdown are not known. There can be a multitude of possible definitions that can and have been used in various experiments. These include the onset of light emission or laser absorption, visual observation of the spark and so on. Theoretically, threshold can be defined as the laser power which will give a certain value of the electron-ion density at the focus. This problem is discussed in greater detail in Chapter III.

A description of the various experimental procedures and setups used are presented in Chapter IV. The various diagnostics performed on the uv photoplasma and the electric discharge are presented in Chapters V and VI. Chapter V also includes a discussion of probe theory which attempts to extend existing probe theories for high pressure flowing plasmas reported in the literature. In Chapter VII, a cascade model of gas breakdown is constructed and numerical calculations are performed which adequately explain the experimental results. The measured breakdown thresholds are reported in Chapter VIII. A comparison with cascade theory predictions are made. The possibility of using the breakdown phenomenon as a diagnostic for electron and neutral densities is explored. Finally, Chapter IX contains a discussion and summary of the important results of this investigation.

CHAPTER II

REVIEW OF PREVIOUS LASER INDUCED GAS BREAKDOWN WORK

2.1 Outline

A brief review of previous work on laser induced gas breakdown is presented. Multiphoton and cascade ionization as possible electron production mechanisms occurring in the laser focus are discussed. The dependence of the breakdown threshold on pressure, focal length, pulse length, ionization potential, frequency, and other parameters as predicted by theory and as measured by various investigators are summarized. Cascade theory is seen to apply to gas breakdown at high pressures when using long laser pulses.

2.2 Stages of Gas Breakdown

The first observation of laser induced gas breakdown was reported by P.D. Maker, R.W. Terhune, and C.M. Savage in 1963[1]. This was subsequently followed by vigorous research by many investigators. Reviews of laser induced breakdown work up to 1971 are available in the literature[2-5].

The breakdown phenomenon is usually divided into four stages as follows:

1. preionization or initiation
2. cascade stage
3. plasma development and expansion
4. extinction

In this work, only the cascade stage will be discussed in any detail. The

other stages are thoroughly discussed in the review papers quoted above. A good discussion of the initial stages of breakdown is given by Papoular[6].

A striking feature of laser induced gas breakdown is the sudden change in the opacity of the gas to laser light. This is due to the sudden increase in the plasma density at the focal volume in the presence of the intense optical field. Figure 2.1 shows typical laser pulse shapes transmitted with and without breakdown[7]. Two processes that can explain the ionization by high intensity light are multiphoton ionization and cascade ionization.

2.3 Multiphoton Ionization

In multiphoton ionization, several photons are absorbed simultaneously by a bound electron resulting in its detachment from the parent atom. This is the ionization mechanism believed to operate during the preionization stage of gas breakdown. At this time gas atoms or impurities with low ionization potentials are directly ionized by the laser electric field.

The theory of multiphoton ionization has been developed into an elegant mathematical theory by numerous authors[7-11]. All multiphoton theories basically lead to a common prediction. The number of ions N_i produced by light of intensity I is

$$N_i \propto N_a \, (Ih\nu)^{N_o}$$

where N_a is the neutral atom density and N_o is the number of photons whose total energy is equal to or greater than the ionization potential of the gas. Experimentally, multiphoton ionization can be observed by going to

very low pressures so that the electron mean free path is greater than the focal spot diameter or by using ultrashort laser pulses such that the pulse length is shorter than the characteristic cascade time. In all cases, theoretical predictions are orders of magnitude higher than experimental results. This may be due to smearing of levels due to the very high local fields resulting in quasi-resonant transitions.

2.4 Cascade Ionization

In the case of high pressures or long laser pulses cascade ionization is believed to occur in the focus. The first electrons produced either by the multiphoton process or by deliberate preionization of the gas (preionization stage) can absorb energy from the laser field during collisions with neutral atoms via inverse bremsstrahlung. The electrons that acquire kinetic energies greater than the ionization potential of the gas can ionize the gas during collisions with gas atoms. The electron density increases exponentially:

$$N_i = N_o e^{\gamma t} = N_o 2^{t/\tau}$$

where $\gamma = \frac{1}{\tau} \ln 2$ is the cascade development constant and τ is the time it takes to double the electron concentration. A more detailed discussion of cascade theory can be found in Chapter VII. References 12-15 also give good discussions of cascade theory and its basic results. For now we summarize its important features.

1. The rate the electrons gain energy from the field is the same as that in microwave theory, namely

$$\frac{d\varepsilon}{dt} = \frac{e^2E^2}{m} \frac{\nu_{eff}}{\omega^2 + \nu_{eff}^2}$$

Here $\nu_{eff} = n_a v\sigma_{tr}$ is the collision frequency, n_a is the neutral atom density, v is the electron velocity, σ_{tr} is the collision cross-section for momentum transfer, e and m are the charge and mass of the electron and E and ω are the intensity and frequency of the laser electric field.

2. The significant loss mechanisms during the electron build-up are electron diffusion out of the focal volume, elastic and inelastic collisions, and at high pressures, electronic recombination. Excitation may sometimes be a gain process depending on the closeness of the excited energy level to the ionization continuum, the laser intensity and the photon energy or when the excited level is a quasi-resonant level. Diffusion loss dominates at very low pressures and is manifested as a characteristic p^{-2} dependence of the threshold on pressure. At moderate pressures and long pulses, the threshold is determined by the laser pulse length and the initial electron density and is seen as a p^{-1} dependence of the threshold on gas pressure. The elastic loss term is independent of pressure and becomes important only at very high pressures. Excitation loss is more important at lower laser fluxes and since the threshold decreases with increasing pressure, its effect is relatively greater at high pressure. Excitation thus weakens the pressure dependence of the threshold especially

in the case of gases with many excited levels such as molecular gases[16,17]. Numerical calculations[13,18-19] taking into account these gain and loss mechanisms have been performed and have successfully accounted for measured breakdown thresholds.

2.5 Experimental Results

Dependence of the breakdown threshold on gas pressure

The pressure dependence of the threshold has been determined using ruby, neodymium and CO_2 lasers[12-21]. Attention has been focused on noble gases, nitrogen, and CO_2. For example, Meyerand and Haught[20] studied breakdown of He and Ar. In Figure 2-2 the results of Hill, James and Ramsden[17] using a CO_2 laser are reproduced showing the typical pressure dependence of the threshold. The slopes in the decreasing portion of the curves are between -1 and -2 as predicted by cascade theory. The existence of the threshold minimum when $\omega \simeq \nu_{eff}$ is also predicted by cascade theory. A high magnetic field will tend to reduce the diffusion loss out of the focal volume. Hence it is expected that there will be a decrease in the breakdown threshold upon application of an external magnetic field. This was observed by Cohn, *et.al.*[13].

Dependence of the threshold on the ionization potential of the gas

Experimental results show[22-23] that the threshold generally increases with increasing ionization potential. This is predicted by both cascade and multiphoton theories. The only exception is Ne which has a higher breakdown threshold than He.

Dependence of the breakdown threshold on the radiation frequency

The frequency dependence of the breakdown threshold has been studied by Buscher, *et. al.*[24], Akhmanov, *et. al.*[25], Smith[12], and Morgan, *et. al.*[15]. Buscher, *et. al.* and Akhmanov, *et. al.* used 1.06 μm radiation from a Nd glass laser and its harmonics. Morgan, *et. al.* used ruby, Nd, and a tunable dye laser. It is generally observed that the threshold increases with frequency as ω^2 in agreement with theory. However, at still higher frequencies, the threshold starts to decrease. This might be due to enhancement of the photoionization of the excited atoms and an increase in the probability of producing the priming electrons from impurities.

Dependence of the threshold on the mode pattern of the laser output

A multimode laser when focused will produce a very inhomogeneous intensity distribution. Some areas in the focal spot will have intensities up to 2 orders of magnitude higher than the mean intensity. For a Gaussian mode pattern, on the other hand, the maximum value of the intensity at the center of the spot is only 1.4 times the average value. Smith and Tomlinson[26] and Alcock, *et. al.*[27] have found no significant difference in the breakdown threshold when one uses a single mode or multimode laser. This suggests that the diffusion processes are effective in averaging out the effect of the inhomogeneities and breakdown occurs under the effect of the average field.

Dependence of the breakdown threshold on the focal volume

The focal length dependence of the threshold has been studied and reported in references 28-30. The threshold is a function of the focal length since the focal spot diameter and therefore the diffusion length is proportional to it. However, even at high pressures, the threshold has been observed to depend on the focal length. Experimental results also tend not to agree with theoretically predicted thresholds. It is believed that this anomalous focal spot size dependence is due to the presence of dust or other impurities which are easily ionized[30]. The larger the focal spot, the greater the probability of finding an impurity particle in it and hence, the lower the breakdown threshold.

Dependence of the breakdown threshold on the laser pulse length

The dependence of the threshold on the pulse length is determined by the dominant loss mechanism. For short laser pulses, diffusion loss can be neglected and the threshold varies inversely as the pulse length. For very long laser pulses, the threshold is practically independent of the pulse length, depending mainly on the peak intensity. The pulse length dependence of the breakdown threshold has been experimentally determined by several investigators for long and short pulses[29,31,32]. Measurements by Hacker, Cohn and Lax[21] point to the conclusion that cascade theory can describe the breakdown process.

Dependence of the breakdown threshold on the initial electron density

Little work has been done on this aspect of laser induced gas breakdown to the present. Breakdown thresholds in uv preionized Ar were

performed but the thresholds were not related to the actual initial electron concentration[33-34]. Others have focused the laser right into a discharge[35,36]. In this case the initial electron concentration can be estimated from the current and voltage across the discharge if the electron temperature is assumed to be equal to the gas temperature which was taken to be 300 K.[36] In all measurements with preionization, a depression of the breakdown threshold was observed with increasing electron preionization. This was attributed to a transition from free to ambipolar diffusion loss during the cascade. Also, the higher the initial electron density, the lower number of electron generations required before breakdown as would be expected for a cascade process. A closer investigation of this aspect of laser induced breakdown and in particular breakdown of uv preionized Ar is the subject of the present work.

2.6 Expansion and Extinction Stages

After the occurrence of breakdown, the plasma becomes highly absorbing and is rapidly heated up by the incident laser pulses. Hydrodynamic expansion and shock expansion now take place. The spark tends to move toward the direction of the laser aside from the usual radial expansion. The expansion towards the laser is similar to a detonation wave. At the end of the pulse, the plasma cools down and decays mainly by recombination and diffusion. These stages of gas breakdown are discussed in great detail in references 2-4 and 37-38.

2.7 Summary

The cascade theory of laser induced gas breakdown has adequately explained most of the experimental results obtained to date, especially in

the case of high pressure and long laser pulses. The question of the effect of excitation on the breakdown process is not yet clear and further work needs to be done.

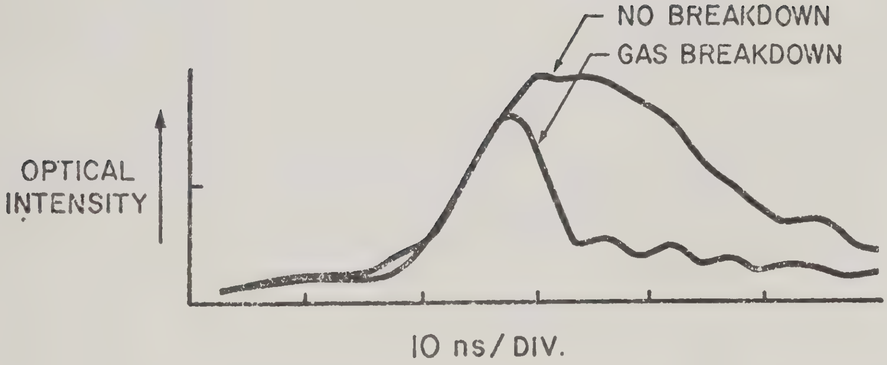

Figure 2-1 Transmitted Laser Pulse Shapes With and Without Breakdown (7)

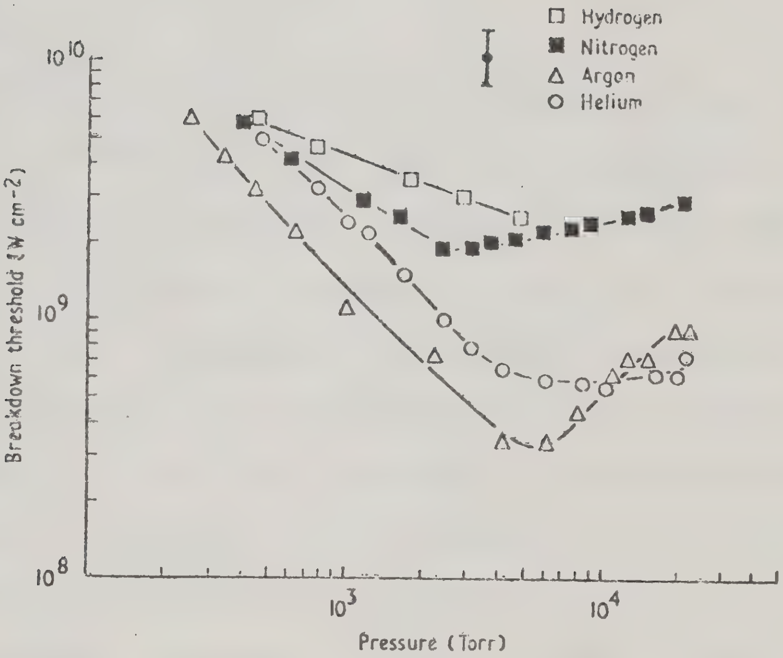

Figure 2-2 Pressure Dependence of CO_2 Laser Induced Breakdown Thresholds for Various Gases (17)

CHAPTER III

DEFINITION OF GAS BREAKDOWN THRESHOLDS

3.1 Outline

Breakdown threshold has not been defined in the same manner by different workers in this field. These varying definitions as reported in the literature are discussed. Regardless of the definition used, however, the probability of breakdown is found to be a strong function of the laser power. In this work, the breakdown threshold, ϕ is defined as a 50% probability of visually observing the formation of the spark. This is the most common definition of breakdown threshold and by far the most convenient to apply experimentally. The effects of various experimental conditions on measured thresholds are considered and the procedures implemented to eliminate these problems are discussed.

3.2 The Breakdown Threshold

Breakdown is usually achieved by focusing the laser by a lens or mirror of short focal length to create a very high radiation field in the focal spot. The dimensions of the focal spot can be measured experimentally or computed theoretically. However, there is sufficient inaccuracy in the spot size thus arrived at such that in breakdown work, agreement between two sets of measurements by different people within a factor of two may be considered very good agreement. This will account for the differences in the thresholds published.

The breakdown threshold, ϕ is determined by the pulse length. For long pulses (> 10 ns) breakdown occurs when the rate of energy absorption overcomes electron losses due to diffusion and recombination and energy losses such as elastic and inelastic collisions[1,2]. In this case ϕ is usually given by the peak laser intensity in W/cm^2. For sufficiently short pulses, the losses are negligible and breakdown occurs when the pulse has sufficient energy to rapidly ionize the gas. Here, ϕ is measured in terms of energy flux and is given in J/cm^2.

Experimentally, ϕ can be defined in several ways which may not be equivalent to each other. For example, breakdown threshold, ϕ has been defined as the laser energy or power that will give a 50% probability of visually observing a spark[3,4]. Others have chosen other probability values such as 20%[5]. Still others monitor the amount of light emitted by the plasma with photomultipliers. Breakdown can then be defined as the instant when a certain amount of light is emitted by the plasma[6]. Still another way of defining the occurrence of breakdown is the point when the total transmitted laser energy is a predetermined fraction of the incident laser energy[7,8]. Charge collection plates may be used to measure the total number of electron-ion pairs created in the focus with breakdown being defined as the certain value of the electron concentration.

Regardless of the definition of breakdown threshold selected, the threshold measured experimentally is well defined. For example, Tomlinson and Damon[7] measured the transmitted energy and plotted this against the incident laser energy. Their results are reproduced in Figure 3-1. The sharpness of the curve near threshold indicates the sharp distinction between no breakdown and breakdown.

In the present work, breakdown threshold is defined as the laser power that will give a 50% probability of observing the appearance of the spark. ϕ was measured without preionization from very low (25 Torr) to high pressure (600 Torr). The results are shown in Figure 3-2. Note that the threshold is a very strong function of the incident laser power, i.e., a small change in incident power will lead to a large change in the probability of observing a spark. In these measurements, a CO_2 laser was focused by a 5 cm focal length NaCℓ lens in Ar. Hacker, *et. al.*[9] also observed a change in probability from 0% to 100% with a 5% change in laser energy. In the present work, the laser is fired into the breakdown chamber and the number of sparks in every ten shots times ten is the probability of breakdown in percent. Because of the sensitivity of the probability of breakdown to incident laser power, in most experiments it is sufficient to determine the probability of observing a spark at two values of the laser energy and interpolating or extrapolating to 50% probability. Of course, these two probability values should not equal 0% or 100%.

3.3 Dependence of ϕ on Experimental Conditions

Small amounts of impurities can alter the breakdown threshold[10]. These impurities may have low ionization potentials and can easily be ionized by the laser providing large amounts of initial electrons to start the avalanche. Avalanche breakdown assumes that there is at least one electron in the focal volume at the start of the laser pulse. Since the focal volume is usually very small ($V \simeq 10^{-5} cm^3$) while the background electron density $n_o \simeq 10^{-3} cm^{-3}$ without deliberate preionization, the

probability of finding an electron at the focal volume to initiate the avalanche is small. Changing n_o can change ϕ in a very complicated manner. Large particulates present in the focal volume may be ionized leading to formation of shock waves. In the region of the shock, ϕ will be changed due to increased neutral atom density.

These considerations indicate the need to condition the gas before measurements are made in order to ensure that the thresholds obtained are true avalanche thresholds and free from the effects of impurities, particulates and the statistical nature of breakdown at low initial electron densities. Conditioning is achieved by firing the laser above threshold into the gas thus producing a spark consistently. The laser has to be fired into the breakdown chamber at a sufficiently rapid rate so that there is at least one electron at the focal volume at the start of the next pulse. The energy of the incident beam is then gradually attenuated until the desired probability of breakdown is reached. In gases conditioned in this way, the thresholds will be much more reproducible indicating the presence of priming electrons. That the conditioning is not due to dust or impurities that may have been blown off the lens or the walls of the chamber can easily be experimentally verified[10]. Breakdown measurements are usually performed in chambers with static gas fills. It is not unusual to observe that it is harder to break down fresh gas compared to gas that has been broken down several times. It is tempting to say that this is due to dust blown off from the walls of the chamber. If this is indeed the case, then we expect a continuous lowering of the discharge as we fire more and more shots into the gas. However, this is not observed. In actual fact, the threshold levels off after a few shots. Furthermore, if the laser is now

pulsed at a slow rate, the statistical nature of the breakdown returns and the gas becomes more difficult to break down. This suggests that conditioning is not due to dust or particulates blown from the chamber walls. A rate of 1 pulse/sec was found to be sufficient to condition the gas and assure the presence of priming electrons in the focus at the start of each pulse. Thus the thresholds obtained are true avalanche thresholds.

3.4 Breakdown Threshold in Numerical Calculations

In most theoretical work, breakdown is defined as the occurrence of a fixed electron density, n_{bd} in the focus. The exact concentration at breakdown is difficult to determine, however. Many workers just assume full ionization as a reasonable value. Charge collection experiments,on the other hand, indicate that 10^{13} electron-ion pairs are created when a spark is produced. However, this may be different from the electron number at the focus at breakdown since it includes all charges created after breakdown. At best it sets only an upper limit to n_{bd}. A charge collector was constructed in an attempt to measure the electron density, n, as a function of the incident laser power. This will be described in more detail later on. However, the strong dependence of the breakdown probability on the laser power doomed this attempt from the start. Nevertheless, it managed to set a lower limit to n_{bd}. How this problem can be circumvented in numerical calculations will be discussed in Chapter VII.

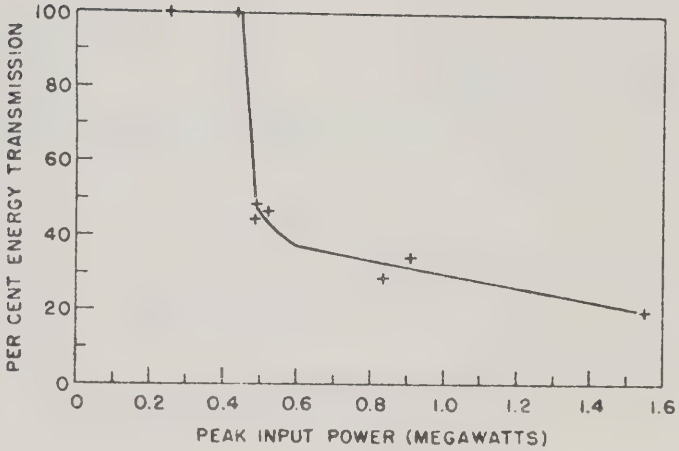

Figure 3-1 Dependence of Transmitted Laser Energy on the Incident Laser Energy (7)

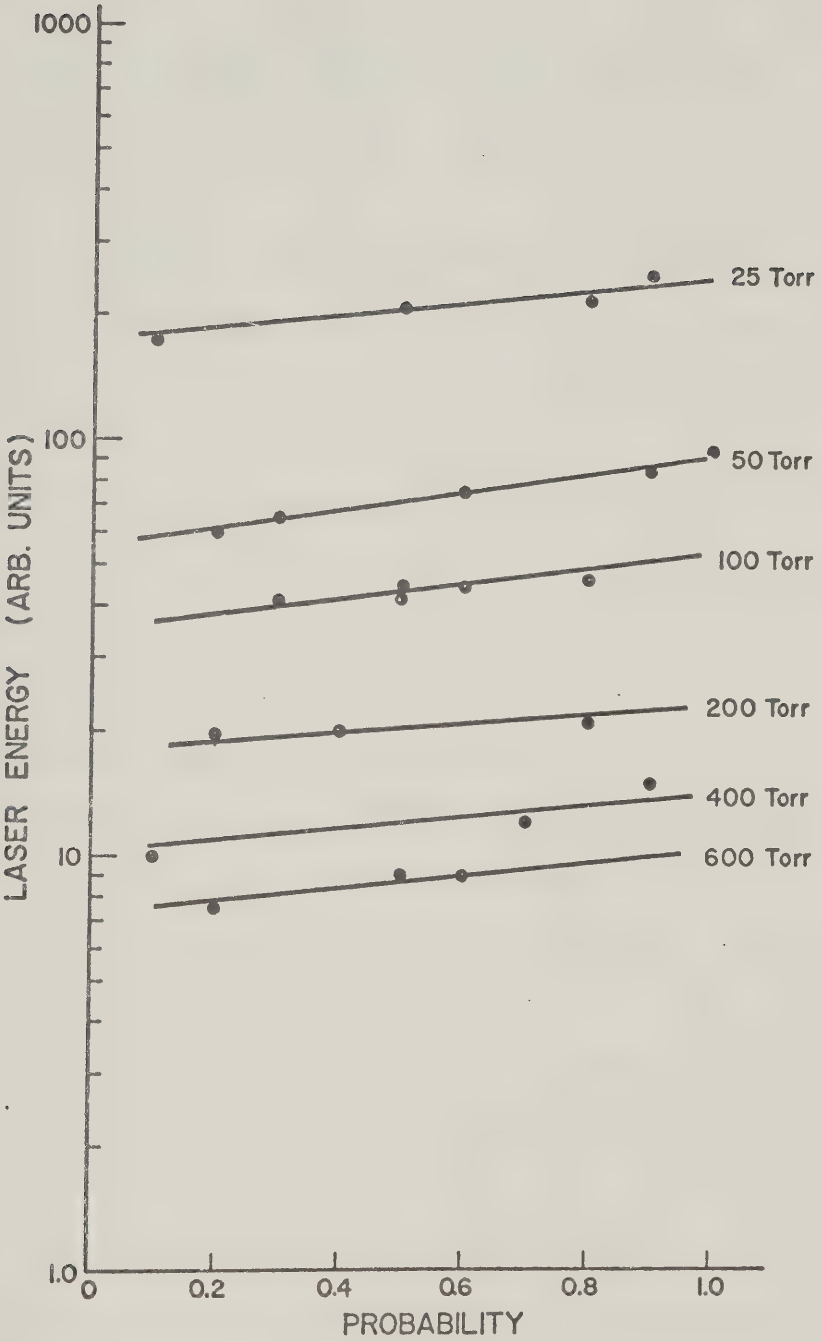

Figure 3-2 Dependence of Laser Energy on the Probability of Breakdown. Threshold is defined as 50% probability of breakdown.

CHAPTER IV

CO_2 LASER SYSTEM AND ELECTRIC DISCHARGE PREIONIZER

4.1 Outline

The experimental setup used is described in detail. Parameters of the TEA CO_2 laser system used in the breakdown measurements are given. Pulse shape, energy, mode pattern and stability of the laser output are also discussed.

The electric discharge preionizer used in the experiment is studied in detail. Current and voltage across the discharge as a function of time are presented.

4.2 Description of Experimental Setup

The experimental setup consisted of three main components: a CO_2 oscillator-amplifier system, the electric discharge preionization source, and the breakdown chamber. A schematic diagram of the setup is shown in Figure 4-1. The output of the CO_2 oscillator-amplifier system was focused by a 5 cm focal length NaCℓ lens into the breakdown chamber which had been filled with Ar gas at pressures varying from 100-6000 Torr. The laser was focused inside and outside the discharge region. The volume occupied by the discharge was ionized by the electric current and the gas outside it preionized by uv photons from the discharge. By varying the time delay between firing of the discharge and the laser and the distance between the focused beam and the discharge, a large range of initial electron densities was obtained. Most of the measurements were made at 200, 400, and 600

Torr. A small fraction of the incident beam was sampled by using an NaCℓ beam splitter in conjunction with a photon drag detector and an energy detector which had been calibrated against a commercially available Gen-Tec energy detector. An attenuation cell placed between the laser and the breakdown chamber permitted regulation of the laser intensity incident on the breakdown chamber. Regulation was achieved by varying the pressure of propylene gas inside the cell[1,2].

4.3 Pulsed Laser-Amplifier System

The pulsed laser-amplifier system used has been discussed before in detail[3]. The laser oscillator was a helical TEA CO_2 discharge laser with a peak power of approximately 1 MW and a total energy of 0.5 J. The output pulse had a rise time of approximately 60 ns and a width of 200 ns followed by a long tail several microseconds long.

The amplifier was a Rogowski profile uv preionized TEA discharge unit. It had a typical peak small signal gain of 0.04 cm^{-1}. The oscillator output was made to pass three times through the amplifier providing a peak power gain of ~ 10 and an energy gain of ~ 6. The initial part of the oscillator pulse was amplified more than the later part thus producing an output pulse with the same rise time as the oscillator pulse but with a half-width of only 100 ns. Oscillograms of the oscillator and amplifier outputs are shown in Figure 4-2 (a) and (b), respectively. Oscillator self-mode locking could not be observed in these oscillograms due to oscilloscope bandwidth limitation.

Synchronization of the oscillator and amplifier discharge was important not only for maximum laser output but more importantly, to prevent

arcing in the amplifier discharge.[3] If the oscillator was fired before the amplifier, sufficient oscillator power was generated which can cause localized preionization and arcing in the amplifier. Synchronization was achieved using multivibrator delay units.

The laser output consisted of 3 to 4 transitions in the P branch: P16, P18, P20, and P22. However, most of the energy was concentrated in the P20 transition. The contribution of each line in the total output was not determined since it is not critical in gas breakdown measurements.

The oscillator output energy varied less than 10 percent from shot to shot when fired at the rate of one pulse a second. The oscillator-amplifier system was not as stable, the output varying by about 15% which is still an acceptable value. Figures 4-3 (a) and (b) show the variation in the output energy of the oscillator and the oscillator-amplifier system, respectively.

Although the mode pattern of the output did not remain the same for all shots, most were "Gaussian-like" as observed on burn patterns on polaroid film. This was possible only with an iris inside the laser cavity which suppressed all other modes except the fundamental. A pinhole (< .5 mm diameter) and an energy detector was used to scan the beam energy distribution. Profiles obtained are presented in Figures 4-4 (a) and (b). The half-width of the beam was approximately 1 cm and was not affected by the amplifier.

By scanning the beam at two positions 1 meter apart, the beam divergence can be determined. The beam divergence was approximately 2 mrad which is in close agreement with the theoretically computed value using Gaussian beam optics for the far field pattern.

4.4 Electric Discharge Preionizer

The circuit diagram for the electric discharge preionizer is shown in Figure 4-5. A 0.2 μF capacitor charged to 25 kV was fired through a spark gap between two pointed tungsten electrodes 14 mm apart. The current in this circuit as measured with a current transformer was a damped ringing current with a period of approximately 200 ns. The current did not damp out sufficiently fast enough which interfered with the probe measurements to be described later. Hence, a 7Ω series resistor was added to critically damp the discharge current. With this modification the discharge current was measured to be less than 40 mA fifty microseconds after the discharge was fired. Peak current was 2.8 kA and it was not sensitive to gas pressure. Oscillograms of the current are shown in Figure 4-6(a).

The voltage across the discharge was measured using a divider consisting of a liquid resistor in series with a 1 Ω carbon resistor with a divider ratio of 3,200:1. The divider was calibrated by applying the output of an EG & G pulse across it and the voltage output observed with an oscilloscope. The EG & G voltage was monitored using a Tektronix high voltage probe. The Tektronix high voltage probe could not be used to measure the discharge voltage directly because of inductance effects. Oscillograms of the discharge voltage are shown in Figure 4-6(b). By integrating the product of the voltage and the current, the total energy dissipated in the discharge was estimated.

The rapid release of energy in the discharge will cause an expanding shock wave to propagate through the gas. The shock will affect the breakdown thresholds as they pass through the laser focus. It will be necessary to know the shock energy in order to relate the density in

the shock to the breakdown thresholds.

The total energy converted to mechanical energy will not be equal to the total energy dissipated in the discharge but will be this energy minus the energy expended to ionize the gas and energy lost as radiation. This mechanical energy in turn can be related to the shock strength anywhere in the gas or to the gas density. If radiation losses are neglected then the total electrical energy converted to mechanical energy can be related to the total voltage across the discharge minus the voltage in the anode and cathode drops.

The technique[4] employed to determine the total energy converted to shock energy is well known. Oscillograms of the voltage across the discharge were taken for the following electrode separations: 0.4, 1.4, and 2.4 cm at pressures of 200, 400, and 600 Torr. All other parameters were held constant ($C = .2\mu F$, $L = 1\mu H$, $V = 25kV$). At a fixed instant in time one could plot the dependence of the voltage on the gap size. These graphs are shown in Figures 4-7 (a) - (c). There is a linear dependence between the voltage and the gap size.

$$V_g = V_f + E\ell$$

Here, V_g is the voltage across the gap, $V_f(t)$ is the sum of the cathode and anode fall voltages, $E(t)$ is the average electric field in the plasma and ℓ is the electrode separation. By extrapolating the data to $\ell=0$ we arrive at an estimate of the electrode voltage drops as a function of the total gap voltage. This relationship is shown in Figure 4-7 (d). Note that the cathode and the anode drops are independent of the gas pressure at the pressures considered. By subtracting this voltage from the total

gap voltage and integrating its product with the current, we arrive at values for the total electrical energy converted to shock wave energy.

$$E_{200} = 0.9 \text{ J}$$

$$E_{400} = 1 \text{ J}$$

$$E_{600} = 1.2 \text{ J}$$

The total energy dissipated in the cathode and anode fall regions was less than 1% of the total shock energy. On the other hand, approximately 85% of the initial energy stored in the capacitors was dissipated in the 7Ω series resistor.

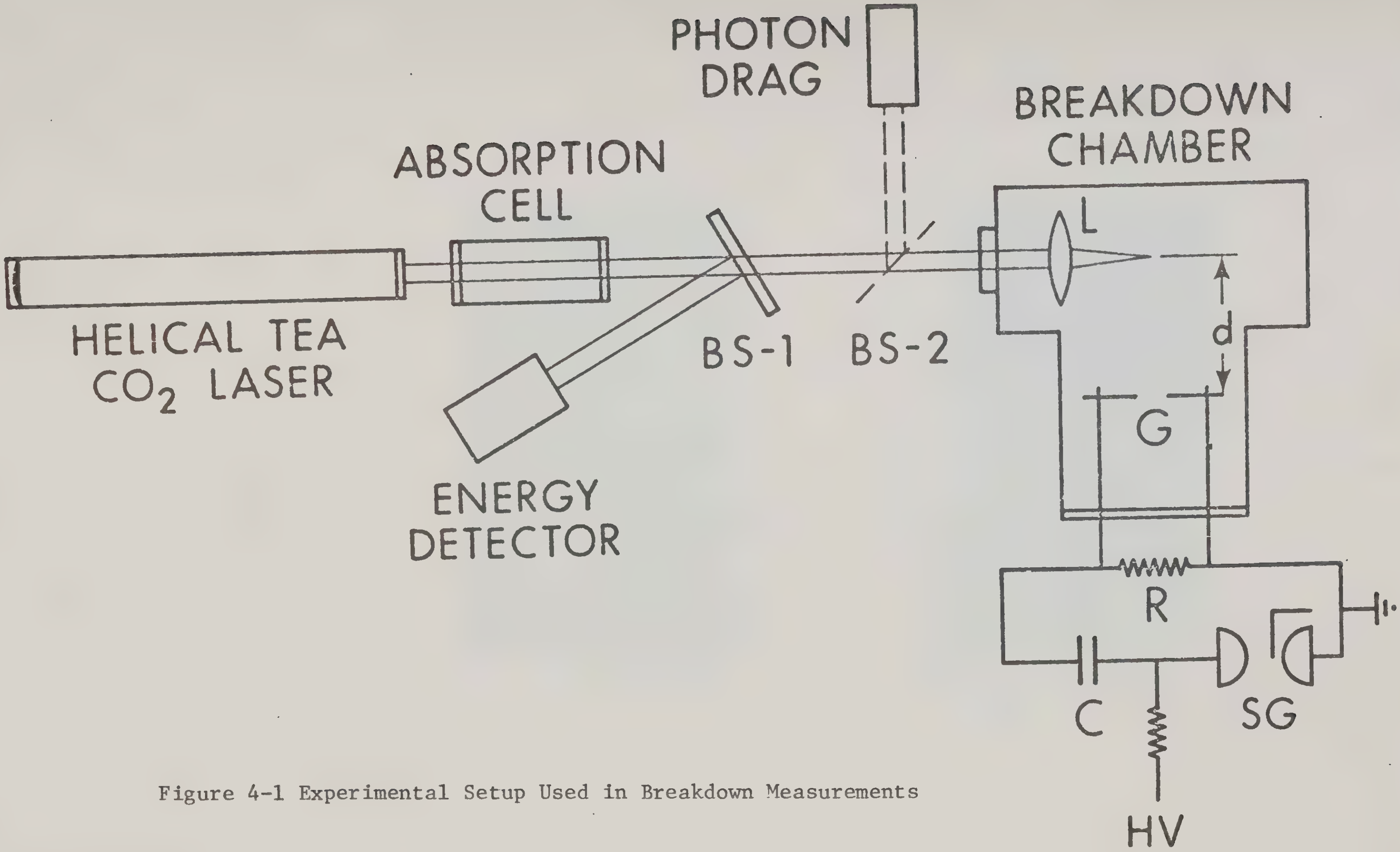
PHOTON
DRAG
BREAKDOWN
CHAMBER
ABSORPTION
CELL
L
d
HELICAL TEA
CO_2 LASER
BS-1
BS-2
G
ENERGY
DETECTOR
R
C
SG
HV

Figure 4-1 Experimental Setup Used in Breakdown Measurements

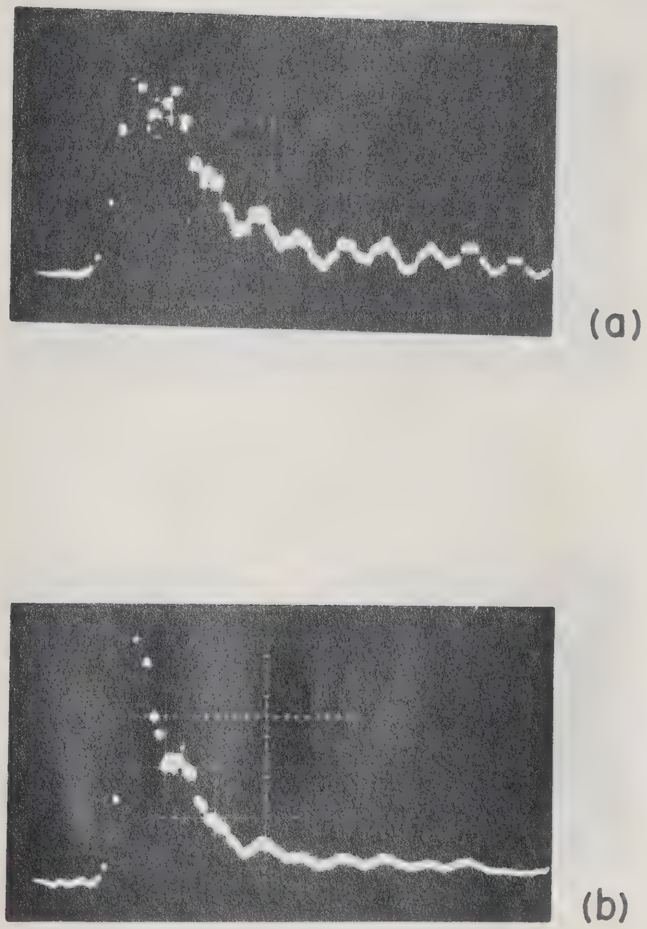

Figure 4-2 CO_2 Laser Output Pulse Shapes.
(a) Helical TEA Oscillator. (b) Oscillator-Amplifier System. The Sweep Speed is 100 ns/div.

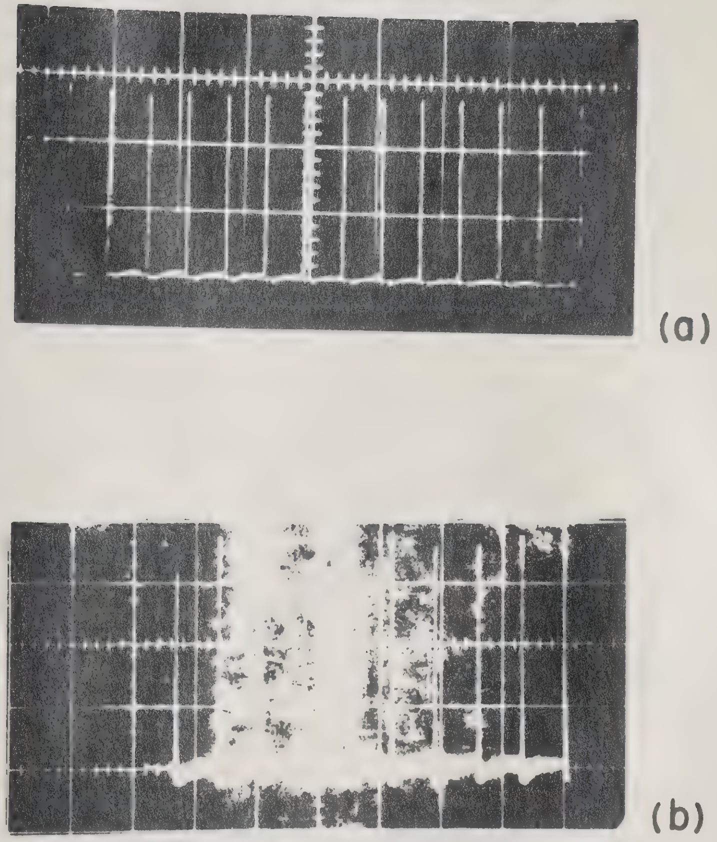

Figure 4-3 Stability of Laser System Output

(a) Oscillator Only. (b) Oscillator-Amplifier.

The pulse rate is once a second.

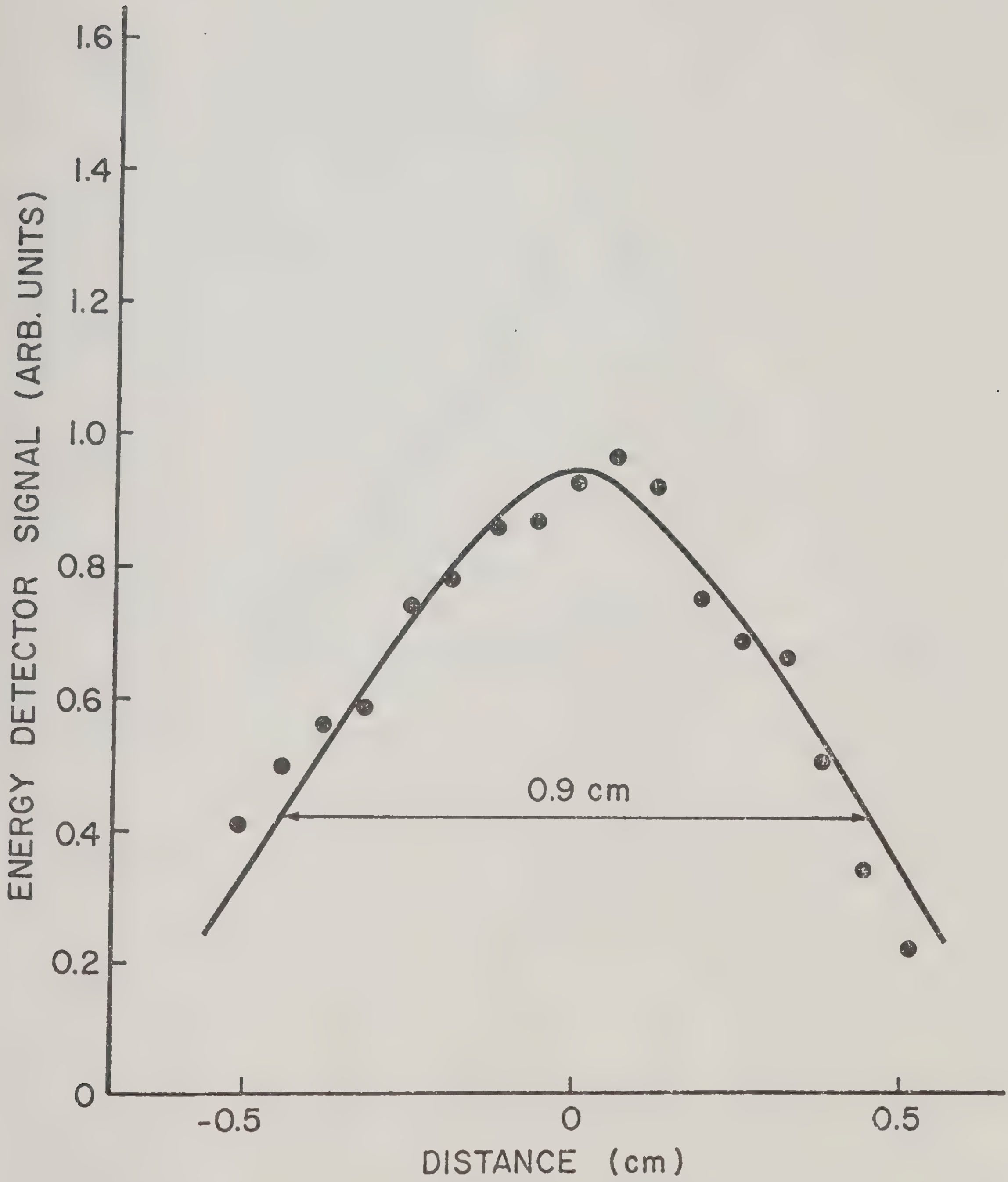

Figure 4-4(a) Beam Profile of Laser Oscillator

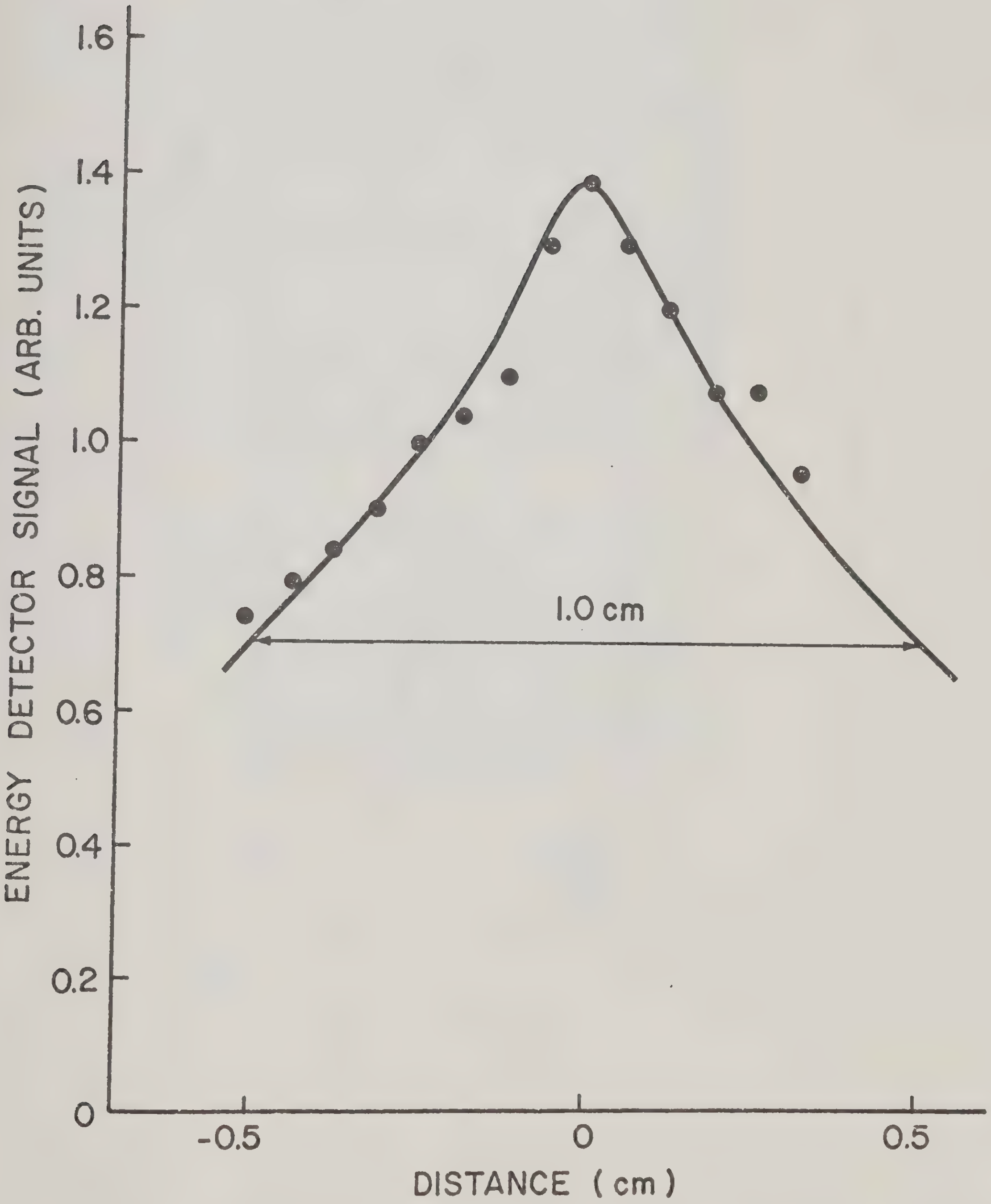

Figure 4-4(b) Beam Profile of Laser Oscillator-Amplifier System

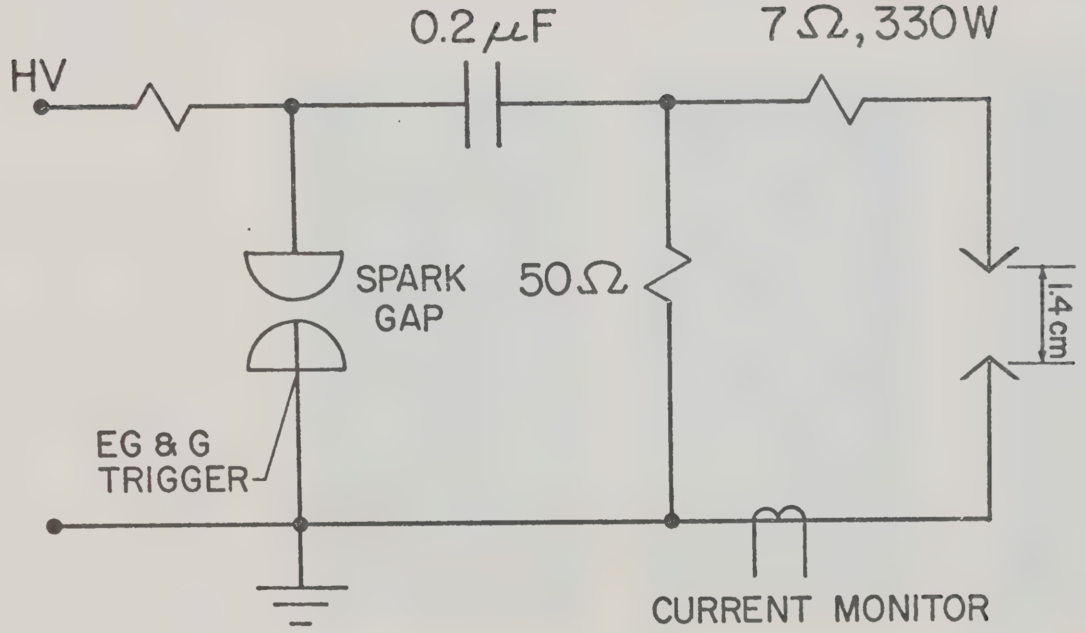
HV
0.2 μF
7 Ω, 330W
SPARK GAP
50 Ω
1.4 cm
EG & G TRIGGER
CURRENT MONITOR

Figure 4-5 Electric Discharge Circuit Diagram

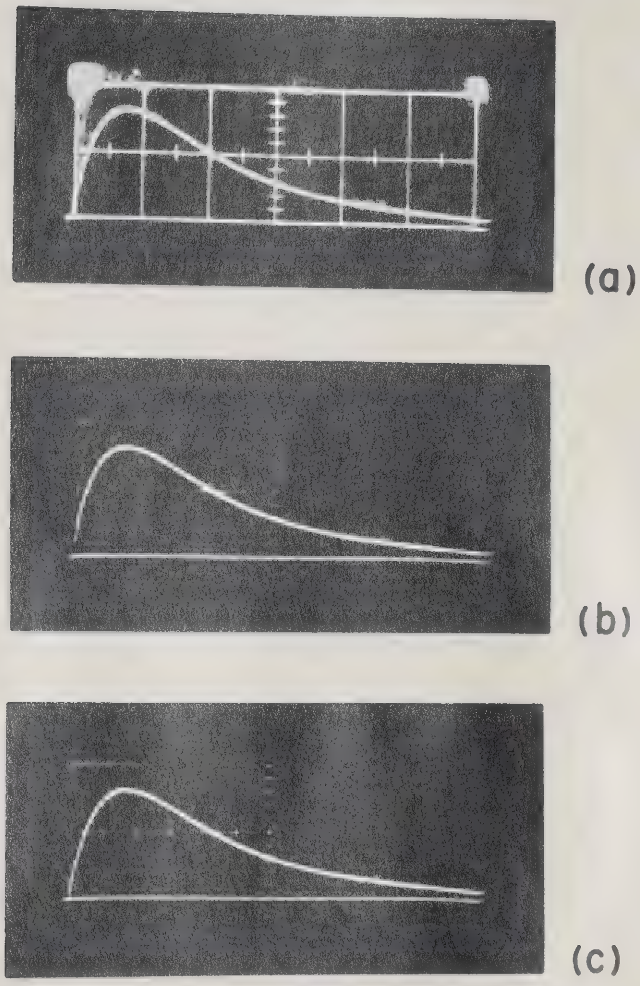

Figure 4-6(a) Electric Discharge Current.Vertical: 1.8 kA/div; Horizontal: 200 ns/div (a) 200 Torr (b) 400 Torr (c) 600 Torr

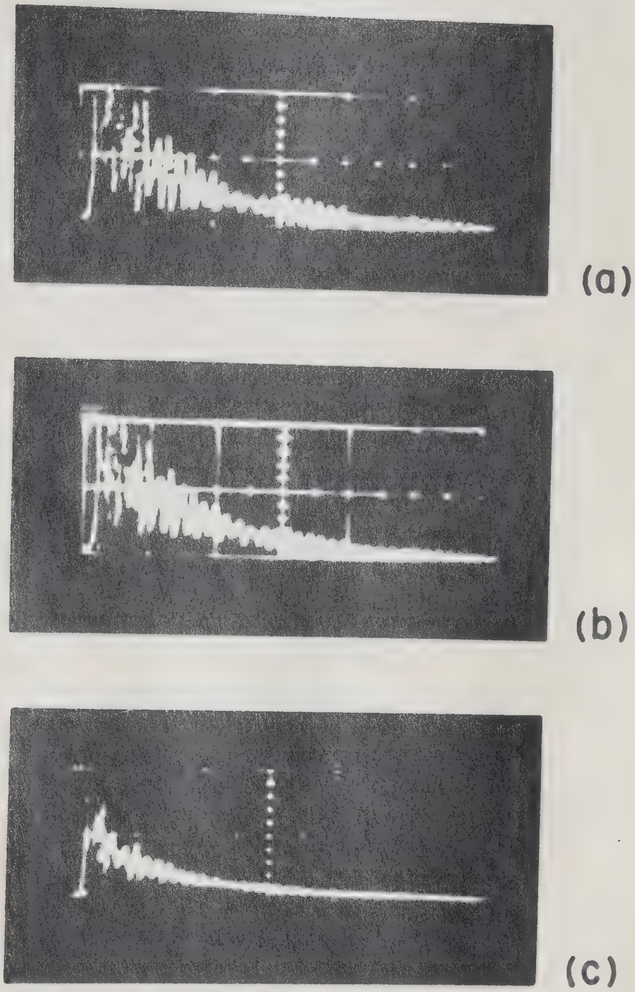

Figure 4-6 (b) Electric Discharge Voltage.Vertical: 25 kV/div; Horizontal: 200 ns/div (a) 200 Torr (b) 400 Torr (c) 600 Torr

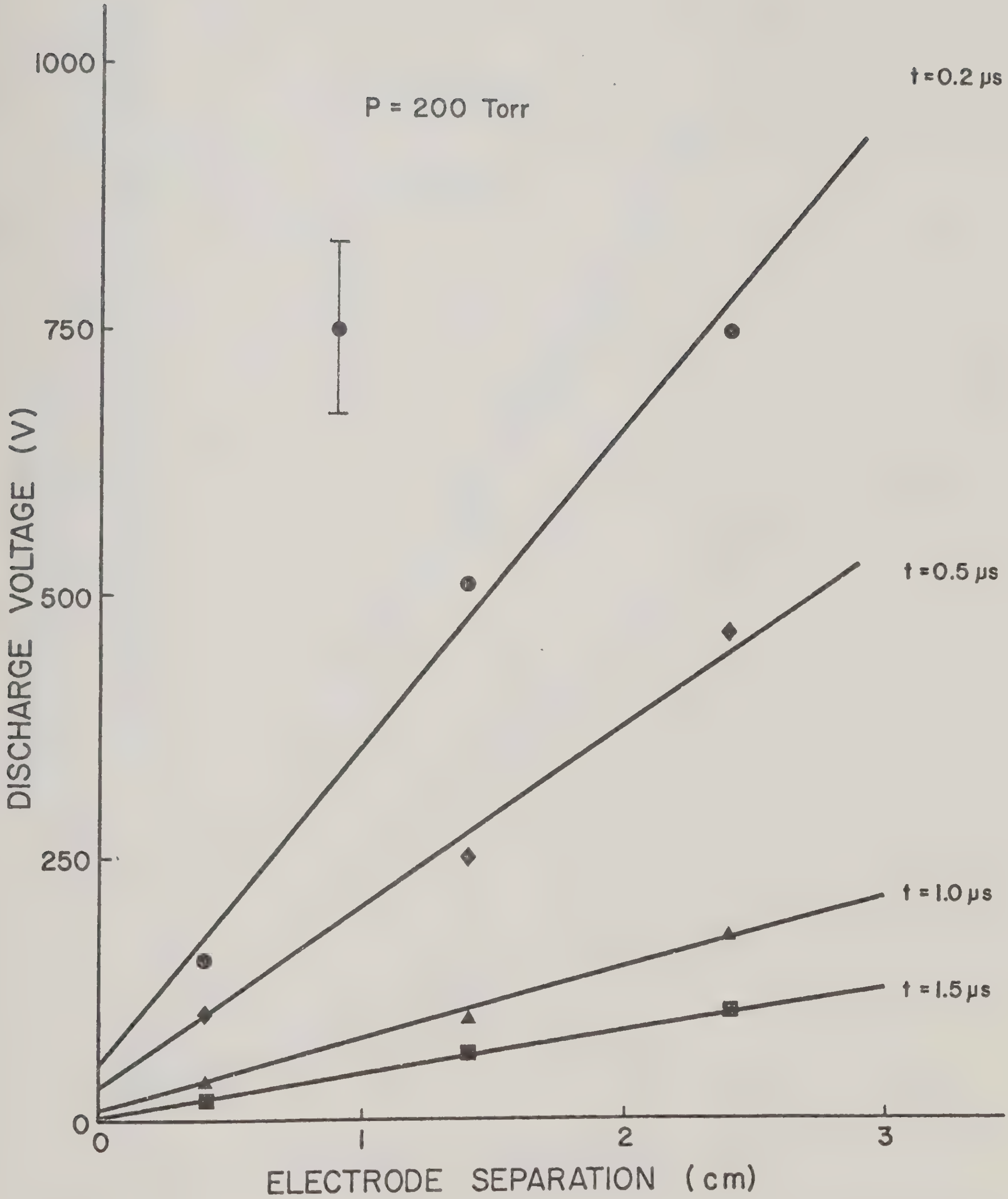

Figure 4-7(a) Dependence of Discharge Voltage on Electrode Separation

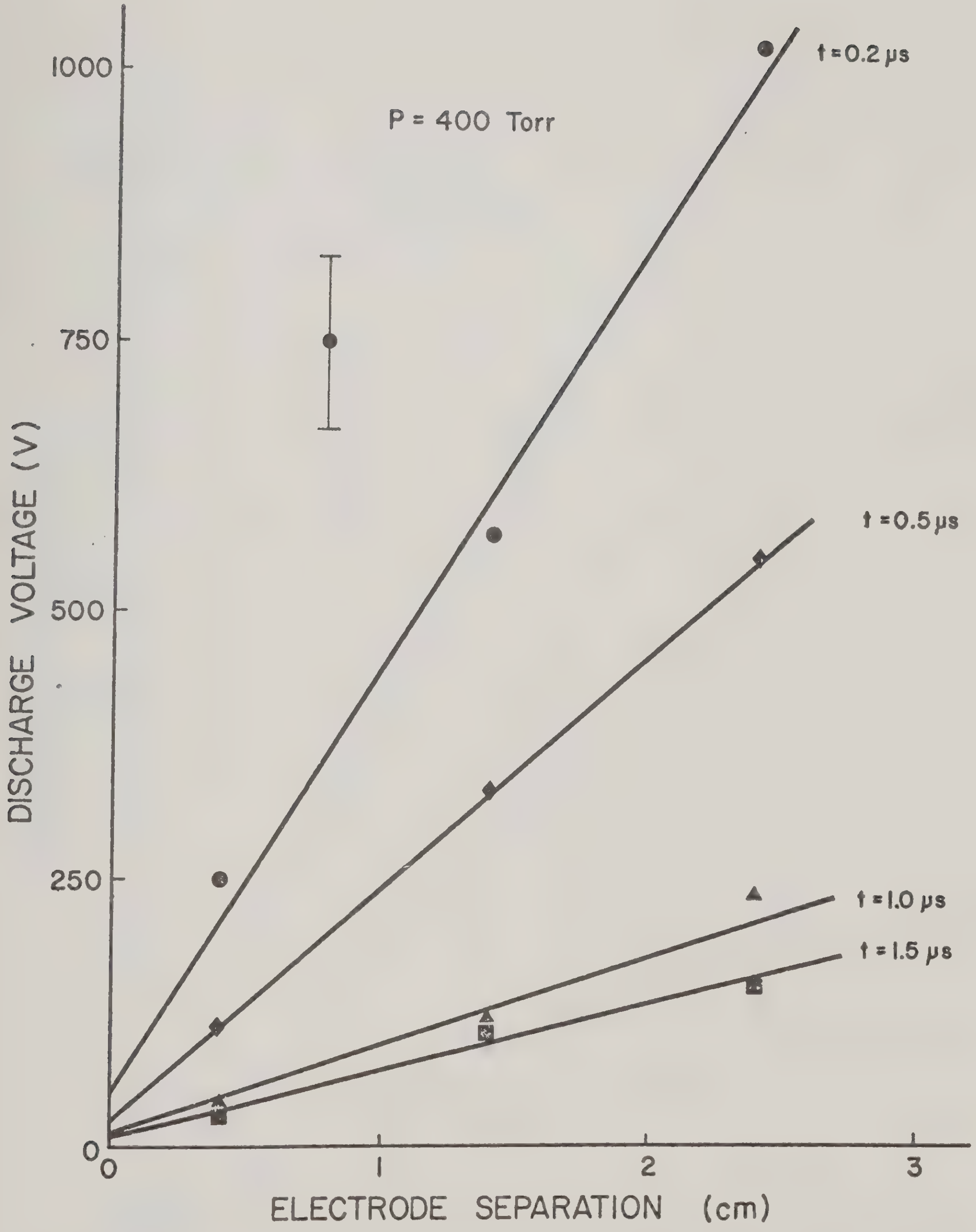

Figure 4-7(b) Dependence of Discharge Voltage on Electrode Separation

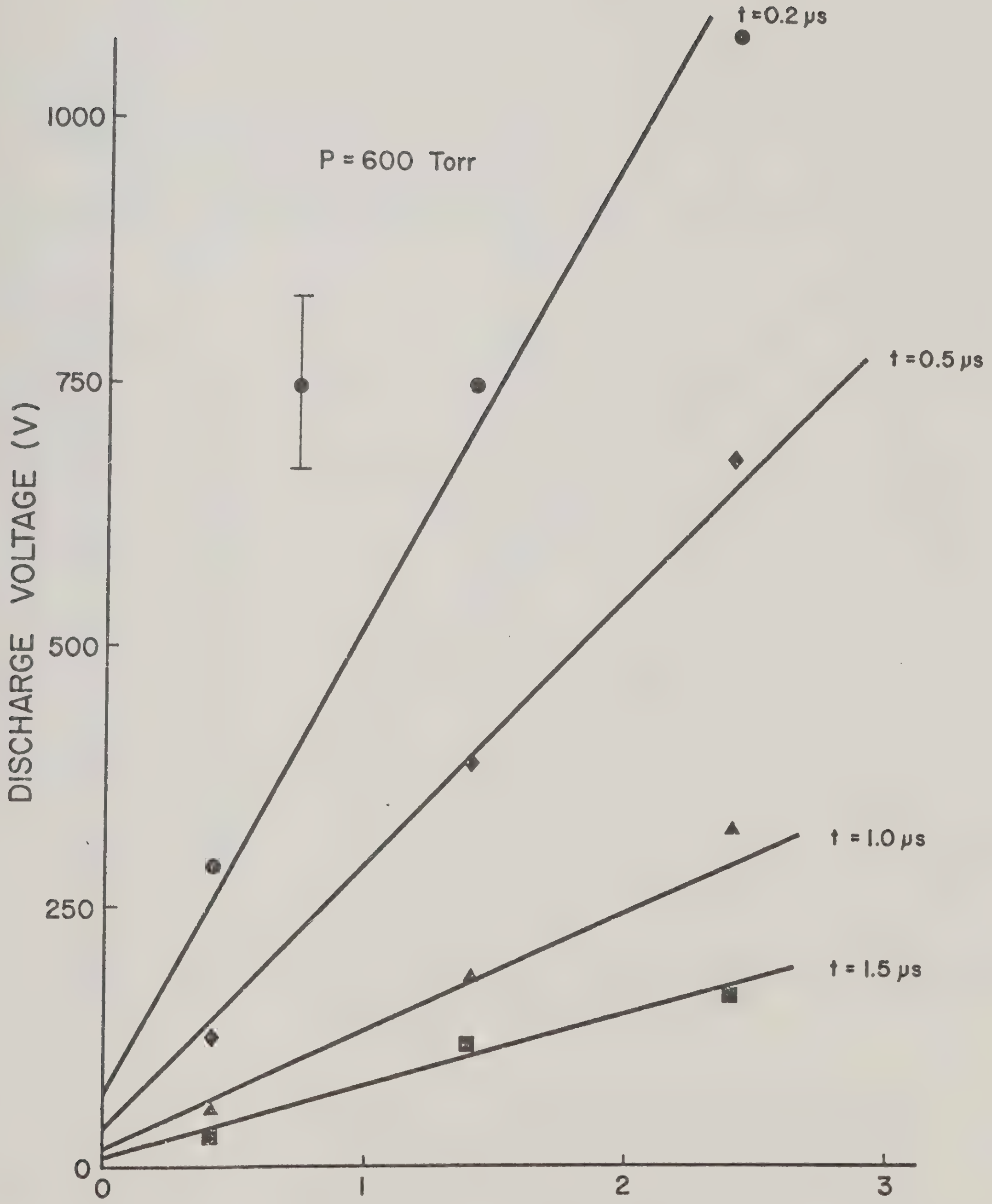

Figure 4-7(c) Dependence of Discharge Voltage on Electrode Separation

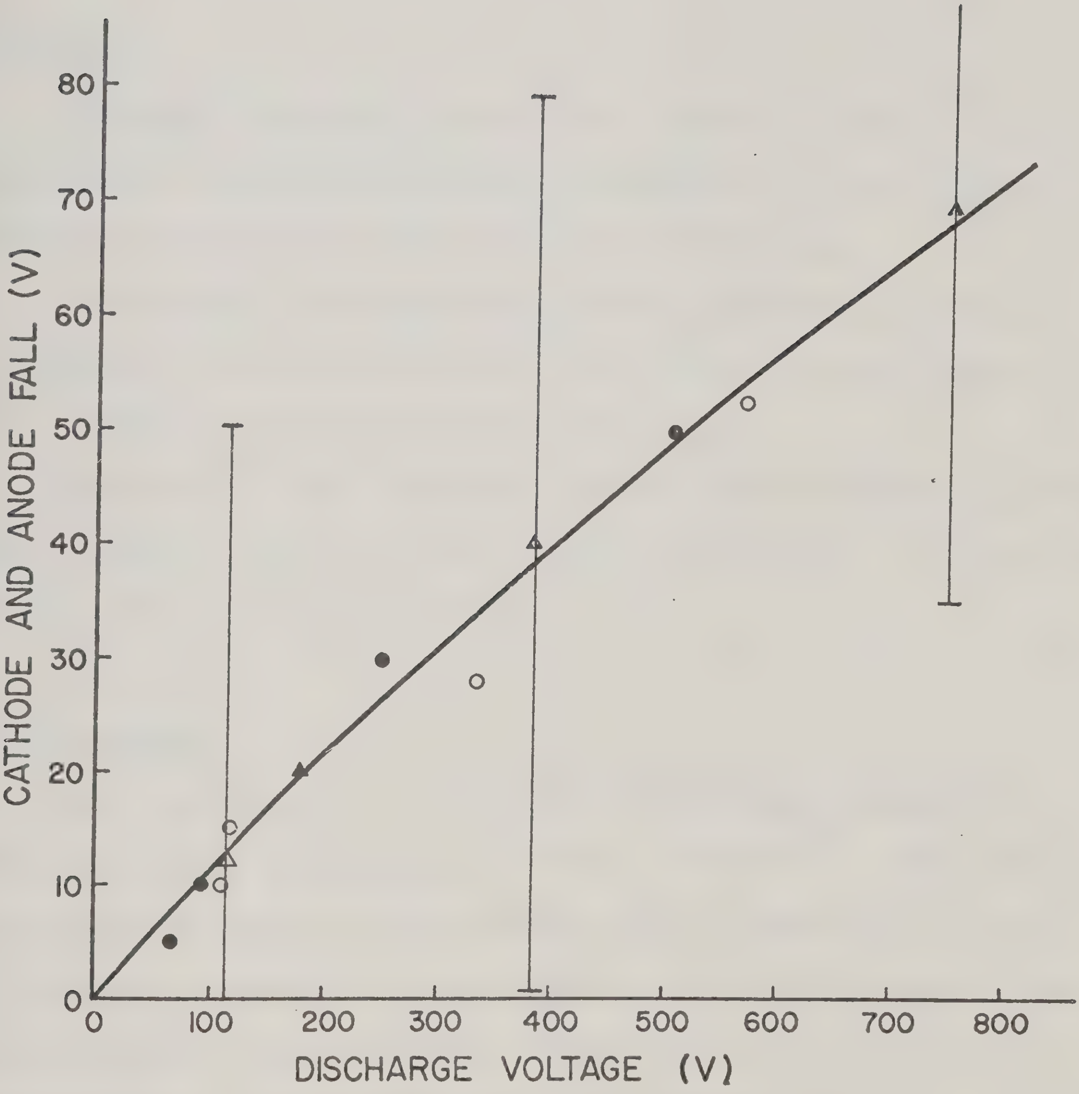

Figure 4-7(d) Cathode and Anode Fall Voltage Versus Total Discharge Voltage. ● 200 Torr: ○ 400 Torr: ▲ 600 Torr

CHAPTER V

ELECTRON, ION, AND NEUTRAL ATOM DENSITY: THE REGION OUTSIDE THE DISCHARGE

5.1 Outline

Diagnostics performed to measure the electron-ion density in the region outside the electric discharge were performed. Probe techniques were used as these afforded good space and time resolution.

A probe model is developed which extends the theories reported in the literature. The theory applies to high pressure plasmas flowing to a cylindrical probe surrounded by a thick sheath.

The strength of the shock wave created by the discharge was measured using a piezoelectric pressure probe. Using shock theory, the neutral atom density at the shock can be calculated.

5.2 Introduction

Recent measurements of uv photoionization-created plasmas have employed microwave interferometry or charge collection[1,2]. These methods do not give good space or time resolution which is important if we want to accurately determine the initial density in the focal volume that will initiate avalanche laser breakdown. These measurements indicate that uv photoplasmas typically have densities in the range $n \lesssim 10^{12}$ cm^{-3}. Electron-ion densities as low as 10^{6} cm^{-3} can be measured using swinging Langmuir probes with good space and time resolution[3].

5.3 Probe Theory

Probe theories have been developed for a large range of ion densities in high pressure flowing plasmas[3-12]. A review of these theories is available in the literature[3]. In high pressure probe theories, parameters such as probe geometry, plasma flow, bias voltage, sheath thickness, hydrodynamic and thermal effects, and so on should be considered. These parameters are discussed in terms of the following nondimensional quantities:

$R_e = v_f L/(\mu K T_e/e)$ = electric Reynold's number

$\alpha = \lambda_D/L$

and $\chi = eV_p/KT_e$

where

v_f = plasma flow velocity

L = characteristic length = $2r_p$ for cylindrical probes

r_p = probe radius

μ = ion mobility

K = Boltzmann constant

T_e = electron temperature

e = electronic charge

$\lambda_D = (\varepsilon_o K T_e/n e^2)^{1/2}$ = Debye length

ε_o = permittivity of free space

n = ion density

V_p = probe bias voltage (negative for ion collection)

For low densities such as in uv photoplasmas, the current to a moving probe is described by the so-called sheath/convection theory which

is applicable when $R_e\alpha^2\chi^2 > 1$. In this theory it is assumed that a thick sheath is established around the probe (sheath thickness $r_o \gg r_p$). The sheath is thick if $R_e^{-1}\alpha^2\chi^2 \gg 1$[5].

The current to a cylindrical probe may be limited by the space charge or by the electric field in the plasma sheath. In the first case, $R_e\alpha/\sqrt{\chi} \ll 1$ and the sheath electric fields are so large that ion motion in the sheath is radial and all ions that enter the sheath eventually reach the probe. The case has been studied by Clements and Smy[6]. In the second case, $R_e\alpha/\sqrt{\chi} \gg 1$ and only ions that enter the sheath within a limited range of impact parameters can reach the probe, the rest passing through the sheath. This is shown in Figure 5-1. In the transition region, $R_e\alpha/\sqrt{\chi} \simeq 1$, it has been suggested that one should use the model predicting the smaller probe current or equivalently, for a measured probe current, the theory predicting the smaller ion density may be used[3].

The space charge limited and field limited models are very similar and a closer look reveals that the two are not inherently different but are limits at high and low densities. The following is an attempt to extend these theories and account for the ion current to the probe for all values of $R_e\alpha/\sqrt{\chi}$.

5.3.1 Derivation of Formulae

The same assumptions made by Smy and Noor[3] are made, namely:

1. The current is convection dominated, i.e., the current due to diffusion of ions into the sheath is negligible ($R_e\alpha^2\chi^2 \gg 1$).

2. The sheath is thick and hence, hydrodynamic effects are negligible ($r_o >> r_p$, $R_e^{-1}\alpha^2\chi^2 > 1$).
3. The sheath is cylindrical with uniform charge density en and there are no end effects. This assumption is most reasonable when $R_e\alpha/\sqrt{\chi} >> 1$, i.e., when n is very small. When $R_e\alpha/\sqrt{\chi} << 1$, Smy[13] has shown that the sheath charge density is not uniform but increases from a small value near the probe to a maximum before decreasing to zero at the sheath edge, $r = r_o$. Therefore, the greatest error in the model should be expected when n is large.
4. The electric field and potential at the sheath edge are zero. In the case of large bias voltages which are usually the case in experiments, the quasi-neutral transitional zone where there is a voltage $\approx KT_e/e$[6,7] can be neglected.

The charge per unit length, $-Q$ on the probe is:

$$Q = \pi ne(r_o^2 - r_p^2) \tag{5.1}$$

where r_o is the radius at the sheath edge and r_p is the probe radius. The electric field per unit length due to this line charge and the surrounding plasma sheath is:

$$E = -\frac{dV}{dr} = -\frac{(r_o^2 - r^2)ne}{2\varepsilon_o r} \quad , r_p \le r \le r_o \tag{5.2}$$

Integrating, the probe voltage becomes:

$$V_p = \frac{ner_p^2}{2\varepsilon_o} \left(\frac{r_o}{r_p} \right)^2 \left(\ln \frac{r_o}{r_p} - \frac{1}{2} + \frac{1}{2} \frac{r_p^2}{r_o^2} \right) \tag{5.3}$$

This equation can easily be solved for r_o/r_p by iteration. Figure 5-2 shows the dependence of r_o/r_p on $2\varepsilon_o V_p/ner_p^2$.

From the electric field $\vec{E}$ and the flow velocity $\vec{v}_f$, the ion orbits inside the sheath can be determined. The velocity inside the sheath is:

$$\vec{v} = \vec{v}_f + \mu\vec{E} \tag{5.4}$$

while outside $\vec{v} = \vec{v}_f$. Taking the x-axis to be parallel to $\vec{v}_f$, then in cylindrical coordinates:

$$\vec{v}_f = v_f \, \vec{i}_x = v_f(\vec{i}_r \cos\theta - \vec{i}_\theta \sin\theta). \tag{5.5}$$

$\vec{E}$ is radial and hence,

$$\vec{E} = - \frac{ne}{2\varepsilon_o} \left(\frac{r_o^2 - r^2}{r} \right) \vec{i}_r. \tag{5.6}$$

Therefore,

$$\vec{v}_f = \vec{i}_r \left[v_f \cos\theta - \frac{ne\mu}{2\varepsilon_o} \left(\frac{r_o^2 - r^2}{r} \right) \right] - i_\theta \, v_f \sin\theta \tag{5.7}$$

This equation can be converted to a non-dimensional equation by the transformation $r = \rho \left(\frac{ner_o^2 \mu}{2\varepsilon_o v_f} \right)$. Separating the r and θ components and converting to non-dimensional variables:

$$\frac{d\rho}{dt} = \left(\frac{2\varepsilon_o v_f}{ner_o^2\mu}\right)\left[v_f\cos\theta - \left(\frac{ne\mu r_o}{2\varepsilon_o v_f}\right)^2 v_f\left(\frac{\rho_o^2-\rho^2}{\rho}\right)\right] \tag{5.8a}$$

$$\frac{d\theta}{dt} = -\left(\frac{2\varepsilon_o v_f}{ner_o^2\mu}\right)\frac{v_f\sin\theta}{\rho} \tag{5.8b}$$

Dividing the first equation by the second yields the differential equation for the ion orbits:

$$\frac{d\rho}{d\theta} + \rho\cot\theta + \frac{\rho^2}{\rho_o^2}\csc\theta = \csc\theta \tag{5.9}$$

where ρ_o is the dimensionless radius at the sheath edge.

5.3.2 Asymptotic Solutions

The field limited case occurs when $n \to 0$, $r_o \to \infty$, $\rho_o \to \infty$. This is the case of very weak shielding by the plasma sheath. When $\rho_o \to \infty$, the third term on the left of Equation 5.9 approaches zero. Its solution is:

$$\rho\sin\theta = \theta + \text{constant} \tag{5.10}$$

and

$$I/\ell = \frac{\pi\mu}{\varepsilon_o}(ner_p^2)\left(\frac{r_o}{r_p}\right)^2 \tag{5.11}$$

This is the field limited solution of Smy and Noor[3].

The space charge limited case (sheath/convection) is described by $\rho_o \to 0$, $n \to \infty$, $r_o \to 0$. The asymptotic solution can easily be obtained if

we solve for $d\theta/d\rho$:

$$\frac{d\theta}{d\rho} = - \frac{\rho_o^2 \sin\theta}{\rho_o^2 \rho \cot\theta + \csc\theta (\rho^2 + \rho_o 2)} \tag{5.12}$$

Taking the limit as $\rho_o \to 0$,

$$\lim_{\rho_o \to 0} \frac{d\theta}{d\rho} = 0 \tag{5.13}$$

Hence, for the space charge limited case,

$$\theta = \text{constant} \tag{5.14}$$

$$I/\ell = 2nev_f r_p \left(\frac{r_o}{r_p} \right) \tag{5.15}$$

This is approximately the same result as in reference 6.

5.3.3 Transition Region

The full differential equation (Equation 5.9) has to be solved in the transition region. This has been done numerically using a fourth order Runge-Kutta method. There are two classes of ion orbits. Depending on the initial value of the impact parameter $Y = \rho_o \sin\theta$, the ions either reach the probe or pass on to $X = \rho\cos\theta = \infty$. The solution which separates these two classes of orbits enters the sheath at the point (ρ_{01}, θ_{01}) where $\rho_{01} = \rho_0$. It is easy to show that this orbit should include the point $(\rho_{crit}, 0)$ which is the solution of the equations $\dot{r}=0$ and $\theta=0$. The radial

motion of the ions is due to the net radial velocity under the influence of the electric field and the fluid flow. The ions move towards the probe as long as $\dot{r}$ is negative. If $\dot{r}$ becomes positive for $0 \leq \theta \leq \pi$, then the ion will never reach the probe. The maximum radial component due to the fluid flow is equal to the flow velocity itself and this occurs when $\theta=0$. Clearly, the condition $\dot{r}=0$, $\theta=0$ gives the ion orbit which separates the orbits of captured and uncaptured ions.

In the actual computer program, the solution was started at ρ_{crit} and $\theta=\theta_{min}$ where θ_{min} was a very small angle ($\simeq 10^{-3}$ radian) which will not cause computer overflow. The solution was then generated by going backwards in time. This yielded (ρ_{01},θ_{01}). The values of θ_{01} and $Y_{01}=\rho_{01}\sin\theta_{01}=\rho_0\sin\theta_{01}$ are plotted in Figure 5-3 as a function of ρ_0^{-2}. For small values of ρ_0^{-2}, $Y_{01} \rightarrow \pi$ which is the field limited solution. When ρ_0^{-2} is large, $Y_{01} \rightarrow \rho_0$ and $\theta_{01} \rightarrow \pi/2$ which is the space charge limited case. From the values of Y_{01} in Figure 5-3, the ion current to the probe can now be written:

$$\frac{I}{\ell} = 2\, Y_{01} \left(\frac{\mu n e r_o^2}{2\varepsilon_o v_f} \right) n e v_f$$

$$= \frac{\mu Y_{01}}{\varepsilon_o} (n e r_p)^2 \left(\frac{r_o}{r_p} \right)^2 \qquad (5.16)$$

Thus, for particular values of V_p, μ and r_p, Equation (5. 3) can be used to solve for r_o/r_p as a function of n or r_o/r_p can be read off from Figure 5-2. Knowing $\rho_o = \frac{2\varepsilon_o v_f}{n e r_o \mu}$ and Y_{01} (see Figure 5-3), plots of I/ℓ versus n can be constructed. From these plots n can be read off for

each experimental value of I/ℓ. An example of such a plot is shown in Figure 5-4 together with I/ℓ predicted by the space charge limited and field limited theories. It is to be noted that the present model applies to all values of $R_e \alpha/\sqrt{\chi}$. In the transition region, the difference between the predictions of the present model and previous theories mentioned above is approximately 50%. Figures 5-5(a) - (b) show probe characteristics for two values of the electron density. The agreement with experiment is quite good.

The sensitivity of the probe currents calculated numerically to the exact form of the sheath density distribution has been tested by trying other charge density profiles. Specifically, the following profiles were used.

$$\rho_{charge} = Fen, \quad F = 0.8, .5, .1 \tag{5.17a}$$

$$\rho_{charge} = ne(1 - r^2/r_o^2) \tag{5.17b}$$

$$\rho_{charge} = ne(1 - r/r_o) \tag{5.17c}$$

$$\rho_{charge} = ne\left(\frac{r_p}{r_o}\right)\left(\frac{r}{r_p} - 1\right) \tag{5.17d}$$

$$\rho_{charge} = ne\left(\frac{r_p}{r_o}\right)^2\left(\frac{r^2}{r_p^2} - 1\right) \tag{5.17e}$$

$$\rho_{charge} = Fen\, r_p^{1/2}\left(\frac{1}{r_p^{1/2}} - \frac{1}{r^{1/2}}\right), \quad F=1, .5, .1 \tag{5.17f}$$

These profiles cover a broad range of possible charge distributions in the sheath including cases where there is charge depletion and no charge depletion[13]. In all cases considered there was no significant change in the predicted probe current. As expected the largest error (∿ 20%) occurred at the high density limit. The error may be due to the fact that in this limit $r_o/r_p < 2$ and hence, the condition of a very thick sheath is not

satisfied. A possible solution to this problem is changing the assumed constant flow to the following inviscid solution which takes into account the effect of the finite size of the probe.

$$\vec{v}_f = v_f[\vec{i}_r(1-r_p{}^2/r^2)\cos\theta - \vec{i}_\theta(r + r_p{}^2/r)\sin\theta] \qquad (5.18)$$

This was not done in this work since the measured probe currents were far from this asymptotic limit.

5.4 UV Photoion Measurements

5.4.1 Experimental Setup

The experimental setup used is depicted in Figure 5-6. A serious problem with using probes to measure uv photoionization is photoelectric emission from the probe if it happens to be exposed to the same uv radiation. To overcome this problem, a metal plate was placed between the discharge and the probe. The plate blocked all radiation from the discharge except that which passed through a 3.2 mm diameter hole. The rotating probe was kept in the shadow of the plate up to 50μs after firing the discharges. At this time, the discharge current was less than 40 mA. This low current minimized the possibility of unwanted photoelectric emission from the probe. A volume ionization in the shape of a cylinder was produced in the measurement chamber. The photoion density was measured 1 cm from the metal plate.

5.4.2 Probe Design

The probe had to be sturdily constructed and well balanced to withstand the tremendous stresses on it when operating at very high rotational speeds. The probe was driven by an electric motor outside the measurement chamber

at about 7200 rpm giving a probe speed of approximately 100 m/s. Oil lubricated rubber seals ensured that the measurement chamber was vacuum tight. The probe can be operated safely up to 10,000 rpm. At higher speeds, the oil lubricated seals started to fail due to the excessive heat from friction. The probe was made of 0.025 cm diameter stainless steel wire. This was placed and cemented inside a ceramic-lined stainless steel tube kept at ground potential. The tube also served as an electromagnetic shield against noise. Figure 5-7 shows the probe circuit and the probe construction. A 55 volt battery provided the negative bias and the total resistive load was varied from 600Ω to 10kΩ. Electrical connection between moving and fixed parts of the probe circuit was through a mercury pool. Measured probe currents ranged from approximately 250nA to 20μA.

The time resolution of a moving probe is approximately a few times the time it takes the probe to traverse a distance equal to its diameter[14]. For $r_p = 1.27 \times 10^{-2}$ cm and $v = 10^4$ cm/s, this is about 2.54×10^{-6}s. Hence, with a probe time resolution of ≃ 5μs, the RC time of ≃ 1μs for the probe circuit is adequate.

Figure 5-8 shows typical oscillograms of the probe current at different times after firing the discharge. The upper traces are probe current signals while the lower traces are reference signals obtained from a phototransistor when a He-Ne beam was chopped by the probe arm. This reference signal located the probe relative to the plasma.

5.4.3 UV Photoion Density in Ar

Since the probe length was greater than the diameter of the cylindrical plasma, the effective length of the probe, ℓ_{eff} (see Equation 5.16) at any time when the probe is in the plasma is equal to a chord of a circle as

shown in Figure 5-9(a). For convenience, this length was estimated by the distance, ℓ, corresponding to the full width at half maximum of the probe signal trace. Hence,

$$\ell_{eff} \simeq \ell = v\Delta t \qquad (5.19)$$

where $\Delta t = t_2 - t_1$ is the FWHM of the signal trace (see Figure 5.9(b)) and v is the probe velocity. Referring to Figure 5-9(c), let R_1 and R_2 be the radii of the plasma at times t_1 and t_2 such that $\Delta t = t_2 - t_1$. At t_1 and t_2 the probe is positioned a distance r_1 and r_2, respectively from the center of the plasma as shown in the figure. Then $\ell = r_1 + r_2$. Since $r_1 \leq \ell_{eff} \leq r_2$ and since the plasma does not expand rapidly at the time the measurements were taken ($t > 50 \mu s$) (see Figure 5-1), then it can be seen that ℓ reasonably estimates ℓ_{eff}. This value of ℓ will yield the ion density, $n_{ave}(t)$ averaged over a diameter.

Probe currents as a function of position and time can also be obtained from the oscillograms. From these data, the density as a function of position and time can be obtained after an Abel inversion. However, the procedure described above was adequate because the results were not sufficiently accurate to warrant an Abel inversion.

The plasma expanded radially due to ambipolar diffusion, ℓ increasing in time as t^2 (see Figure 5-10) which is to be expected for an unbounded gas diffusing in two dimensions.

It will be shown later that $T_e \stackrel{\sim}{-} 1$ eV and using the experimental parameters $V_p = 55$ volts, $v_f + 10^4$ cm/s, $r_p = 1.27 \times 10^{-2}$ cm, $\mu_r = 2$ cm^2/V-s and $p = 100$ Torr, the conditions $R_e \alpha^2 \chi^2 > 1$ and $R_e^{-1} \alpha^2 \chi^2 \leq 1$ yield $n \leq 5 \times 10^{10}$ cm^{-3}.

Therefore, the theory discussed in Sec. 5.3 applies when $n \leq 5 \times 10^{10} cm^{-3}$.

Measurements were made for pressures of 100, 200, 400, and 600 Torr at distances of 2.5, 3.8, 5.1, 7.6 and 10.2cm from the discharge. The discharge chamber was not isolated from the measurement chamber and, therefore, the pressure in these two chambers change together. Thus, it is not expected that the source spectrum will be the same for the different pressures considered. Impurities such as mercury from the probe connector and oil from the seals could also leak into the measurement chamber. No attempt was made to eliminate these impurities nor were attempts made to determine to what extent these impurities affected the results. The reason is because the breakdown measurements reported here were done in systems which were far from pure.

The results of the measurements are shown in Figures 5-11 (a) - (d). The points are experimental values while the solid curve is a fitting of a theoretical expression to be discussed later. The ion mobility[15] was chosen to be:

$$\mu_r = 2.0 \left(\frac{760}{p}\right) \quad cm^2/V\text{-}s \tag{5.20}$$

The densities obtained are of the same order of magnitude as those obtained by Seguin, *et. al.*[1] in a laser mix. The results of Babcock, *et. al.*[2] are about three orders of magnitude smaller. The differences could be due to different current pulse magnitude and shape, total discharge energy, discharge gases, distance from source, target gas, and the gas through which the uv photons pass. All these parameters affect the emitted uv spectrum and intensity and the photoionization efficiency[4,16,17].

5.4.4 Curve Fitting and Extrapolation

The photoplasma decays due to recombination and ambipolar diffusion. Diffusion along the length of the cylindrical plasma can be neglected compared to radial diffusion or recombination losses. The ion density decay is described by the following equation:

$$\frac{dn_{ave}(t)}{dt} = - \frac{D_A}{\Lambda_r^2} n_{ave}(t) - \alpha_R n_{ave}(t)^2 \tag{5.21}$$

where Λ_r is the radial diffusion length, D_A the ambipolar diffusion coefficient, and α_R is the recombination coefficient. Equation (5.21) can be solved if an expression approximating Λ_r can be found.

To do this consider a two dimensional, freely expanding plasma, where diffusion is the only loss mechanism. Then the density distribution is Gaussian[18]:

$$n(r,t) = \frac{n(0,0)}{R_o^2+4D_At} \exp\{- \frac{r^2}{R_o^2+4D_At}\} \tag{5.22}$$

R_o is the plasma radius at t=0 and $R^2=R_o^2+4D_At$ is the mean square radius, i.e., the radius where n equals 1/e of its central value. Hence, we identify $\ell^2 \simeq R^2$. From Figure 5-10 which gives ℓ as a function of time, D_A can be calculated using $\ell^2 \simeq R^2=R_o^2+D_At$. R_o^2 = .22cm is just the radius of the uv port. Assuming that T_i=300K[19], the electron temperature, T_e can be estimated using

$$D_A = \mu_i (\frac{kT_i}{e}) (1 + \frac{T_e}{T_i}) \tag{5.23}$$

The values of T_e consistent with the data in Figures 5-11(a) - (d) can

be found in the inserts on the figures.

Averaging n(r,t) over a diameter:

$$n_{ave}(t) = \frac{2}{\ell} \int_{o}^{\ell/2} n(r,t)dr \simeq \frac{1}{R} \int_{o}^{R} n(r,t)dr \simeq \frac{1}{R} \int_{o}^{\infty} n(r,t)dr \tag{5.24}$$

or

$$n_{ave}(t) = \frac{n_{ave}(0)}{1 + 4\frac{D_A}{R_o^2} t} \tag{5.25}$$

By assumption, this satisfies:

$$\frac{dn_{ave}}{dt} = - \frac{D_A}{\Lambda_r^2} n_{ave} = - \frac{D_A n_{ave}(t)}{\frac{1}{4} (R_o^2 + 4D_A(t))} \tag{5.26}$$

Therefore,

$$\Lambda_r^2 = \frac{1}{4} (R_o^2 + 4D_A t) = \frac{1}{4} \ell^2 \tag{5.27}$$

This is the desired expression for the radial diffusion length. The solution of Equation (5.21) using Equation (5.27) is:

$$n_{ave}(t) = \frac{n_{ave}(0)}{(1 + \frac{4D_A t}{R_o^2})[\alpha_R n_{ave}(0) \frac{R_o^2}{4D_A} \ln(1 + \frac{4D\ t}{R_o^2}) + 1]} \tag{5.28}$$

By a suitable choice of α_R and $n_{ave}(0)$, Equation (5.28) can be fitted to the experimental points. The solid lines in Figures 5-11 (a) - (d) were obtained using such a procedure. There is reasonable agreement

between experiment and theory. The values of α_R used varied from $1.0\text{x}10^{-8}$ to $2.7\text{x}10^{-7} \text{cm}^3/\text{s}$. These are typical recombination coefficients for dissociative molecular recombination process[20].

5.4.5 Error in $n_{ave}(t)$

The uncertainty in $n_{ave}(t)$ will be due to errors in r_p ($\simeq$10%), error in μ_i, error in estimating ℓ, and variations in the current from shot to shot (10%). There is error in estimating ℓ because it is not exactly equal to ℓ_{eff} as discussed previously. Taking a relative error of 10% for μ, 20% for ℓ and taking the field limited expression for the density for example, the uncertainty in n_{ave} can be estimated. In the field limited case $n\ (\frac{I}{\ell})^{.77}\mu^{-.77}r^{-.46}$. Hence, $\frac{\Delta n}{n} = .77\ \frac{\Delta I}{I} + .77\frac{\Delta\mu}{\mu} + .46\ \frac{\Delta r}{r} + .77\ \frac{\Delta\ell}{\ell} = 35\%$. This is typical for probe measurements.

5.4.6 UV Photoionization Mechanism

Figure 5-12 shows the initial photoion density obtained by extrapolation of the data to t=0 using Equation (5.28), plotted against the distance from the discharge. Two photoionization mechanisms can be considered: single photon ionization of Ar or of impurities and two photon ionization. For single photon ionization of Ar or of impurities, n_{ave} should vary with distance, d, as $\frac{1}{d^2}\ e^{-\mu p d}$ where p is the pressure of the uv absorber and μ is the absorption coefficient. No single value of μ will fit the data of Figure 5-12 for all pressures considered and, therefore, we conclude that Ar is not photoionizaed by a single photon. On the other hand, impurities cannot have the large pressure required to fit the data. Hence, single photon ionization is ruled out.

For a two photon process, the rate ions are created, W, is proportional to the square of the light flux, F

$$W = CF^2 \tag{5.29}$$

and

$$\frac{dn_e}{dt} = Wn_{gas} \tag{5.30}$$

From the conservation of energy,

$$\frac{dF}{dr} + \frac{2F}{r} = - 2n_{gas} W \tag{5.31}$$

which is applicable for a point source of photons. The solution to this set of equations is:

$$F(r) = F_o[(1+2n_{gas}Cr_oF_o) \frac{r^2}{r_o^2} - 2n_{gas}CF_or_o(\frac{r}{r_o})]^{-1} \tag{5.32}$$

$$n \simeq CF_o^2n_{gas}\Delta t_d \; [(1+2n_{gas}CF_or_o) \frac{r^2}{r_o^2} - 2n_{gas}CF_or_o \; (\frac{r}{r_o})]^{-2} \tag{5.33}$$

where r_o is the source radius (spherical), $F_o=f(r_o)$ and Δt_d is the duration of the discharge current. Since Ar is transparent to uv longer than 800 Å, $2n_{gas}CF_o^2r_o<<1$. Hence,

$$n \simeq CF_o^2r_o^4n_{gas}\Delta t_d/r^4 \sim r^{-4} \tag{5.34}$$

The solid lines in Figure 5-12 is a fitting of Equation (5.34) to the

data. It can be seen that an r^{-4} dependence is not incompatible with the data.

The effective photons may come from the Ar continuum around 1200 Å[23,24]. When a CaF_2 sindow was placed on the uv port, the probe current was reduced to 10% of its value without windows. However, it is known that a high uv flux such as that near a discharge degrades the transmission characteristics of uv windows such as CaF_2[17]. It is then very probable that the actual transmission limit of the window used in the experiment was higher than that published for CaF_2 (≈1100 Å). This could explain the reduced probe current with the window in the uv port. In fact, in uv preionized CO_2 lasers, it was at first thought that the effective photons were in the region $\lambda<1100$ Å since the arc-suppressing effect of the uv discharge was inhibited by CaF_2 windows[17,25].

The fact that 10% probe current still persisted even with a window precluded the possibility of the ions coming from the discharge directly via an ionization wave. When a NaC window was used, no ionization was observed. This means that $\lambda<1700$ Å.

All this discussion is only speculation, however, A more detailed study of photoionization in Ar has to be performed before the question can be definitely answered. In breakdown measurements, it suffices to know the ion density without regard to how they are created.

5.5 Pressure Probe Measurement of Shock Wave Strength

5.5.1 Pressure Probe Characteristics

The shock wave created by the rapid introduction of energy into the discharge column was measured using an LD-25 blast wave pressure

transducer. The transducer had been calibrated in a shock tube[26] and the response was within the manufacturer's specifications of .15V/psi or 2.2 V/atm.

Figure 5-13 shows a typical pressure transducer signal response to a weak pressure jump. The oscillations are due to vibration of the piezoelectric crystal at its natural frequency after it is excited by the shock.

Measurements were made with the piezoelectric crystal (lead zirconate titanate) face perpendicular to the wave direction. Hence, recorded pressure jumps were the sum of the actual pressure jump plus the equivalent pressure exerted by the fluid flow.

The linearity of the transducer was checked by plotting the transducer signal against the initial energy stored in the discharge capacitor bank. Assuming the energy in the shock remains a fixed fraction of the initial charging energy, Figure 5-14 shows that the transducer had a linear response.

5.5.2 Measurement of Shock Strength

The shock wave was monitored for pressures of 200, 400, and 600 Torr in Ar at distances varying from 0.8 cm to 10 cm from the discharge. The total transducer signal, Δp_t is:

$$\frac{\Delta p_t}{p_o} = \frac{\Delta p}{p_o} + \frac{\rho_1 u^2}{p_o} \qquad (5.35)$$

where Δp is the actual pressure jump, p_o is the ambient pressure, ρ_1

is the mass density of the compressed gas and u is the gas velocity. For a perfect gas with constant specific heats the following relations hold:[27]

$$\frac{p_1}{p_o} = \frac{(\gamma+1)\rho_1 - (\gamma-1)\rho_o}{(\gamma+1)\rho_o - (\gamma-1)\rho_1} \tag{5.36}$$

$$\frac{\rho_0}{\rho_1} = \frac{(\gamma+1)(p_1/p_0) + (\gamma-1)}{(\gamma-1)(p_1/p_0) + (\gamma+1)} \tag{5.37}$$

$$u = |u_0 - u_1| = [(p_1 - p_0)(\frac{1}{\rho_0} - \frac{1}{\rho_1})]^{1/2} \tag{5.38}$$

where, p_1, ρ_1, u_1 and p_o, ρ_0, u_0 are the pressures, mass densities, and velocity of the gases with respect to the discontinuity of the compressed and undisturbed gases, respectively. γ is the ratio of the specific heats. From Equation (5.38):

$$\frac{\rho_1 u^2}{p_0} = \frac{\rho_1}{p_0} (p_1 - p_0) (\frac{1}{\rho_0} - \frac{1}{\rho_1}) = \frac{\Delta p}{p_0} (\frac{\rho_1}{\rho_0} - 1) \tag{5.39}$$

where $\Delta p = p_1 - p_0$

Hence,

$$\frac{\Delta p}{p_0} = \frac{\rho_0}{\rho_1} \frac{\Delta p_t}{p_0} \tag{5.40}$$

For Ar, $\gamma = 5/3$ and

$$\frac{\rho_1}{\rho_0} = \frac{\frac{4\Delta p_t}{p_0} + 5}{\Delta p/p_o + 5} \tag{5.41}$$

Solving Equations (5.40) and (5.41) yields:

$$\frac{\Delta p}{p_0} = \frac{1}{8}\left\{\left(\frac{\Delta p_t}{p_0} - 5\right) + \left[\left(\frac{\Delta p_t}{p_0} - 5\right)^2 + 80\,\frac{\Delta p_t}{p_0}\right]^{1/2}\right\} \tag{5.42}$$

Equation (5.42) gives the actual pressure jump in the shock from pressure transducer signals. The results are shown in Figures 5-15 (a) - (c).

Theoretical investigations have been performed for spherical shocks by Brode[28] and by Plooster[29] for line sources. For spherical shocks, Brode finds:

$$\frac{\Delta p}{p_0} = \frac{.137}{\lambda^3} + \frac{.119}{\lambda^2} + \frac{.269}{\lambda} - .019 \tag{5.43}$$

where $\lambda = r/\varepsilon$ and $\varepsilon^3 = E/p_0$. E is the total energy converted to shock energy. This has been determined previously. (Chapter IV).

For cylindrical shocks, Plooster reports:

$$\left[\frac{2(\gamma+1)}{\gamma}\right]\frac{\Delta p}{p_0} = \{\alpha[(1+\beta\lambda^2)^{3/8} - 1]\}^{-1} \tag{5.44}$$

where

$$\alpha = \left(\frac{3}{8}\right)^{3/5} c^{8/5}, \quad \beta = c^{-8/5}\left(\frac{8}{3}\right)^{8/5}, \quad \lambda = r/R_0,$$

$$R_0 = (E/b\gamma p_0)^{1/2}$$

Plooster suggests c=.7 and b=3.94 for air. The same values of c and b have been used here for Ar.

The solid lines in Figures 5-15 (a) - (c) are from Equation (5.43) and the dashed lines are from Equation (5.44). It is to be noted that the shock seems to start out as a cylindrical shock and becomes spherical at large distances. This is reasonable to expect since the discharge looks like a line source at close distances but looks like a point source at large distances.

5.5.3 Discussion

The sudden increase in gas pressure when the shock front arrives at the laser focus should reduce the laser-induced breakdown threshold. This should happen because the pressure jump due to shock corresponds to an increase in the gas density as can be seen from Equation (5.41). The dependence of the breakdown threshold on the neutral density is known or measureable (see Section (2.5)). Therefore, it may be possible to measure rapidly changing neutral atom densities with a high degree of spatial resolution with lasers. This indeed is the case and this will be discussed in greater detail in later chapters.

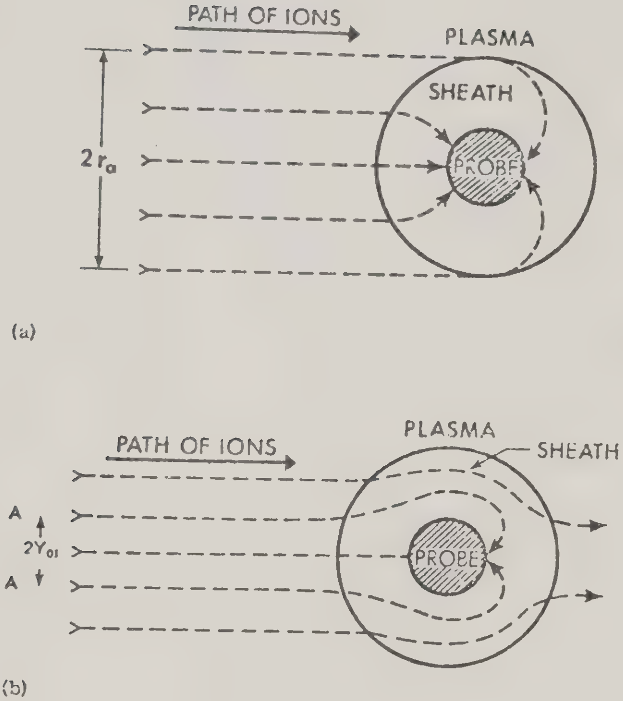
PATH OF IONS
PLASMA
SHEATH
2r_a
PROBE
(a)
PATH OF IONS
PLASMA
SHEATH
A
2Y_01
A
PROBE
(b)

Figure 5-1 Ion Orbits in Plasma Sheath

(a) Sheath/Convection Regime

(b) Field Limited Case

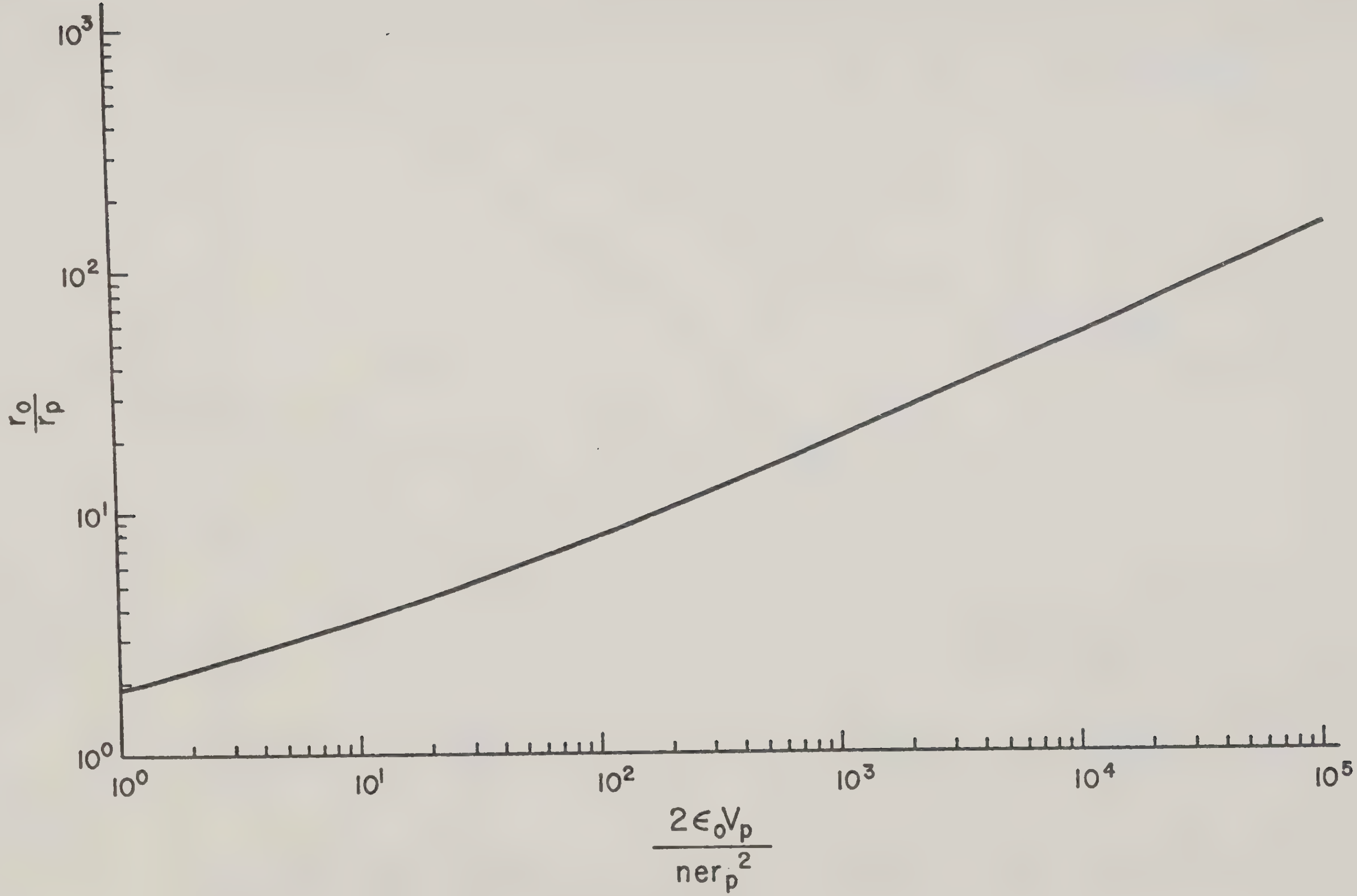

Figure 5-2 Radius of Plasma Sheath Around Cylindrical Probe

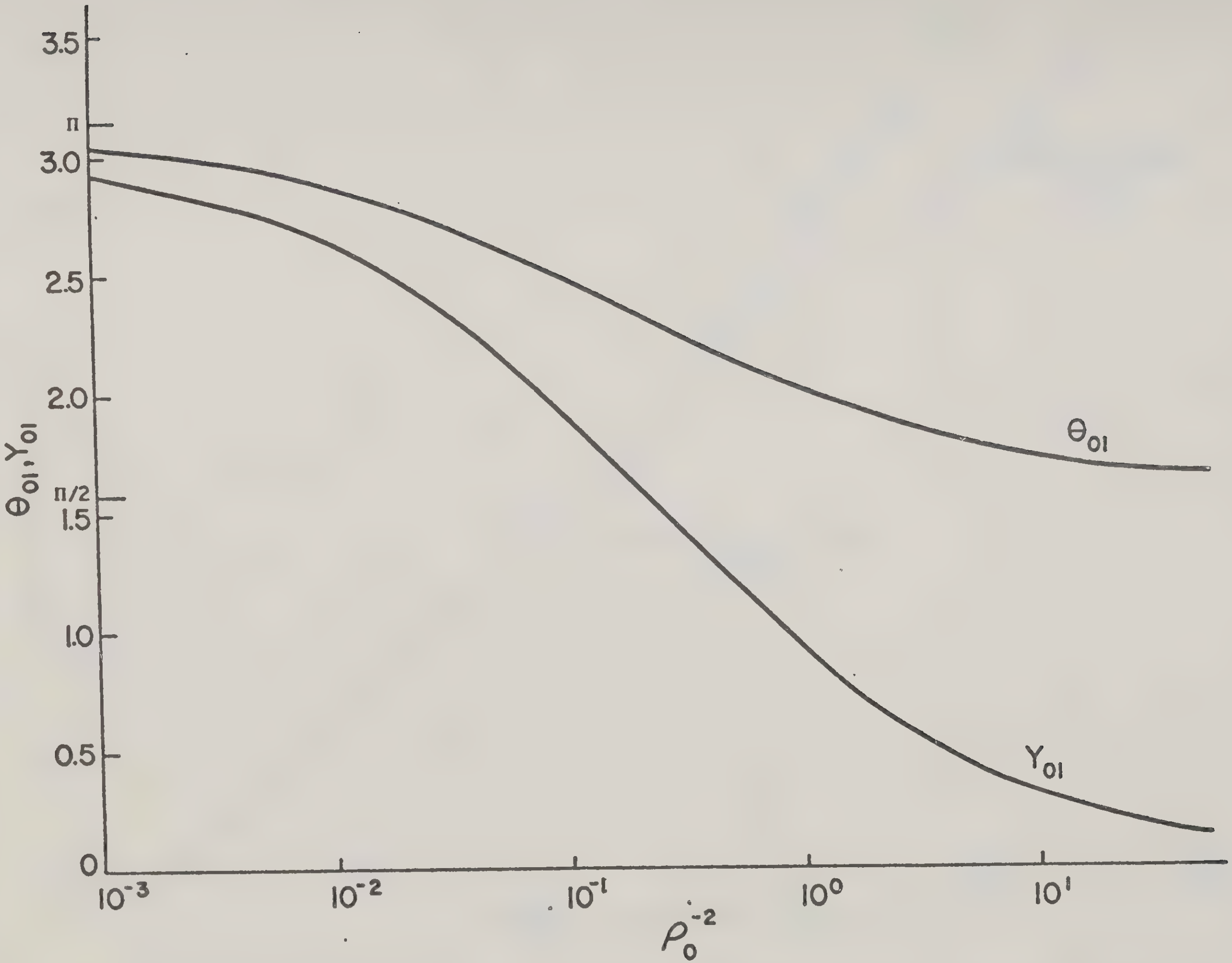

Figure 5-3 Impact Parameter Y_{01} and θ_{01} as a Function of ρ_0^{-2}. When $\rho_0^{-2} \rightarrow \infty$, $Y_{01} \rightarrow \rho_0$, $\theta_{01} \rightarrow \pi/2$. When $\rho_0^{-2} \rightarrow 0$, $Y_{01} \rightarrow \pi$

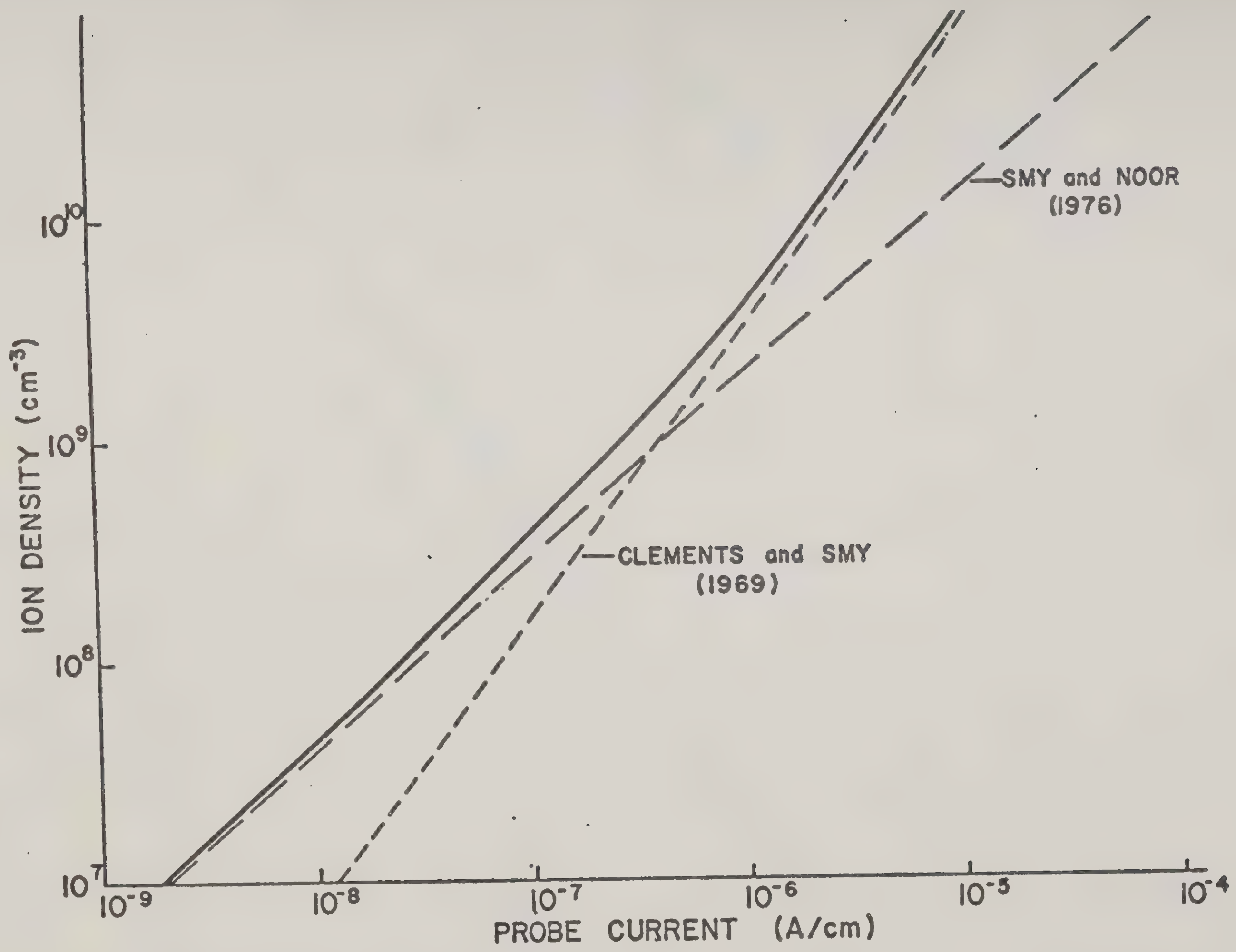

Figure 5-4 Ion Density as a Function of Probe Current. The solid curve is from Equation (5.16) and the dashed curves are from Clements and Smy[6], and Smy and Noor[3]. μ=15.2cm^2/V-s; r_p=1.27x10^{-2}; v=10^{4}cm/s; V_p=55V

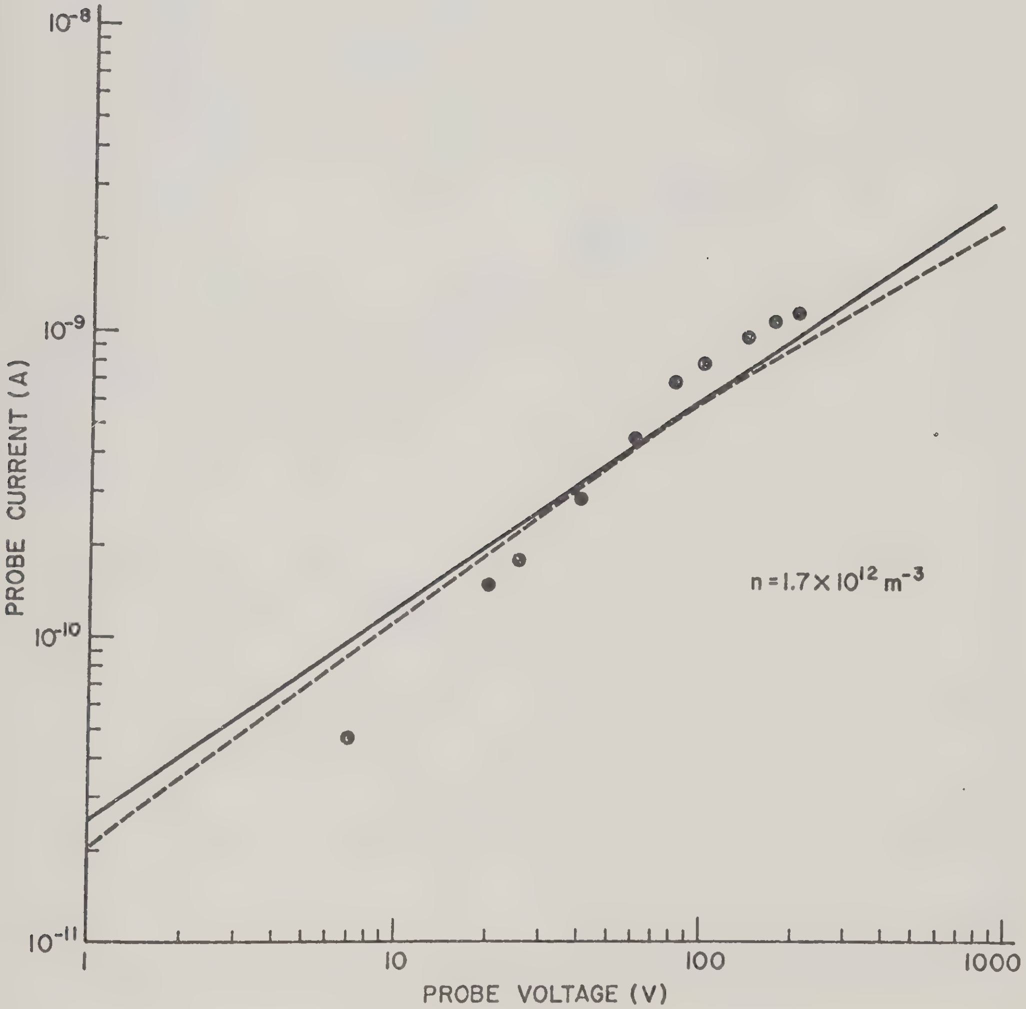

Figure 5-5(a) Probe Current Versus Probe Bias Voltage. Dashed line is from Equation (5.16). The solid line and the experimental points are from Reference 3.

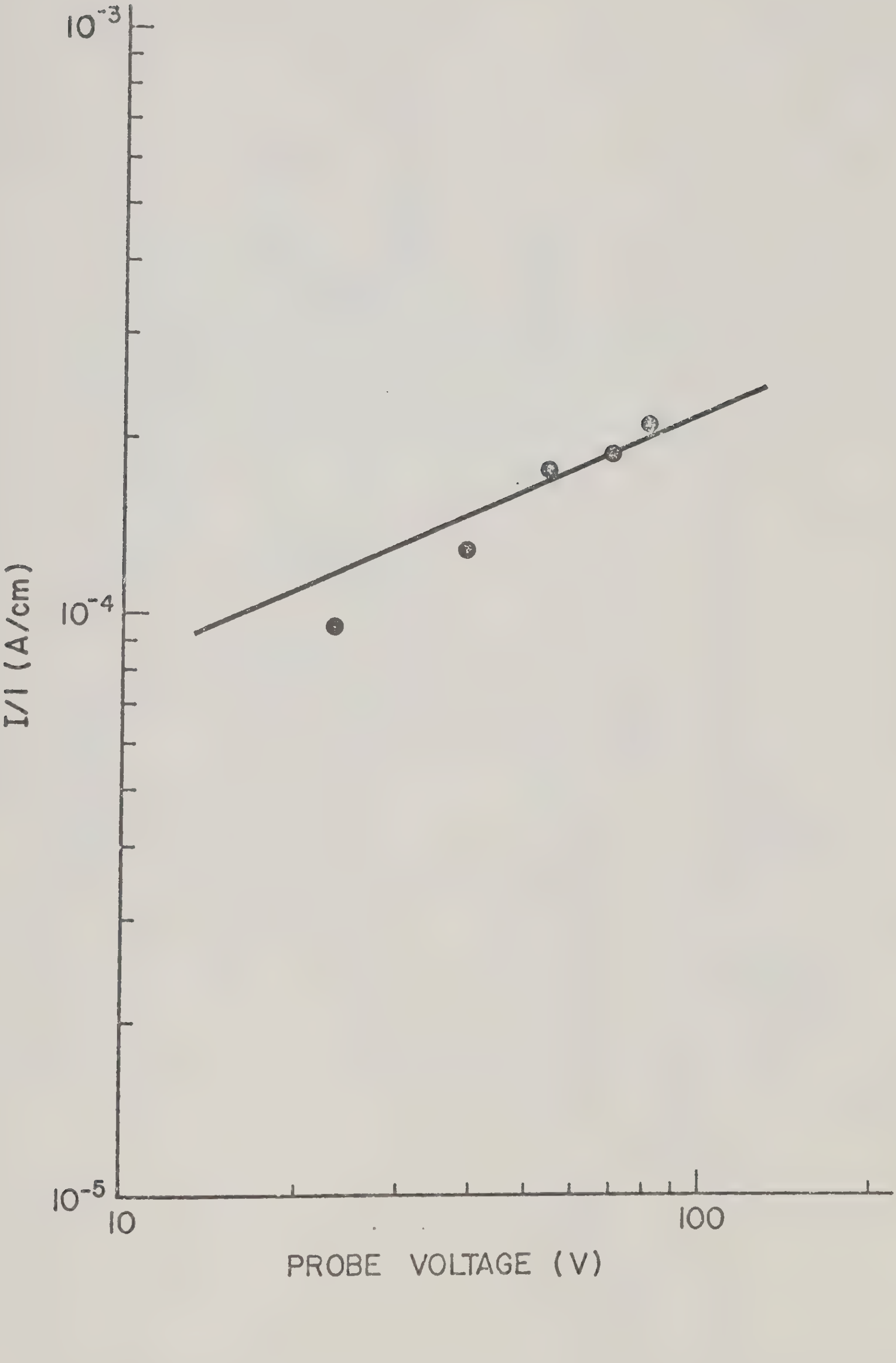

Figure 5-5(b) Probe Current per Unit Length as a Function of Bias Voltage. Solid line is from Equation (5.16).

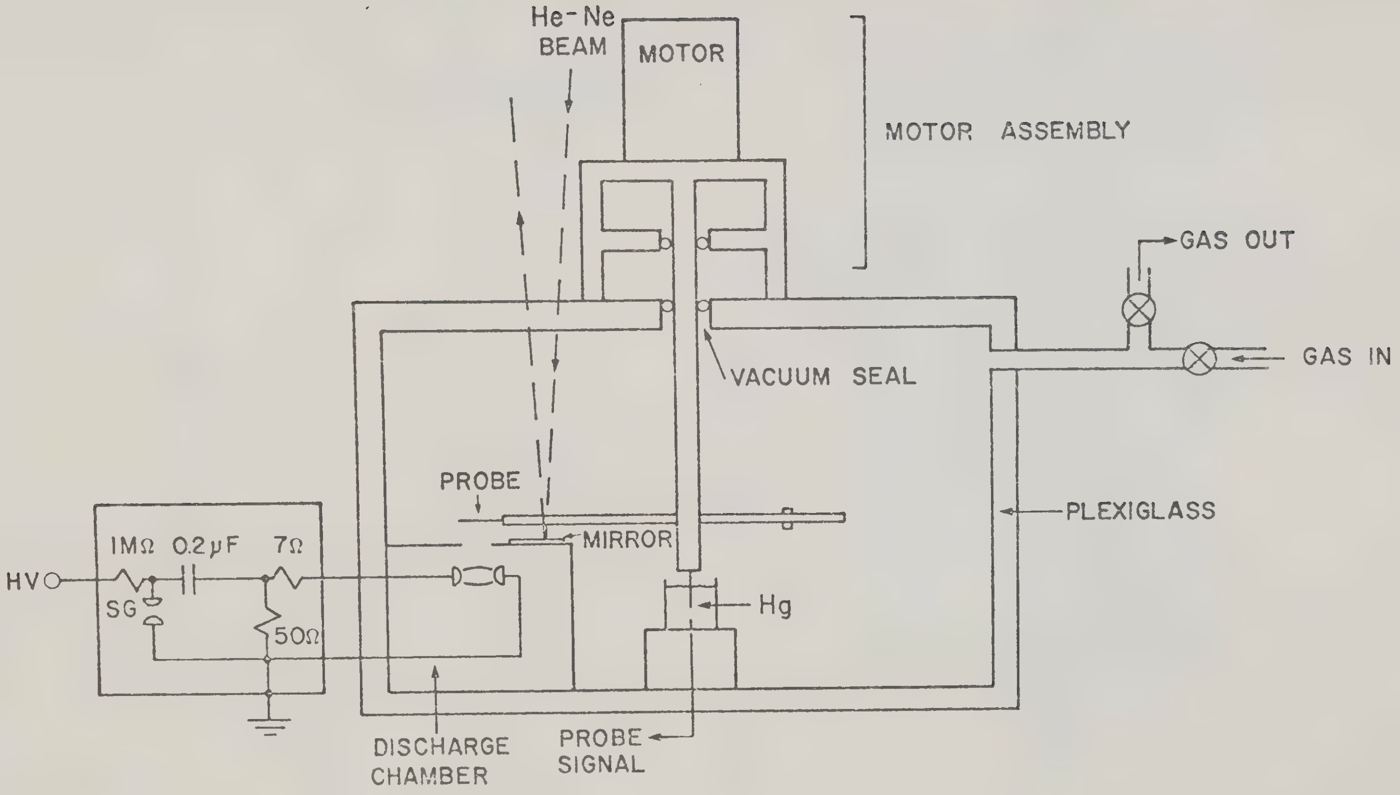
He-Ne
BEAM
MOTOR
MOTOR ASSEMBLY
GAS OUT
GAS IN
VACUUM SEAL
PROBE
MIRROR
PLEXIGLASS
1MΩ
0.2μF
7Ω
HV
SG
50Ω
Hg
DISCHARGE
CHAMBER
PROBE
SIGNAL

Figure 5-6 Experimental Setup Used in Probe Measurement

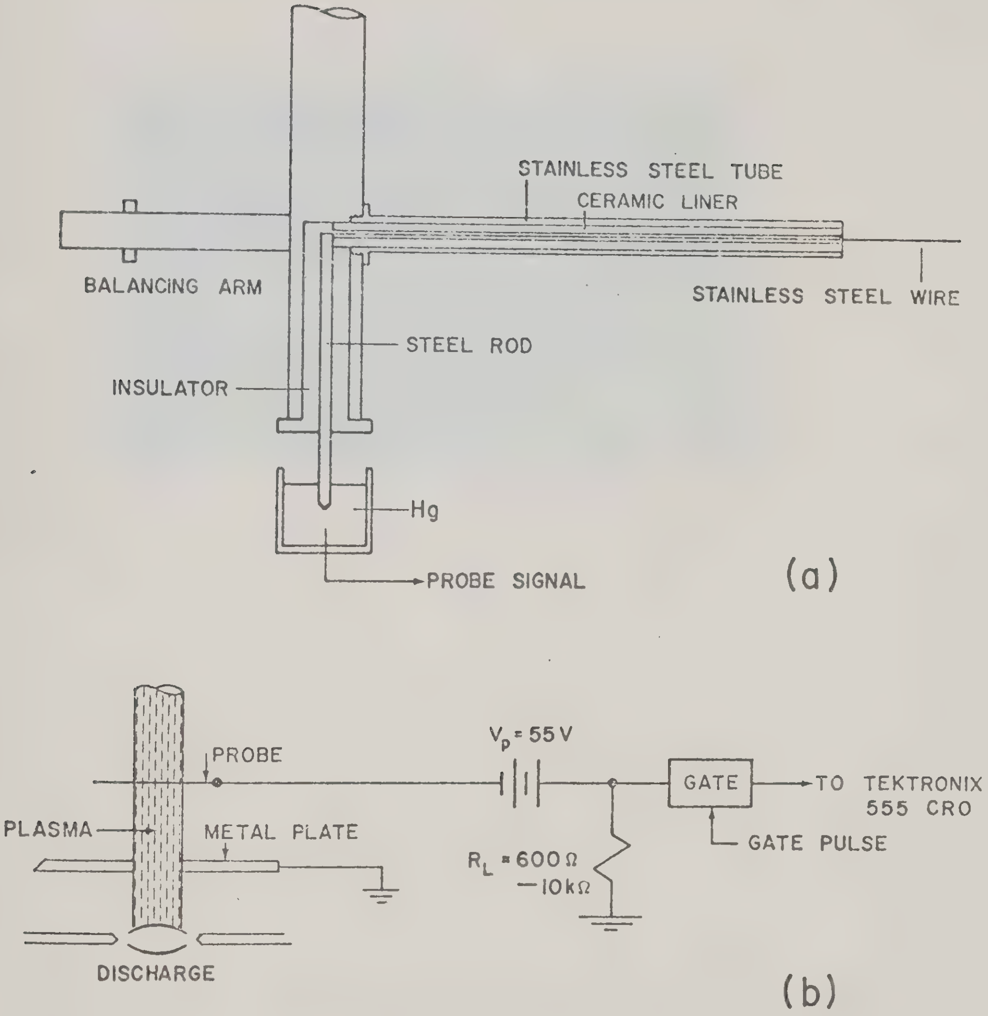
STAINLESS STEEL TUBE
CERAMIC LINER
BALANCING ARM
STAINLESS STEEL WIRE
STEEL ROD
INSULATOR
Hg
PROBE SIGNAL
(a)
$V_p = 55V$
PROBE
GATE
TO TEKTRONIX 555 CRO
PLASMA
METAL PLATE
GATE PULSE
$R_L = 600\Omega - 10k\Omega$
DISCHARGE
(b)

Figure 5-7 Probe Design and Circuit

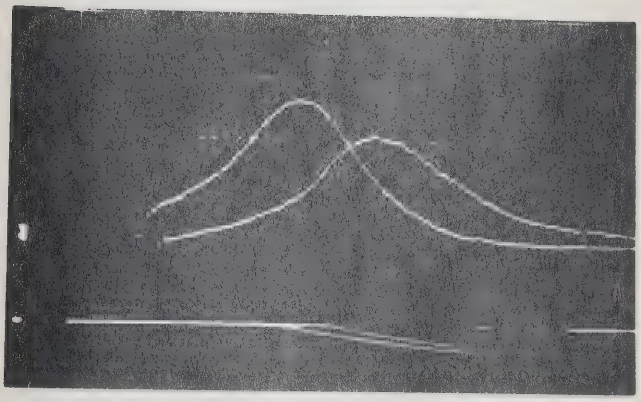

Figure 5-8 Photoplasma Probe Currents. Typical oscillogram of probe currents at two different times. The lower traces are the reference signals (see text). Sweep speed is 20μs/div.

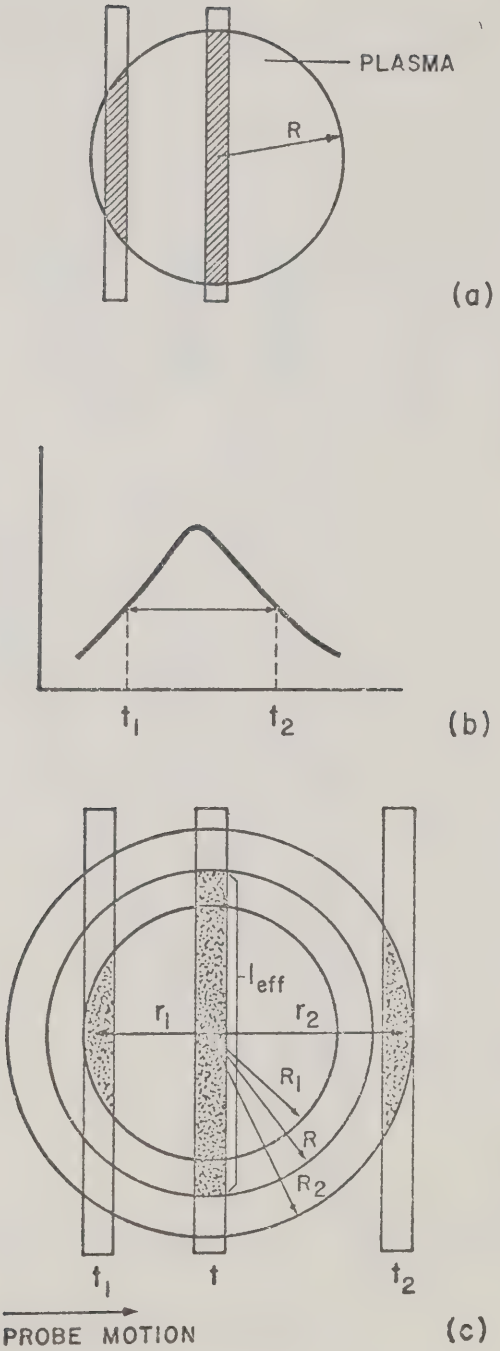
PLASMA
R
(a)
t1
t2
(b)
l_eff
r1
r2
R1
R
R2
t1
t
t2
PROBE MOTION
(c)

Figure 5-9 Schematic Diagram Showing ℓ_{eff} at Various Times

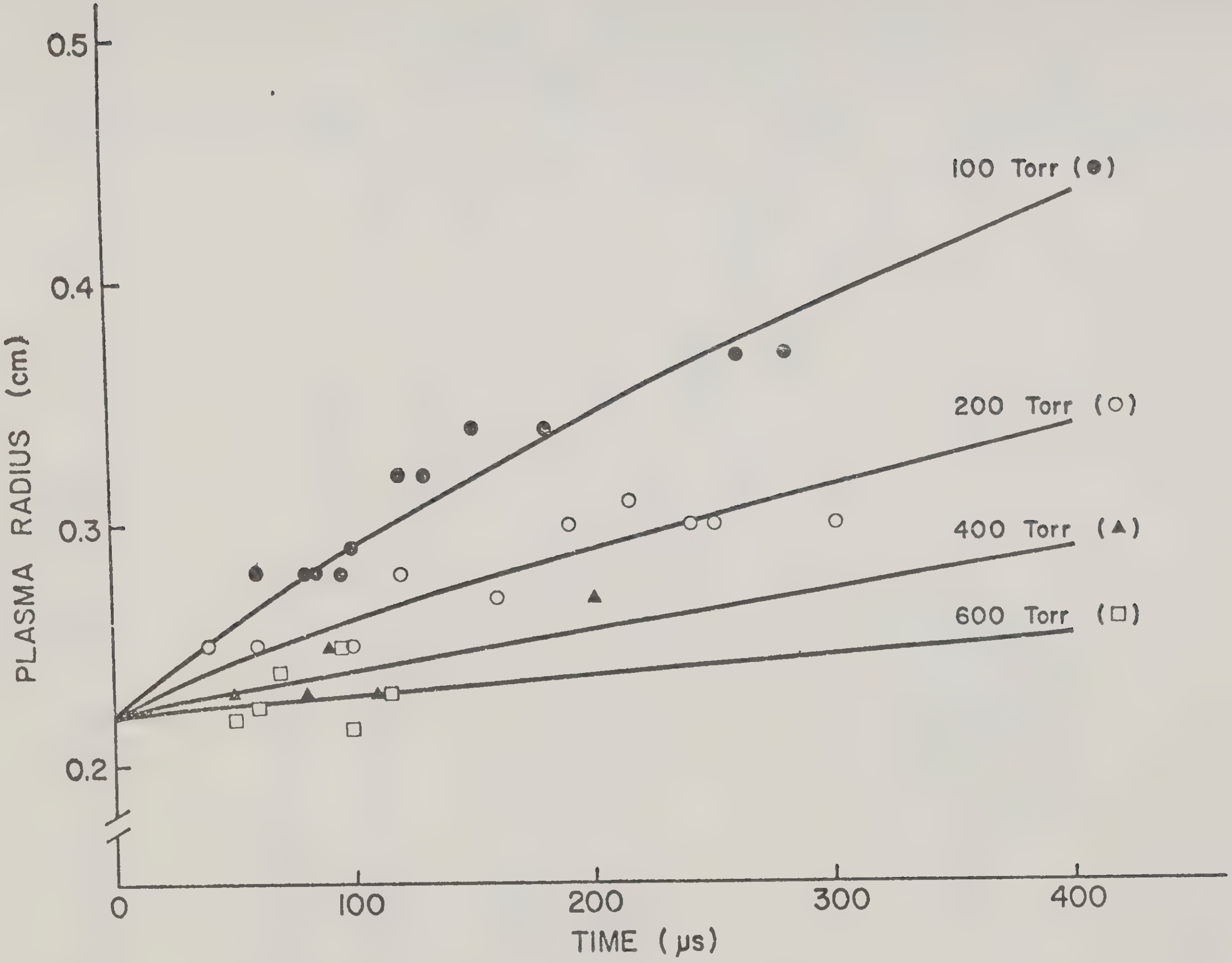

Figure 5-10 Plasma Radius, $\ell_{eff}/2$ Versus Time

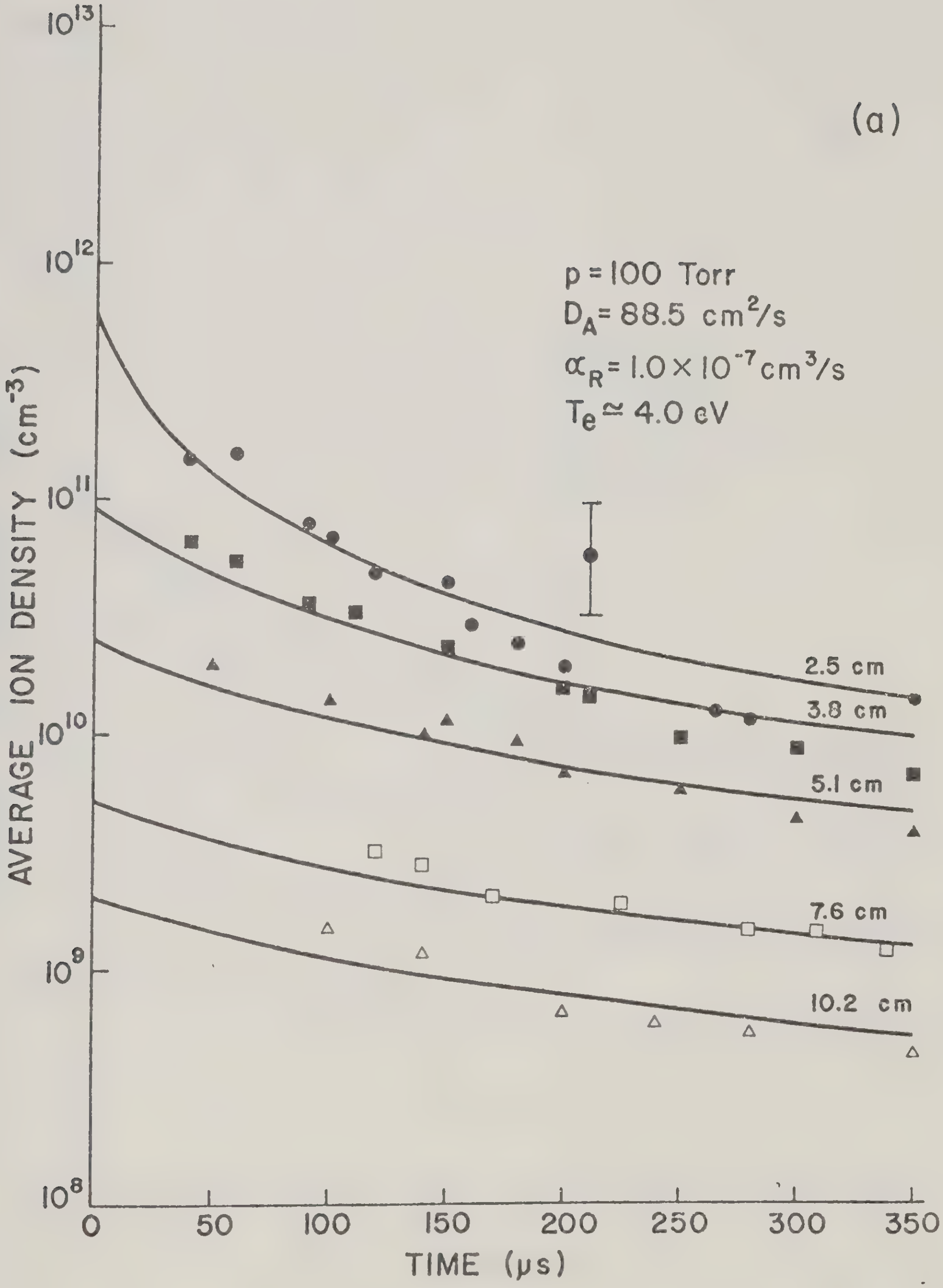

Figure 5-11(a) Photoplasma Density Versus Time

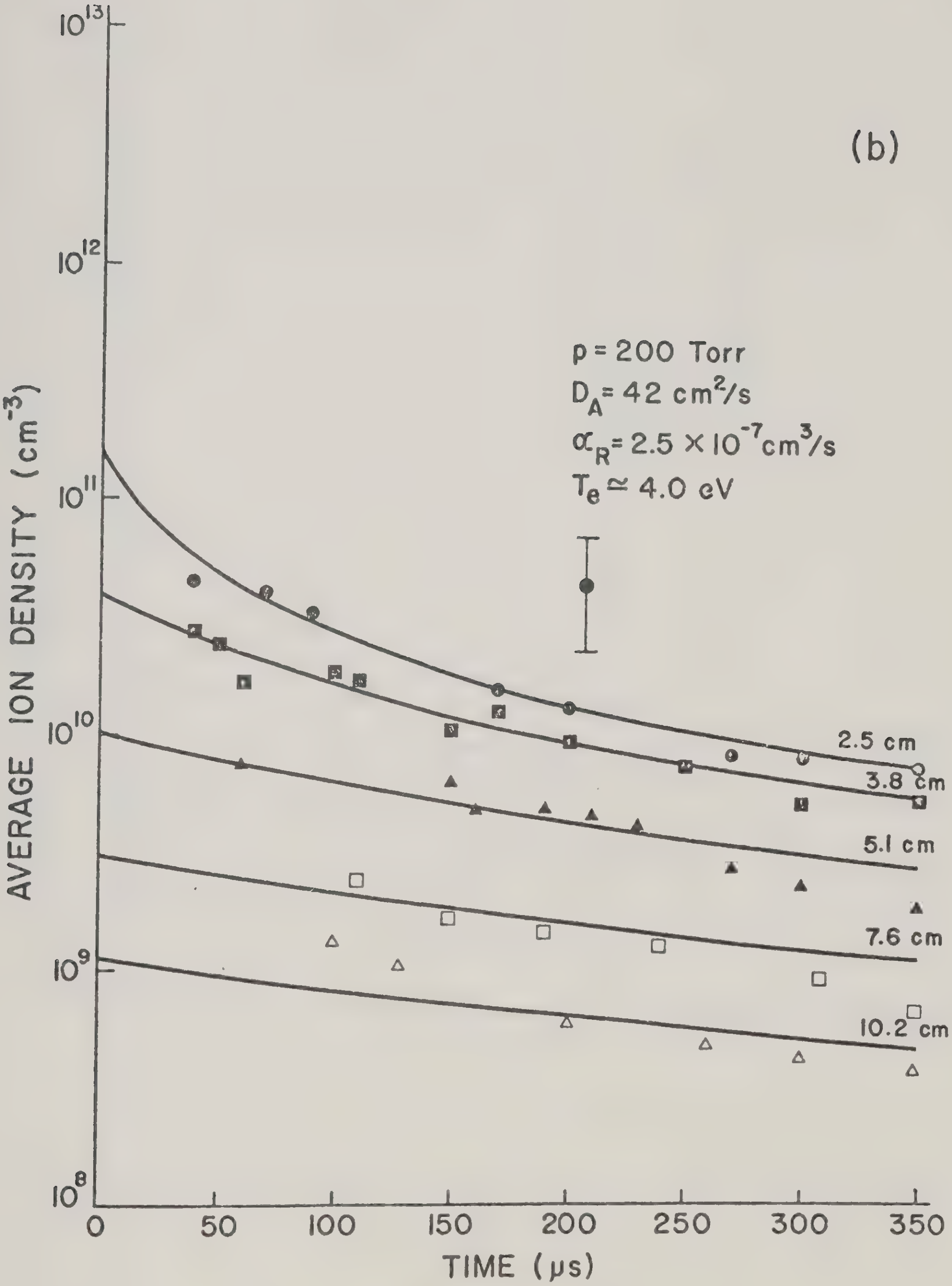

Figure 5-11(b) Photoplasma Density Versus Time

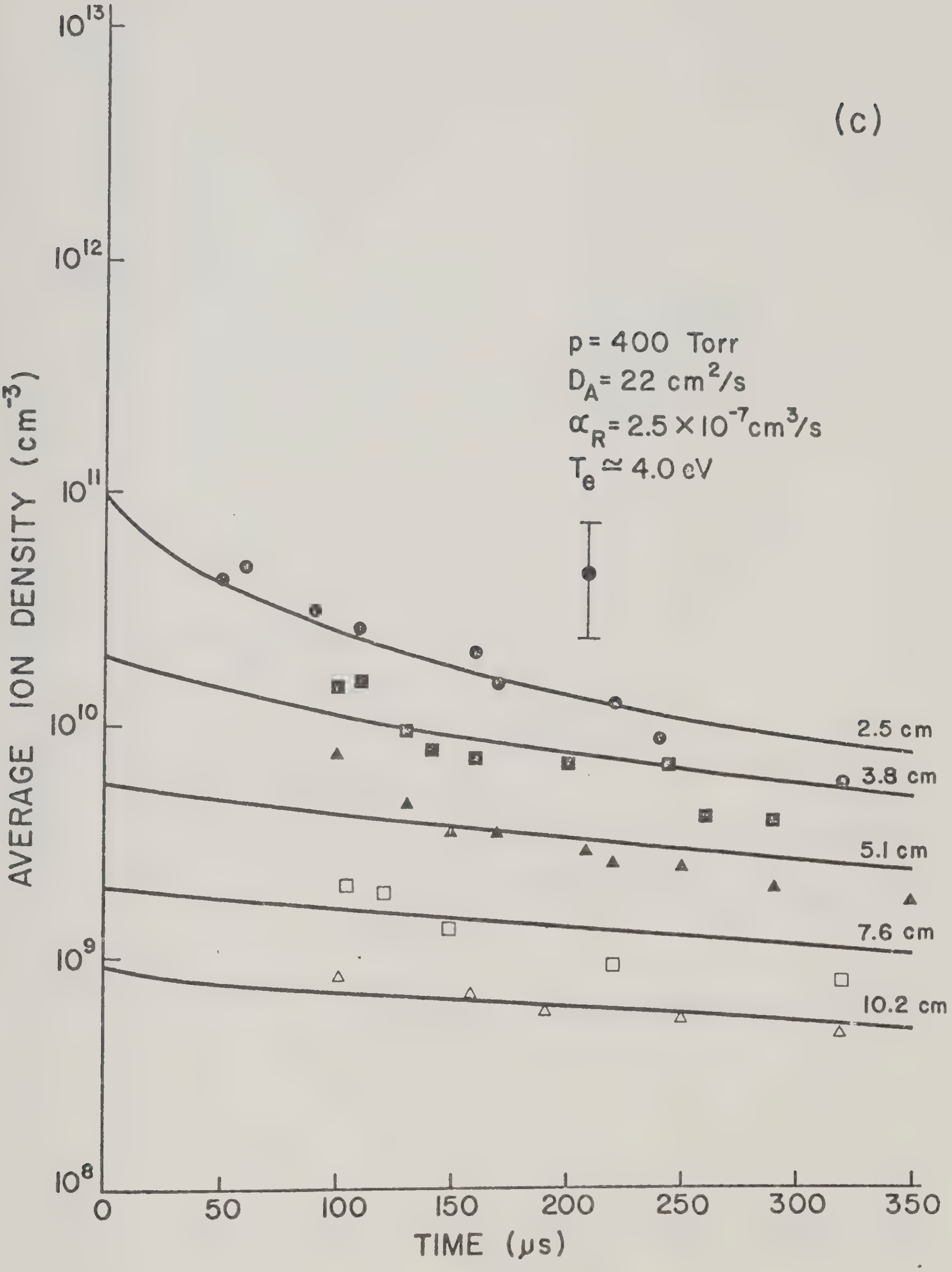

Figure 5-11(c) Photoplasma Density Versus Time

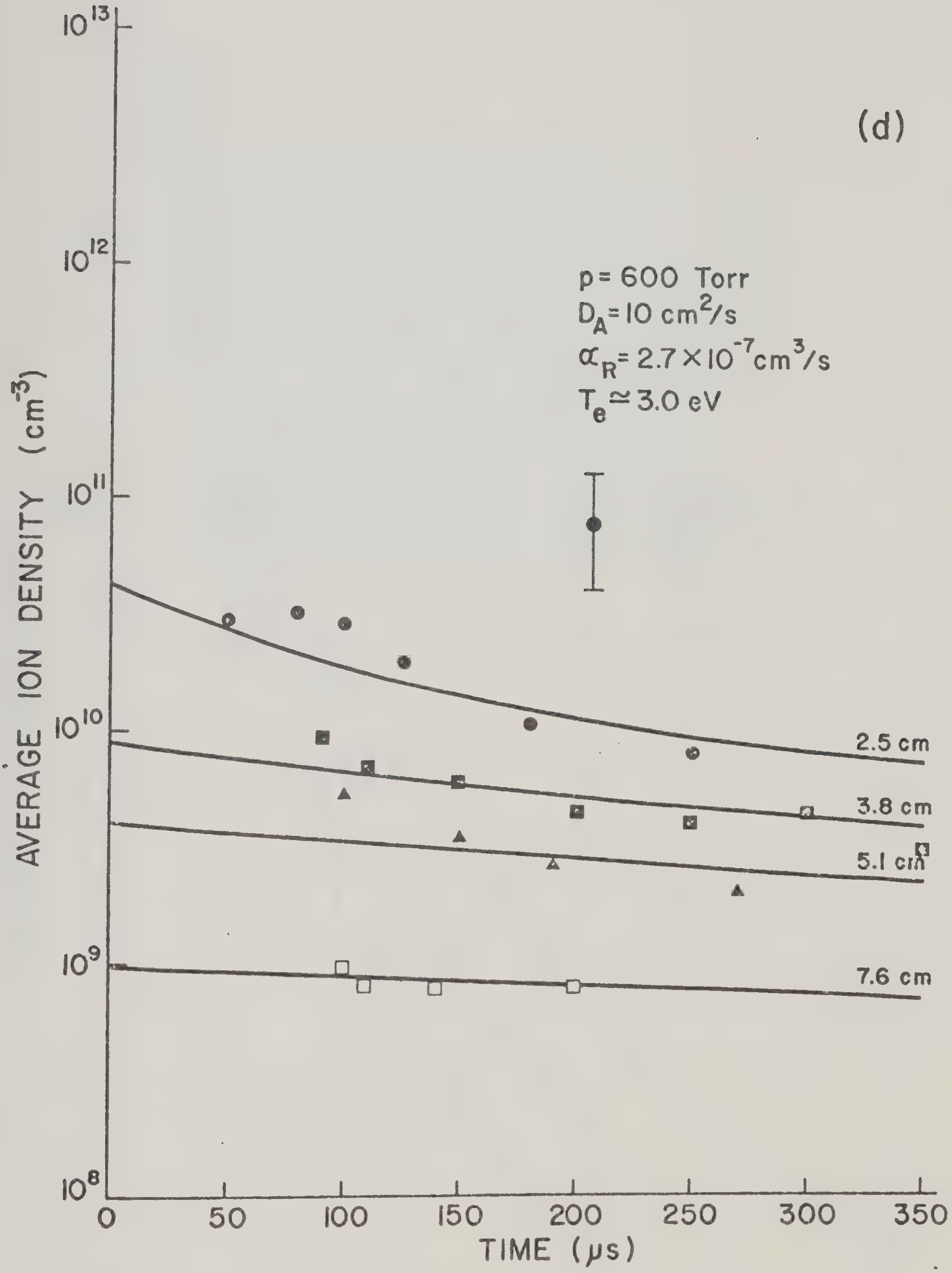

Figure 5-11(d) Photoplasma Density Versus Time

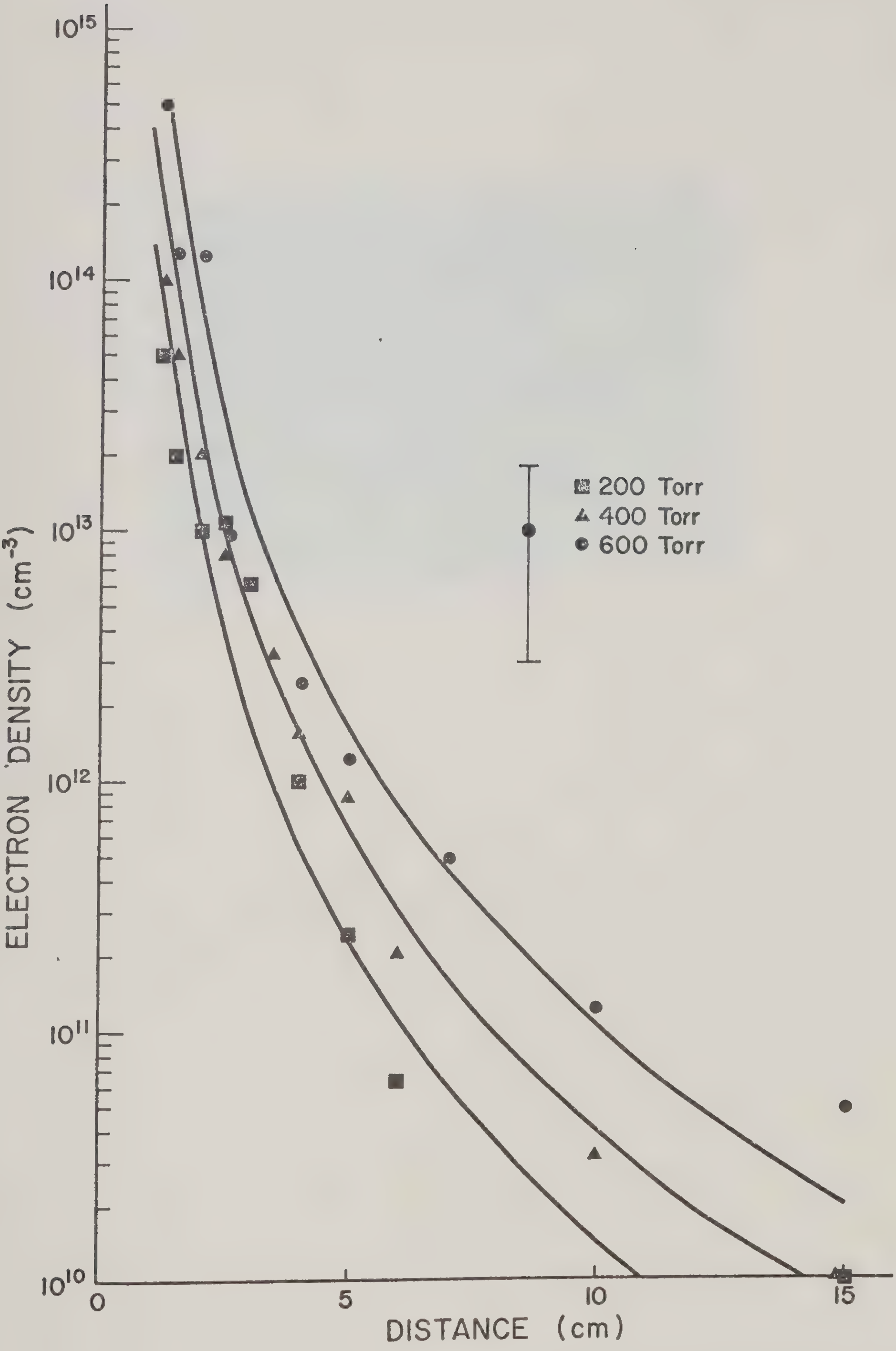

Figure 5-12 Variation of Photoplasma Density with Distance from UV Source

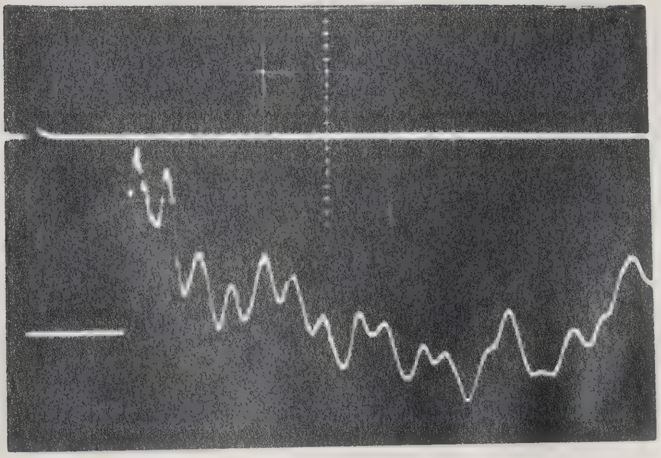

Figure 5-13 Pressure Transducer Signal. Sweep speed is 10μs/div.

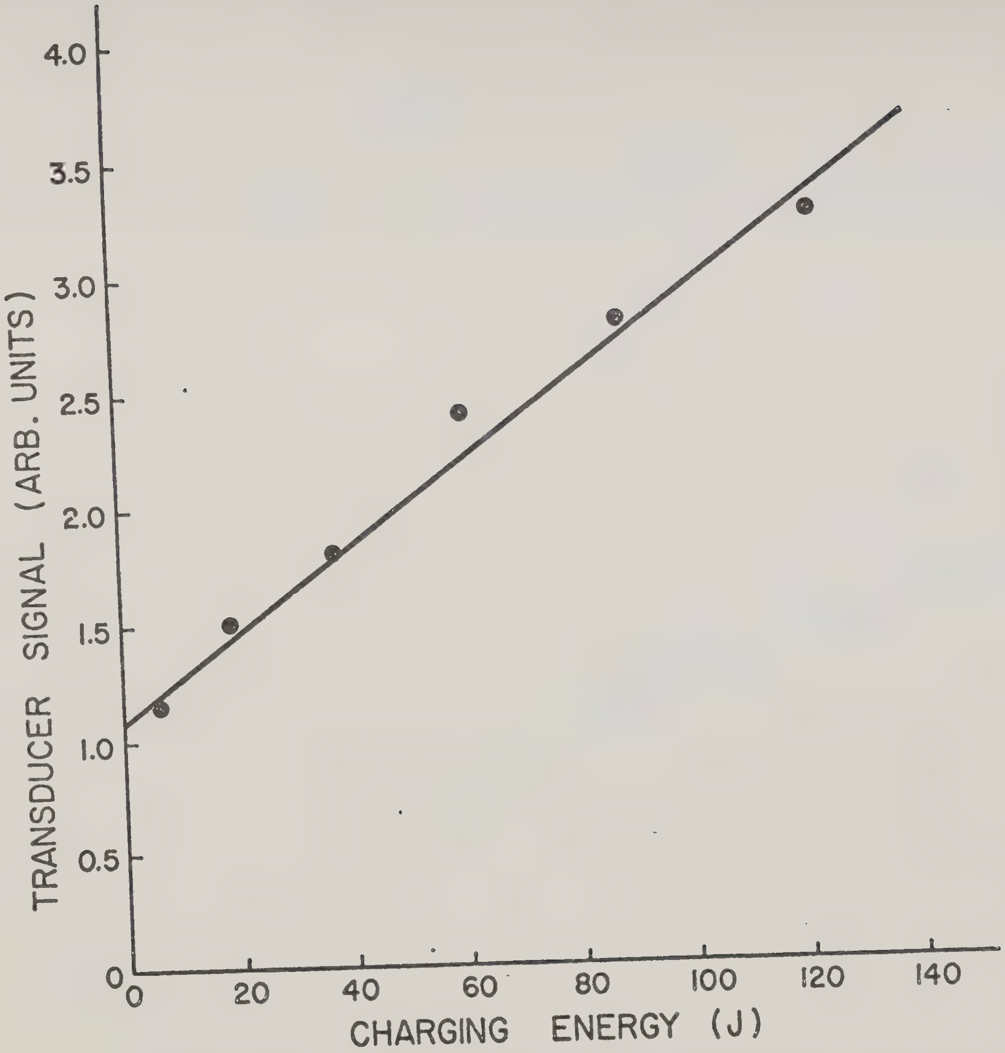

Figure 5-14 Linearity of Piezoelectric Pressure Transducer Response

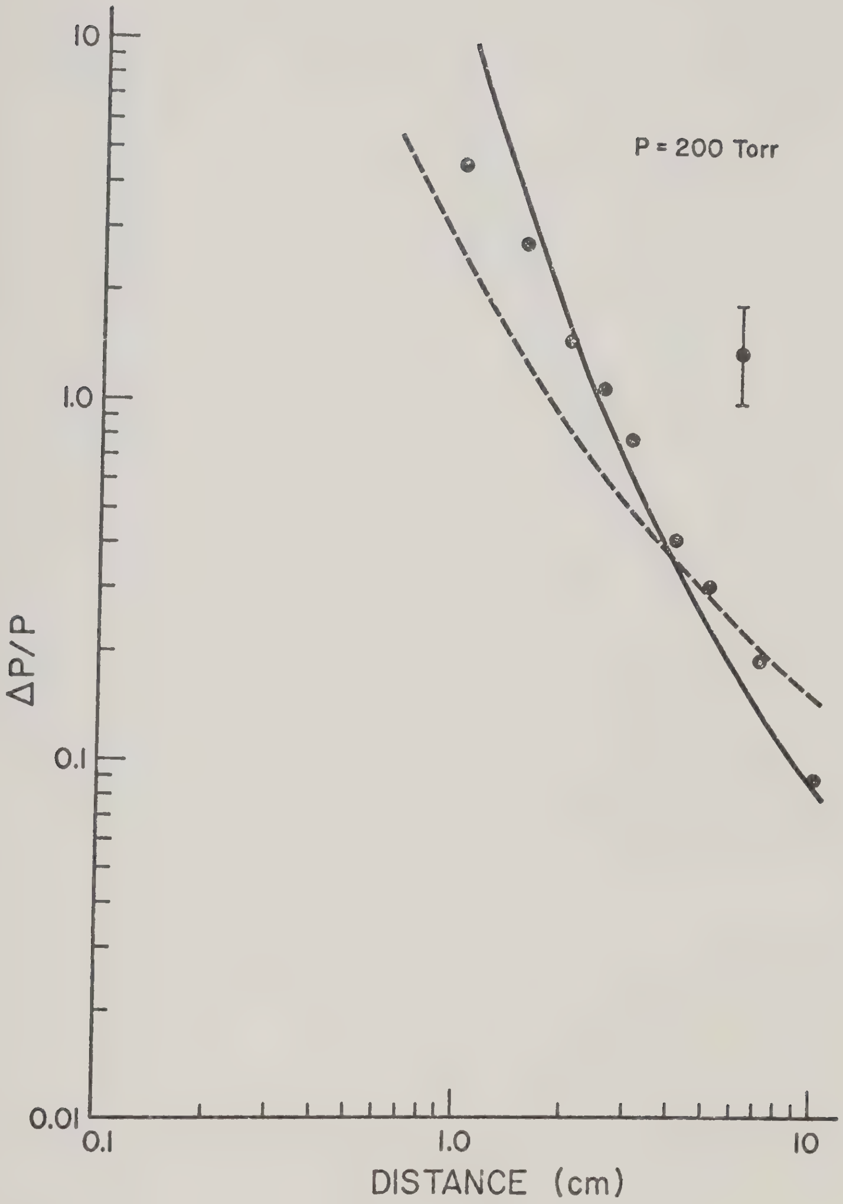

Figure 5-15(a) Shock Strength as a Function of Distance. The solid line is from Reference 28 (spherical shock wave) while the dashed line is from Reference 29 (cylindrical shock).

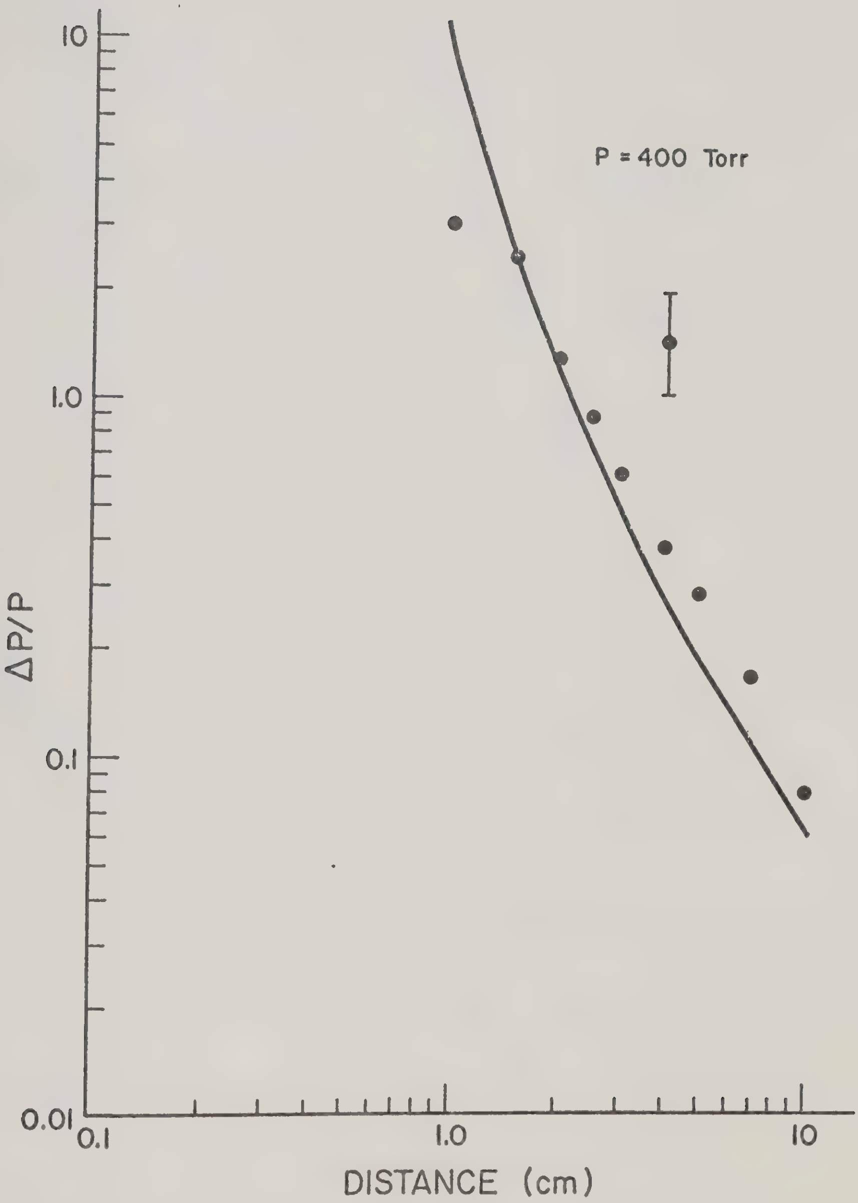

Figure 5-15(b) Shock Strength Versus Distance. The solid line is the theoretical prediction assuming spherical shock.

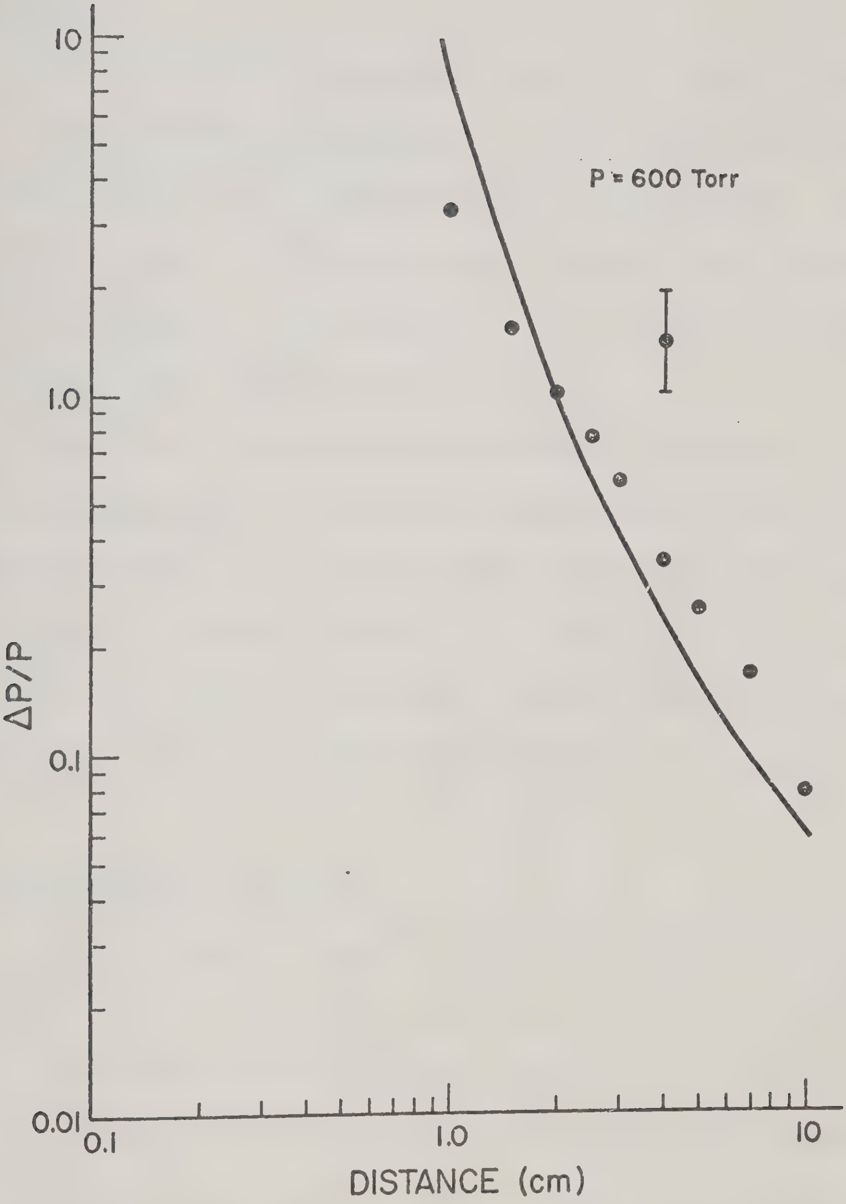

Figure 5-15(c) Shock Strength Versus Distance. The solid line is the theoretical prediction assuming a spherical shock.

CHAPTER VI

ELECTRON, ION, AND NEUTRAL DENSITY: IN THE DISCHARGE

6.1 Outline

Interferometric measurements using a CO_2 laser (10.6μm) and a He-Cd laser (441.6nm) are described. A Mach-Zehnder interferometer was used to measure the electron density at early times. A Jamin interferometer was used in conjunction with a He-Cd laser to measure the neutral gas density. Fringe shifts in the latter case are contributed by electrons, ions, and neutrals.

Absorption measurements were performed to estimate the discharge electron temperature. The absorption mechanism at 10.6μm is inverse bremsstrahlung which is related directly to the electron temperature.

Finally, a rotating Langmuir probe measurement of the electron density for late times is described. Interferometric and probe results are complementary. The plasma decay mechanism is discussed.

6.2 Interferometer Principles

An interferometer measures the index of refraction of a given transparent sample. All interferometers operate on the same basic principle. A light beam is divided into component beams (wavefront division, amplitude division, or polarization division) and then recombined. The sample is placed in one of the component beams. Interference fringes formed by the recombined beams are observed; changes in the optical refractivity of the sample are seen as shifts in the interference fringes.

6.3 Interferometric Measurement of Electron Density

6.3.1 Optical Refractivity of an Ar Plasma

The total index of refraction of a plasma is the sum of the indices of refraction due to electrons, ions, and neutrals[1]. For an argon plasma, the index of refraction is given by[2]:

$$\mu = 1 + (A + B/\lambda^2)\, n_a - C\lambda^2\, n \qquad (6.1)$$

where

$A = 1.039 \times 10^{-23} \mathrm{cm}^3$

$B = 5.82 \times 10^{-34} \mathrm{cm}^5$

$n_a = n_n + 0.8\, n_{ion}$

$\quad = n_n + 0.8n$

n = electron density

n_n = neutral density

$C = 4.48 \times 10^{-14} \mathrm{cm}$

λ = wavelength of light source (cm)

The contribution of the charged and the neutral particles in a plasma are strongly dependent on the wavelength. Hence, by using two light sources at different wavelengths it is possible to separate the contribution of the charged particles from that of the neutrals.

With $\lambda_1 = 4.416 \times 10^{-5}$cm (He-Cd laser) and $\lambda_2 = 1.06 \times 10^{-3}$cm ($CO_2$ laser) the indices of refraction are respectively:

$$\mu_1 = 1 + 1.069 \times 10^{-23}\, n_n - 7.855 \times 10^{-23}\, n \qquad (6.2)$$

$$\mu_2 = 1 + 1.039 \times 10^{-23}\, n_n - 5.033 \times 10^{-20}\, n \qquad (6.3)$$

The contribution of the electrons to the total index of refraction at 10.6μm is three orders of magnitude greater than that of the neutrals. Hence, if the change in the neutral density, Δn_n, is not much greater than the change in the electron density, Δn, the change in the index of refraction, $\Delta\mu_2$, is:

$$\Delta\mu_2 \simeq 1 - 5.033 \times 10^{-20} \Delta n \qquad (6.3a)$$

6.3.2 Mach-Zehnder Interferometer

Figure 6-1 shows the setup of a Mach-Zehnder interferometer. Coated NaCℓ beam splitters were used for M_2 and M_3. The discharge was placed in an arm of the interferometer. Scanning of the plasma was made possible by placing the whole discharge system on a movable base. Changes in the index of refraction of the plasma caused shifts in the fringe pattern which were observed with a Ge-Au detector. A filter provided rejection of the discharge emission. The number of fringe shifts P_2 is:

$$P_2 = \frac{\Delta\mu_2 \ell}{\lambda_2} \qquad (6.4)$$

where ℓ is the optical path length and λ_2 is the wavelength. One fringe shift implies (λ_2 = 10.6μm)

$$\langle n\ell \rangle = 2 \times 10^{16} \mathrm{cm}^{-2} \qquad (6.5)$$

6.3.3 Cylindrical Geometry

The plasma was assumed to be cylindrically symmetric and since it was illuminated "side on", the fringes observed as a function of the radius

had to be subjected to an Abel inversion to obtain the refractive index as a function of the radius. Referring to Equation (6.4) and Figure 6-2, the fringe shift at $r = r_i$ is:

$$P_2(r_i) = \frac{2}{\lambda_2} \int_o^{y_s} \Delta\mu_2 dy$$

$$= \frac{2}{\lambda_2} \int_{r_i}^{r_s} \frac{\Delta\mu_2(r) r dr}{\sqrt{r^2 - r_i^2}} \tag{6.5}$$

This is Abel's integral equation. The solution for this equation is[3]:

$$\Delta\mu_2(r_i) = -\frac{\lambda_2}{\pi} \int_{r_i}^{r_s} \frac{dP_2}{dr} (r^2 - r_i^2)^{-1/2} dr \tag{6.6}$$

From Equation (6.6) and Equation (6.3a) the radial electron density distribution is obtained.

6.3.4 Electron Density Distributions

Figure 6-3 shows a typical oscillogram of the fringe shifts. The fringes are counted from the right. To avoid confusion regarding the fringe turnover point, fringes were counted no earlier than 30μs after the discharge was fired. Figures 6-4(a)-(c) show the fringe shifts plotted against the radius at four different times and pressures of 200, 400, 600 Torr. A polynomial of the form:

$$P_2 = ar^4 + br^2 + c \tag{6.7}$$

was fitted to the data. This is just a fourth order power series expansion with the coefficients of the odd powers of r equated to zero since they lead to a discontinuity in the derivative of n at $r = 0$. This is clearly

physically impossible. Substituting Equation (6.7) into Equation (6.6):

$$\Delta\mu_2(r) = -6.7 \times 10^{15} (r_s^2 - r^2)^{1/2} (a'r^2 - b') \qquad (6.8)$$

where a' and b' are expressed in terms of a, b, and r_s.

The results are depicted in Figures 6-4 (d) - (f). These are comparable to the results of Offenberger, *et. al.*[4] in a CO_2 laser spark in Ar.

6.4 Absorption of 10.6μm Radiation

By blocking the reference arm of the interferometer the absorption of CW CO_2 radiation by the discharge plasma was measured. The absorption process is inverse bremsstrahlung and the absorption coefficient, α, at 10.6μm , is given by:

$$\alpha = 1.8 \times 10^{-35} \left(\frac{n^2}{T_e^{3/2}}\right) [1 - e^{-\varepsilon_\gamma/T_e}] \frac{T_e}{\varepsilon_\gamma} \qquad (6.9)$$

where n is the electron density in cm^{-3}, T_e is the electron temperature in eV and ε_γ is the photon energy in eV. The transmission of the laser beam:

$$T = \exp[-\int\alpha(\ell)d\ell]$$

allows one to compute the electron temperature since the density is known. Figure 6-5 is an oscillogram of the transmitted CW signal showing absorption. By using a large collecting lens (f = 20 cm, f/3.3) the effect of refraction at the higher electron densities was reduced. This was verified when the beam was apertured and the percentage transmission remained approximately

the same.

Figure 6-6 shows the measured transmission at the pressures considered. The averaged central electron temperatures were obtained using Equation (6.9) and the results of Section 6.3 and are summarized in Table 6.1. These temperatures together with the electron densities previously measured allows one to calculate the parameters R_e, α, and χ which will indicate the conditions under which the probe was operated. This is discussed in the following section.

TABLE 6.1

AVERAGE ELECTRON TEMPERATURE

Time (μs)	Electron Temperature (eV)		
	200 Torr	400 Torr	600 Torr
30	0.8 ± .2	0.7 ± .2	0.7 ± .2
50	0.4 ± .1	0.3 ± .1	0.3 ± .1
100	0.2 ± .05	0.1 ± .03	0.1 ± .03

6.5 Probe Measurements

6.5.1 Probe Theory

The high electron density in the discharge implies that the plasma sheath around a rotating cylindrical probe is "thin". In this case, the probe current is either due to diffusion or convection of ions into the sheath. The current is dominated by diffusion if $R_e\alpha^2\chi^2<1$ and by convection if $R_e\alpha^2\chi^2>1$. In the first case, the probe current per unit probe length

is:[5]

$$I = 4e^{1/2}\,\mu_i^{1/2} r_p^{1/2} v_f^{1/2} (KT_e)^{1/2} n \tag{6.10}$$

Here e is the electron charge, μ_i the ion mobility, r_p the probe radius, v_f the probe speed, K is the Boltzmann constant, T_e the electron temperature, and n is the electron density. In the second case[5],

$$I = 5.3\, n^{3/4} e^{3/4} v_f^{3/4} V^{1/2} (\mu_i\, \varepsilon_o r_p)^{1/4} \tag{6.11}$$

where V is the probe voltage and ε_o is the permittivity of free space. The most significant difference between the two cases as seen in Equations (6.10) and (6.11) is in the voltage dependence of the probe current.

Clements, *et. al.*[6] have measured the probe current in the range where a transition from diffusion to convection dominated current is expected. In agreement with Equations (6.10) and (6.11), a gradual change from $V^{1/2}$ to V^0 dependence of the probe current was observed. However, the measured currents were up to one order of magnitude smaller than the predicted value (Equation (6.10)) when $R_e\alpha^2\chi^2 < 1$.

6.5.2 Probe Circuit

The same probe as described in Section 5.4.2 was used to measure the electron density in the discharge. The density could not be measured earlier than 50μs after firing the discharge because of arcing from the high voltage electrode to the probe. The oscilloscope was protected from accidental arcs by a metal oxide varistor. Unfortunately, this device had a large

capacitance which reduced the bandwidth of the probe circuit. The response time was estimated to be 20 μs. The probe was biased negatively with a battery pack and the voltage was selected with a turn of a potentiometer divider. This was bypassed by a 15μF capacitor. The load was varied from 10Ω to 10kΩ depending on the probe current. The probe signal voltage was kept much less than the bias voltage; currents were measured as high as 90mA.

6.5.3 Results of Measurement

A typical oscillogram of the probe current is shown in Figure 6-7. As described in Section 5.4.2, the lower trace is a reference signal to locate the probe relative to the plasma. Probe current was not very reproducible with up to 50% variation from shot to shot. The discharge also tended to develop at slightly different locations. Hence, it was necessary to take many shots and average the results. Probe current was measured from 50μs to 1 ms after the discharge was fired. Five shots were taken per data point.

From the known probe speed, the probe current can be recorded as a function of position and time. The total current to the probe is:

$$I_t = 2 \int_o^{y_{max}} I(y)dy$$

or

$$I_t(r_i) = 2 \int_{r_i}^{r_s} \frac{I(r)rdr}{\sqrt{r^2-r_i^2}} \tag{6.12}$$

where I(r) is the appropriate formula for the probe current per unit length. Equation (6.12) is of the same form as Equation (6.5). Hence:

$$I(r_i) = -\frac{1}{\pi} \int_{r_i}^{r_s} \frac{dI_t}{dr} \frac{dr}{\sqrt{r^2-r_i^2}} \qquad (6.13$$

which yields n(r).

If T_e is expressed in degrees Kelvin, and p in Torr, then the following relations hold:

$$\alpha = 272 \left(\frac{T_e}{n}\right)^{1/2}$$

$$\chi = \frac{5.8\text{x}10^5}{T_e}$$

$$R_e = 1.85\text{x}10^3 \left(\frac{p}{T_e}\right)$$

$$R_e\alpha^2\chi^2 = 4.6\text{x}10^{19} \left(\frac{p}{T_e^2 n}\right)$$

$$R_e^{-1}\alpha^2\chi^2 = 1.35\text{x}10^{13} \left(\frac{1}{pn}\right) \qquad (6.14)$$

$$\frac{R_e^3\alpha^2}{\chi^2} = 1.39\text{x}10^3 \left(\frac{p^3}{n}\right)$$

The conditions $R_e\alpha^2\chi^2>1$, $R_e^{-1}\alpha^2\chi^2<<1$, and $R_e^3\alpha^2/\chi^2<<1$ specify the range of electron density where Equation (6.11) applies. Equation (6.11) is valid when:

200 Torr: $6.75\text{x}10^{10}<<n<<9.2\text{x}10^{21}/T_e^2$

400 Torr: $8.9\text{x}10^{10}<<n<<1.84\text{x}10^{22}/T_e^2$

600 Torr: $3\times10^{11} \ll n \ll 2.76\times10^{22}/T_e^{\,2}$

From the measured values of n and T_e, it is seen that Equation (6.11) does not apply up to 100μs after the discharge is fired. Furthermore, the measured probe currents were about one order of magnitude less than that predicted by Equation (6.10). This is in agreement with the results of Reference 6.

For times later than 100μs, the electron density and the temperature have decayed sufficiently and Equation (6.11) applies. To check that this is indeed the case, the probe current was measured at different bias voltages. The results are shown in Figures 6-8. The $V^{1/2}$ dependence of the probe current indicates that the current was convection dominated. The electron density for t=100μs and later are shown in Figure 6-9 at the three pressures considered.

6.5.4 Plasma Decay Mechanisms

The results of the interferometric measurement and the probe measurement were combined and Figure 6-10 depicts the decay of the electron density at r=0. The rate of decay is determined by recombination, diffusion, and cooling of the discharge.

The cooling time due to conduction by neutrals can be expressed using simple kinetic theory as[7]:

$$\tau_c \simeq 10^{-1}\, L^2/(\bar{v}\lambda) \tag{6.15}$$

where L is the electrode separation, $\bar{v}$ and λ are the mean thermal

velocity and mean free path of the neutrals, respectively. $\tau_c \simeq 300\mu s$ while the experimentally obtained cooling time is approximately $40\mu s$ (see Table 6.1). Therefore, other cooling mechanisms such as line radiation operate. Because of the rapid cooling of the plasma, the charge density decay is not determined by the cooling rate.

Referring to Figure 6-10, the plasma decay time is $\tau \simeq 30\mu s$. The diffusion time of the ions is approximately equal to τ_c and hence, diffusion is ruled out as the dominant loss mechanism.

The recombination time is $\tau_R = \frac{1}{\alpha_R n}$. The recombination coefficient varies quite rapidly with density and temperature so it is hard to estimate the actual τ_R. Recombination can account for the observed decay if,

$$\alpha_R = \frac{1}{n\tau} \simeq \frac{3x10^4}{n} \quad cm^3/s$$

The above condition yields α_R in general agreement with published values[8,9] ($n>10^{11}cm^{-3}$). Of course, for sufficiently long times, diffusion loss will eventually become the dominant loss mechanism.

6.6 Jamin Interferometry

A Jamin interferometer was set up to measure the neutral atom concentration in the discharge. A He-Cd laser was chosen as the light source (λ_1=441.6nm). This means that the neutrals as well as the charges will contribute to the observed fringe shifts. Since the electron density is already known, it is easy to separate the contribution of the electrons and ions to the total optical refractivity. The pertinent equations needed were already discussed in Section 6.3.

Figure 6-11 depicts the experimental setup while a typical oscillogram of the observed fringe shifts is shown in Figure 6-12. Unfortunately, it was quite difficult to determine the exact time when the fringes turn over (fringe shifts change sign). Therefore only the fringe shifts at $r = 0$ were considered reliable because there was no question where the fringes should turn over. During the initial part of the current pulse the electron density will be increasing while the neutral density decreases. In the afterglow, the electron density will be decreasing and the neutral density increasing. Both electrons and neutrals will therefore produce fringe shifts in the same direction. Furthermore, the contribution of the electrons were negligible at the times considered. From the oscillograms, the average atom density was computed assuming that the electron, ion and neutral gas distributions in the discharge had approximately the same boundary. These are shown in Figure 6-13. The uncertainty in the gas density is quite large because the total fringe shift for a change in density from ambient to vacuum at 400 Torr is only approximately 3.5 fringes ($\ell \approx 1$cm).

There is a factor of two difference between the measured gas density and the theoretical equilibrium value at a temperature equal to the measured electron temperature. This discrepancy is not surprising considering the uncertainties in the neutral density and electron temperature measurements.

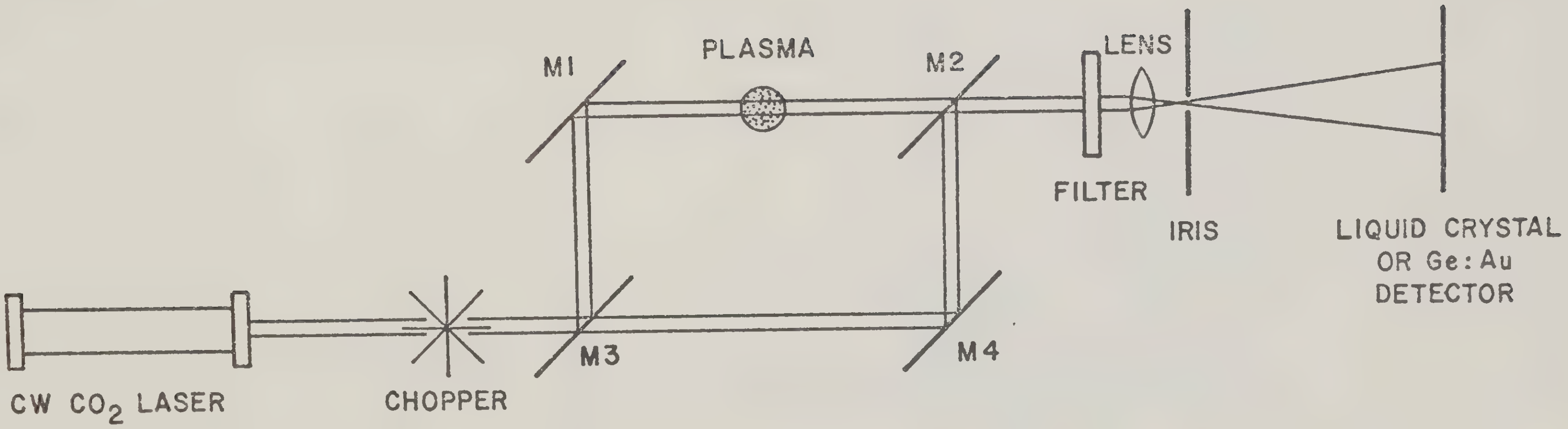
M1
PLASMA
M2
LENS
FILTER
IRIS
LIQUID CRYSTAL
OR Ge:Au
DETECTOR
CW CO_2 LASER
CHOPPER
M3
M4

Figure 6-1 Mach-Zehnder Interferometer

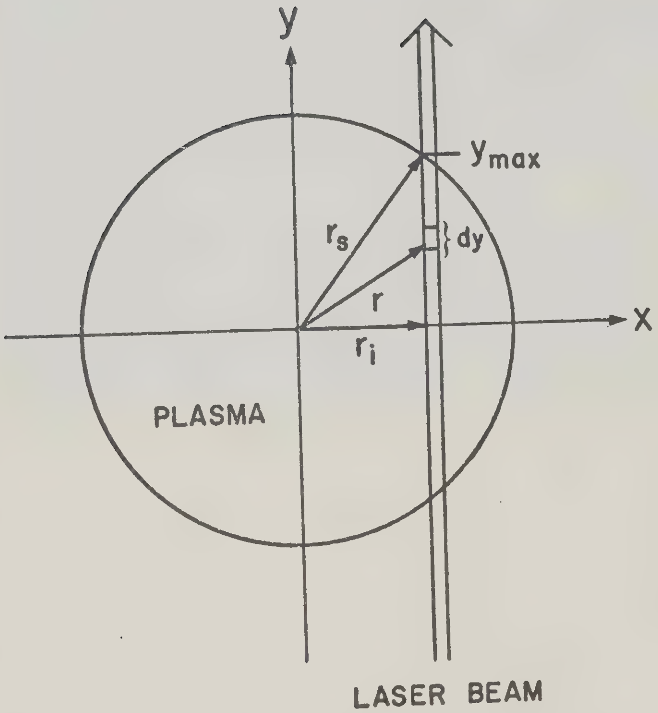
y
y_{max}
r_s
dy
r
X
r_i
PLASMA
LASER BEAM

Figure 6-2 Diagram Used in Abel Transformation

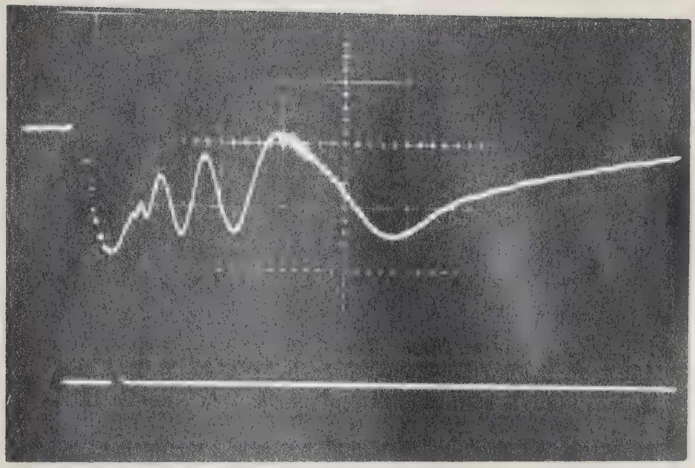

Figure 6-3 Mach-Zehnder Interferometer Signal

The signal from the Ge:Au detector shows typical fringe shifts. The sweep speed is 5μs/div. The decrease in signal is due to plasma absorption.

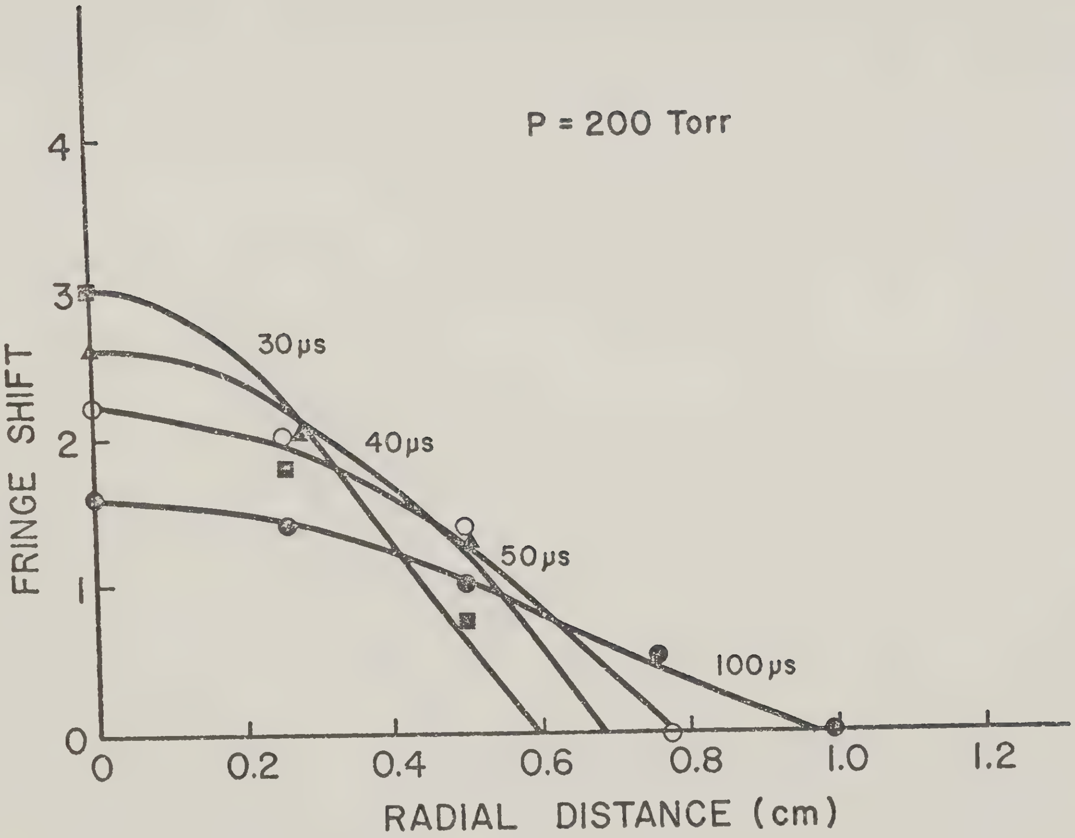

Figure 6-4(a) Observed Fringe Shifts at Various Times.
The solid line is from a power series fitted into the data (see text).

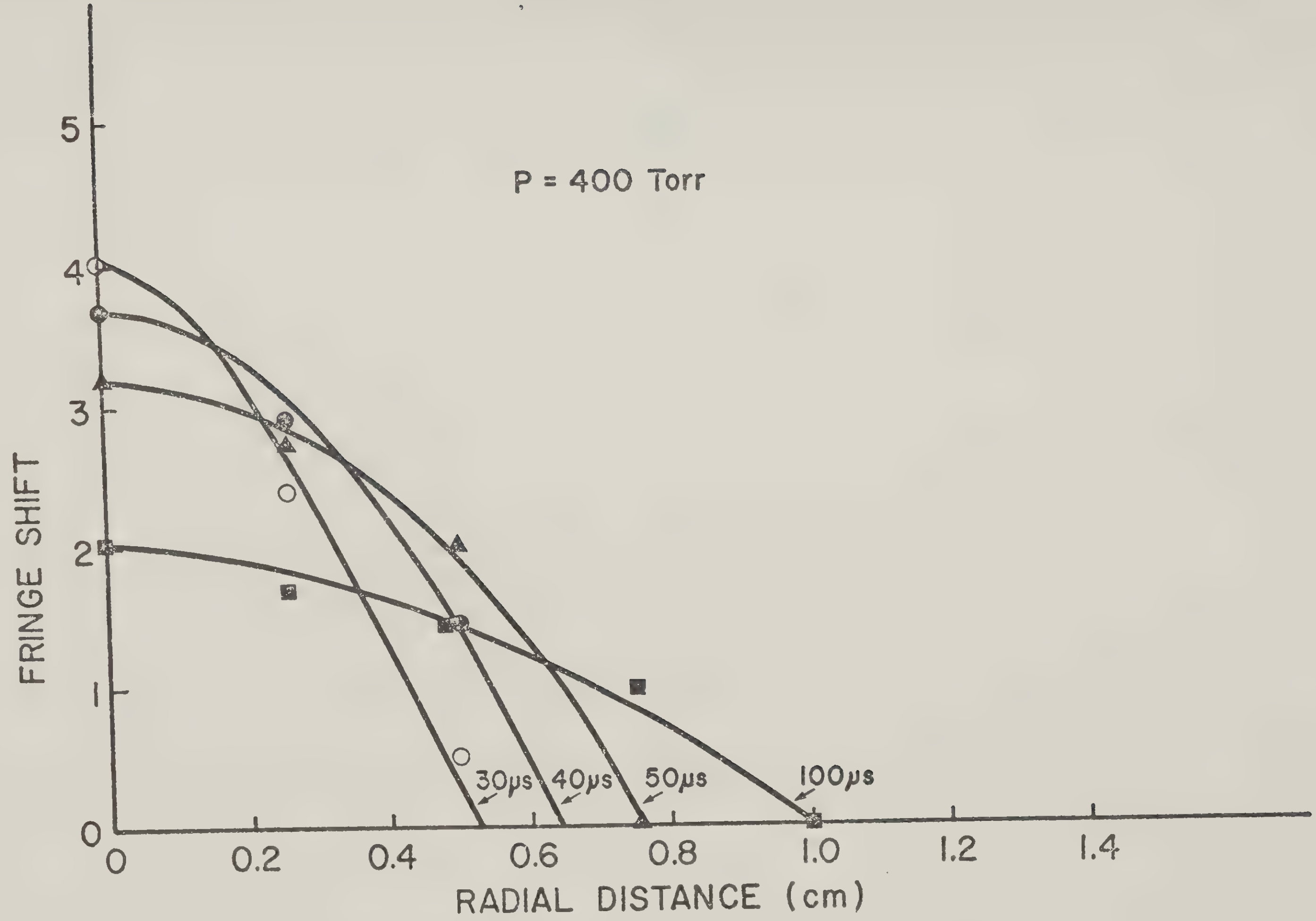

Figure 6-4(b) Observed Fringe Shifts at Various Times.

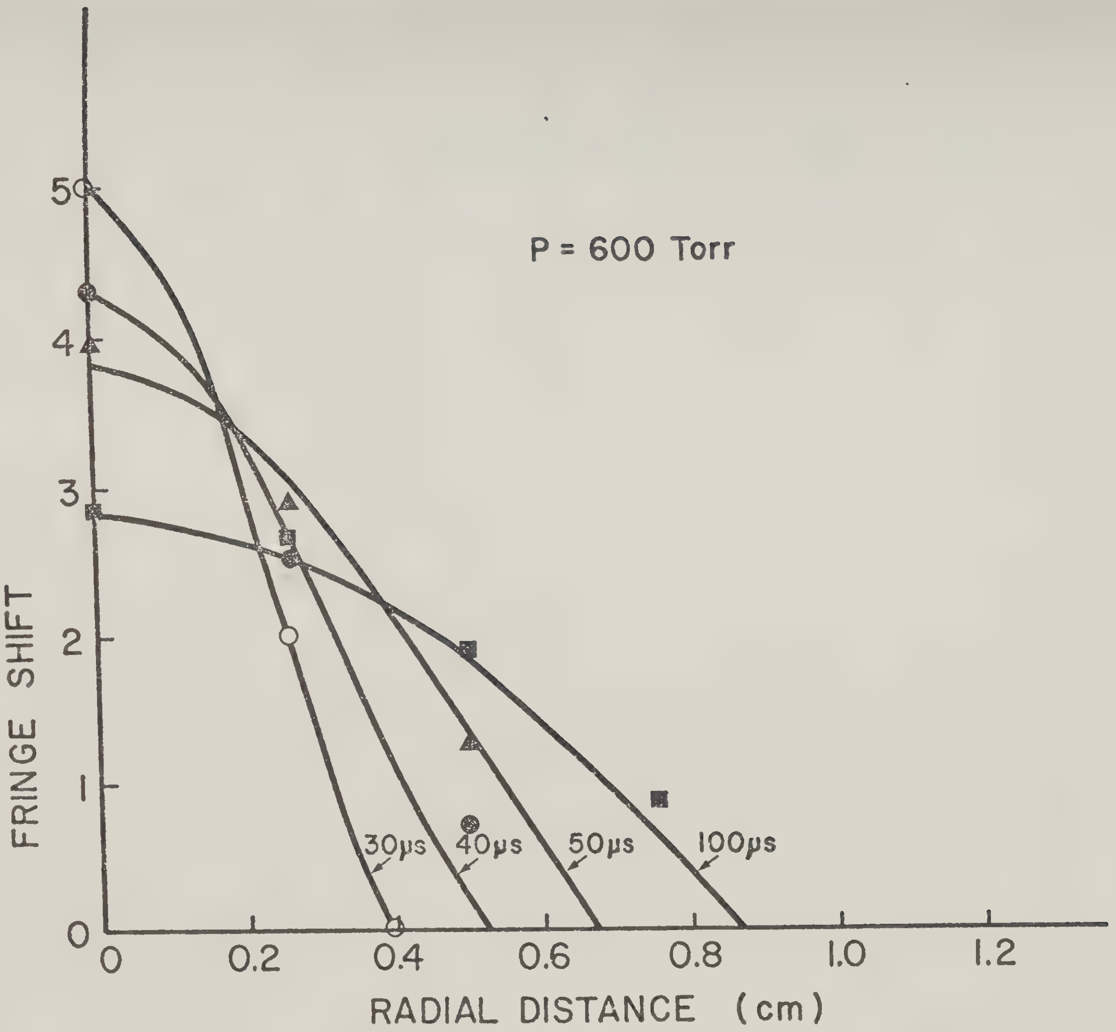

Figure 6-4(c) Observed Fringe Shifts at Various Times.

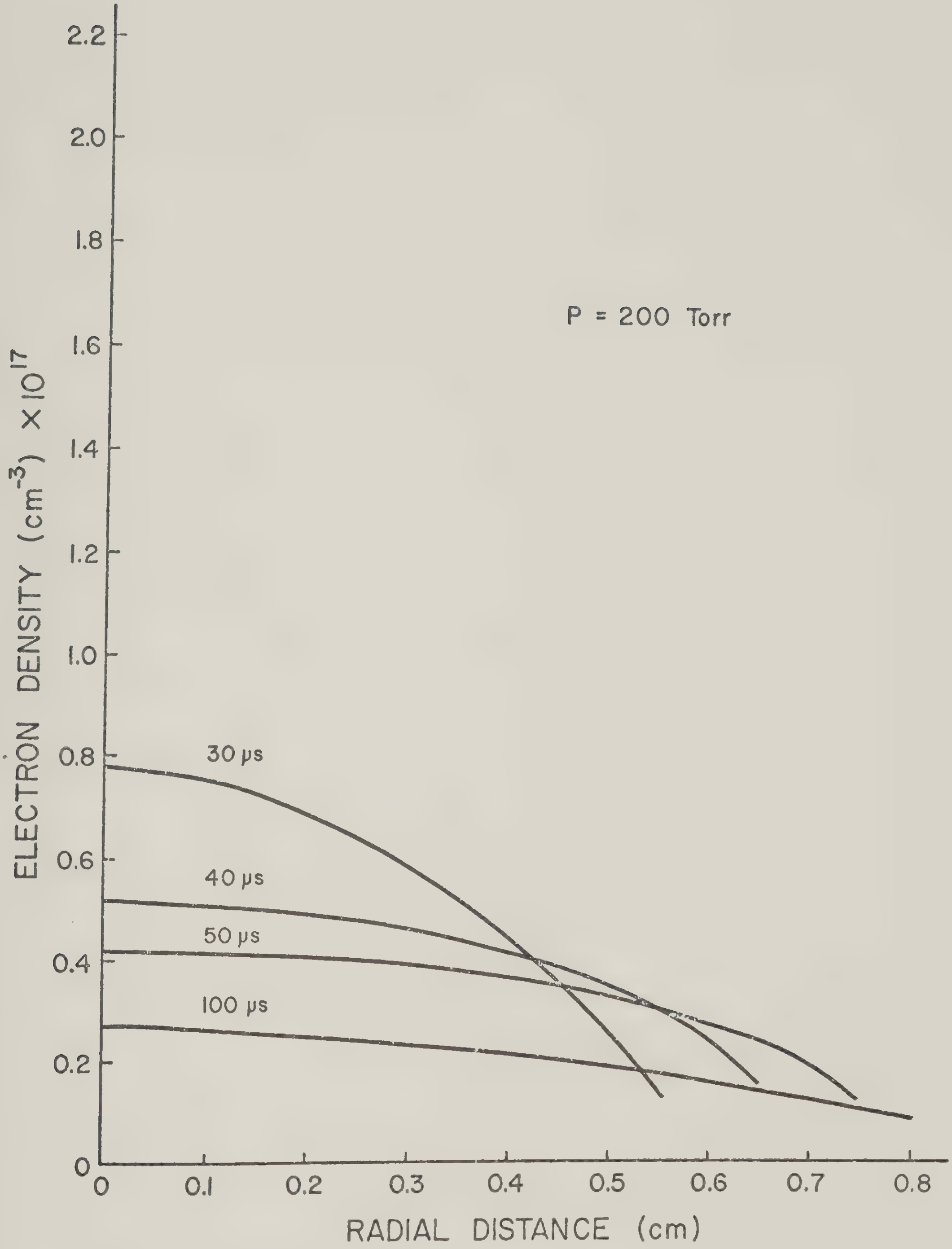

Figure 6-4(d) Electron Density as a Function of Radius.

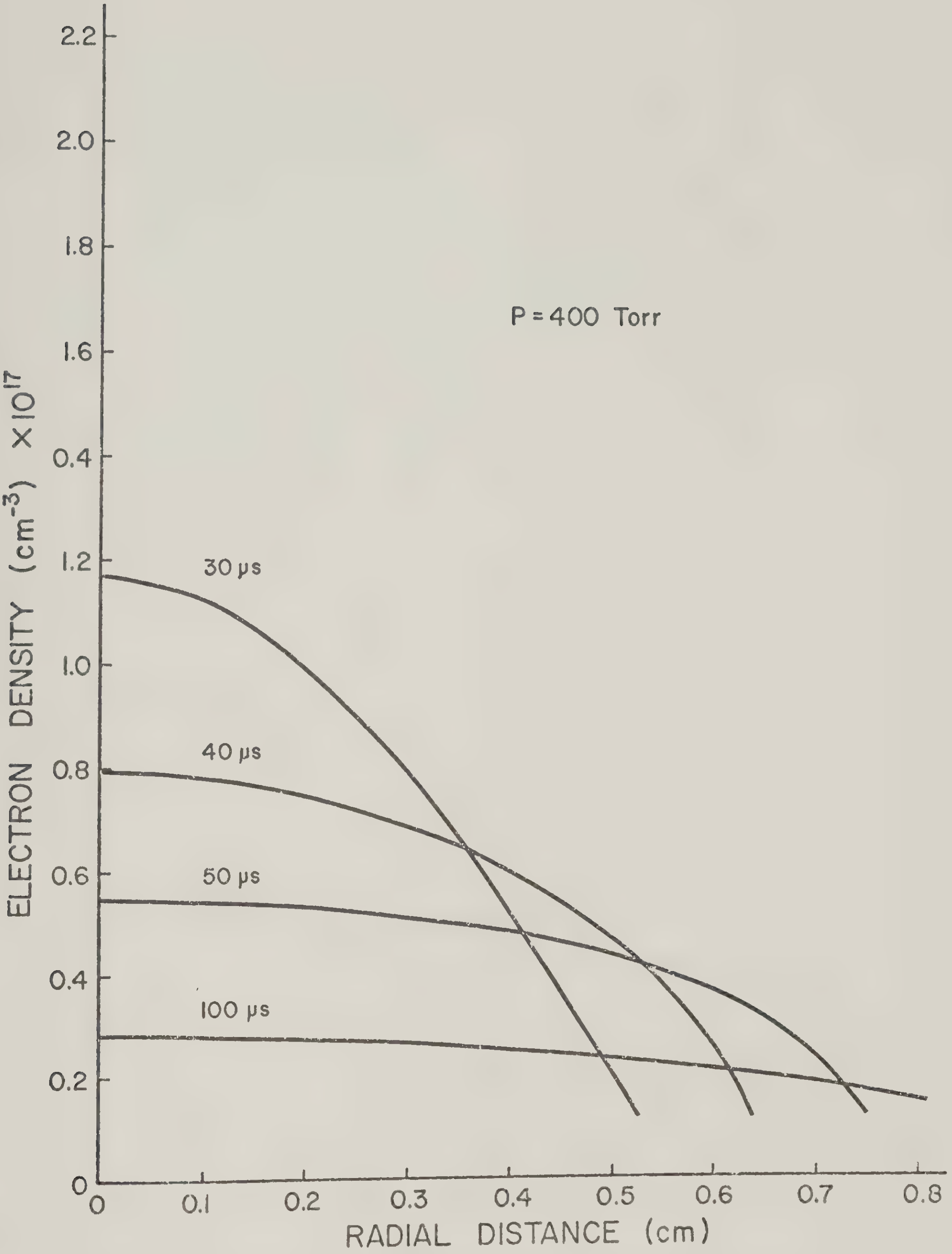

Figure 6-4(e) Electron Density as a Function of Radius.

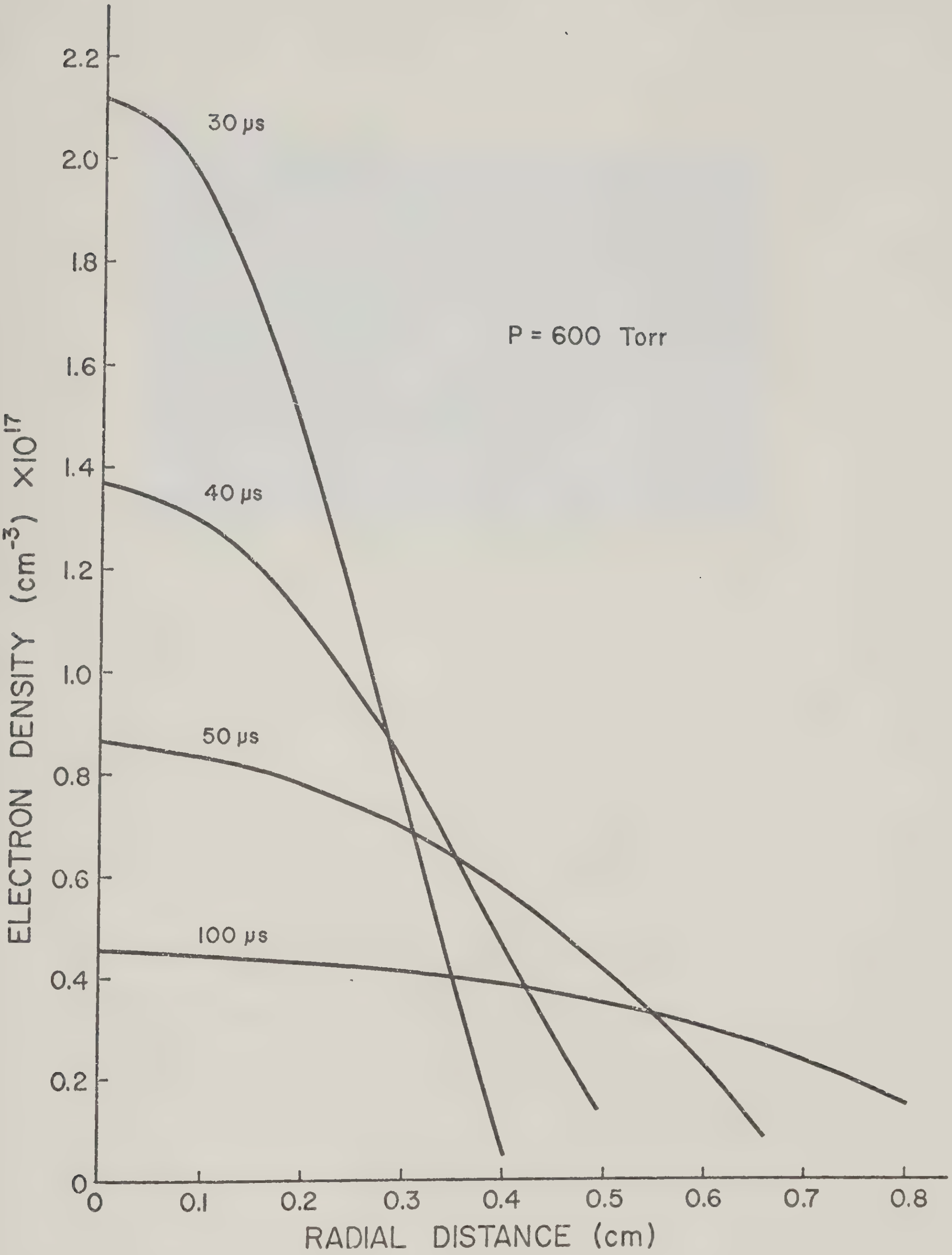

Figure 6-4(f) Electron Density as a Function of Radius.

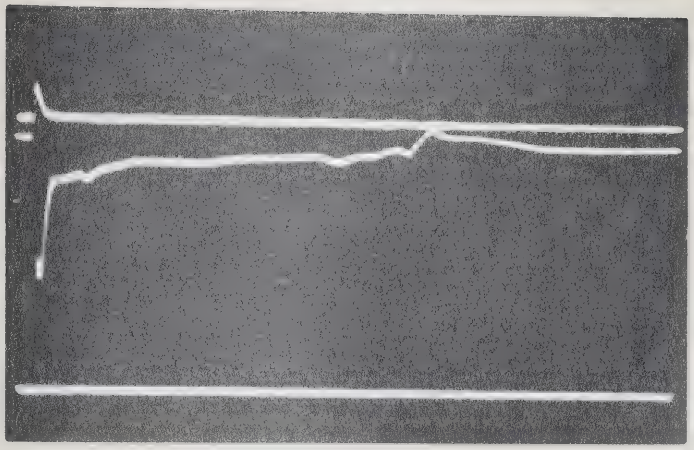

Figure 6-5 CO_2 Absorption by Discharge Plasma. The upper trace is the discharge current pulse; the middle trace is the Ge:Au detector signal showing absorption; the lower trace is the detector signal when the laser is blocked. Sweep speed is 20 μs/div.

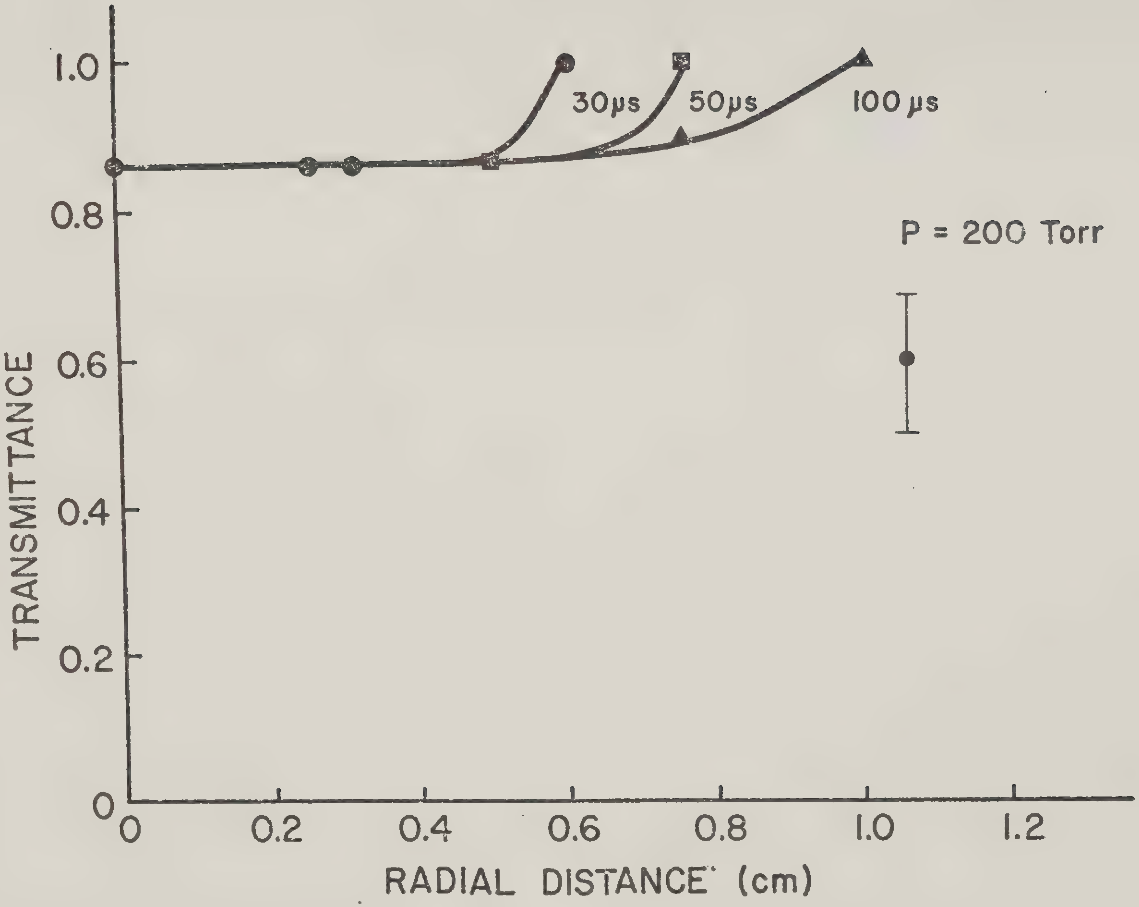

Figure 6-6(a) Discharge Plasma Transmittance of 10.6μm Radiation.

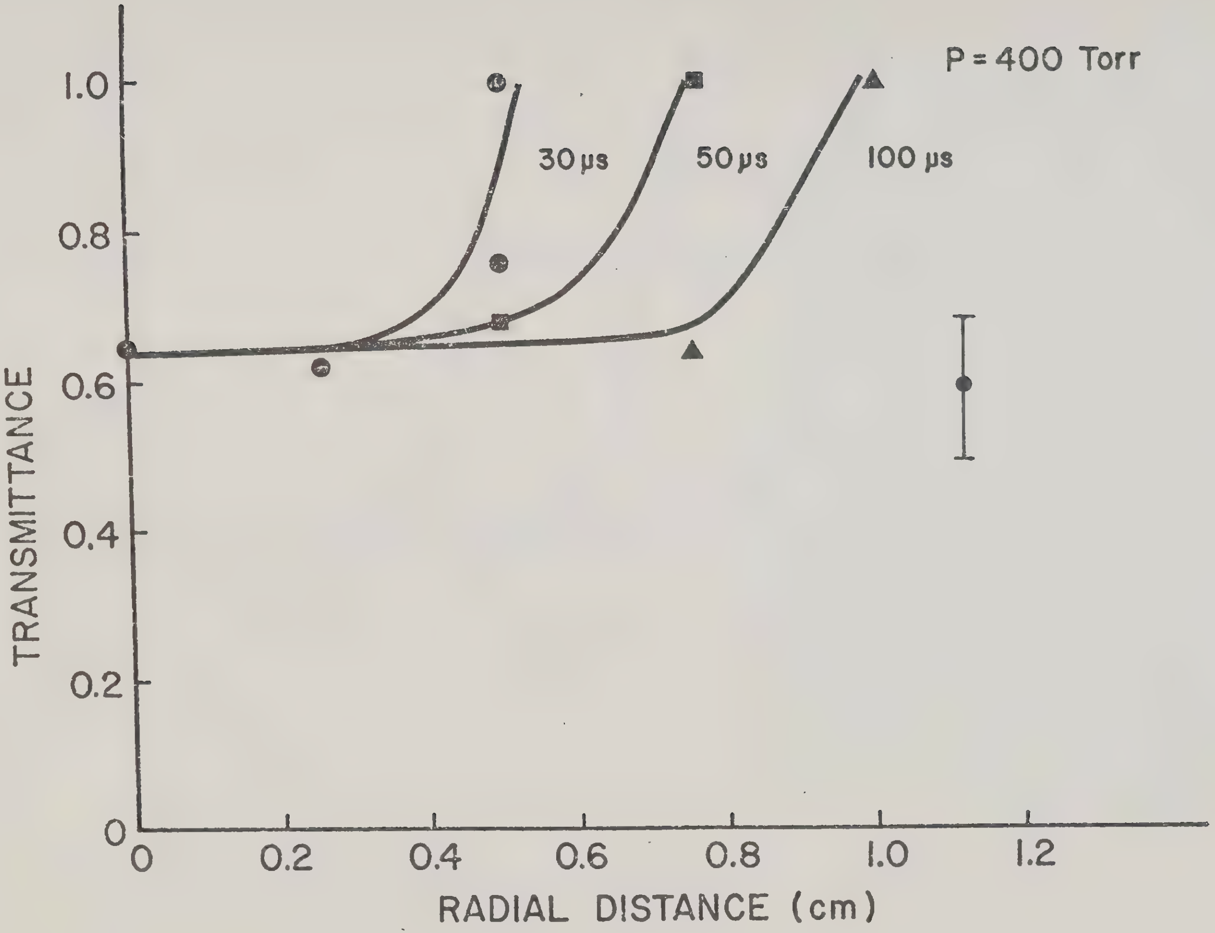

Figure 6-6(b) Discharge Plasma Transmittance of 10.6μm Radiation.

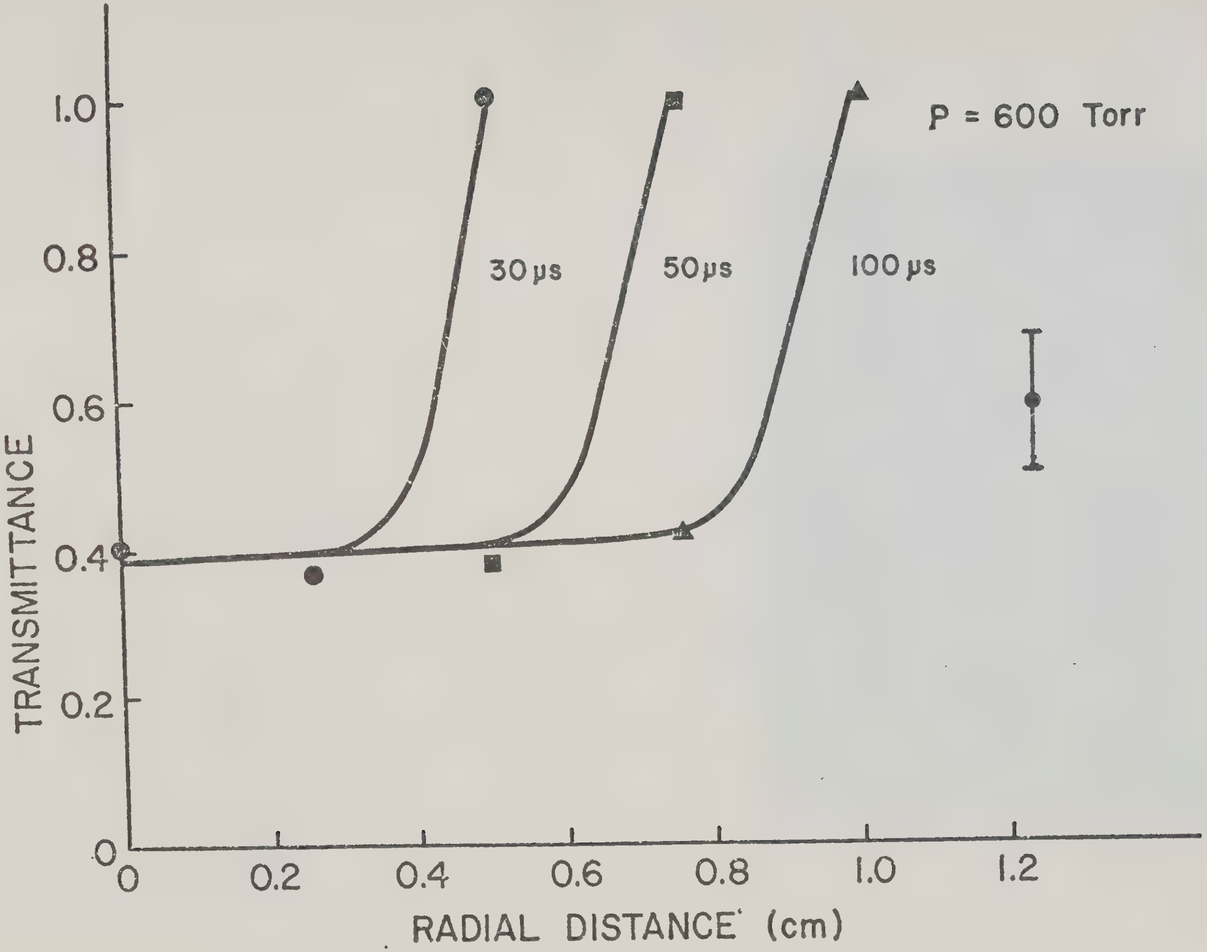

Figure 6-6(c) Discharge Plasma Transmittance of 10.6μm Radiation.

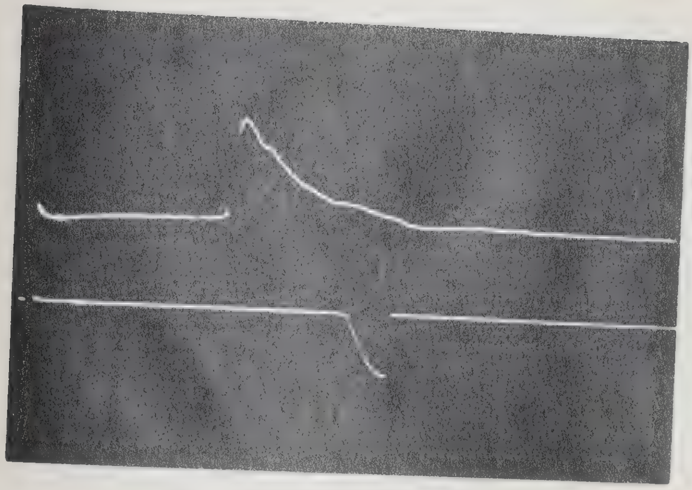

Figure 6-7 Langmuir Probe Current. The upper trace is the probe signal as it passes through the discharge. The lower trace locates the probe relative to the plasma. Horizontal: 50 μs/div; Vertical: 1 μA/div; p=600 Torr.

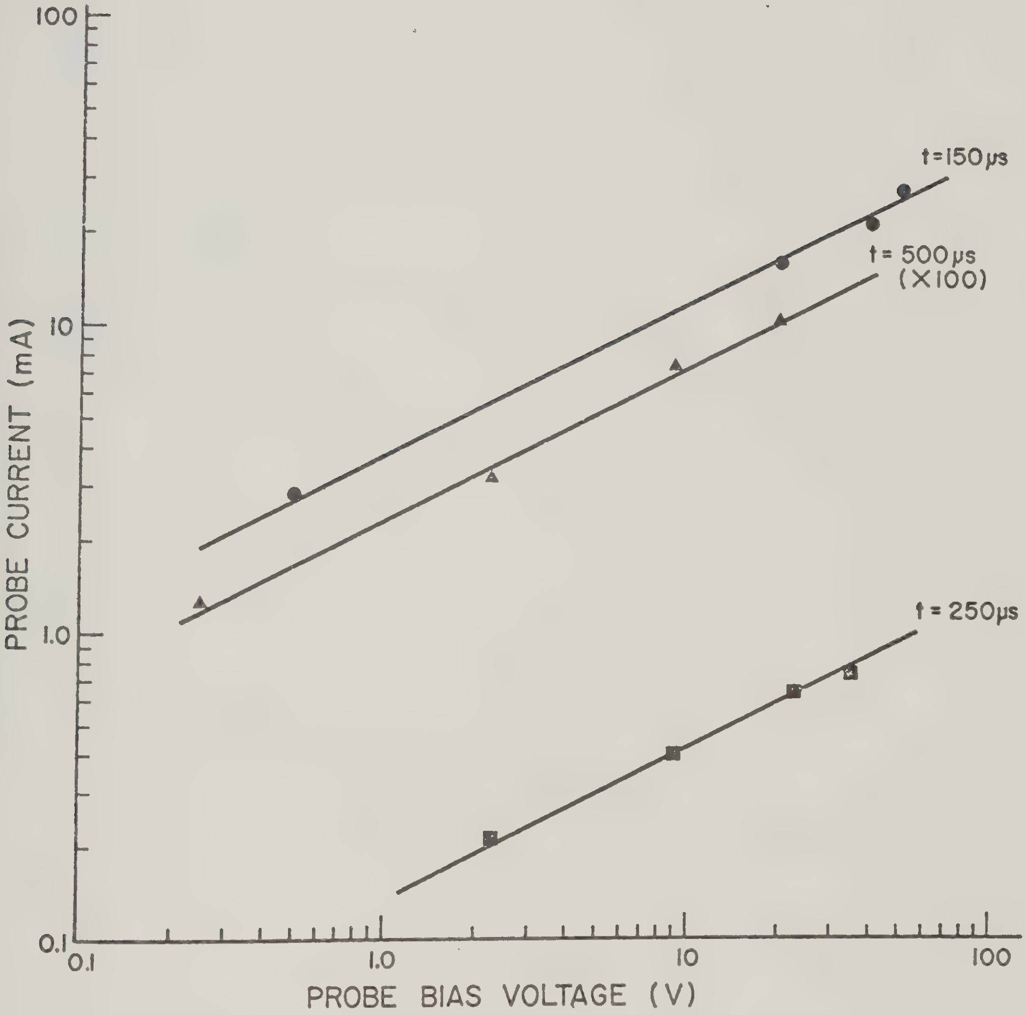

Figure 6-8 Probe Current Versus Probe Bias Voltage.
The slope of 1/2 implies that the probe is operated in the sheath/convection regime.

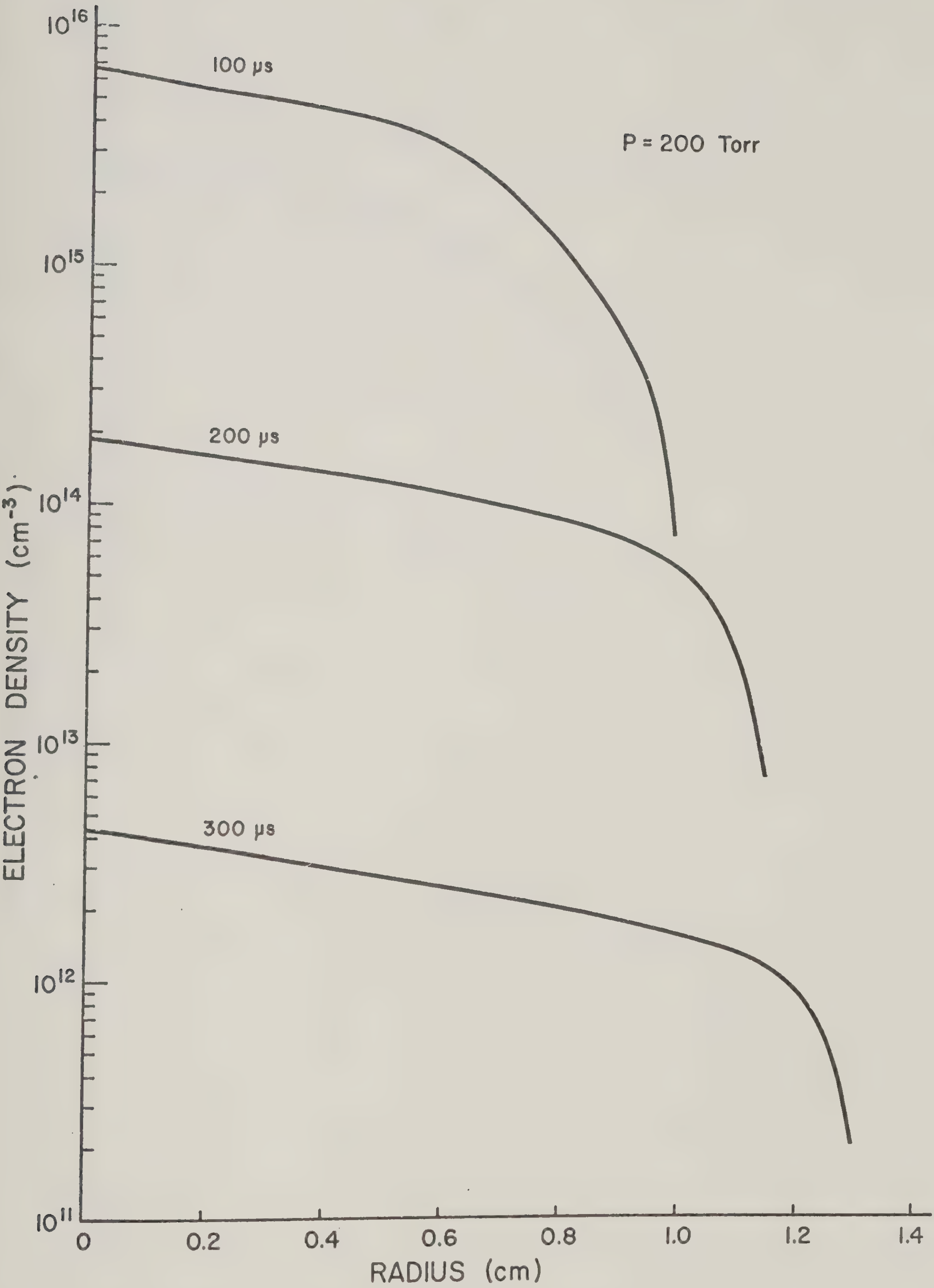

Figure 6-9(a) Radial Electron Distribution.

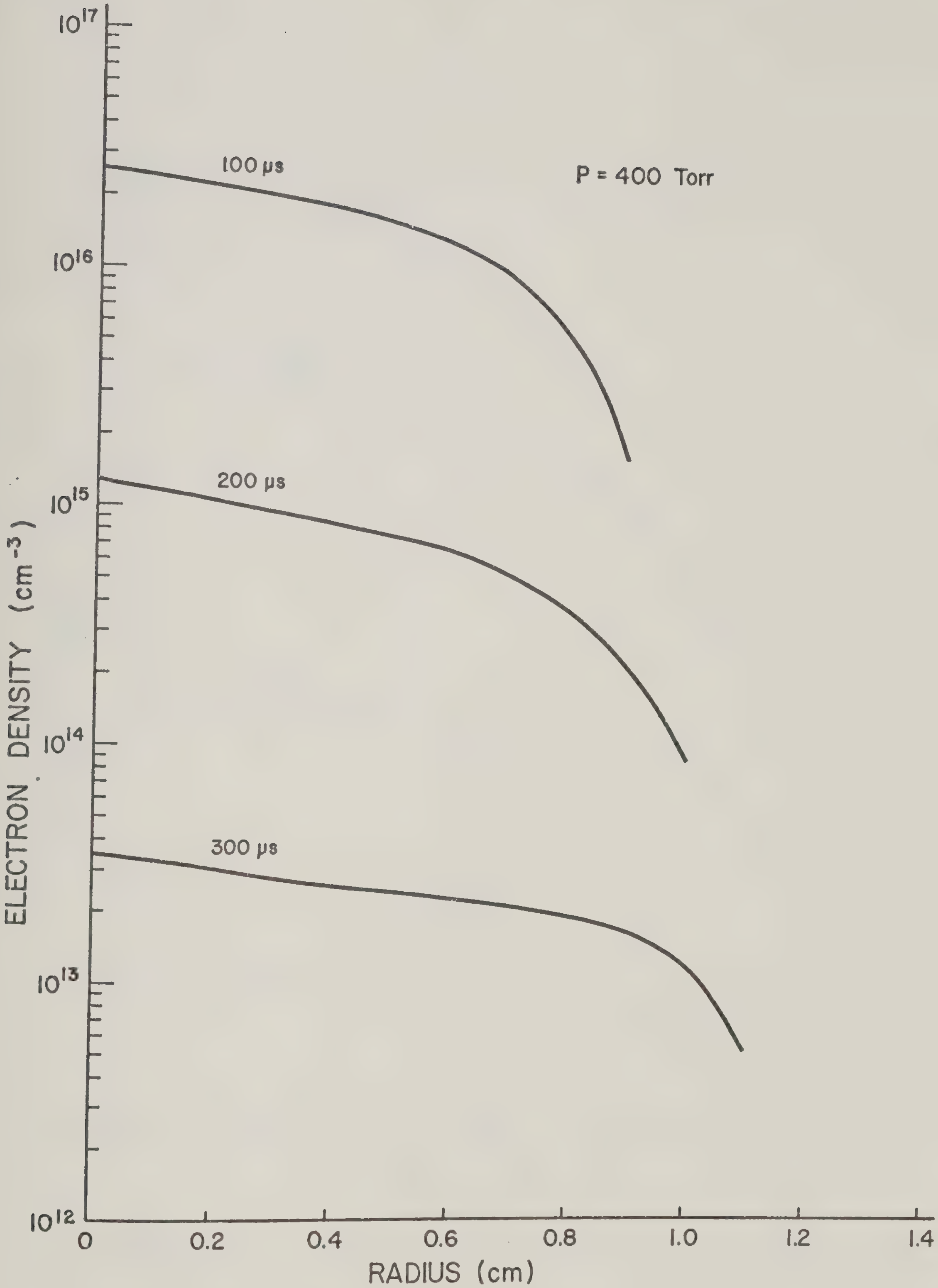

Figure 6-9(b) Radial Electron Distribution.

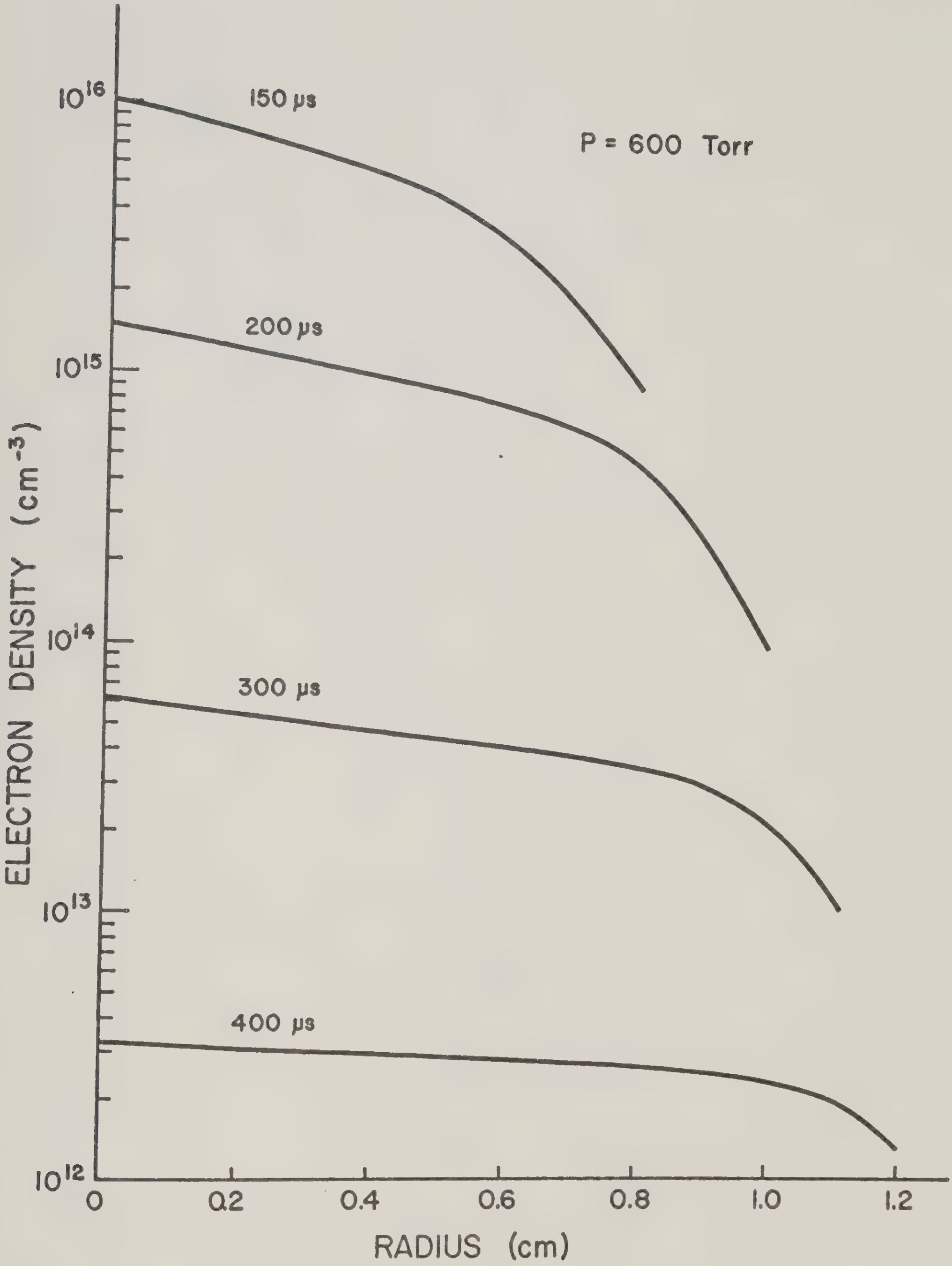

Figure 6-9(c) Radial Electron Distribution

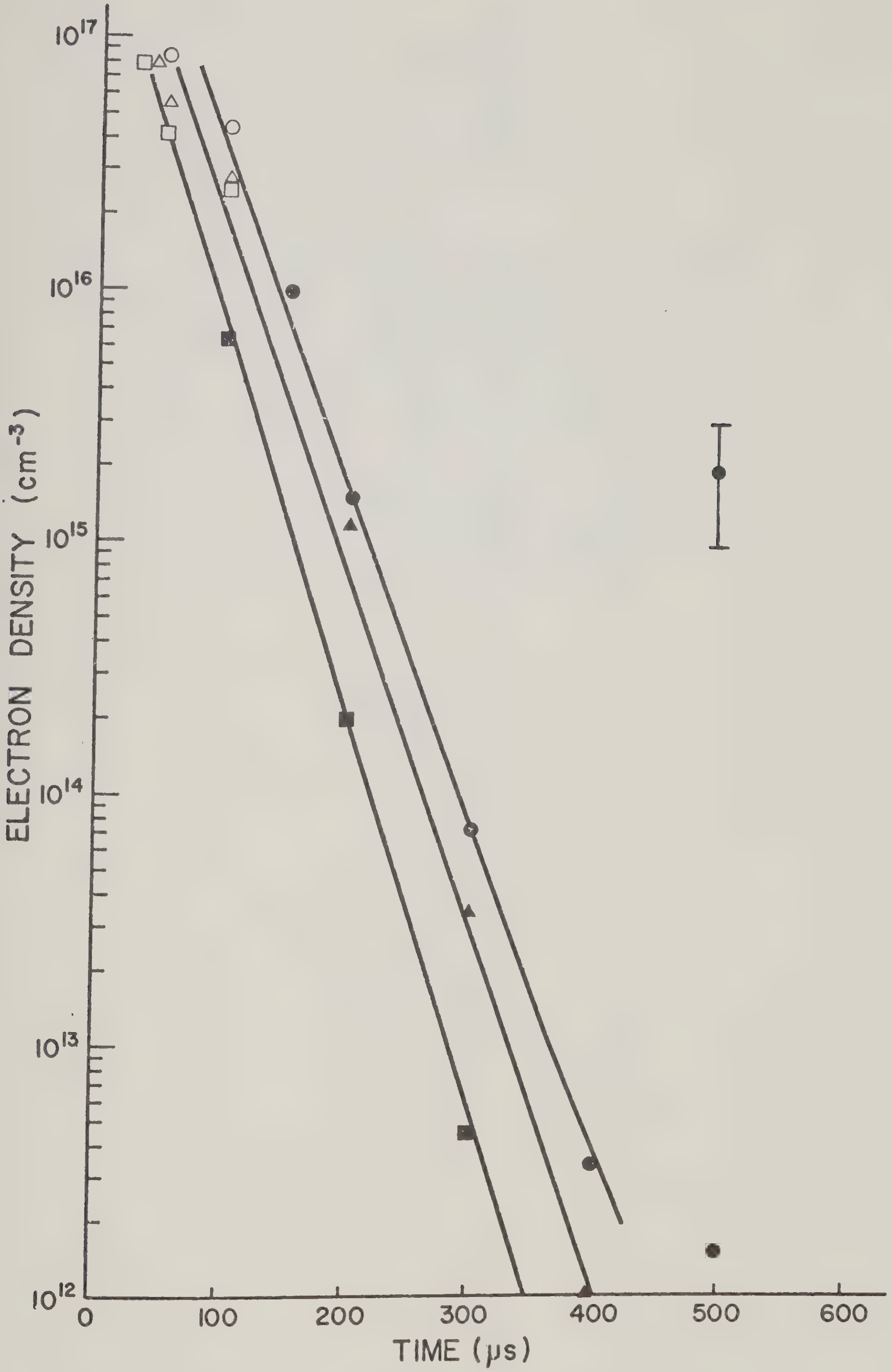

Figure 6-10 Decay of Discharge Electron Density.
□, △, ○ : Interferometry; ■, ▲, ● : Probe Measurements

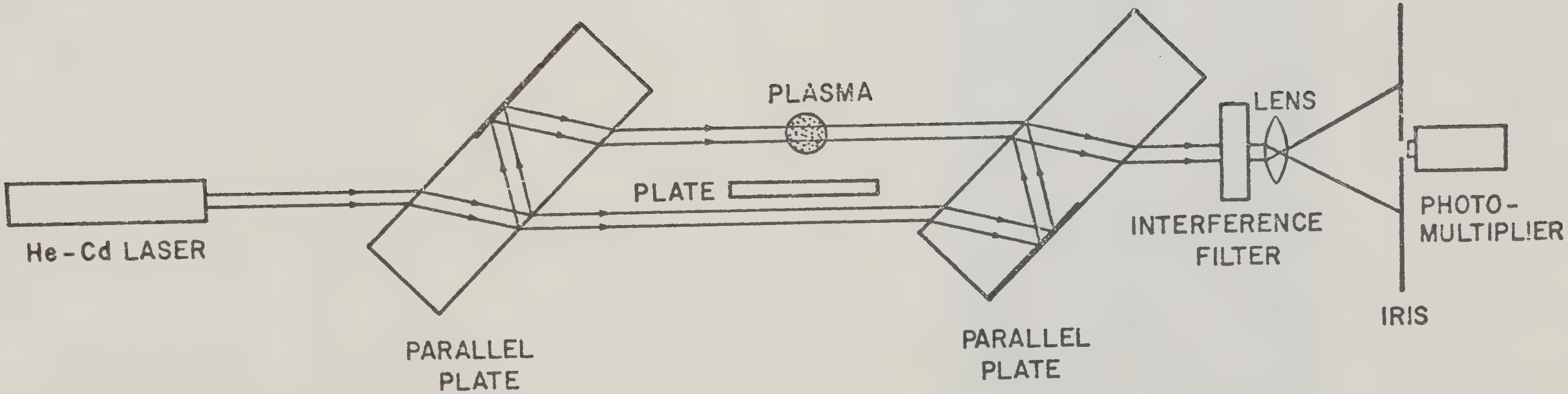
He-Cd LASER
PARALLEL PLATE
PLASMA
PLATE
PARALLEL PLATE
LENS
INTERFERENCE FILTER
IRIS
PHOTO-MULTIPLIER

Figure 6-11 Jamin Interferometer.

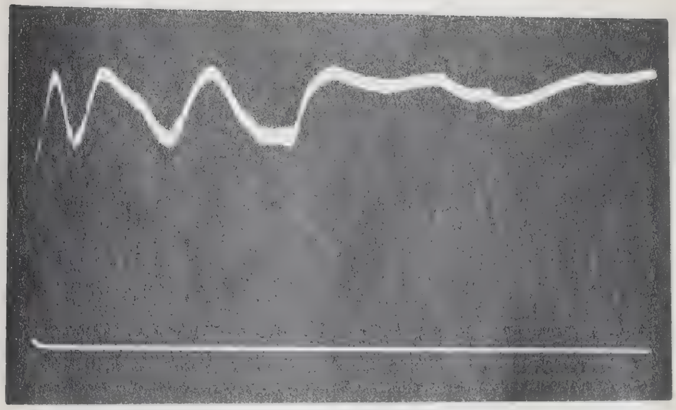

Figure 6-12 Jamin Interferometer Fringe Shifts

d = 0; p = 200 Torr; Sweep speed is 20 μs/div.

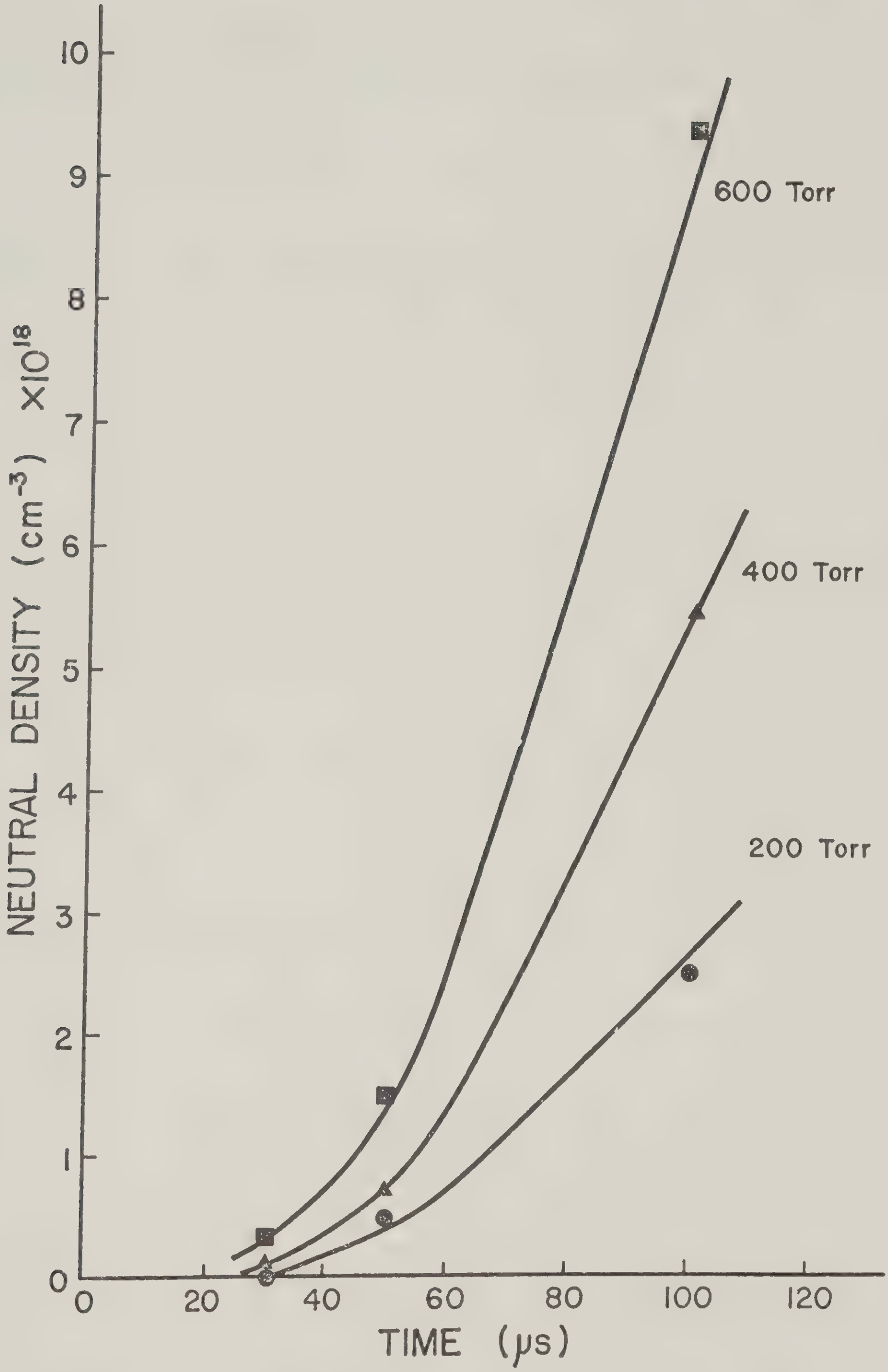

Figure 6-13 Neutral Density in the Discharge Versus Time

CHAPTER VII

A CASCADE MODEL OF LASER INDUCED GAS BREAKDOWN

7.1 Outline

A cascade model that describes the breakdown of Ar under the influence of a CO_2 laser beam is described. The validity of a classical analysis of the laser plasma interaction is discussed.

The breakdown condition is derived from a square pulse approximation taking into consideration the significant loss mechanisms during the plasma buildup in the focus. The breakdown condition is assumed to apply to the more realistic but complicated case of a time varying pulse.

An attempt to verify the breakdown condition experimentally is described. A charge collector system was used to measure the electron density at breakdown. The results were inconclusive, however.

Numerical solutions of the cascade process are performed. The agreement with experimental results is good.

7.2 Introduction

The problem of cascade breakdown under the influence of light was first theoretically investigated by Zel'dovich and Raizer[1]. In their fundamental paper, the quantum kinetic equation for the electron distribution function was solved in the "classical limit". The energy absorption mechanism was inverse bremsstrahlung absorption by electrons during collisions with neutrals. In the classical limit the rate of energy absorption via inverse bremsstrahlung is the same as that used in microwave theory, namely:

$$\frac{dW}{dt} = \frac{e^2}{m} \frac{\nu_c E^2}{\nu_c^2+\omega^2} \quad \text{(Gaussian units)}$$

The validity of the classical analysis was investigated by Friedland[2]. He showed through particle simulation that for CO_2 laser breakdown of Ar, classical theory is applicable even though the conditions set forth by Zel'dovich and Raizer on the constancy of the collision frequency is not met. Consequently, the breakdown of Ar by an intense CO_2 pulse is described by the classical Boltzmann equation with the appropriate collision terms which will be discussed later in this chapter.

Aside from Reference 1, a good presentation of laser cascade breakdown including detailed derivation of absorption coefficients can be found in Reference 3.

Assuming there are a few initial electrons in the focal volume, the build up of electrons may be described by a differential equation for the electron density, n:

$$\frac{dn}{dt} = (\nu_g - \nu_\ell)n \tag{7.1}$$

where ν_g is the electron gain rate due to energy absorption by electrons via inverse bremsstrahlung and ν_ℓ is the loss rate due to electron diffusion out of the focal volume and energy losses during collisions. The solution of Equation (7.1) gives the electron density as a function of time $n=n(t)$. If breakdown occurs at the end of the pulse, $t=\tau$ with $n=n_b$, then $n_b=n(\tau)$. The breakdown threshold, therefore, is the laser power P_{max} required to give n_b at the end of the pulse.

In order to solve Equation (7.1) several things must be taken into consideration. First, the density at breakdown n_b is unknown. Secondly, the loss and gain rates are not constant. Hence, as the electron temperature varies with the instantaneous laser power, the rates will be changing in a complicated manner. The rates are also dependent on the electron density. Thirdly, the plasma might not be in equilibrium, i.e., the distribution function is non-Maxwellian. This will affect the gain and loss rates. These are considered in the following sections.

7.3 Breakdown Condition

Although the density at breakdown, n_b is unknown it is still possible to obtain a condition for n_b at breakdown. There are two possible energy gain mechanisms: electron-ion inverse bremsstrahlung and electron-neutral inverse bremsstrahlung. During the early part of the charge build up, the electron density is low. For this reason the electron-ion inverse bremsstrahlung term was neglected in previous work[4-8]. In References 4-8, breakdown was defined arbitrarily as full ionization or in some cases, $n_b=10^{18}\text{cm}^{-3}$ with an initial density, $n_o=10^4\text{cm}^{-3}$[4,5]. Still others have defined breakdown as 43 electron generations in the cascade[6]. It will be shown that the electron-ion term is important in that it sets a condition for an effective value of n_b. It will also be shown that although the electron-ion term is important, it can be disregarded when solving Equation (7.1) for the charge build up thereby simplifying the differential equation as long as the breakdown condition to be derived is used.

Define ν_g^1 as the gain rate due to electron-neutral inverse bremsstrahlung and ν_g as the gain rate due to electron-neutral and electron-ion inverse bremsstrahlung. Then[1,3,4]:

$$\nu_g^{1} = \frac{1}{U_i} \frac{e^2}{m} \frac{E^2 \nu_c}{\nu_c^{2} + \omega^2} \tag{7.2}$$

Here, U_i is the ionization potential of the gas, E is the rms electric field strength of the laser, e and m the electron charge and mass, respectively, ν_c is the collision frequency for momentum transfer and ω is the laser angular frequency. The absorption coefficient corresponding to this gain rate is:[3]

$$K_{en} = U_i \nu_g^{1} n/F$$

Here, F is the light flux. The electron-ion inverse bremsstrahlung absorption coefficient is[3]:

$$K_{ei} = \frac{4}{3} \left(\frac{2\pi}{3mkT_e} \right)^{1/2} \frac{Z^2 e^6}{hcm\nu^3} n^2$$

$$= \frac{3.69\times10^{8} n^2}{T^{1/2}\ \nu^3}\ \text{cm}^{-1}\ (Z=1) \tag{7.4}$$

Taking the ratio of K_{ei} to K_{en}:

$$\frac{K_{ei}}{K_{en}} = \frac{3.69\times10^{8} \pi mcn}{e^2 \nu\ \nu_c T^{1/2}(\text{deg})} \quad (\omega >> \nu_c)$$

Later calculations will show that $T_e \simeq 2\text{-}3\text{eV}$. For $T_e = 2\text{eV}$,

$$\frac{K_{ei}}{K_{en}} = \frac{3.19\times10^{-5} n}{\nu_c} \tag{7.5}$$

But

$$\frac{K_{ei}}{K_{en}} = \frac{\nu_g - \nu_g^1}{\nu_g^1}$$

Hence:

$$\frac{dn}{dt} = (\nu_g^1 - \nu_\ell)n + \frac{3.19\text{x}10^{-5}}{\nu_c} \nu_g^1 n^2 \qquad (7.6)$$

Equation (7.6) reduces to the case of no electron-ion inverse bremsstrahlung absorption when the density is low so that the second term on the right hand side of the equation becomes much smaller than the first.

Assuming further that E, ν_g^1 and ν_ℓ are constants, the solution of Equation (7.6) is:

$$n(t) = \frac{n_o \exp(\nu_g^1 - \nu_\ell)t}{1 - n_o a\{\exp(\nu_g^1 - \nu_\ell)t - 1\}} \qquad (7.7)$$

where

$$a = \frac{3.19\text{x}10^{-5} \nu_g^1}{(\nu_g^1 - \nu_\ell)\nu_c}$$

The density at the end of the pulse is:

$$n(\tau) = \frac{n_o \exp(\nu_g^1 - \nu_\ell)\tau}{1 - n_o a\{\exp(\nu_g^1 - \nu_\ell)\tau - 1\}} \qquad (7.8)$$

Taking the logarithm of Equation (7.8):

$$(\nu_g^1 - \nu_\ell)\tau = \ell n \frac{n(\tau)}{n_o} + \ell n[1 - n_o a\{\exp(\nu_g^1 - \nu_\ell)\tau - 1\}] \qquad (7.9)$$

Figure 7-1 is a plot of $(\nu_g^1-\nu_\ell)\tau$ versus $n(\tau)$ with $n_o=10^5\text{cm}^{-3}$ and a=0, $1.77\text{x}10^{17}$, and $1.06\text{x}10^{16}$. For a given laser power and gas pressure, the density at the end of the pulse, $n(\tau)$, will lie along the curves shown in Figure 7-1, e.g., point A on line $\overline{AB}$. If the laser power is increased, $n(\tau)$ may correspond to point B. If electron-ion inverse bremsstrahlung were disregarded, the solution will be along the straight line $\overline{AD}$. Note that point C corresponds to the same $(\nu_g^1-\nu_\ell)\tau$ as point B and in fact approximately corresponds to any point where $n(\tau)>1/a$. Therefore, the electron-ion term can be disregarded as in previous work if the calculation is terminated at $n(\tau) = 1/a = n_b$. Returning to Equation (7.1), its solution assuming constant E,ν_g^1, and ν_ℓ is:

$$n(\tau) = n_o\exp\{(\nu_g^1-\nu_\ell)\tau\} \tag{7.10}$$

Setting $n_b=n(\tau) = 1/a$ in Equation (7.10) is seen to be approximately equivalent to setting the denominator of Equation (7.8) to zero:

$$1 - an_o\{\exp(\nu_g^1-\nu_\ell)\tau-1\} = 0 \tag{7.11}$$

This is a sufficient condition for breakdown.

The above discussion leads to the following conclusion. When modelling the buildup of electrons in the focus during breakdown, the simplified problem of no electron-ion inverse bremsstrahlung is equivalent to the more realistic case which takes it into account if the density at breakdown n_b is taken to be 1/a. This is true only if the actual density at breakdown is larger than 1/a.

The factor $\frac{\nu_g^1 - \nu_\ell}{\nu_g^1} \simeq 1$. Hence,

$$n_b \simeq 3.13\times10^4 \nu_c \tag{7.12}$$

For argon with $T_e \simeq$ 2-3eV. $\nu_c \simeq 3\times10^9 p$ where p is the gas pressure in Torr.[9] Therefore:

$$n_b \simeq 9.4\times10^{13}\ p \tag{7.13}$$

It can be seen that for moderate pressures, $n_b < 10^{18}\mathrm{cm}^{-3}$ which was used by others in previous calculations. The breakdown condition is pressure dependent and is equivalent to prescribing the degree of ionization of the gas:

$$\frac{n_b}{n_{gas}} \simeq 0.27\%$$

7.4 Charge Collection Results

In an attempt to experimentally determine n_b, a charge collector consisting of two flat parallel plates 5cm by 5cm was constructed. The laser was focused midway between the two plates. Figure 7-2 shows the equivalent input circuit seen by the collector. It can be easily shown following the analysis of Raether[10] that the output voltage signal is:

$$V_S(t) \simeq e^{-t/R_2C_2} \int_o^t e^{t'/R_2C_2} \frac{dV_2}{dt'}\, dt' \tag{7.15}$$

$$\simeq V_2(t) \quad \text{if } t \ll R_2C_2$$

$$V_2(t) \simeq \frac{\exp\{-\frac{t}{R_p(C+C_1)}\}}{C+C_1} \int_o^t \exp[\frac{t'}{R_p(C+C_1)}] I_c(t')dt' \qquad (7.16)$$

$$\simeq \frac{1}{C+C_1} \int_o^t I_c(t')dt'$$

where

$$R_p = \frac{R_1R_2}{R_1+R_2} \gg R$$

$I_c(t')$ = collector current

C = collector capacitance

C_1 = input capacitance of electronics

$C+C_1$ = 100 pF

If the collector field is high, Townsend ionization will take place as the electrons drift towards the anode. Let α be the first Townsend coefficient, N_o the number of electron-ion pairs created by the laser, d the distance between collector plates, v_- and v_+ be the drift velocities of the electrons and ions, respectively and $T_- = d/v_-$, $T_+ = d/v_+$. Since the charges are created midway between the plates the currents due to electron and ion drifts I_- and I_+ are[10]:

$$I_- = \frac{eN_o}{T_-} e^{\alpha v_- t} \qquad 0 \leq t < \frac{T_-}{2}$$

$$I_+ = \frac{eN_o}{T_+} e^{\alpha v_- t} \qquad 0 \leq t < \frac{T_-}{2}$$

$$I_+ = \frac{eN_o}{T_+}\, e^{\frac{1}{2}\alpha d} \qquad \frac{1}{2}T_- \le t \le \frac{1}{2}(T_+ - T_-)$$

$$I_+ = \frac{eN_o}{T_+}\, [e^{\frac{1}{2}\alpha d} - e^{-\alpha v t}] \qquad \frac{1}{2}(T_+ - T_-) \le t \le T_+ + \frac{1}{2}T_- \tag{7.17}$$

where

$$\frac{1}{v} = \frac{1}{v_+} + \frac{1}{v_-}$$

An approximate expression for α good for $E/p \lesssim 30$ is[11]:

$$\frac{\alpha}{p} = \exp[-52/(E/p)] \tag{7.18}$$

It can be seen that for small fields, $\alpha \simeq o$ and

$$V_S \simeq \frac{1}{C+C_1} \int (I_- + I_+)dt$$

$$= \frac{eN_o}{C+C_1} = \frac{Q}{C+C_1} \tag{7.19}$$

When $\alpha \neq 0$, it can be shown that:

$$V_S^- = \frac{eN_o}{(C+C_1)\alpha d}\, e^{\frac{1}{2}\alpha d} = \frac{Q\, e^{\frac{1}{2}\alpha d}}{(C+C_1)\alpha d} \tag{7.20}$$

$$V_S^+ = \frac{Q}{C+C_1}\left(e^{\frac{1}{2}\alpha d} - \frac{e^{\frac{1}{2}\alpha d}}{\alpha d}\right) \tag{7.21}$$

Hence:

$$V_S = V_S^- + V_S^+ \simeq \frac{Q}{C+C_1}\, e^{\frac{1}{2}\alpha d} \tag{7.22}$$

It can be seen that the signal should increase rapidly with E/p due to the increase in α/p.

At very low E/p, the collection time is so long that losses can take place. The electron diffusion time is approximately:

$$t_d \simeq \Lambda^2/D_-$$

where Λ is the diffusion length and D_- is the electron diffusion coefficient. Taking the ratio of T_- and t_d,

$$\frac{T_-}{t_d} = \frac{d^2}{\Lambda^2} \frac{T_e}{V} \qquad (7.24)$$

where T_e is the electron temperature in eV and V is the voltage between the collector plates. Taking d = 1.5cm $\Lambda = L/\pi = 1.6$ cm, then:

$$\frac{T_-}{t_d} \simeq 0.9 \frac{T_e}{V}$$

Hence, except for very low V, diffusion loss can be neglected.

Figure 7-3 (a) and (b) depict the collector characteristics for p = 30 Torr and p = 50 Torr and laser energies E = 2.5J and 1.75J, respectively. For E/p less than 4 V/cm-Torr, the field cannot collect all charges while for E/p greater than 15 V/cm-Torr, Townsend ionization is dominant. A collector field of 10 V/cm Torr was selected as the operating point.

The number of electron-ion pairs created by the laser at threshold were measured for both cases of when a spark was produced and when a spark

was not produced. When a spark was produced, the number of collected ions was consistently 10^{13} regardless of the pressure, as shown in Figure 7-4 (a). When a spark was not produced, the number collected varied considerably from shot to shot. This was also observed by Tulip and Seguin[12]. The smallest number of electron-ion pairs collected was 10^8 as shown in Figure 7-4 (b). This is an order of magnitude less than that obtained by Tulip and Seguin in air. Obviously, the true density at breakdown should be between 10^8 and 10^{13}. With a focal volume of $\simeq 10^{-5} cm^{-3}$, these limits correspond to $n = 10^{13} cm^{-3}$ and $10^{18} cm^{-3}$.

The breakdown condition discussed in Section 7.3 is valid only when the actual density at breakdown (between $10^{13} cm^{-3}$ and $10^{18} cm^{-3}$) is greater than 1/a. To check whether this is satisfied, assume $n_b \simeq 10^{13} cm^{-3}$. The build up from $n_o = 10^5$ to 10^{13} cm^{-3} needs approximately 20 cascade generations. If the gas is preionized such that $n_o \simeq 10^{12} cm^{-3}$, only 4 cascade generations will be required to break down the gas. Since the required laser power to break down the gas is approximately proportional to the number of cascade generations required, a threshold lowering of $\simeq \frac{4}{20} = 0.2$ should be observed if the density at breakdown is $10^{13} cm^{-3}$.

On the other hand, if $n_b = 10^{18}$ cm^{-3}, 30 cascade generations are needed from $n_o = 10^5 cm^{-3}$ while it takes 10 cascade generations from $n_o = 10^{12}$ cm^{-3}. Hence, a threshold lowering of $\simeq \frac{10}{30} = 0.33$ should be expected in this case.

Measurements of the breakdown thresholds reported in the next chapter indicate that with a preionization of $\simeq 10^{12} cm^{-3}$, there is a lowering of the threshold to only 0.4 its value without preionization. This indicates that the actual density at breakdown is closer to $10^{18} cm^{-3}$ than $10^{13} cm^{-3}$.

Hence, the condition discussed in Section 7.3 is satisfied. The breakdown condition obtained in Section 7.3 will be used in the following sections.

7.5 Boltzmann Equation

As previously discussed, the pulse shape, cross sections and varying temperature make ν_g^1 and ν_ℓ variable in time. Expressions for ν_g^1 and ν_ℓ as functions of time (laser power) and electron temperature are needed before Equation (7.1) can be solved. This means that a rate equation for T_e is also needed. These are obtained from the Boltzmann Kinetic Equation.

The Boltzmann equation that describes the time evolution of the electron distribution function has been derived by Allis[13].

$$\frac{\partial f}{\partial t} = \frac{2\varepsilon}{3m\nu_c} \nabla^2 f + \frac{\partial}{\partial \varepsilon} \left(\frac{2}{3} \varepsilon^{3/2} Q_J \frac{\partial}{\partial \varepsilon} \frac{f}{\varepsilon^{1/2}}\right)$$

$$+ \frac{\partial}{\partial \varepsilon} \left(\frac{2m}{M} \varepsilon \nu_c f\right) + \int G(\varepsilon,\varepsilon')f(\varepsilon')d\varepsilon'$$

$$- \sum_i A_{x_i}(\varepsilon)f(\varepsilon) - A_I(\varepsilon)f(\varepsilon) \qquad (7.26)$$

where

f = distribution function

m = electron mass

M = ion mass or atom mass

ν_c = collision frequency for momentum transfer

A_{x_i} = excitation rate of level i

A_I = ionization rate

$$Q_J = \text{heating rate} = \frac{e^2}{m}\ \frac{\nu_c E^2}{\nu_c^{\,2}+\omega^2}$$

The first term gives the changes in f due to diffusion. It is the only space dependent term and so the following approximation was taken:

$$\nabla^2 f = - f/\Lambda^2 \tag{7.27}$$

Also, define:

$$A_D(\varepsilon) = \frac{2\varepsilon}{3m\nu_c(\varepsilon)\Lambda^2}$$

The second term is the heating rate and the third term is the elastic collision term. The last two terms give the losses due to excitation and ionization. The term under the integral sign is due to the appearance of electrons of energy ε after exciting or ionizing collisions of electrons of energy $\varepsilon'>\varepsilon$. Recombination losses are neglected as well as hydrodynamic effects, photoionization, radiation loss, collisions of the second kind, ionization of excited atoms by electron collisions, and heat conduction.

7.5.1 Integral Term

Following the analysis of Chan and Moody[7], consider first the rate of appearance of electrons of energy ε due to electrons of energy ε' exciting an atom during a collision, (excitation energy ε_{x_i}). By the conservation of energy:

$$\varepsilon' - \varepsilon = \varepsilon_{x_i}$$

Hence,

$$G(\varepsilon,\varepsilon')f(\varepsilon')\Big]_{ex} = \sum \delta(\varepsilon'-\varepsilon-\varepsilon_{x_i})A_{x_i}(\varepsilon')f(\varepsilon') \quad (7.29)$$

Similarly, electrons of energy ε' can ionize an atom creating an electron of energy ε_1 and another of energy ε_2 where:

$$\varepsilon_1 + \varepsilon_2 = \varepsilon' - \varepsilon_I \quad (\varepsilon_I = \text{ionization potential}) \quad (7.30)$$

Let $P(\varepsilon, \varepsilon'-\varepsilon_I)$ be the probability that $\varepsilon_1 = \varepsilon$ and $\varepsilon_2 = \varepsilon' - \varepsilon_I - \varepsilon$ and $P(\varepsilon' - \varepsilon_I - \varepsilon, \varepsilon' - \varepsilon_I)$ be the probability that $\varepsilon_2 = \varepsilon$ and $\varepsilon_1 = \varepsilon' - \varepsilon_I - \varepsilon$. $P(\varepsilon, \varepsilon' - \varepsilon_I)$ satisfies the normalization condition

$$\int_0^{\varepsilon'-\varepsilon_I} P(\varepsilon,\varepsilon' - \varepsilon_I)d\varepsilon = 1 \quad (7.31)$$

and

$$P(\varepsilon,\varepsilon'-\varepsilon_I)=0 \text{ if } \varepsilon<0 \text{ and } \varepsilon>\varepsilon'-\varepsilon_I$$

The lower limit in Equation (7.31) corresponds to the case when $\varepsilon_1 = 0$ and the upper limit to the case when $\varepsilon_2 = 0$. Then:

$$G(\varepsilon,\varepsilon')f(\varepsilon')\Big]_{ioniz} = A_I(\varepsilon')f(\varepsilon')[P(\varepsilon,\varepsilon'-\varepsilon_I) + P(\varepsilon'-\varepsilon_I-\varepsilon,\varepsilon'-\varepsilon_I)] \quad (7.32)$$

Adding the excitation and ionization rates, the total rate is:

$$G(\varepsilon,\varepsilon')f(\varepsilon') = f(\varepsilon')[2A_I(\varepsilon')D(\varepsilon,\varepsilon'-\varepsilon_I) + \sum_i A_{x_i}(\varepsilon')\delta(\varepsilon'-\varepsilon_{x_i}-\varepsilon)] \qquad (7.33)$$

where $D(\varepsilon,\varepsilon'-\varepsilon_I) = \frac{1}{2}[P(\varepsilon,\varepsilon' - \varepsilon_I) + P(\varepsilon' - \varepsilon_I - \varepsilon,\varepsilon' - \varepsilon_I)]$

which is symmetic about $\varepsilon = \frac{1}{2}(\varepsilon' - \varepsilon_I)$ because each electron of energy ε produced during an ionizing collision must be accompanied by another of energy $\varepsilon' - \varepsilon_I$. D satisfies :

$$\int_0^{\varepsilon'-\varepsilon_I} D(\varepsilon,\varepsilon' - \varepsilon_I)d\varepsilon = 1 \qquad (7.34)$$

7.5.2 Conservation Laws

It can be shown that the excitation and ionization terms discussed in the preceding section satisfy the conservation laws. Integrating $G(\varepsilon,\varepsilon')f(\varepsilon')$ over all ε and ε',

$$\int G(\varepsilon,\varepsilon')f(\varepsilon')d\varepsilon'd\varepsilon = \int f(\varepsilon')[2A_I(\varepsilon')D(\varepsilon,\varepsilon'-\varepsilon_I) + \sum_i A_{x_i}(\varepsilon')\delta(\varepsilon' - \varepsilon_{x_i} - \varepsilon)]d\varepsilon d\varepsilon' \qquad (7.35)$$

$$= \int f(\varepsilon')[2A_I(\varepsilon') + \sum_i A_{x_i}(\varepsilon')]d\varepsilon'$$

Changing dummy variables from ε' to ε,

$$\int G(\varepsilon,\varepsilon')f(\varepsilon')d\varepsilon' d\varepsilon = \int f(\varepsilon)[2A_I(\varepsilon) + \sum_i A_{x_i}(\varepsilon)]d\varepsilon \qquad (7.36)$$

This is the law of conservation of mass for exciting and ionizing collisions involving electrons of energy $\varepsilon'>\varepsilon$. Similarly:

$$\int \varepsilon G(\varepsilon,\varepsilon')f(\varepsilon')d\varepsilon' d\varepsilon = \int(\varepsilon-\varepsilon_I)f(\varepsilon)A_I(\varepsilon)d\varepsilon + \sum_i \int A_{x_i}(\varepsilon)(\varepsilon-\varepsilon_{x_i})f(\varepsilon)d\varepsilon \qquad (7.37)$$

which is the corresponding law of conservation of energy.

7.5.3 Density and Temperature Equations

The relations:

$$n = \int f(\varepsilon)d\varepsilon \qquad (7.38)$$

and

$$\frac{3}{2}nT_e = \int \varepsilon f(\varepsilon)d\varepsilon$$

are used to obtain the rate equations for the electron density, n and electron temperature, T_e. Integration of Equation (7.26) yields:

$$\frac{\partial n}{\partial t} = - \int A_D(\varepsilon)f(\varepsilon)d\varepsilon + \int A_I(\varepsilon)f(\varepsilon)d\varepsilon = (\overline{A}_I - \overline{A}_D)n \qquad (7.39)$$

$$\frac{\partial}{\partial t} (\frac{3}{2} nT_e) = - \int \varepsilon A_D(\varepsilon)f(\varepsilon)d\varepsilon - \int \frac{2}{3} \varepsilon^{3/2} \, 0_J(\varepsilon) \frac{\partial}{\partial \varepsilon} \frac{f(\varepsilon)}{\varepsilon^{1/2}} d\varepsilon$$

$$- \frac{2m}{M} \int \varepsilon \, \nu_c(\varepsilon)f(\varepsilon)d\varepsilon - \varepsilon_I \int A_I(\varepsilon)f(\varepsilon)d\varepsilon$$

$$- \sum_i \varepsilon_{x_i} \int A_{x_i}(\varepsilon)f(\varepsilon)d\varepsilon$$

Or

$$\frac{\partial T_e}{\partial t} = \frac{2}{3} [- \overline{R}_D + \overline{R}_J - \overline{R}_{el} - \overline{A}_I(\varepsilon_I + \frac{3}{2} T_e)$$

$$- \varepsilon_x \overline{A}_x + \frac{3}{2} T_e \overline{A}_D] \qquad (7.40)$$

where $\overline{A}_I$, $\overline{A}_D$, and so forth have been defined such that for example:

$$\overline{A}_I = \frac{1}{n} \int A_I(\varepsilon)f(\varepsilon)d\varepsilon$$

$\overline{A}_I$ is the average ionization rate, while $\overline{A}_D$ is the average diffusion rate. $\overline{R}_J$ is the joule heating rate, $\overline{R}_{el}$ the elastic collision loss rate, $\overline{R}_D$ the average energy loss due to diffusion, $\varepsilon_I\overline{A}_I$ the energy loss due to ionization and $\varepsilon_x A_x$ is the energy loss due to excitation. Equations (7.39) and (7.40) are the desired rate equations. Its solution will give

$n=n(t)$ and the threshold will just be the smallest laser power that will give $n=n_b$.

7.5.4 Maxwellian Distributions

Because of the deep Ramsauer minimum in the collision cross section of argon, it is expected that the distribution function is not Maxwellian but one which gives greater weight on the low energy side. A numerical solution of the Boltzmann equation[7] and particle simulation[2] show that this is indeed the case. However, the distribution function was not very different from a Maxwellian[3]. Therefore, the terms on the right hand side of Equations (7.39) and (7.4) derived from a Maxwellian distribution are not expected to be very different from their true values. Furthermore, the greatest contribution to these terms come from electrons in the tail of the distribution function. The distribution functions obtained in Reference 3 are Maxwellian in the tail.

Assuming a Maxwellian distribution:

$$f(\varepsilon) = 2n\left(\frac{\varepsilon}{\pi T_e^{3}}\right)^{1/2} e^{-\varepsilon/T_e} \tag{7.41}$$

the collision rates become (energy in eV):

$$\bar{A}_I = \frac{1.13}{T_e^{3/2}} \int A_I(\varepsilon)\varepsilon^{1/2}\, e^{-\varepsilon/T_e}\, d\varepsilon$$

$$\bar{A}_x = \frac{1.13}{T_e^{3/2}} \int A_x(\varepsilon)\varepsilon^{1/2}\, e^{-\varepsilon/T_e}\, d\varepsilon$$

$$\overline{R}_D = \frac{1.32\text{x}10^{11}}{\Lambda^2\ T_e^{\ 3/2}} \int \frac{\varepsilon^{5/2}}{\nu_c(\varepsilon)}\ e^{-\varepsilon/T_e}\ d\varepsilon$$

$$\overline{A}_D = \frac{1.32\text{x}10^{11}}{\Lambda^2\ T_e^{\ 3/2}} \int \frac{\varepsilon^{3/2}}{\nu_c(\varepsilon)}\ e^{-\varepsilon/T_e}\ d\varepsilon \qquad (7.42)$$

$$R_{el} = \frac{1.23\text{x}10^{-3}}{T_e^{\ 3/2}} \int \nu_c(\varepsilon)\varepsilon^{3/2}\ e^{-\varepsilon/T_e}\ d\varepsilon$$

$$\overline{R}_J = \frac{5.02\text{x}10^{23}P}{T_e^{\ 5/2}} \int \frac{\varepsilon^{3/2}e^{-\varepsilon/T_e}\ \nu_c(\varepsilon)}{\nu_c^{\ 2} + \omega^2}\ d\varepsilon$$

where P is the laser power per unit area in the focus.

The collision frequency is defined as:

$$\nu_c = n\sigma_m v_e$$

where σ_m is the cross section and v_e is the electron velocity. Equivalently, ν_c is:

$$\nu_c = 1.92\text{x}10^{24}\ \varepsilon^{1/2}\ \sigma_m(\varepsilon)p \qquad (7.43)$$

where ε is in eV, σ_m in cm^2 and p in Torr. Similarly,

$$A_I(\varepsilon) = 1.92\text{x}10^{24}\varepsilon^{1/2}\ \sigma_I(\varepsilon)p \qquad (7.44)$$

$$A_x(\varepsilon) = 1.92\text{x}10^{24}\varepsilon^{1/2}\ \sigma_x(\varepsilon)p \qquad (7.45)$$

Here, σ_I and σ_x are the electron impact ionization cross-section and the excitation cross-section, respectively. The appropriate expressions and the approximations used in the calculation including reference sources are summarized in Table 7.1. The rates are plotted in Figure 7-5 (a) - (c). A polynomial up to an 8th degree was fitted to the rates and used in the solution of the density and temperature equations (Equations (7.39) and (7.40)).

As the electron density builds up, a point is reached when the diffusion loss will be greatly reduced because of ambipolar effects. To take this into consideration, the diffusion loss terms $\overline{A}_D$ and $\overline{R}_D$ were multiplied by a function F which takes on values from 1 when n is low to D_a/D_e when n is large. The functional form of F was similar to that prescribed by Allis and Rose[18,19] for a plasma between two parallel plates. F plotted as a function of $n\Lambda^2/T_e$ is shown in Figure 7-6.

7.5.5 Numerical Solution

A finite difference method was used to solve Equations (7.39) and (7.40). The following substitution was used:

$$\frac{\partial T_e}{\partial t} \rightarrow \frac{T_e^{\,j+1} - T_e^{\,j}}{\Delta t} \tag{7.46}$$

$$\frac{\partial n}{\partial t} \rightarrow \frac{n^{j+1} - n^j}{\Delta t} \tag{7.47}$$

where t^{j+1} is the present time. The terms on the right hand side of Equation (7.40) were first evaluated at the time t^j. Equation (7.40) then yields a temporary value of $T_e^{\,j+1}$. This value of the temperature

was then used to evaluate $\overline{A}_D$ and $\overline{A}_I$ and Equation (7.39) yields n^{j+1}:

$$n^{j+1} = \frac{n^j}{1 - c^{j+1}\Delta t} \qquad (7.48)$$

where $c^{j+1} = (\overline{A}_I - \overline{A}_D)^{j+1}$. The procedure was then repeated using the new values of T_e and n. Two or three iterations were found to be sufficient for convergence. Accuracy was up to three significant figures. The time step size selected was $\Delta t = 5\text{x}10^{-11}$ second. Other schemes such as the 4th order Runge-Kutta and the Adams predictor-corrector method were tried. No significant advantage of these methods over the one used was found. A program listing is given in the Appendix.

The laser pulse shape was approximated by that shown in Figure (7-7). This should be compared with the actual pulse shape given in Figure 4-2(b).

The procedure described in Chapter III insured that priming electrons are present in the focal volume just before the laser pulse. Since the focal volume is $\approx 10^{-5}\text{cm}^3$ an initial value of $n=10^5\text{cm}^{-3}$ was chosen, i.e. there is one electron in the focal volume to start the avalanche.

The laser peak energy was adjusted and the difference equation solved. The value of the diffusion length is still unknown and how this is set is discussed in the next paragraph. If for a given laser peak power the gas breaks down, the power is reduced by 10% and the differential equation is solved again until there is no breakdown. The threshold is taken as the average of the smallest power with breakdown and that without breakdown.

To determine the value of the diffusion length, Λ, the breakdown threshold was measured using the procedure described in Chapter III, from 50 Torr to 10,000 Torr. A spot diameter of 200μm obtained theoretically

TABLE 7.1

SUMMARY OF CROSS-SECTIONS

Cross-Section	Approximation	Limits	Reference
Momentum Transfer	$3\text{x}10^{-16}$	$0\leq\varepsilon\leq.1$	
Collision Cross-Section	$(.83\varepsilon^{2}+.086\varepsilon+.0503)10^{-16}$	$.1<\varepsilon\leq.9$	Engelhardt and Phelps[14]
	$(.08051\varepsilon^{2}+2.202\varepsilon-1.117)10^{-16}$	$.9<\varepsilon\leq14$	Fletcher and Burch[15]
	$(-.285\varepsilon+17.02)10^{-16}$	$14\leq\varepsilon\leq59$	
Ionization by Electron Impact	0	$0\leq\varepsilon<15.8$	Brown[16]
	$(3.125\ell n\varepsilon-8.53)10^{-16}$	$15.8\leq\varepsilon<40$	
	$3.2\text{x}10^{-16}$	$40\leq\varepsilon<100$	
Excitation by Electron Impact	0	$0\leq\varepsilon<11.5$	
	$3.6\text{x}10^{-17}(\frac{\varepsilon-11.5}{11.5})$ $\text{xexp}\{1-[\frac{\varepsilon-11.5}{11.5}]\}$	$\varepsilon\geq11.5$	Van Atta[17] Brown[16]

assuming Gaussian beam optics was used to calculate the experimental peak power per unit area at threshold. Λ was then adjusted until there was reasonable agreement between the experimentally measured threshold without preionization at p=100 Torr and the results of the numerical calculation. The best fit was obtained with Λ=67μm. This is larger than the theoretical value of 100μm/2.405=41.6μm and this implies that the plasma is not confined to the focal volume. The experimental thresholds without preionization and the results of the numerical modelling are shown in Figure 7-8.

The time breakdown occurs depends on the pressure. At low pressures, breakdown occurred very near the peak of the laser pulse. At very high pressures, on the other hand, it occurred very near the end of the pulse. This was due to the very high particle loss rates when the pressure was low. The time of breakdown plotted against the pressure at threshold is shown in Figure (7-9).

The peak electron temperature varied from 2 to 4 eV. Higher electron temperatures were obtained at low pressures, again due to the nature of the losses. This is also shown in Figure (7-9). Figure (7-10) depicts the laser pulse, electron temperature, and electron density as a function of time when breakdown occurs and when it does not, at p=100 Torr. The electrons are heated rapidly after passing through the Ramsauer minimum. Thereafter, the electron temperature follows the laser pulse. Note also that a small change in the laser power leads to a large change in the peak density generated in the focal volume. This is an indication of the sharpness of the threshold. For comparison, the electron density buildup at 6000 Torr is also shown in Figure (7-10).

Since the electron and neutral densities under experimental conditions are known, the breakdown thresholds can be measured and compared with numerical calculations. If reasonable agreement is obtained, not only has the cascade nature of breakdown been confirmed, but more importantly, the possibility of using breakdown as a diagnostic, especially for neutral atom density measurements, appears very promising.

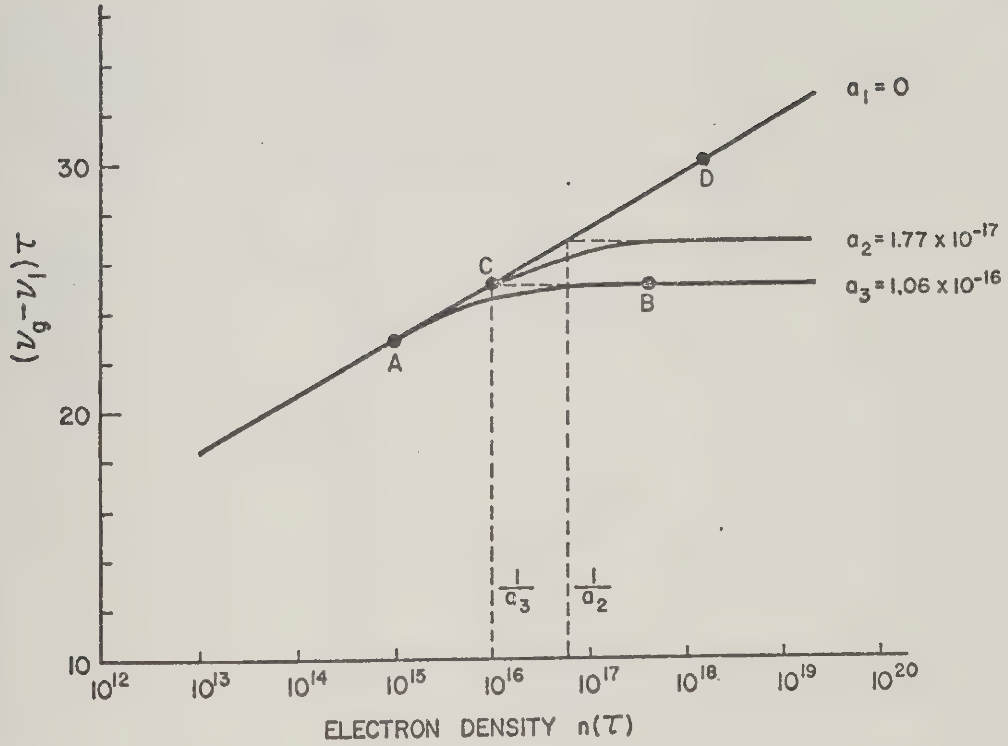

Figure 7-1 Electron Density in the Focus at the End of the Laser Pulse as a Function of $(\nu_g - \nu_\ell)\tau$.

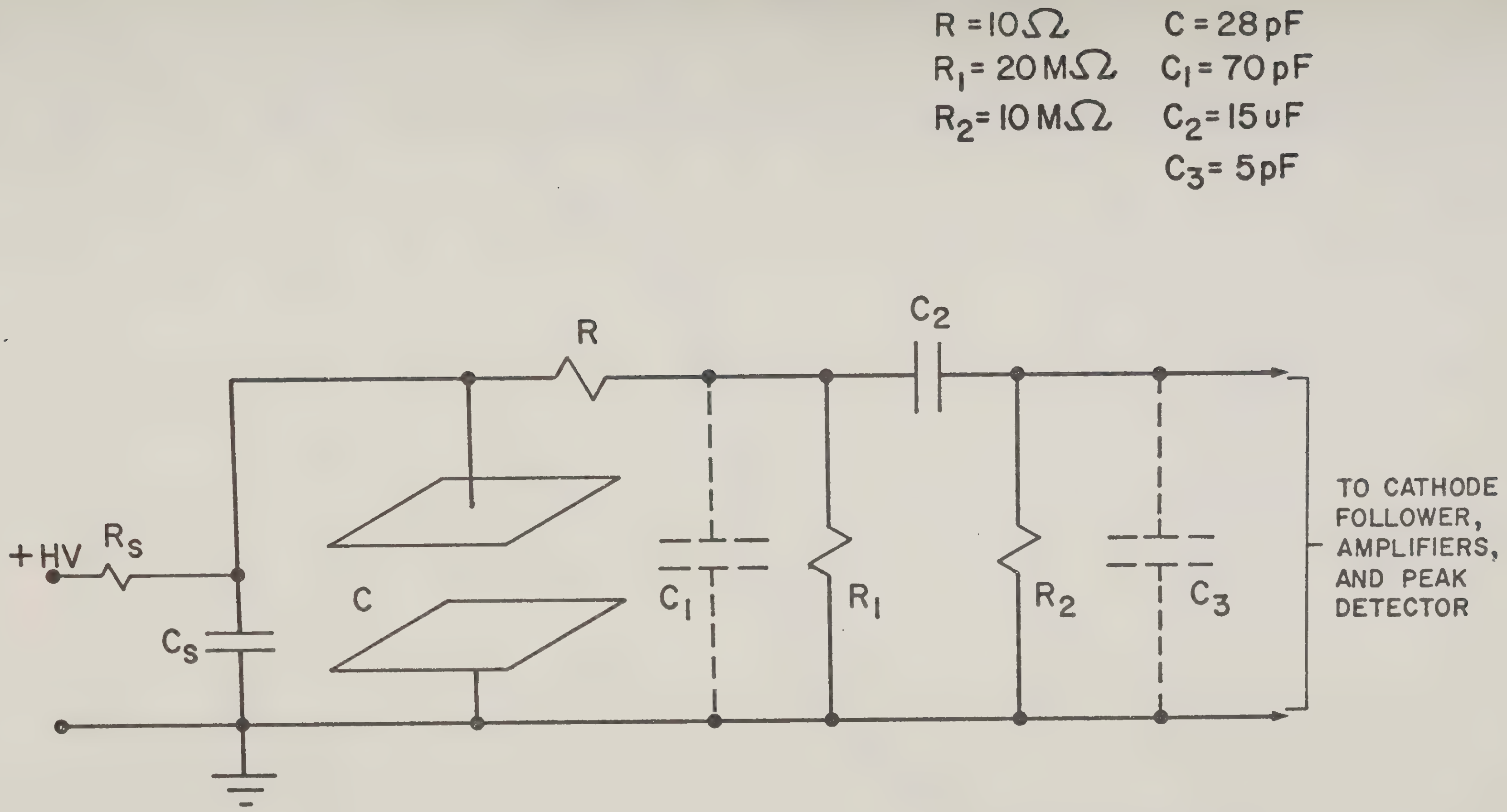
R = 10Ω
R₁ = 20 MΩ
R₂ = 10 MΩ
C = 28 pF
C₁ = 70 pF
C₂ = 15 uF
C₃ = 5 pF
R
C₂
+HV
Rₛ
Cₛ
C
C₁
R₁
R₂
C₃
TO CATHODE FOLLOWER, AMPLIFIERS, AND PEAK DETECTOR

Figure 7-2 Charge Collector Input Circuit

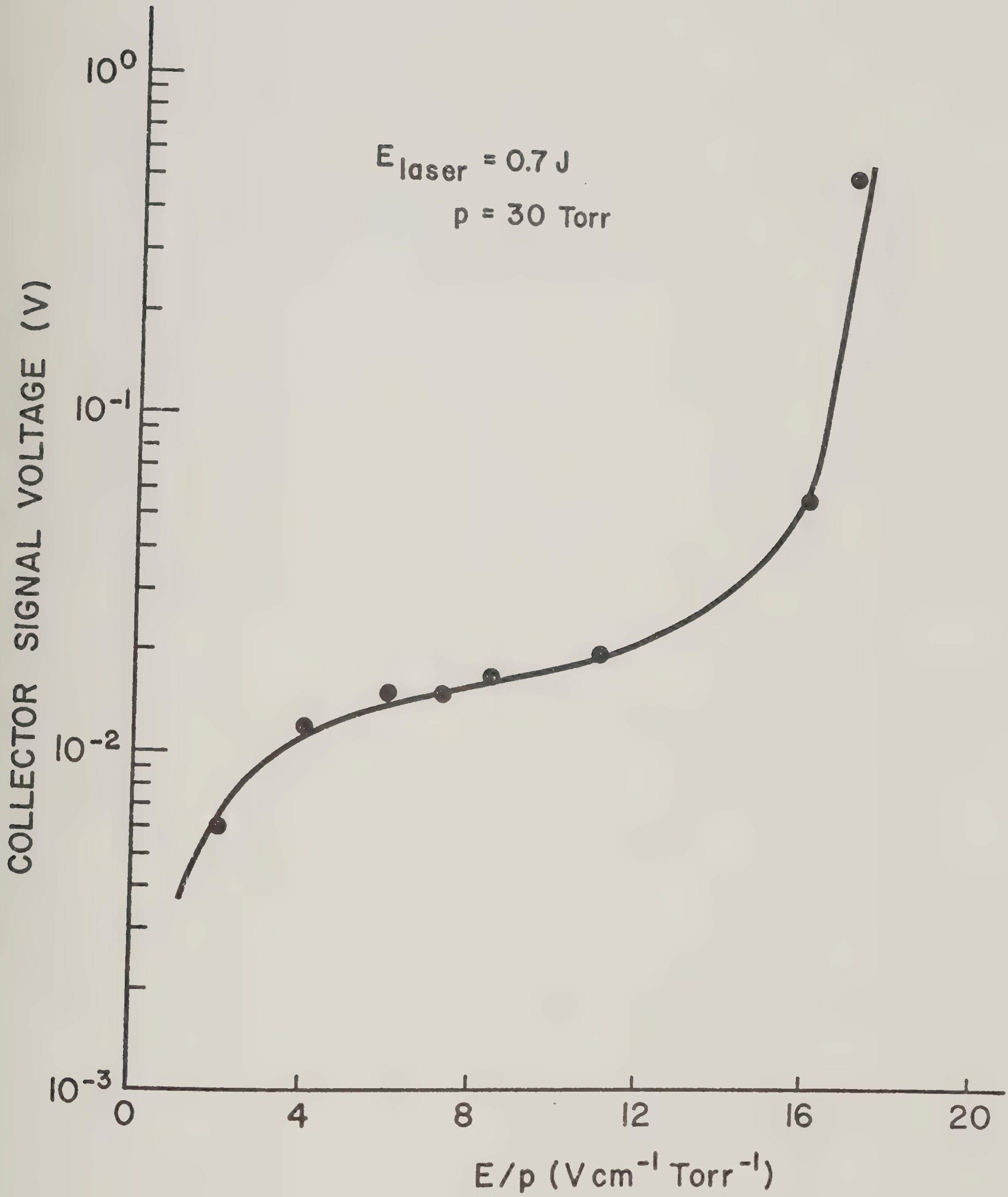

Figure 7-3(a) Charge Collector Characteristic

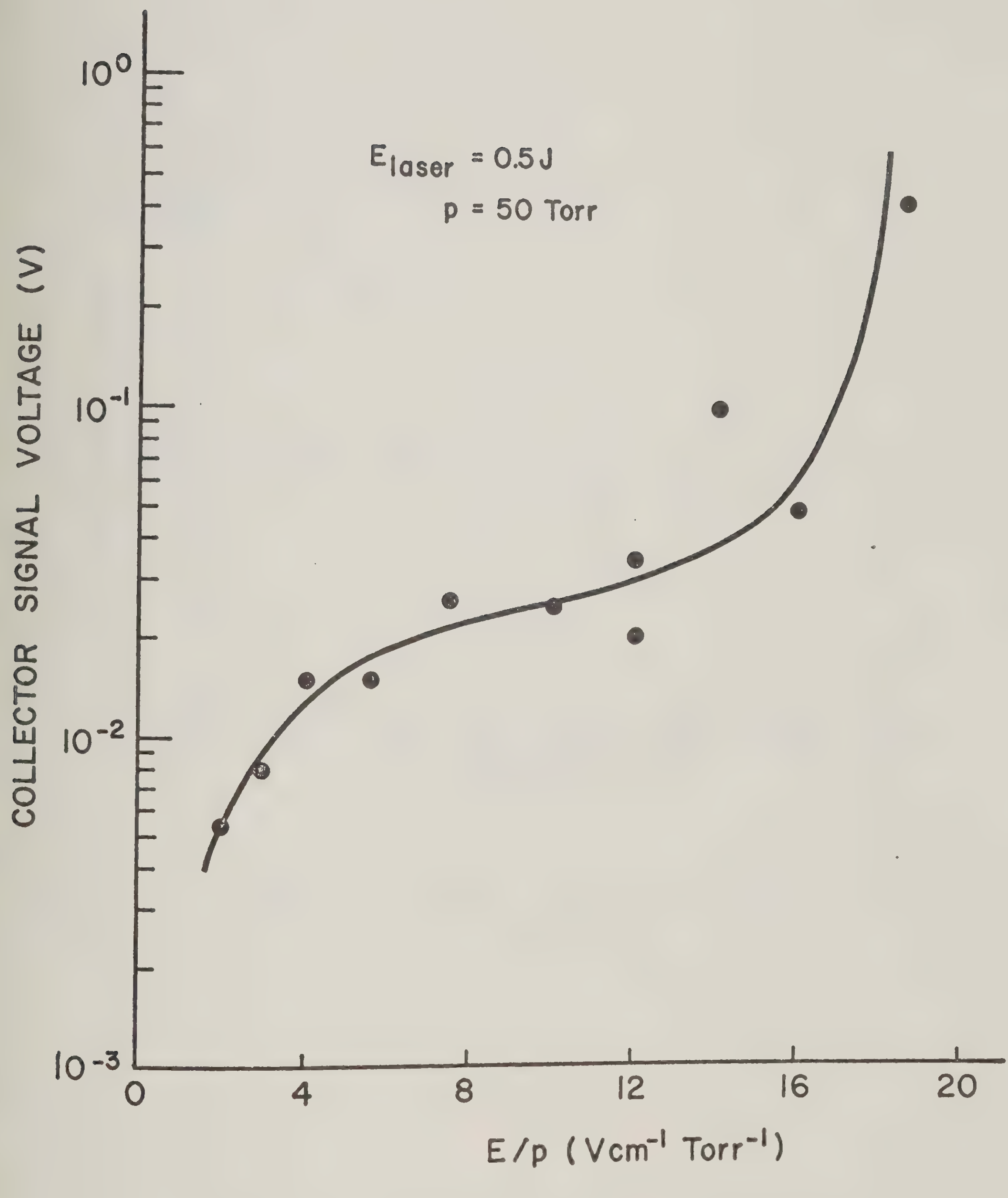

Figure 7-3(b) Charge Collector Characteristic

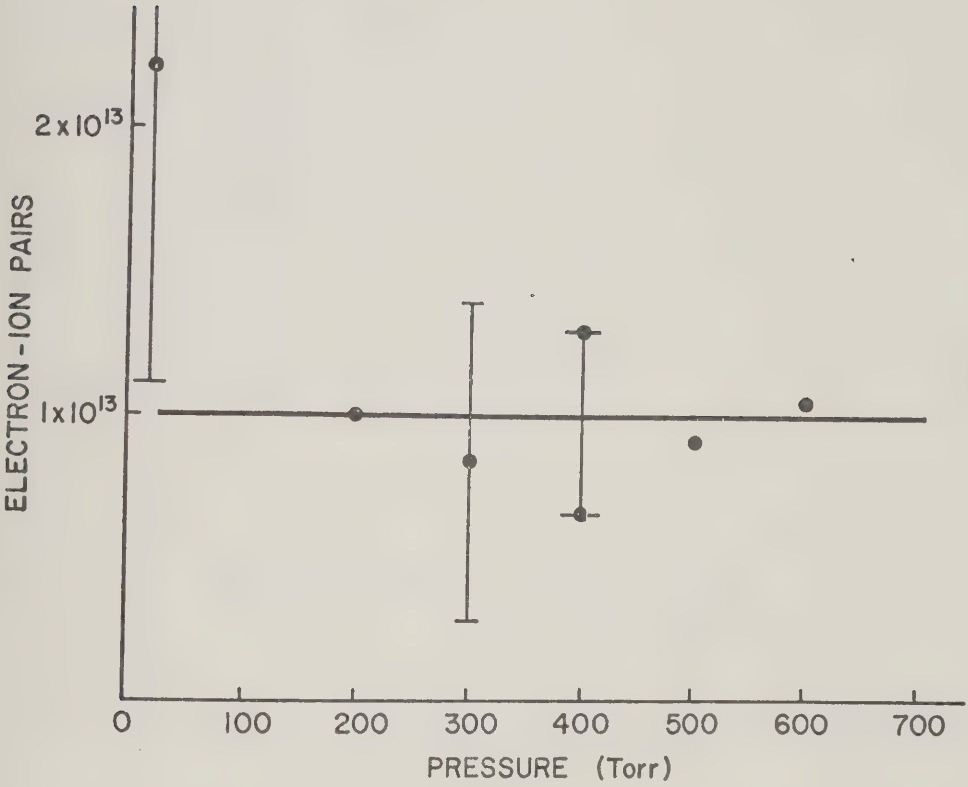

Figure 7-4(a) Number of Electron-Ion Pairs Collected when a Spark is Formed

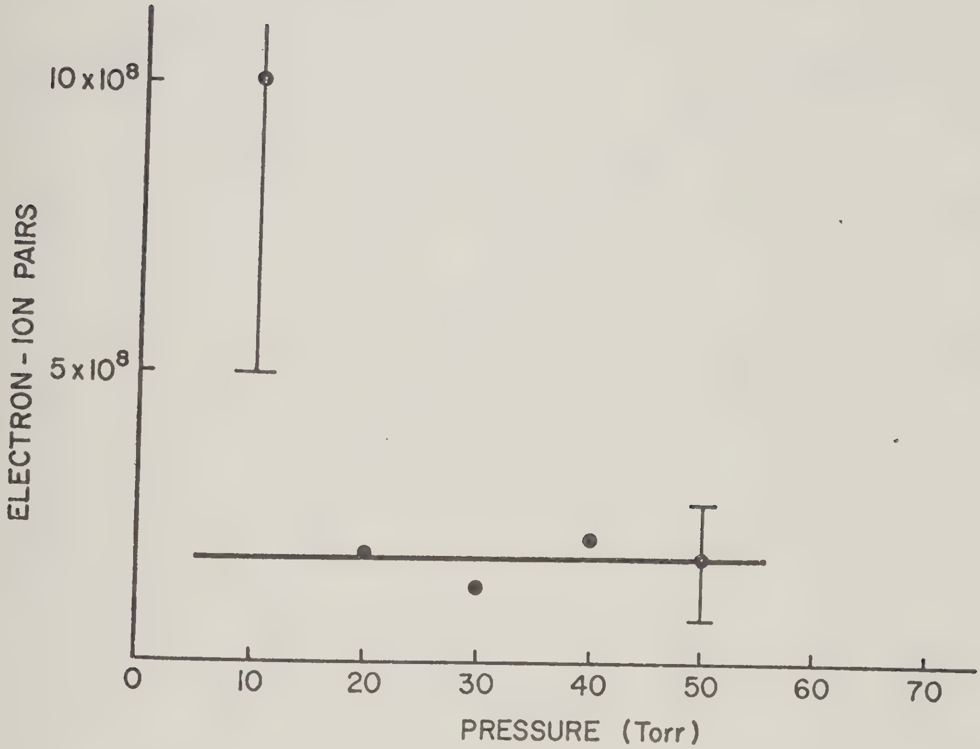

Figure 7-4(b) Number of Electron-Ion Pairs

Collected when a Spark is not Formed

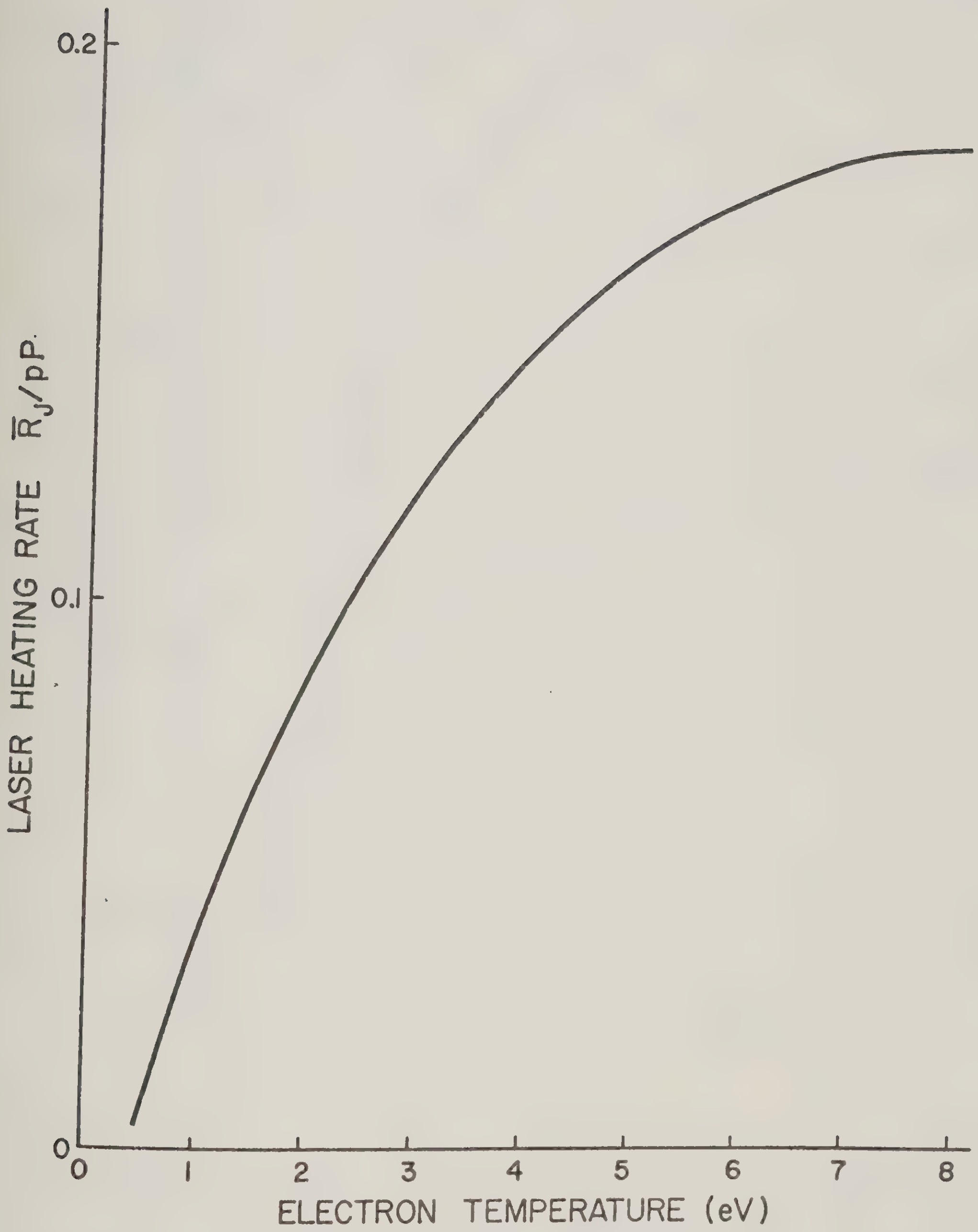

Figure 7-5(a) Laser Heating Rate as a Function of Electron Temperature

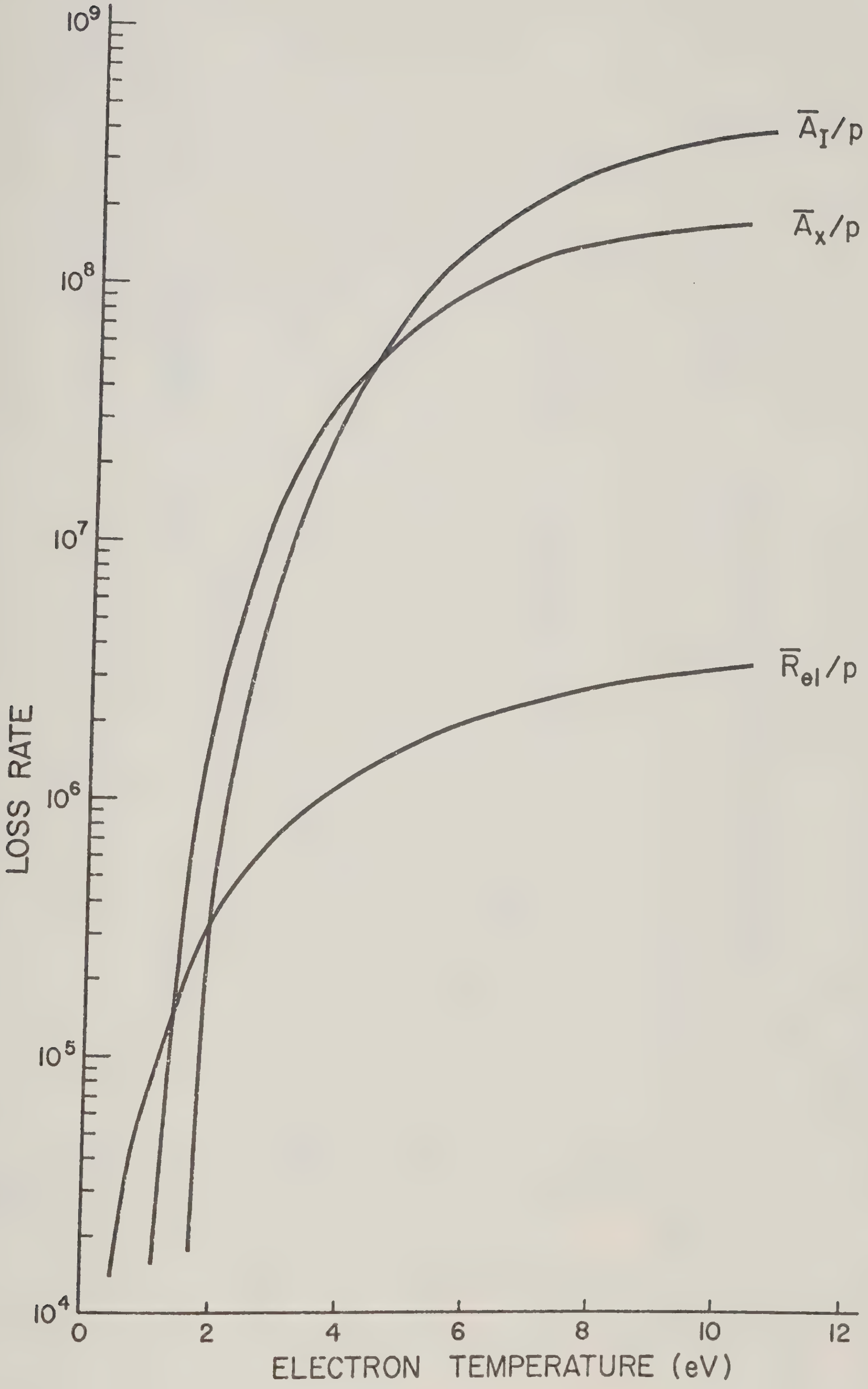

Figure 7-5(b) Ionization, Excitation and Elastic Collision Loss Rates

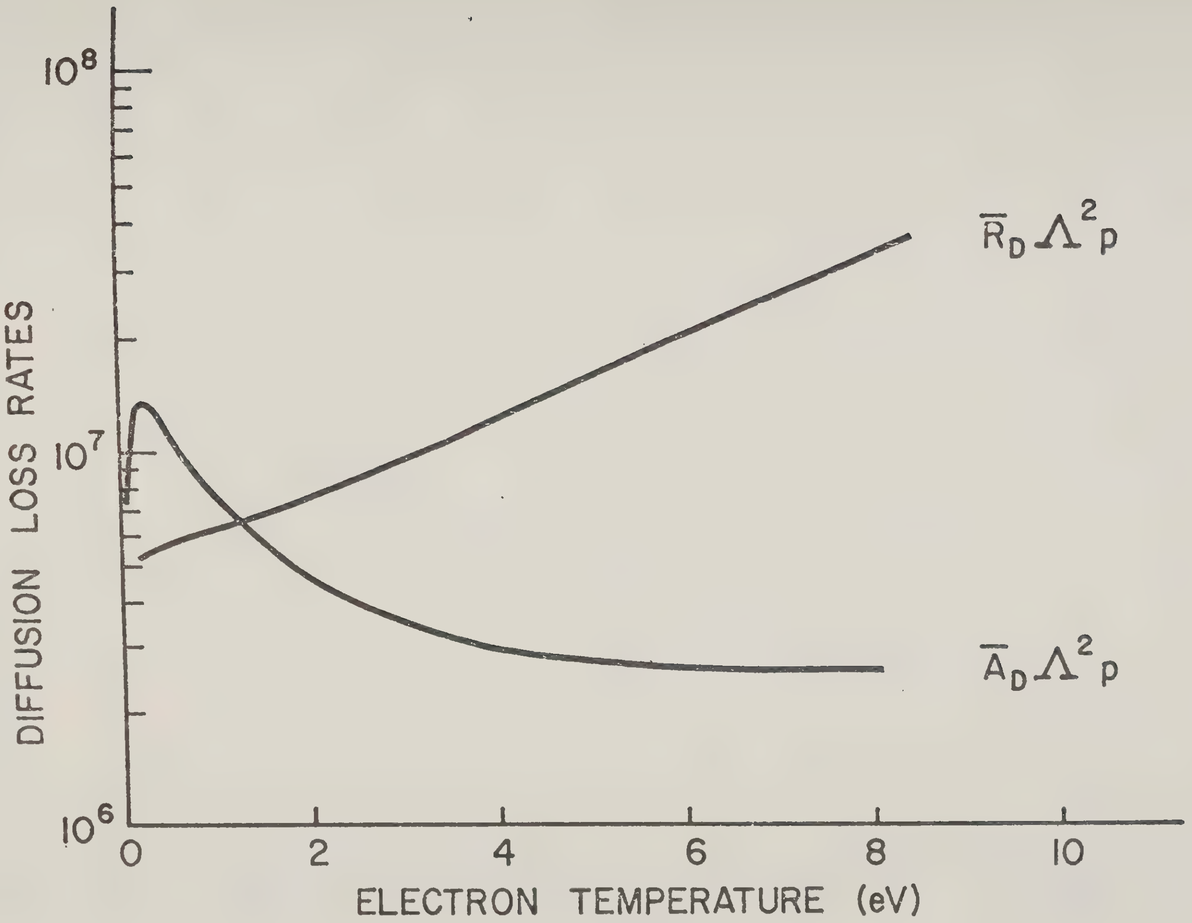

Figure 7-5(c) Diffusion Loss Rates

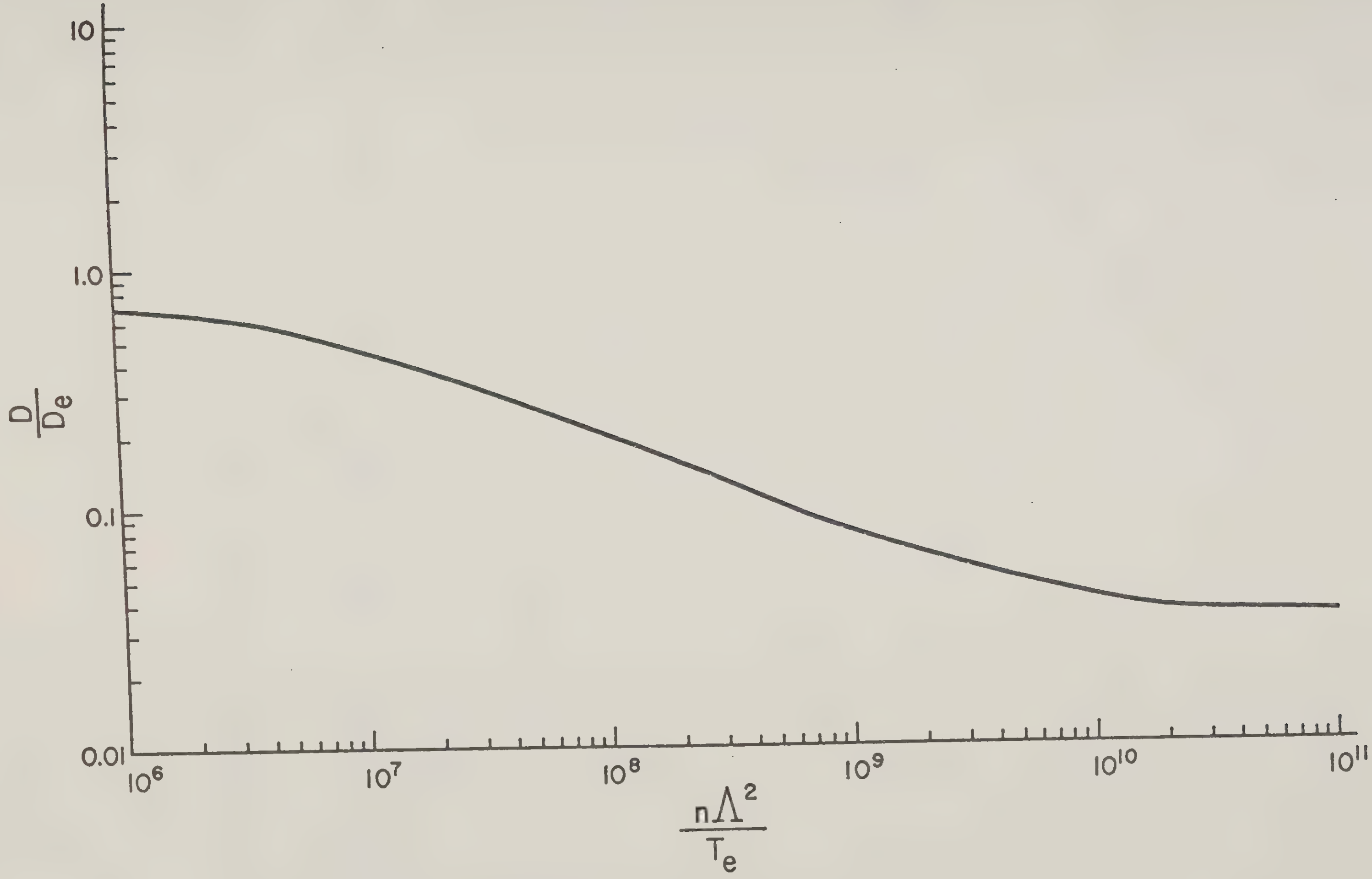

Figure 7-6 Effective Diffusion Coefficient

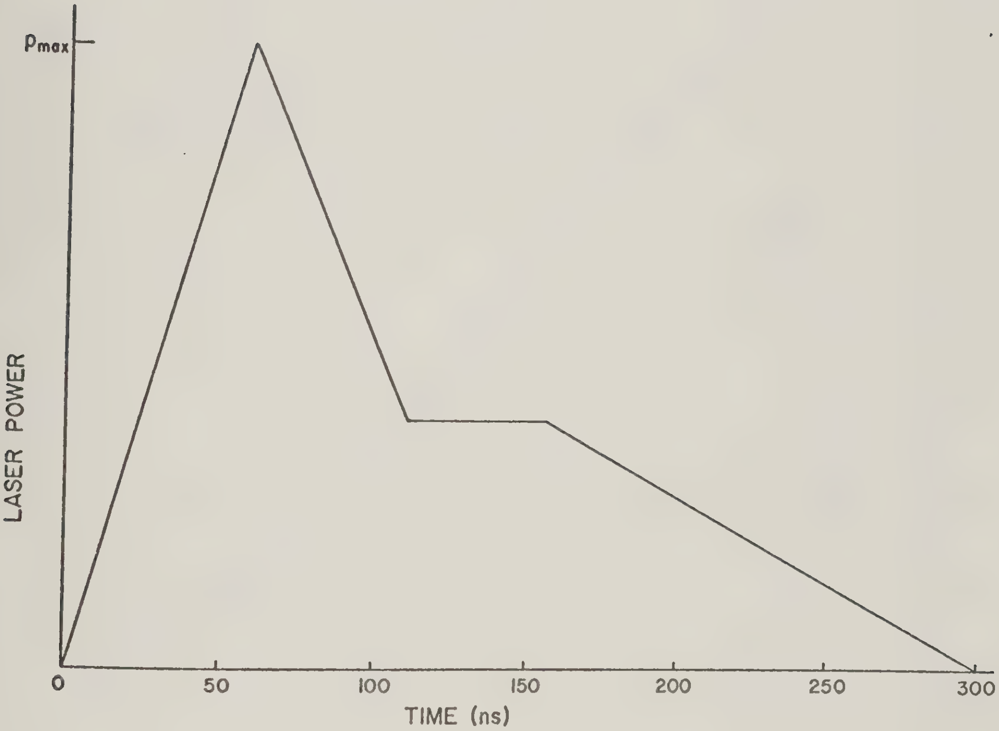

Figure 7-7 Laser Pulse Shape Used in Numerical Calculations

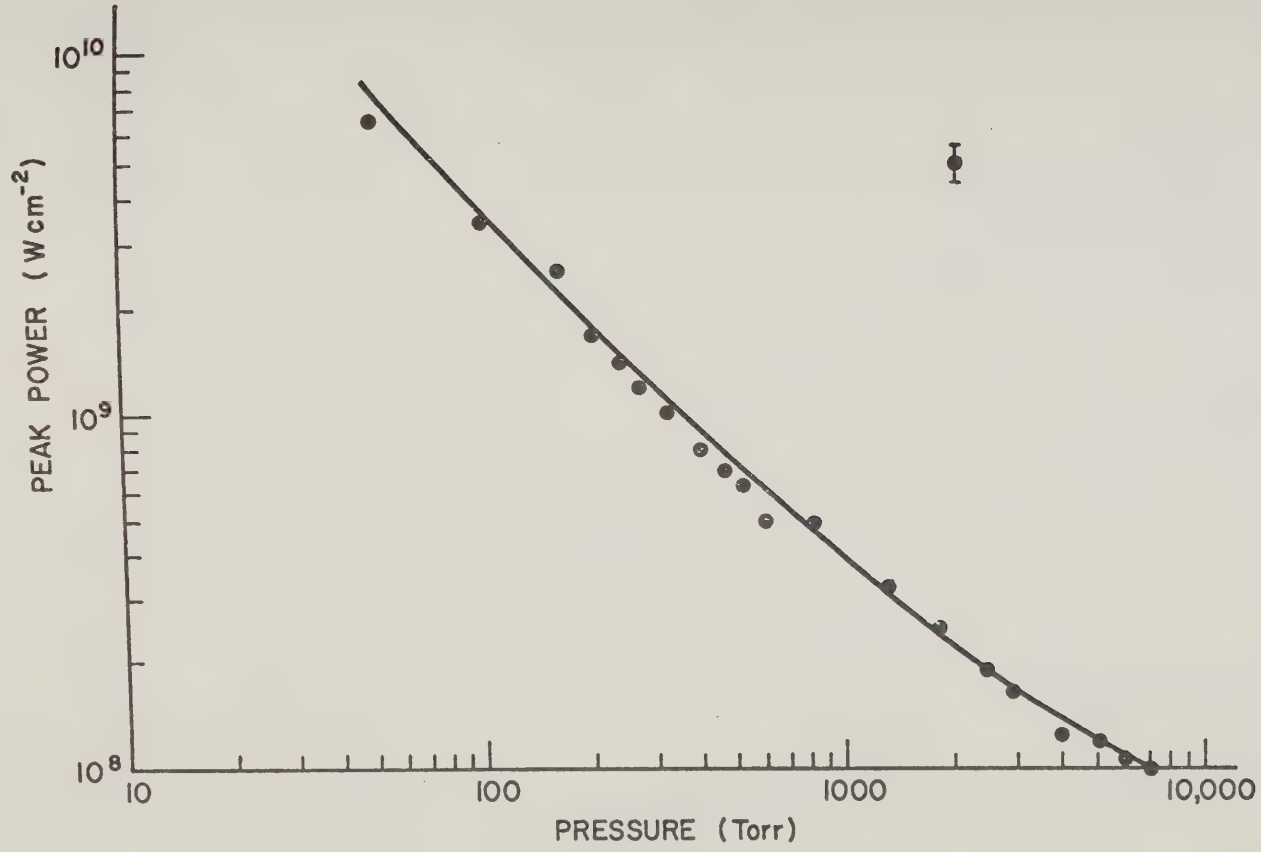

Figure 7-8 Measured and Calculated Thresholds without Preionization

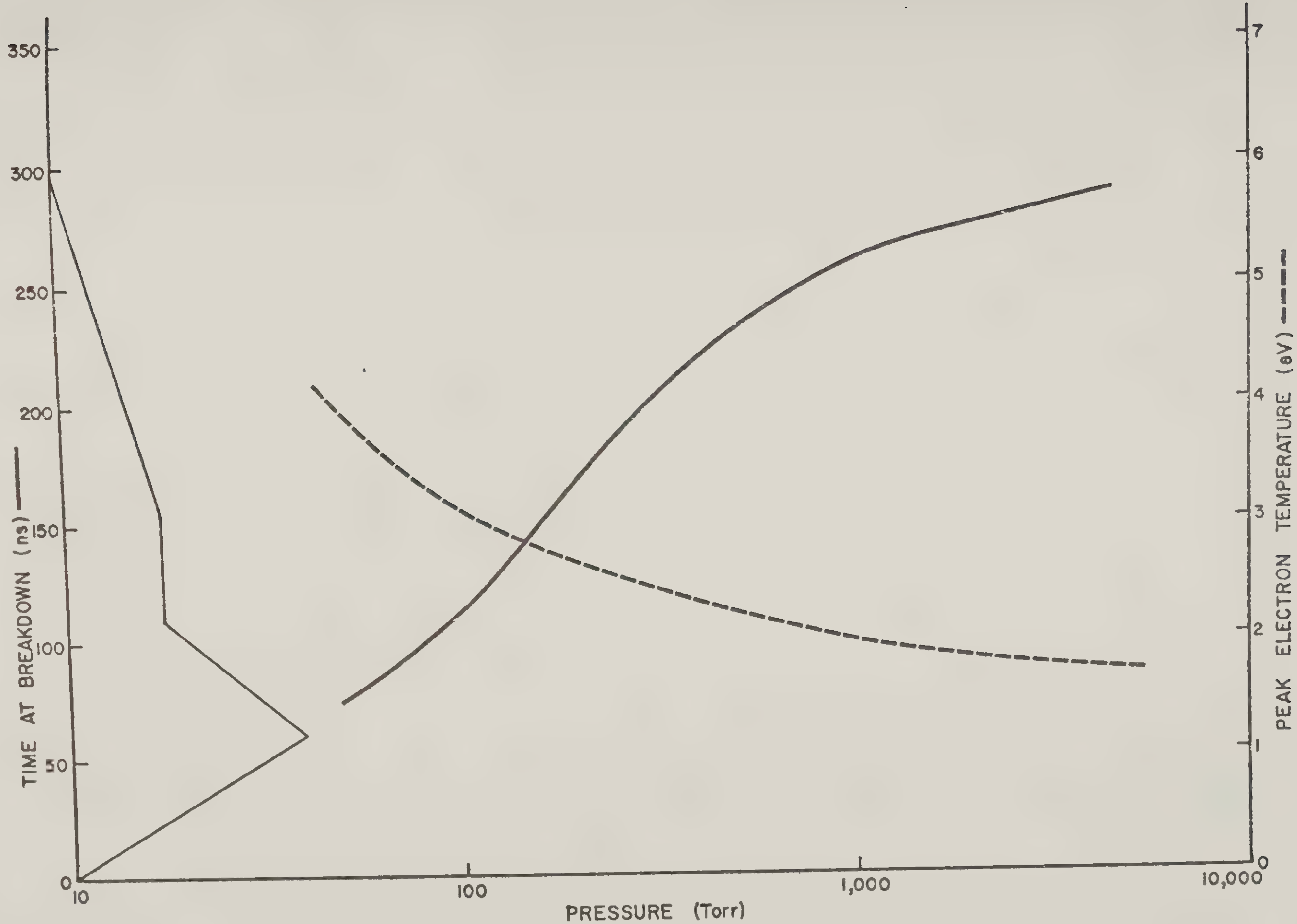

Figure 7-9 Peak Electron Temperature and Time at Breakdown as a Function of Gas Pressure. Also shown is the laser pulse.

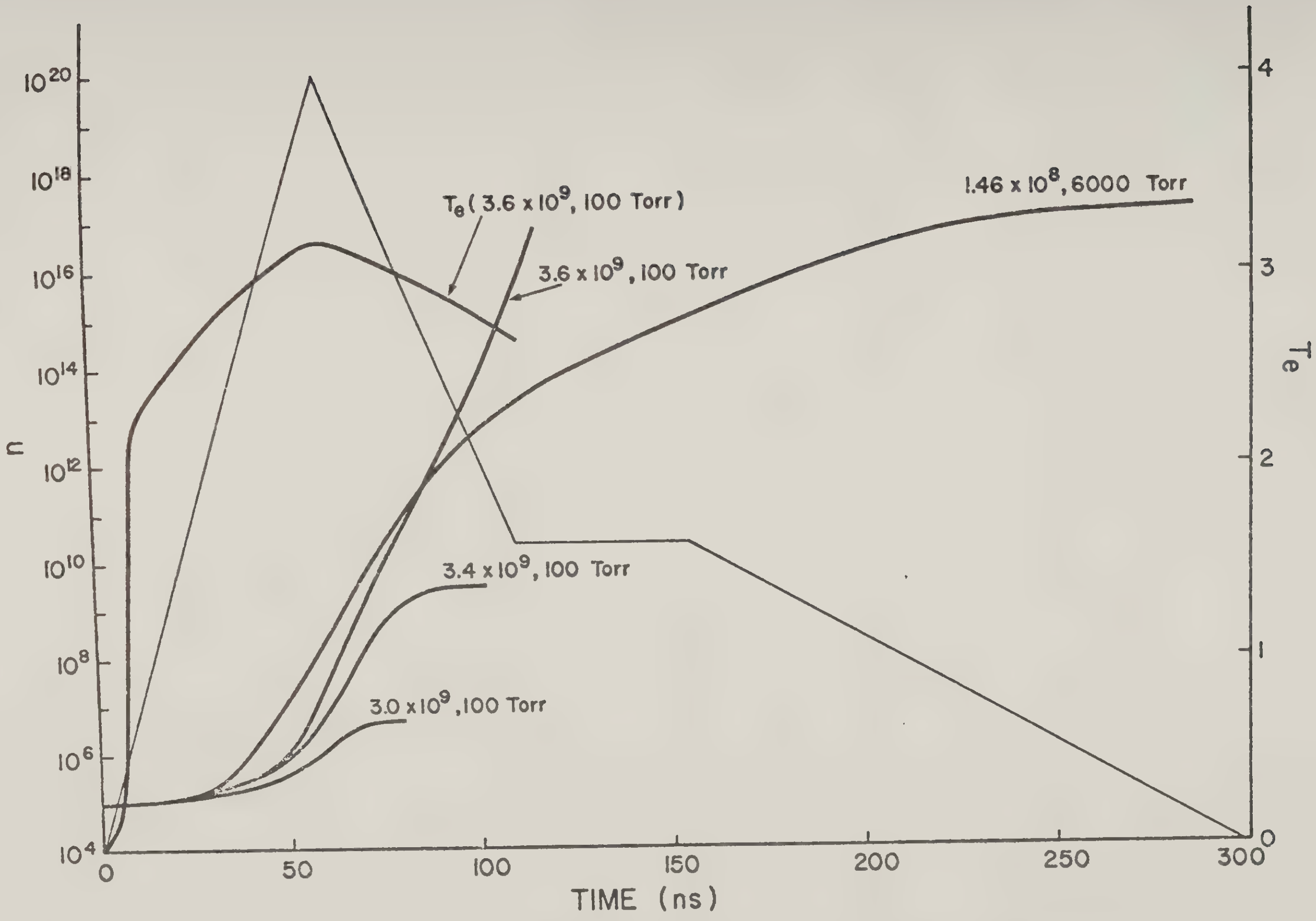

Figure 7-10 Charge Buildup in Laser Focus For Various Laser Energies and Gas Pressures. Also shown is the laser pulse shape and the electron temperature at threshold (p=100 torr).

CHAPTER VIII

BREAKDOWN THRESHOLD MEASUREMENTS: COMPARISON WITH CASCADE THEORY PREDICTIONS

8.1 Outline

The CO_2 laser induced breakdown threshold of Ar in the presence of an electric discharge was measured with the time delay between the initiation of the discharge preionizer and the laser pulse being varied. The CO_2 laser was focused inside and outside the discharge. Outside the discharge the threshold was lowered due to preionization in the focal volume by uv photons and compression of the gas during the passage of a weak shock wave. The measured thresholds were related to the previously determined electron density outside the discharge. It is shown that cascade theory adequately accounts for the experimental thresholds.

The lowering of the breakdown threshold during the passage of a compression wave through the focal volume is observed. Neutral atom densities corresponding to the amount of lowering are compared with pressure probe measurements of the shock strength.

When the laser was focused into the discharge region the changing electron and neutral gas densities combine to alter the breakdown threshold. The possibility of using breakdown to predict either the electron or the neutral density is explored.

8.2 Experimental Setup

The experimental setup has already been described in Chapter IV. Figure 4-1 is reproduced as Figure 8-1. A 5cm NaCℓ lens was used to focus the laser in the breakdown chamber. Since the probe measurements were done with a metal plate shielding the discharge except for a small uv port, a

similar plate was placed in the breakdown chamber when measuring the thresholds outside the discharge. The laser was focused into the center of the approximately cylindrical plasma. The laser was pulsed at a rate of one pulse per second as in the breakdown measurements without deliberate preionization. This was done more for convenience than necessity since the procedure described in Chapter III is not necessary when there is appreciable preionization.

8.3 Breakdown Measurements Outside the Discharge

The breakdown thresholds in Ar were measured at the same pressures and distances from the discharge as the probe measurements were made. The results are presented in Figures 8-2 (a) - (d). The thresholds have been normalized by their values without preionization. The initial time, $t_d=0$ was arbitrarily set to be 4μs after the initiation of the discharge pulse.

The lowering in the thresholds was due to the preionization of the gas by uv photons emitted by the discharge. As the photoplasma decays a gradual increase in the threshold was observed. Aside from the lowering due to the preionization, the passage of a shock wave in the focal volume was detected and manifested as a further lowering of the breakdown threshold. These can be seen in Figures 8-2 (a) - (d), and will be discussed later in the chapter.

Excluding the areas in the measured thresholds where shock effects were present, the experimental values of the thresholds were plotted against the initial electron-ion density in the focus. This is shown in Figure 8-3. At the same time the numerical model discussed in Chapter VII was used to generate theoretical threshold values and are plotted as solid lines in Figure 8-3. The experimental points do not all fall on the theoret-

ical curve. The discrepancy between the two may be due to a higher initial density in the focus in the case of no preionization than previously assumed. Uncertainties in the electron density, spot size, experimental thresholds, and other factors should also be taken into consideration.

The bend in the curve especially at low pressures is due to a transition from free diffusion loss to ambipolar diffusion loss of electrons from the focal volume. This transition was first observed by Brown and Smith[1].

The weak dependence of the breakdown threshold on the initial electron density as indicated in Figure 8-3 and Figure 8-5 makes it very difficult to obtain accurate measurements of the electron density from threshold measurements. A small error in the measured threshold will correspond to a large error in the density. On the other hand, the threshold varies quite rapidly with the neutral atom density (see Figure 7-8) except at very high pressures (10,000 Torr). Therefore, if the electron density can be measured independently, neutral atom concentrations can be obtained with reasonable accuracy. Errors in the electron density will not be very critical because of the weak dependence of the threshold on it.

With the plate shielding the discharge removed, the threshold was remeasured at the time of arrival of the expanding shock wave at the focus. The plate was removed in order to obtain measurements very close to the discharge. The results are shown in Figures 8-4 (a) - (f). The thresholds without the plate are in general lower than those obtained with the metal shield. Furthermore, it takes a longer time for the plasma to decay. These indicate a higher degree of preionization without the shield. The

higher preionization may be due to more efficient use of the photons emitted by the discharge. The effective photons may not be emitted uniformly from all regions in the discharge but mainly come from particular areas such as near the electrodes. Photons from these areas may have been partially blocked by the plate. There are no measurements of the electron density due to uv radiation for this case because the probe cannot be exposed to uv. Therefore, it was assumed that the electron density could be obtained with sufficient accuracy from the measured thresholds. From the known gas pressure and breakdown threshold just before the shock, the electron density can be read from Figure 8-5 which gives the theoretically calculated thresholds as a function of the initial electron density and pressure. The electron density during the passage of the shock is then assumed to be the same as its value just before the shock. With this initial electron density and the new threshold in the shock, the gas pressure and hence, the neutral density can be obtained from Figure 8-5. Interpolation between two curves may be necessary.

The pressure jump in the shock has been measured previously (Chapter V). Assuming the equation of state of the gas is known (perfect gas) and assuming further that $\gamma = 5/3$, the gas density jump in the shock can be computed using shock theory. The results are the solid lines in Figures 8-6 (a) - (c). The data points are from the breakdown measurements. It can be seen that for this case, breakdown threshold is a direct measure of the neutral atom concentration of the gas.

8.4 Breakdown Measurements Inside the Discharge

The breakdown threshold when the laser was focused in the center of

the discharge was measured as a function of time delay between the discharge and laser pulses and the as pressure. The threshold ratio can exceed one[2]. This occurs when there is a reduction in the neutral density which in this case is due to heating of the gas. As the gas cools down, the threshold slowly returns to its initial value. This can be seen in Figure 8-7 which depicts the measured thresholds at the center of the discharge. This can also be seen in Figure 8-4 (a) at approximately 200μs after the discharge was fired. At this time the discharge has expanded to the region of the focus. Although there is also an increase in the electron density as the discharge expands into the focal volume, the effect of the reduced neutral density predominates because of the weak dependence of the threshold on the initial electron density.

From the measurements and the known electron density (Chapter IV) the neutral atom concentration in the discharge can be computed and compared with the results of the interferometric measurements. This is shown in Figures 8-8 (a) - (c). Also shown in the figure are the expected neutral densities if equilibrium is assumed with a temperature equal to T_e obtained from the absorption experiment.

It can be seen from Figure 8-8 that the computed neutral densities from the breakdown measurements are consistently smaller than those obtained from the interferometric or absorption measurements. This may be due to the difficulty in visually observing the laser spark superimposed on the bright arc discharge. In fact, only the tail of the spark which comes out of the discharge is observable. It is then very probable that the thresholds obtained were larger than the actual thresholds; more energy is required to produce a spark which can be observed amidst the bright background. This sets a limitation to the technique which could possibly be overcome if the

threshold were defined in a different manner. The most likely candidate for this would be a measurement of the transmitted laser pulse.

8.5 Discussion

The preceding sections indicate that cascade breakdown can be used to measure electron and neutral atoms densities in rapidly changing plasmas. It is more effective in cold, low density plasmas (e.g. photoplasmas) where radiation does not interfere with the observation of the spark.

If breakdown is used to measure electron densities (provided the neutral density is known), the uncertainty in the results will be large because of the very weak dependence of the threshold on the initial density. Therefore, breakdown possibly gives only order of magnitude estimates.

If the electron density is known, rapid changes in the neutral gas density can be monitored by observing changes in the gas breakdown threshold. Since $\phi \sim \frac{1}{p} \sim \frac{1}{n_n}$ the threshold is more sensitive to changes in n_n than n. The results will be in close agreement with measurements using other well known techniques as long as there is no difficulty in observing the laser spark. The uncertainty in n_n obtained will approximately be of the order of the uncertainty in ϕ since $\phi \sim \frac{1}{n_n}$.

Aside from the limitation of the technique to non-luminous plasmas, the magnitudes of the electron and neutral density will impose limitations on the practicability of using breakdown as a diagnostic. For very high initial electron densities ($\approx 10^{16}\text{cm}^{-3}$), it would be very difficult to control the incident laser energy to obtain probabilities of breakdown between 0% and 100%. An absolute limit to n is, of course, n_b. Furthermore, since avalanche breakdown is assumed to take place, only neutral densities

greater than ≃ $3\times10^{17}\mathrm{cm}^{-3}$ (p = 10 Torr) can be measured. At very low pressures avalanche breakdown does not occur.

As an example of the use of breakdown to determine electron and neutral densities, the breakdown threshold of Ar at a pressure of 600 Torr was measured 8 mm from the center of the discharge. This is shown in Figure 8-9. Since the measurement was performed at a distance much closer than those reported in Figure 8-4, effects of the discharge expanding into the focal volume should be observed. Measurements of the threshold at other pressures and at slightly different distances give similar results. The events that take place in the focus are as follows: For very early times the discharge emission photoionizes the gas which will be detected as a lowering in the threshold. The discharge creates an expanding shock which passes through the focal volume approximately two microseconds after the end of the current pulse. This is observed as a further lowering in the threshold. Meanwhile, the discharge itself is slowly expanding. At approximately $t_d = 150\mu s$ the hot discharge has expanded up to the focus. The higher temperature means a slightly lower gas density compared to the background density and a slight increase in the threshold is observed. The electron density will also increase at this time but the effect of rarefaction is more pronounced. As the gas cools, the electron density decreases and the gas density increases. The threshold gradually approaches its value without the discharge.

The electron and gas densities determined from the thresholds shown in Figure 8-9 are depicted in Figures 8-10 (a) - (b). From $t_d = 150$ to $400\mu s$ the electron densities were obtained from the probe measurements. The initial decay of the plasma is recombination-controlled with a recombination coefficient of $3\times10^{-10}\mathrm{cm}^3/\mathrm{s}$. The electron and neutral atom densities

follow the qualitative picture discussed above.

Finally, the photoplasma density at $t_d=0$ obtained from the breakdown measurements was plotted versus distance from the discharge as shown in Figure 8-11. In this case, the neutral density will be equal to the ambient gas density. As in the previous probe measurements the variation of the initial density with distance is not incompatible with an r^{-4} dependence as shown by the solid lines in the figure.

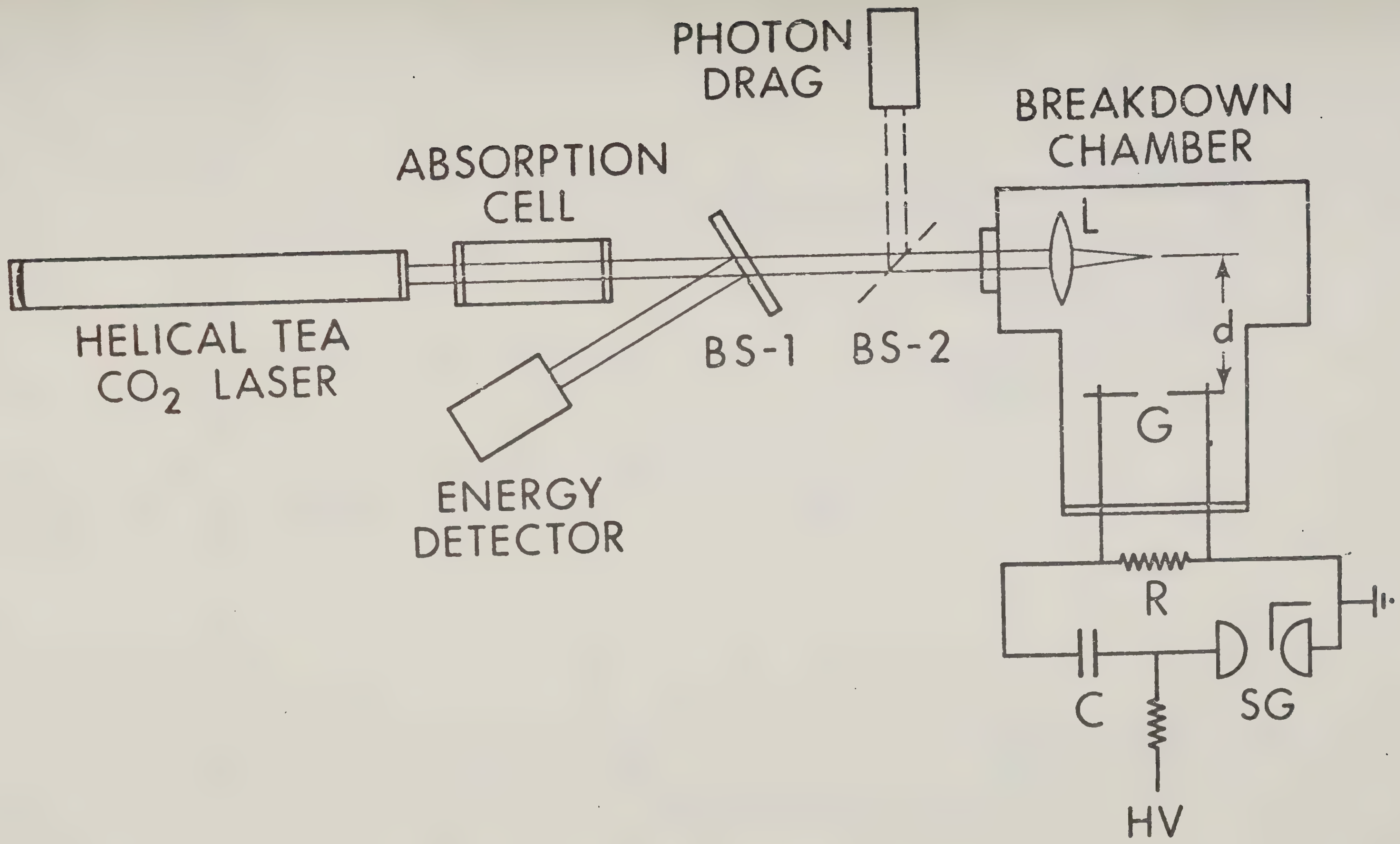
PHOTON DRAG
BREAKDOWN CHAMBER
ABSORPTION CELL
L
d
HELICAL TEA CO_2 LASER
BS-1
BS-2
G
ENERGY DETECTOR
R
C
SG
HV

Figure 8-1 Experimental Set-Up Used in Breakdown Measurements.

This figure is the same as Figure 4-1.

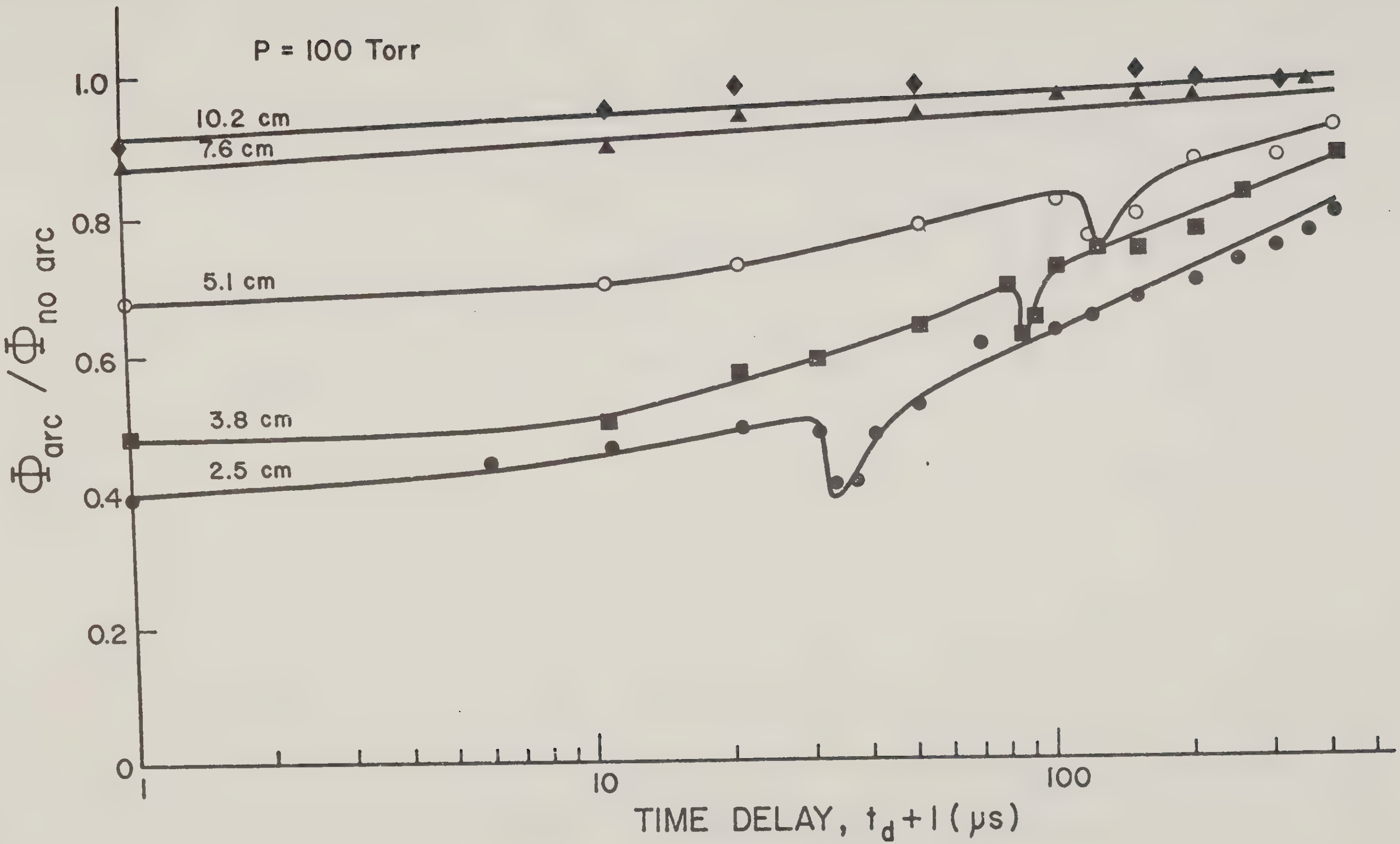

Figure 8-2(a) Breakdown Threshold Outside the Discharge

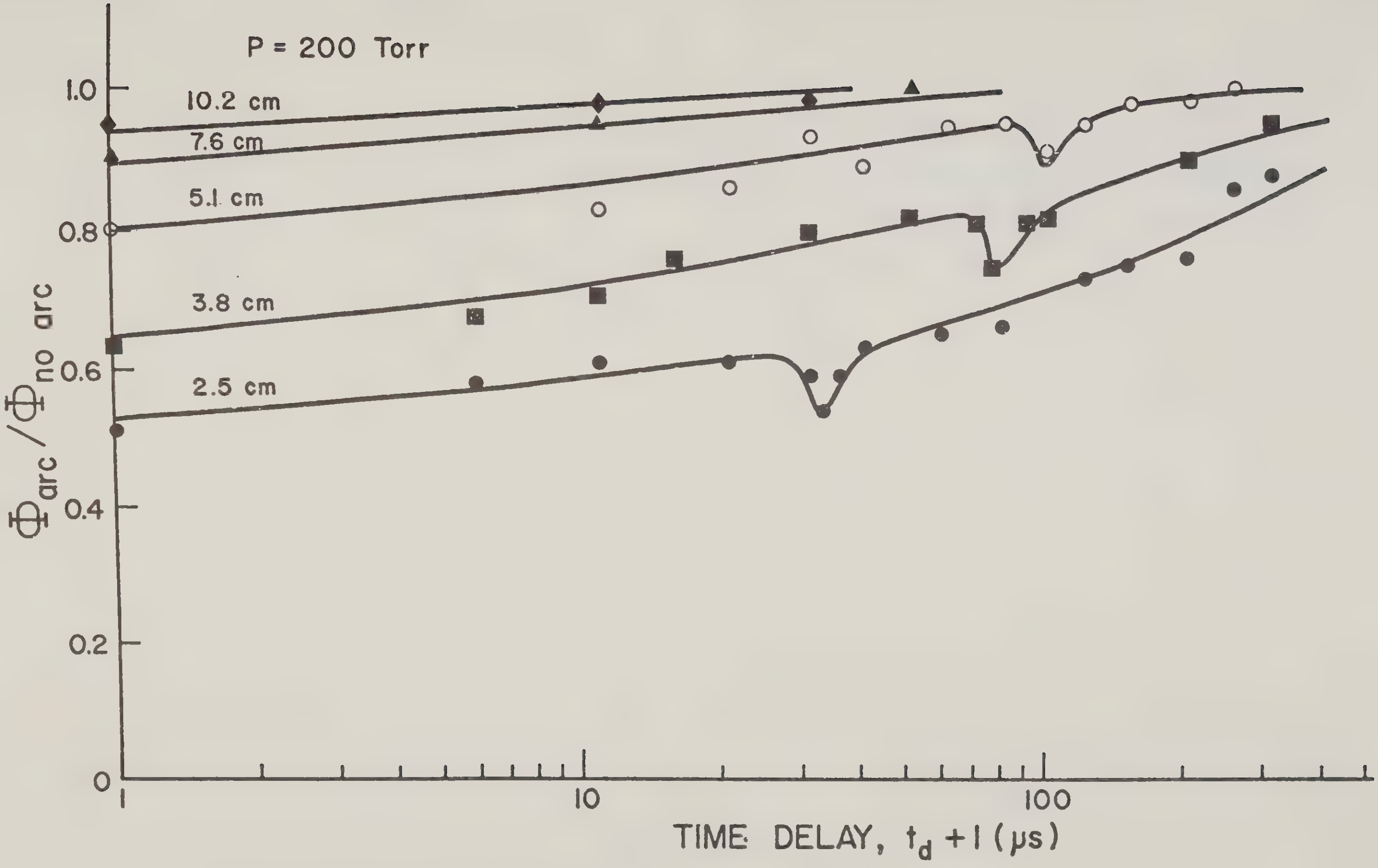

Figure 8-2(b) Breakdown Threshold Outside the Discharge

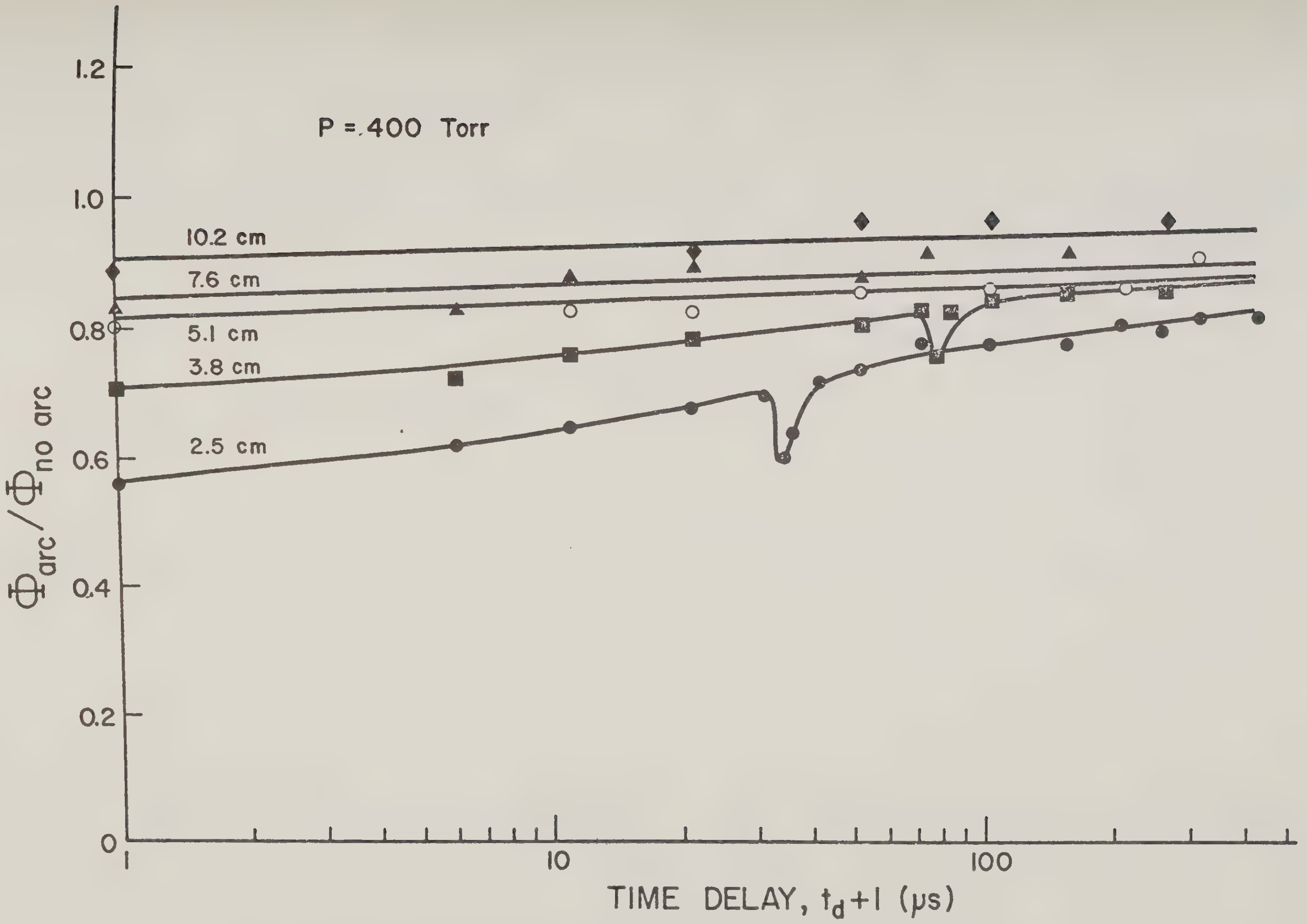

Figure 8-2(c) Breakdown Threshold Outside the Discharge

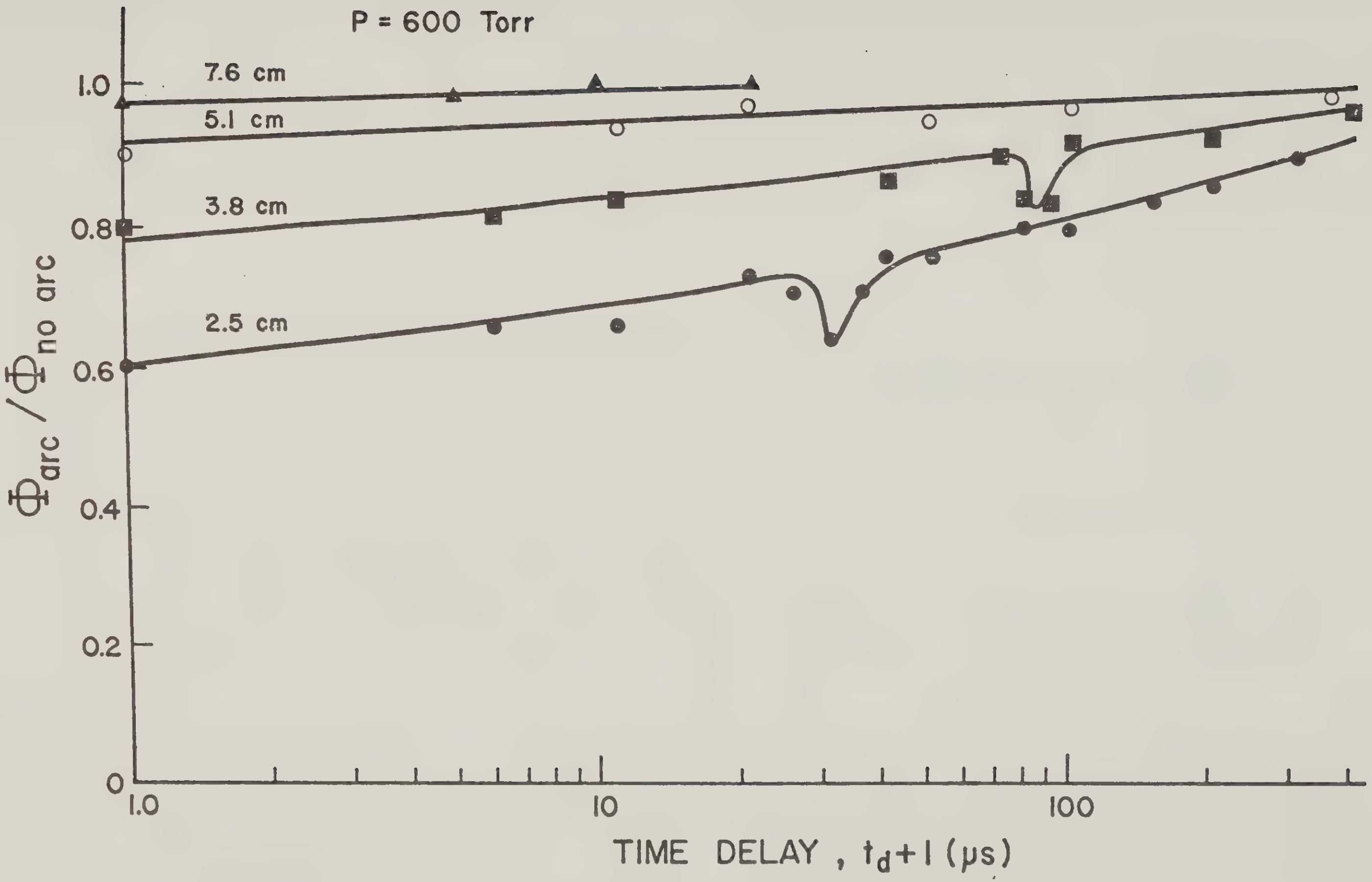

Figure 8-2(d) Breakdown Threshold Outside the Discharge

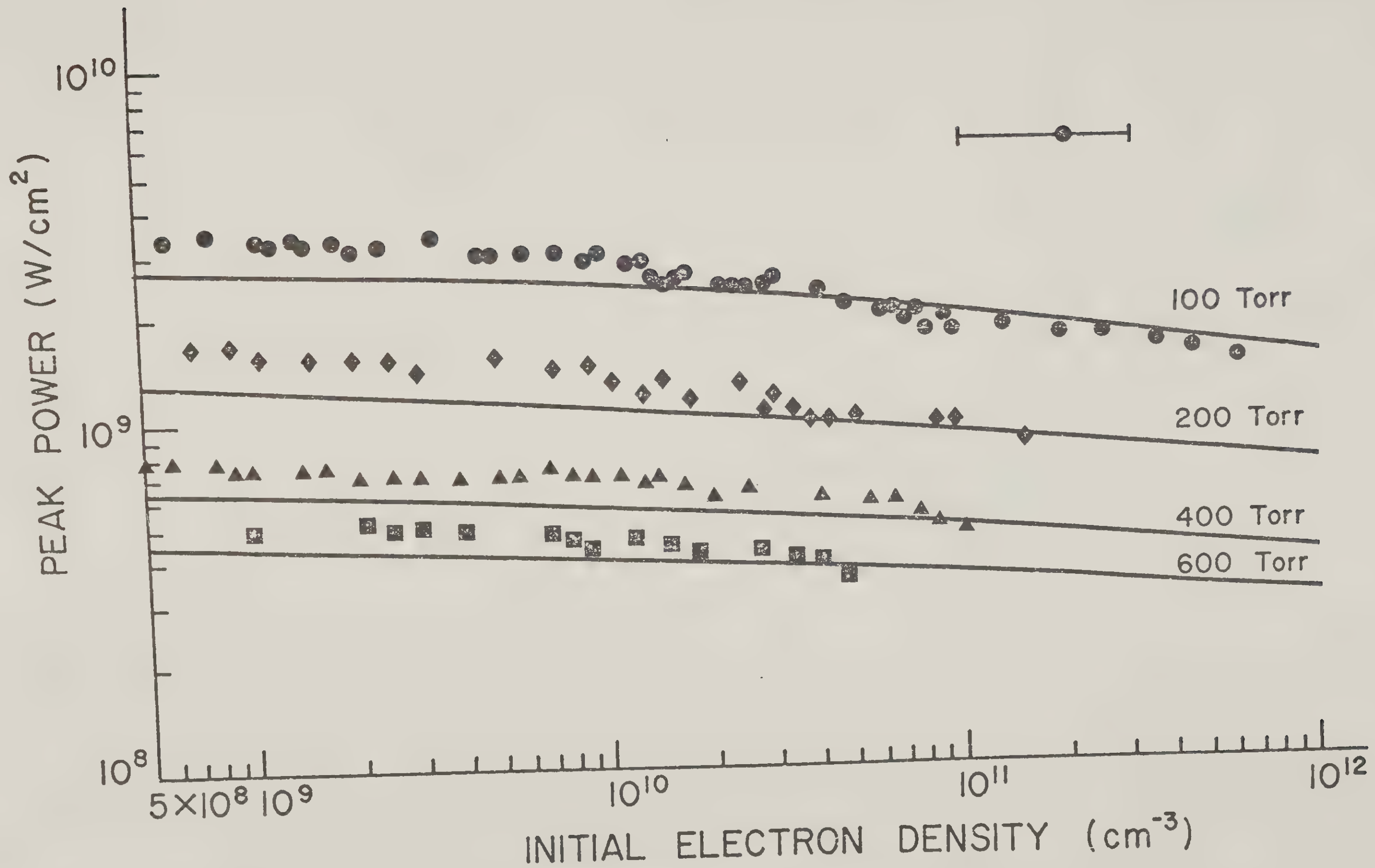

Figure 8-3 Laser Peak Power at Threshold Versus Initial Electron Density at the Focus. The solid lines are the theoretically calculated values.

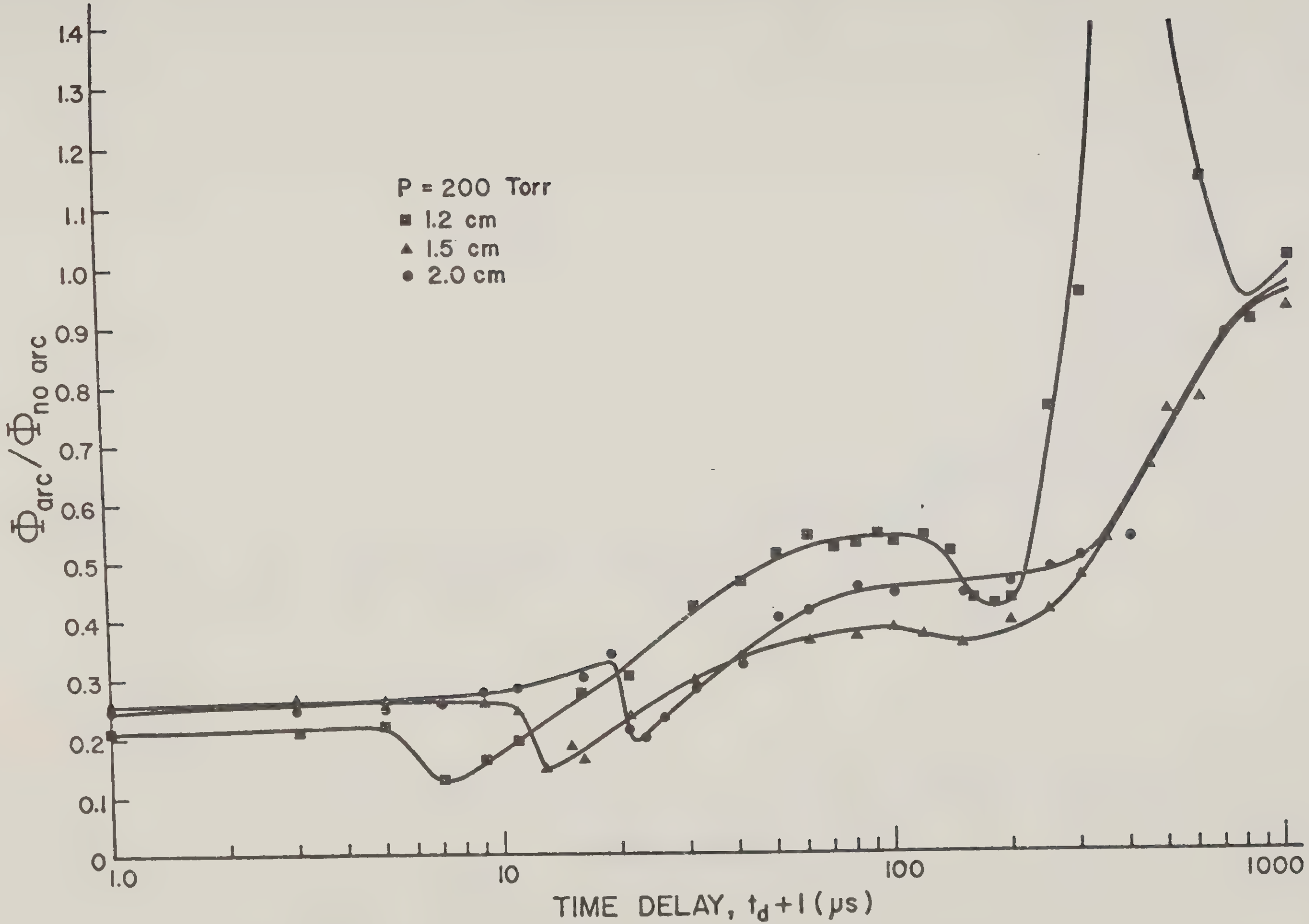

Figure 8-4(a) Breakdown Threshold Outside the Discharge

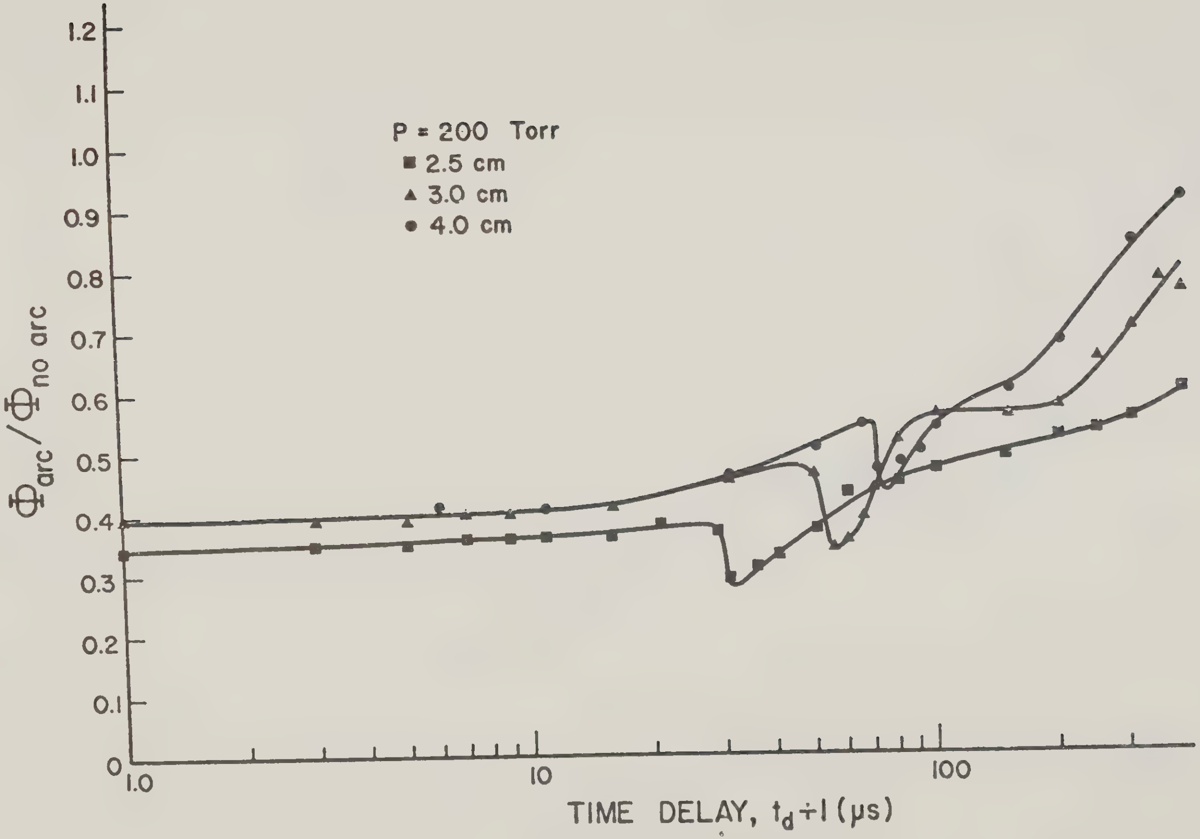

Figure 8-4(b) Breakdown Threshold Outside the Discharge

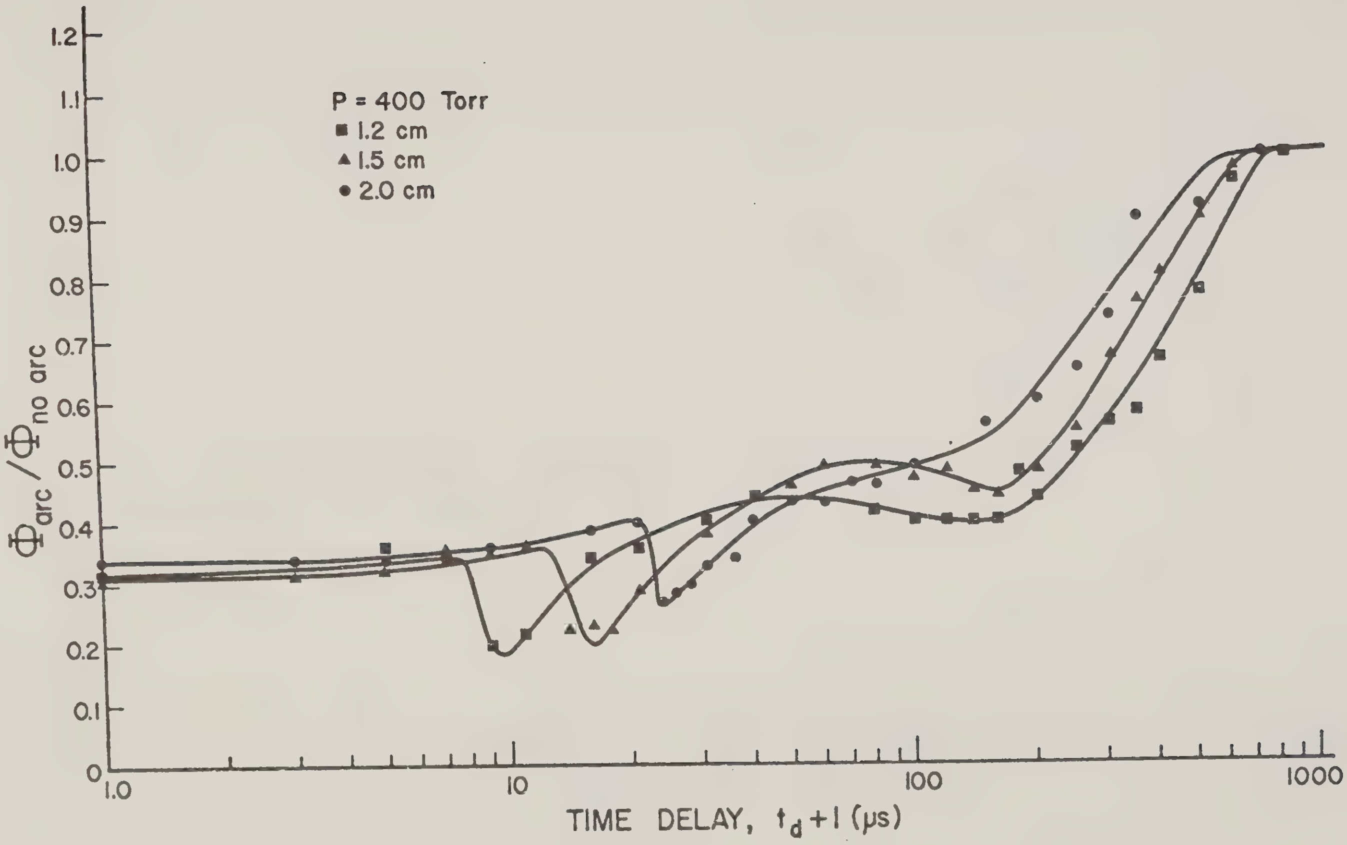

Figure 8-4(c) Breakdown Threshold Outside the Discharge

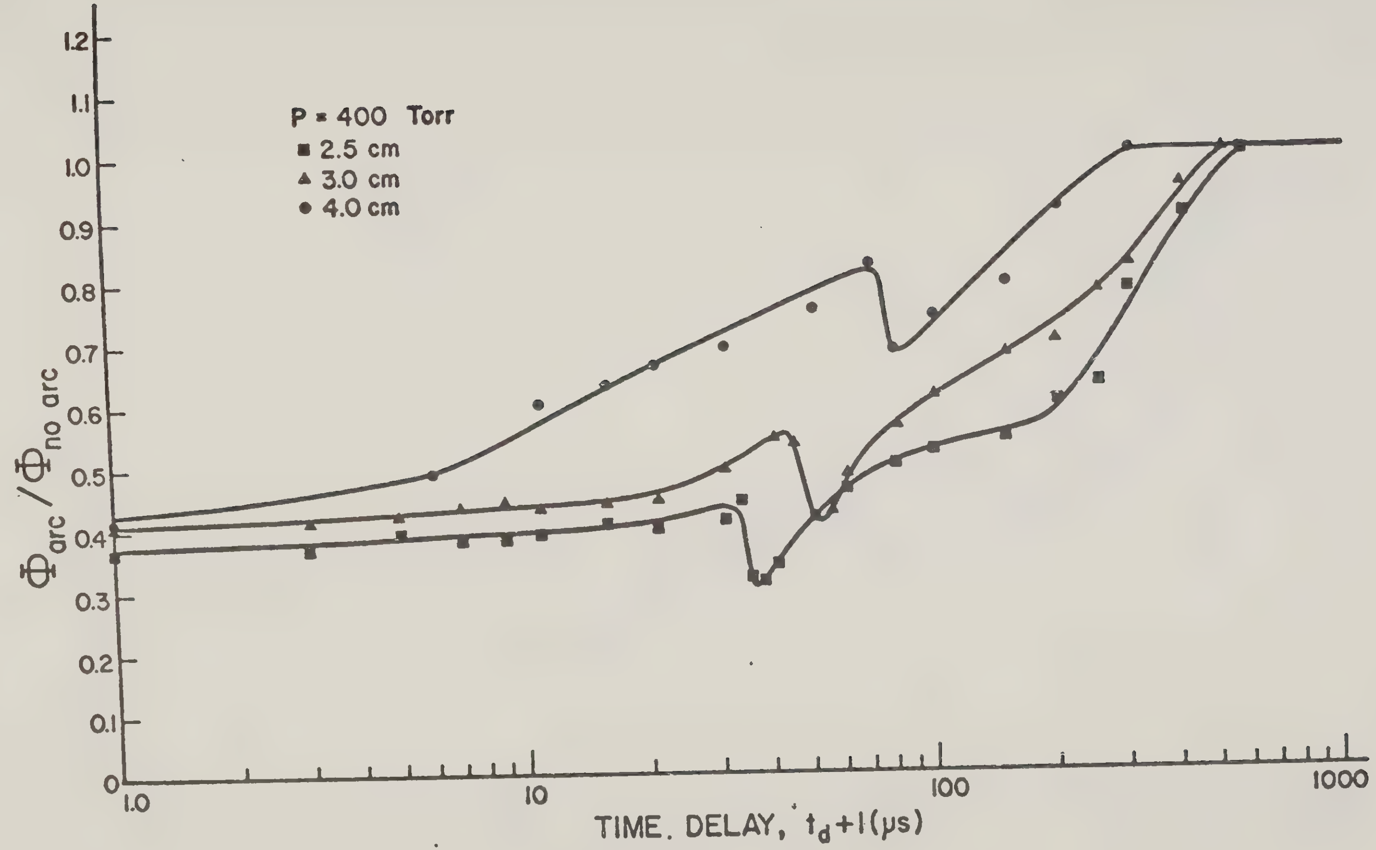

Figure 8-4(d) Breakdown Threshold Outside the Discharge

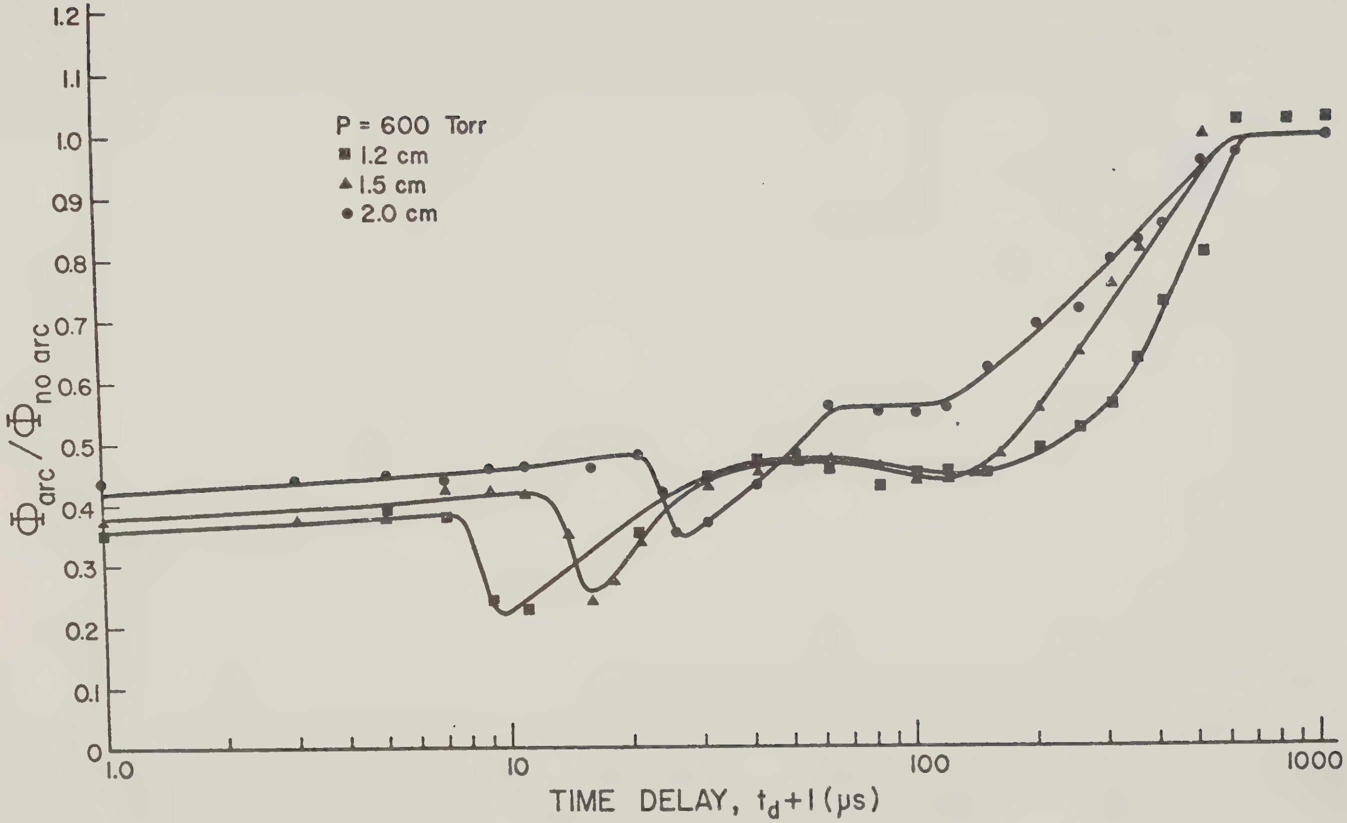

Figure 8-4(e) Breakdown Threshold Outside the Discharge

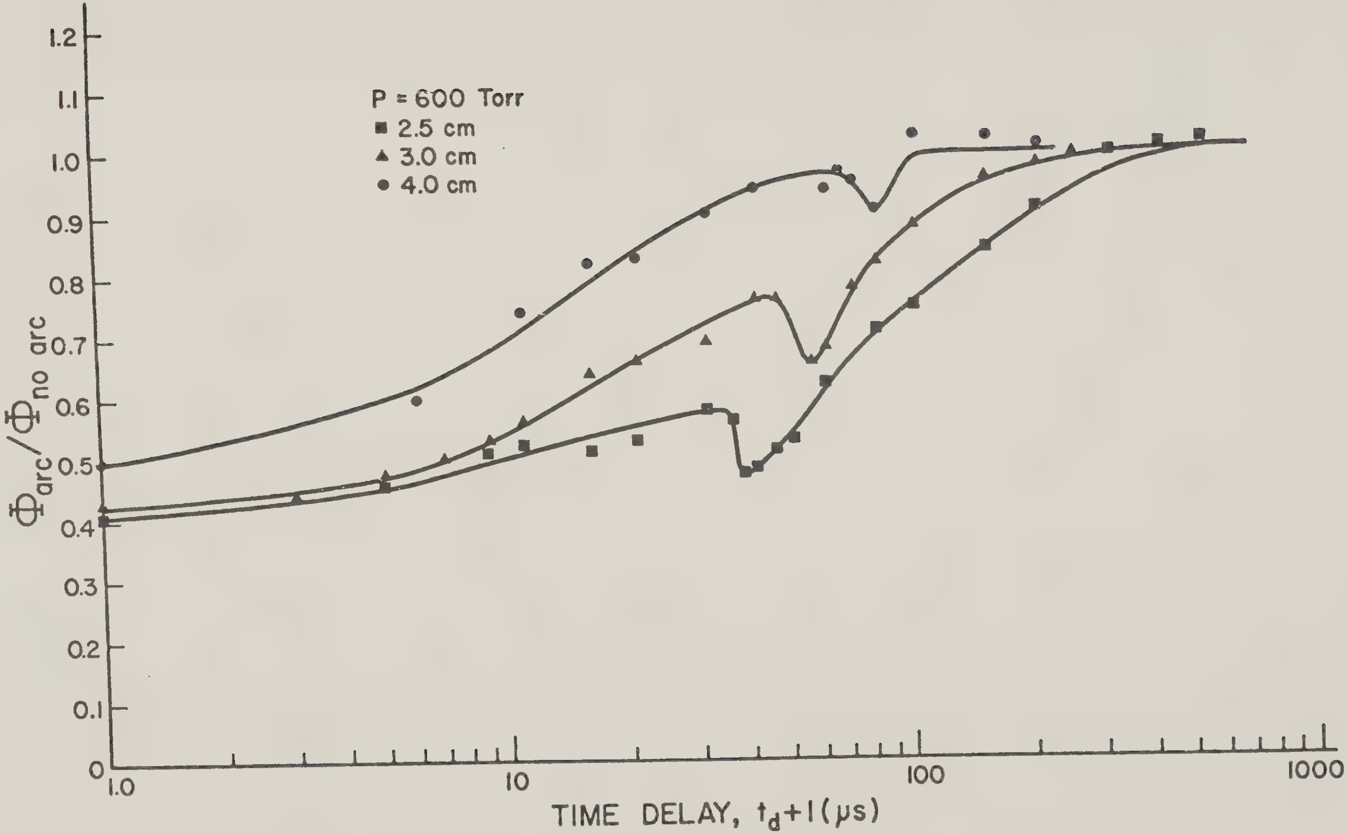

Figure 8-4(f) Breakdown Threshold Outside the Discharge

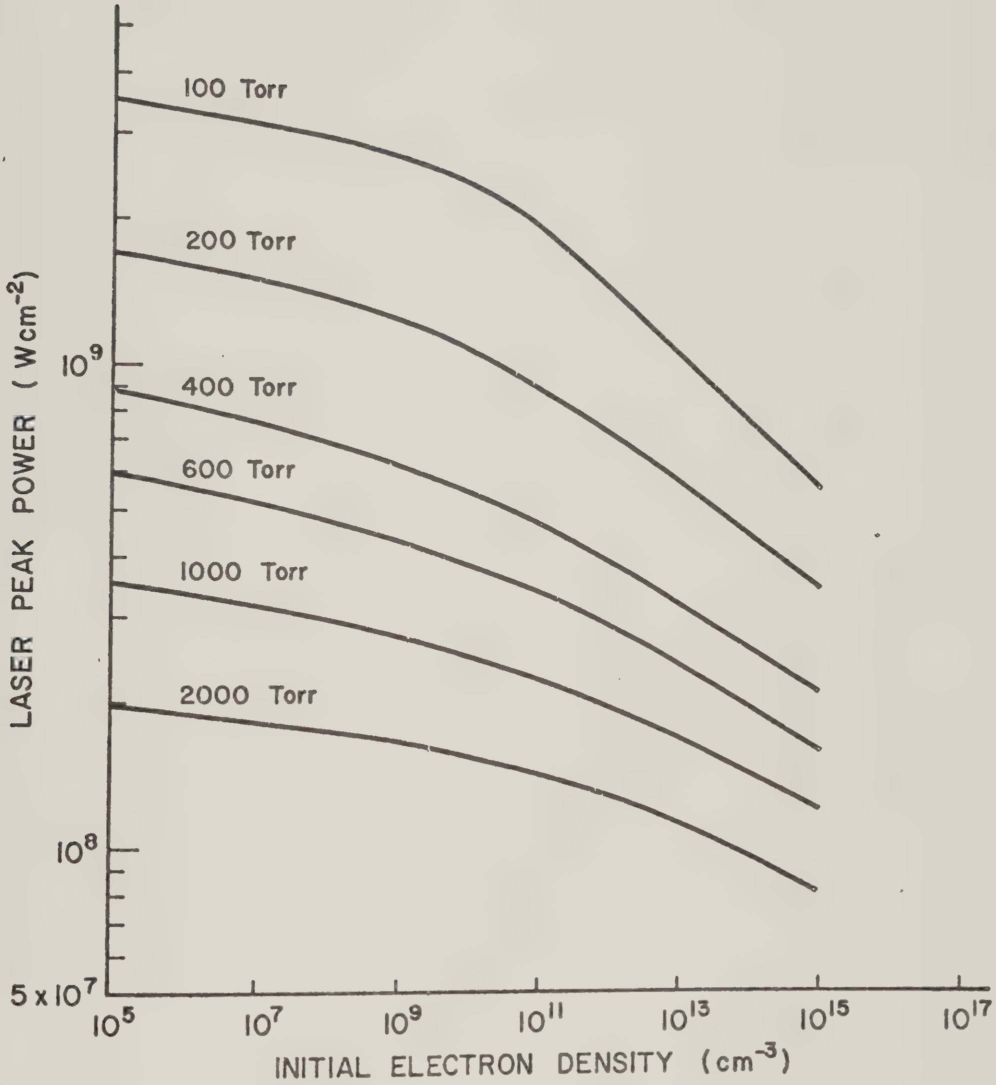

Figure 8-5 Computed Laser Peak Power at Threshold as a Function of the Initial Electron Density

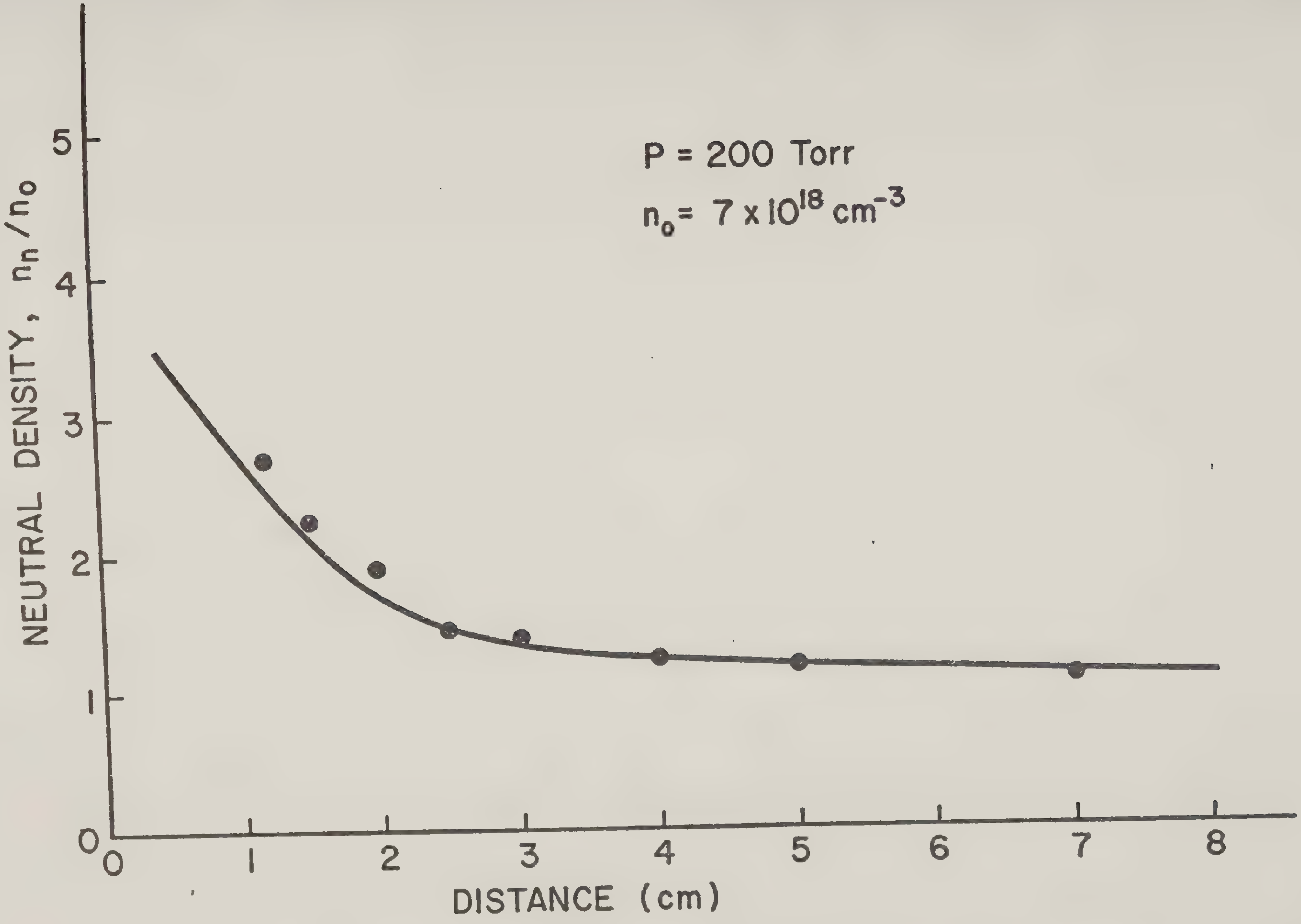

Figure 8-6(a) Neutral Atom Density in the Shock as a Function of Distance. The points are from breakdown measurements while the solid line is the calculated density using pressure probe results.

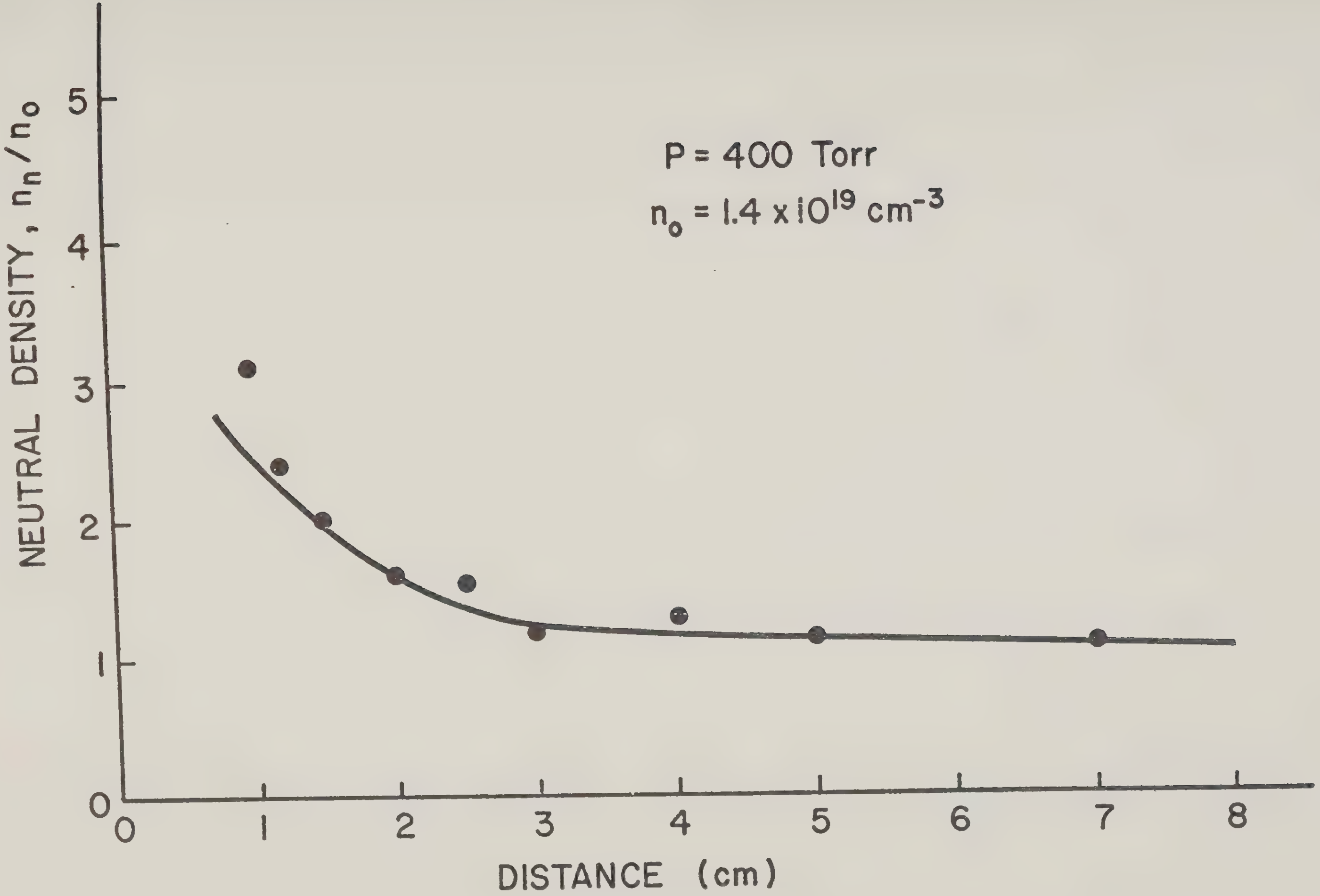

Figure 8-6(b) Neutral Atom Density in the Shock as a Function of Distance

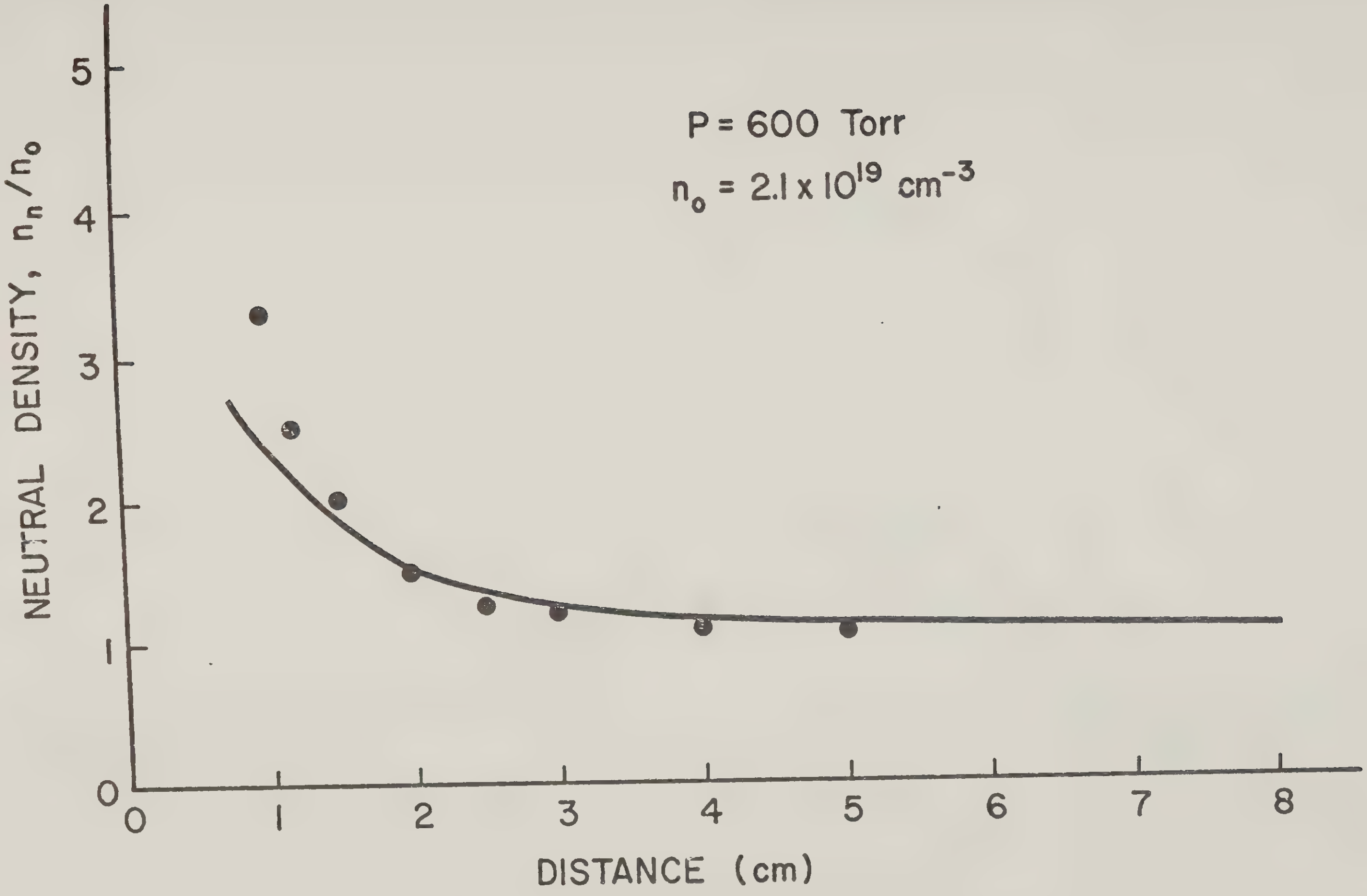

Figure 8-6(c) Neutral Atom Density in the Shock as a Function of Distance

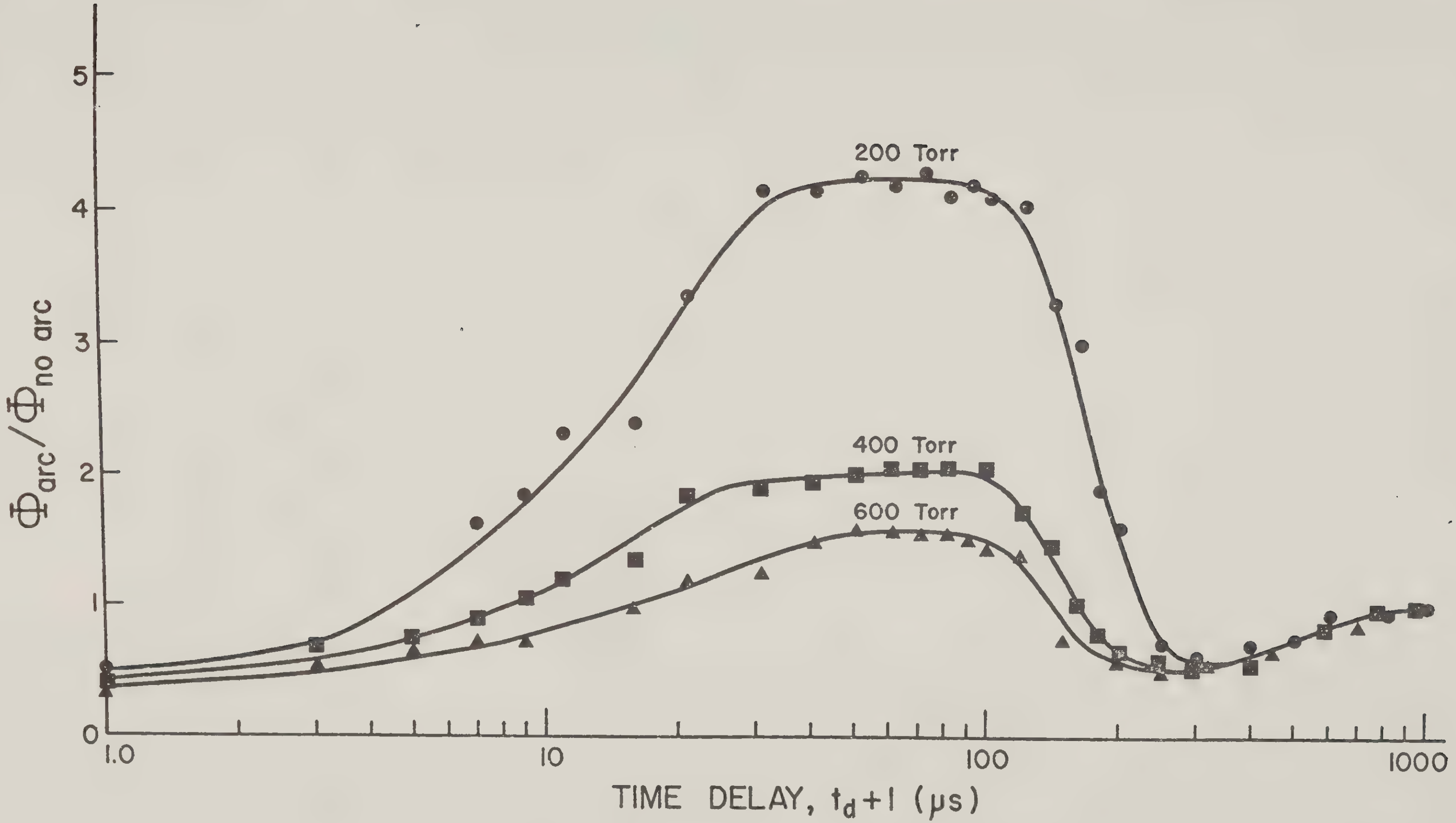

Figure 8-7 Breakdown Thresholds Inside the Discharge Versus Time for Various Pressures

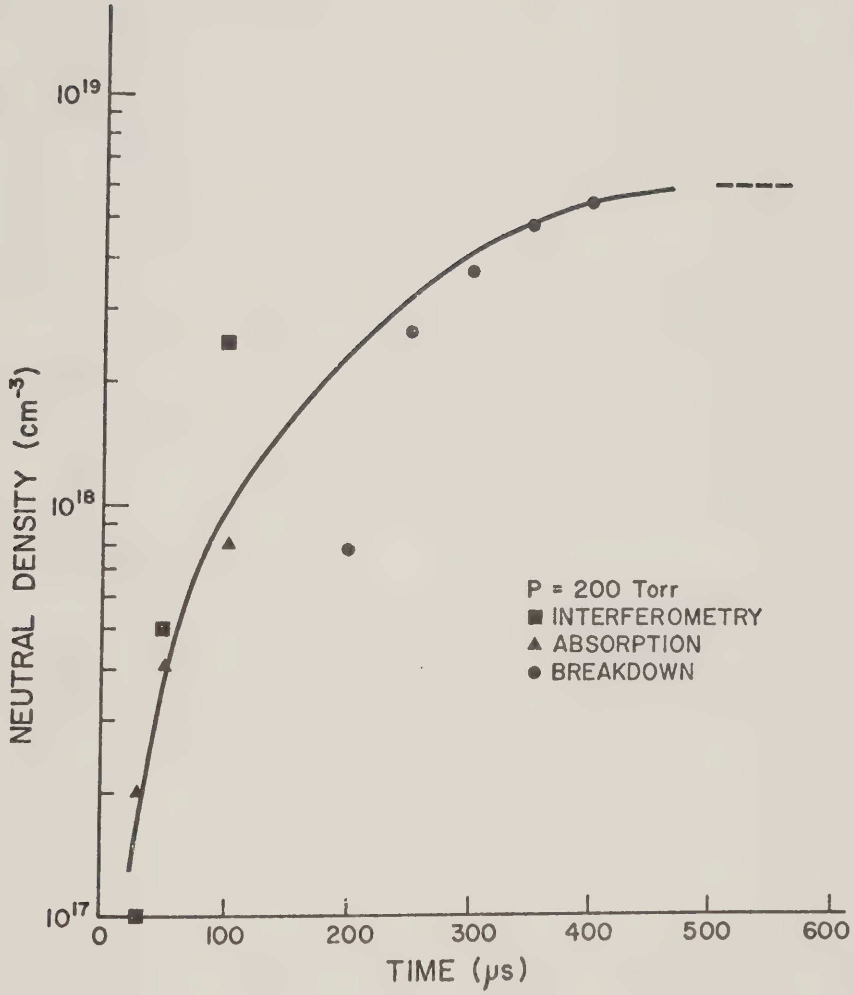

Figure 8-8(a) Neutral Density in the Discharge Versus Time

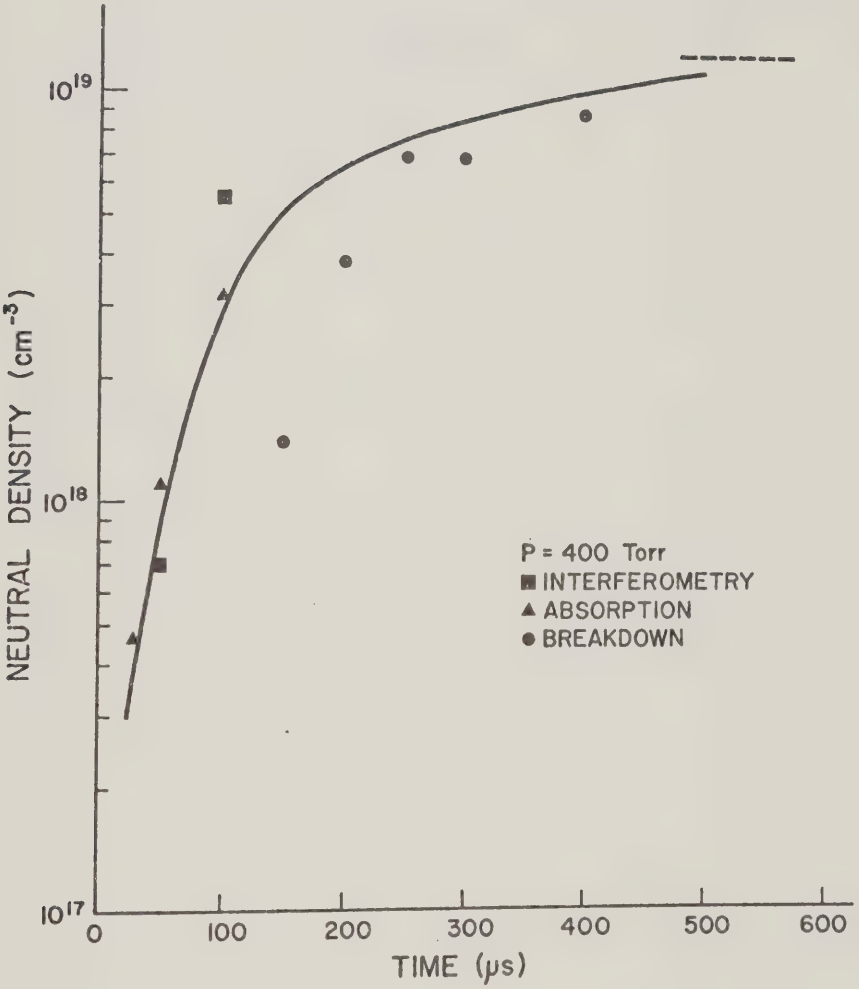

Figure 8-8(b) Neutral Density in the Discharge Versus Time

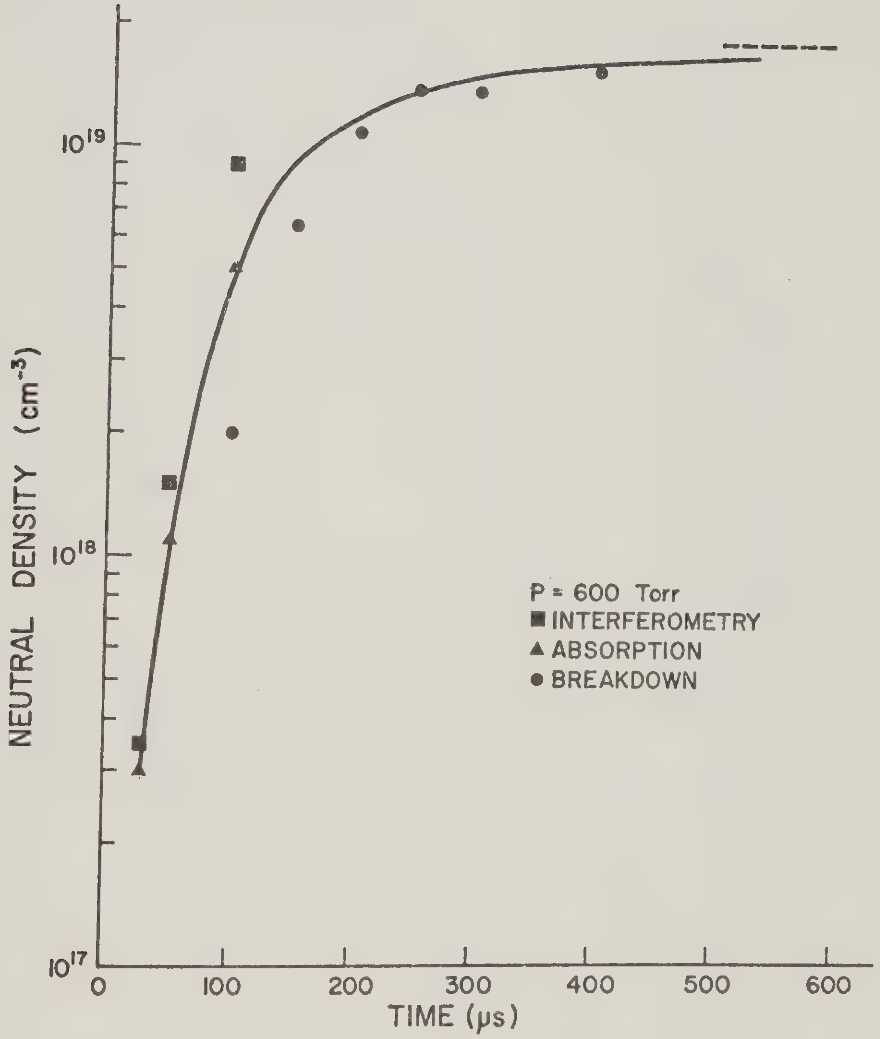

Figure 8-8(c) Neutral Density in the Discharge Versus Time

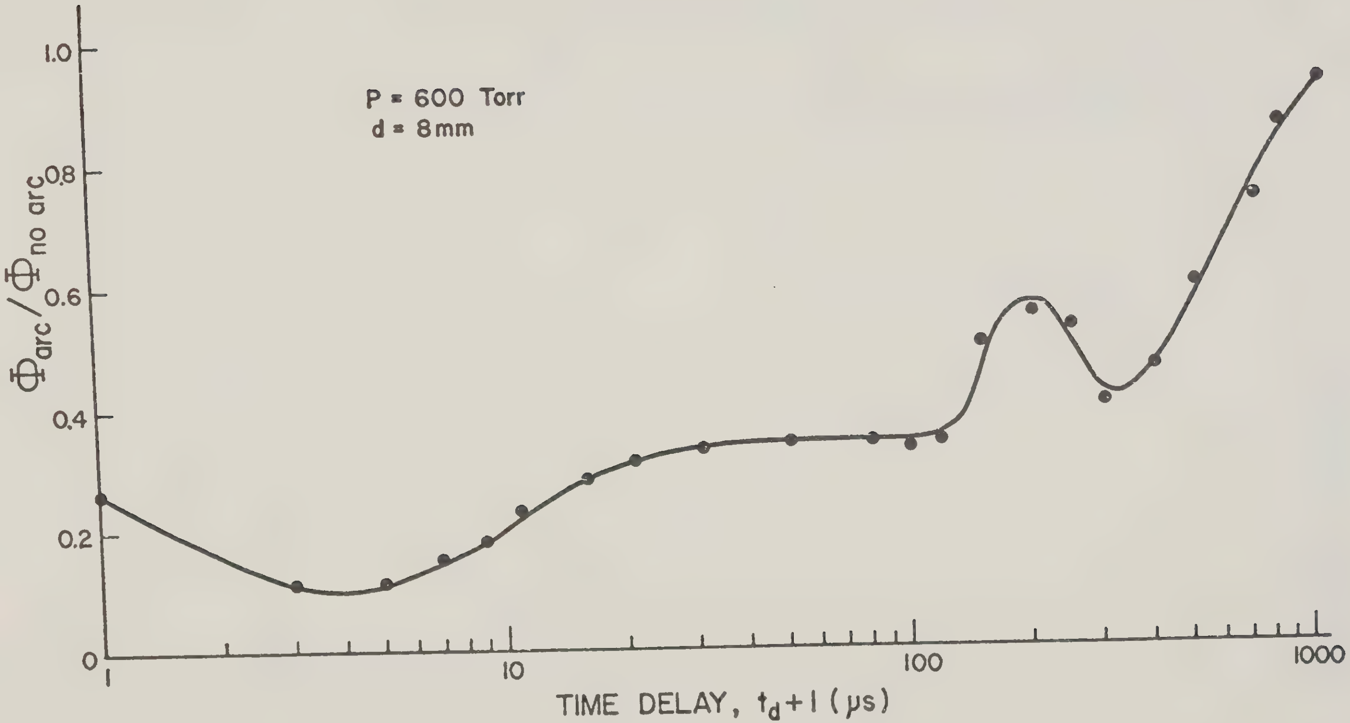

Figure 8-9 Breakdown Threshold 8 mm from the Discharge

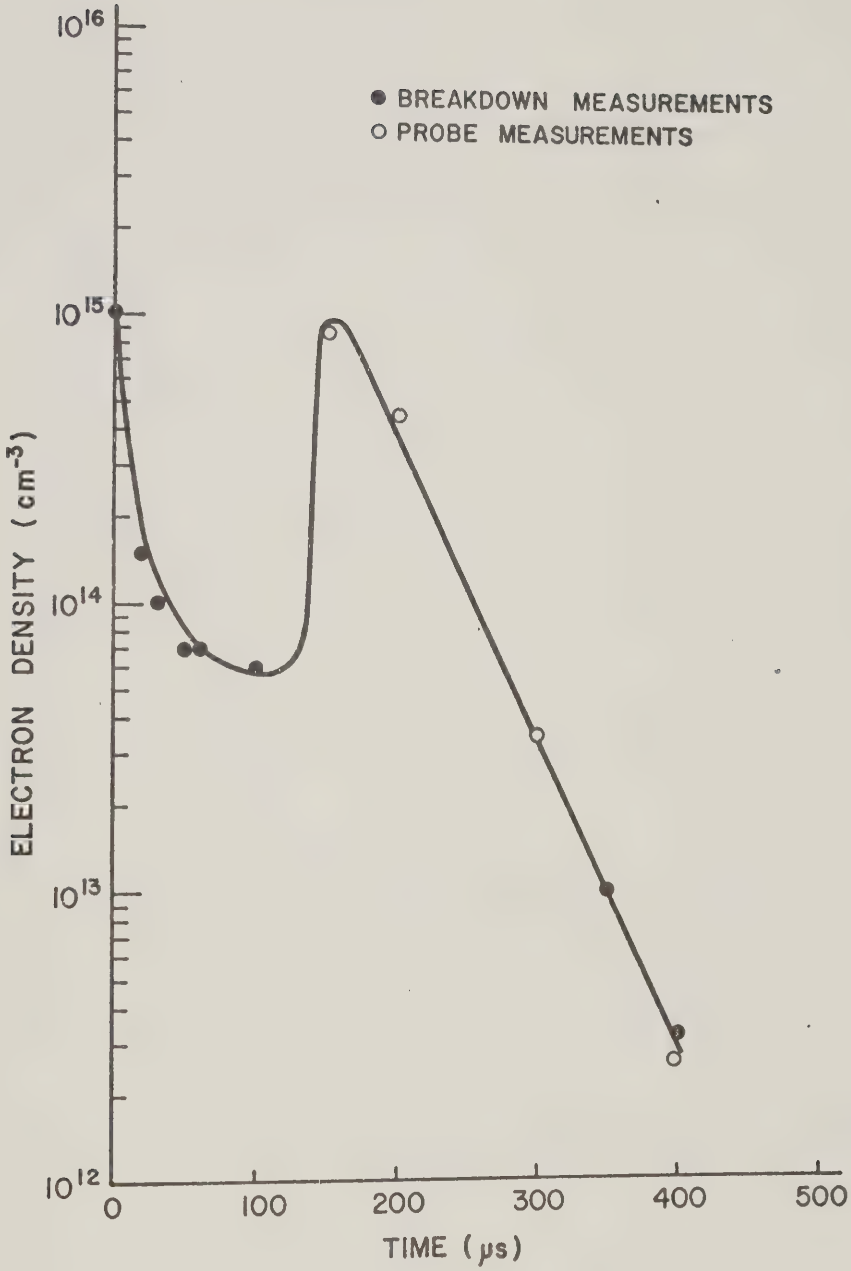

Figure 8-10(a) Electron Density as a Function of Time at a Distance of 8 mm from the Discharge

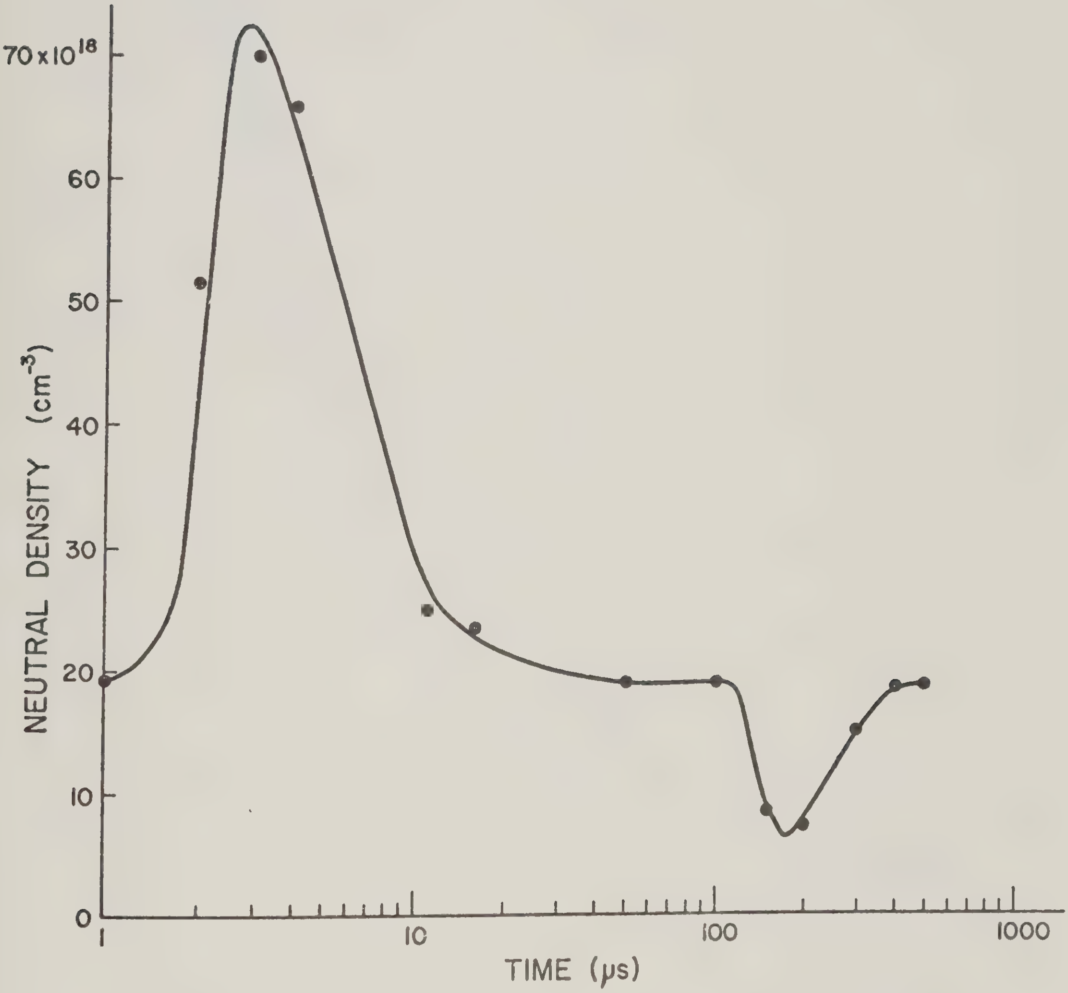

Figure 8-10(b) Variation of Neutral Density with Time 8 mm from the Center of the Discharge

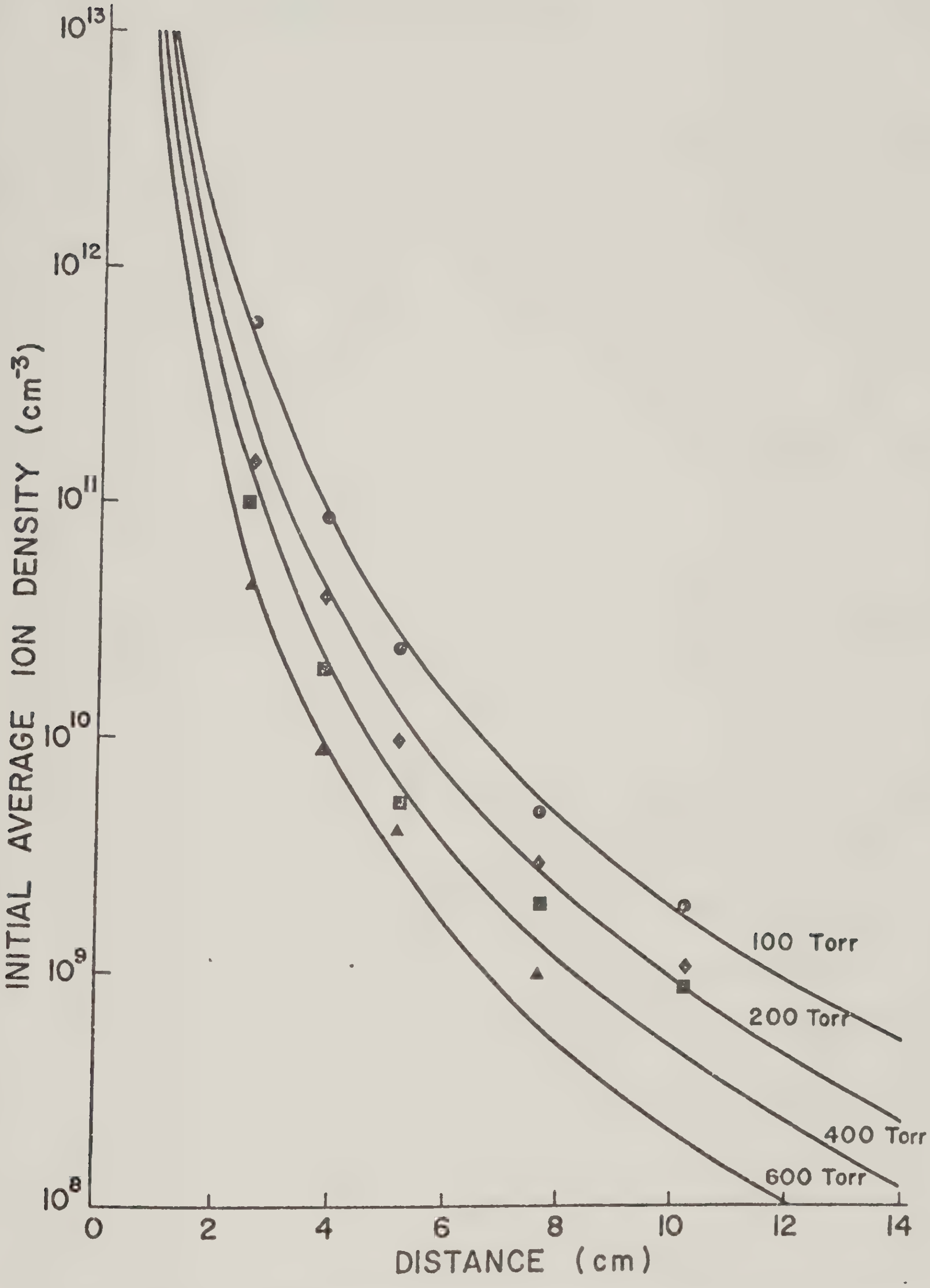

Figure 8-11 Variation of Photoplasma Density with Distance from UV Source

CHAPTER IX

SUMMARY AND CONCLUSIONS

The effects of changing initial values of the electron and neutral densities on the CO_2 laser induced breakdown of argon has been studied experimentally and theoretically. In particular, the thresholds were measured when the laser was fired in conjunction with an electric discharge similar to those used in uv preionized lasers. The experimental setup consisted of a CO_2 laser-amplifier system, a breakdown chamber, and the electric discharge preionizer.

The characteristics of the laser system were presented. As well, the electrical characteristics of the discharge were studied and the energy in the discharge converted to mechanical energy was measured.

The level of preionization due to uv photons from the discharge was measured with a rotating Langmuir probe. To interpret the experimental data, present theory on convection currents to probes as published in the literature was extended. The radial dependence of the measured photoplasma density was not incompatible with an r^{-4} dependence which seems to indicate a two-photon ionization mechanism. This problem is beyond the scope of the present work and points to the need to study the photoionization process taking place in greater detail.

The electron and neutral densities in the discharge were measured using interferometric and probe techniques. A CO_2 laser and a He-Cd laser were used as light sources in the interferometric investigations. By virtue of the long wavelength of the CO_2 laser output, the fringe shifts observed in a Mach-Zehnder interferometer directly yielded electron densities.

The probe was used to determine the electron density later in time. The decay of the plasma was recombination controlled.

An absorption experiment was set up to determine the electron temperature. The plasma was found to cool much more rapidly than would be expected from heat conduction losses. This indicated that other heat loss processes were occurring, most probably line radiation.

A cascade model of the breakdown process was developed taking into account the laser pulse shape, diffusion losses, elastic and inelastic collision losses, and variable collision frequency. Numerical calculations were performed based on this model and the breakdown thresholds were calculated as a function of the initial electron density and the gas pressure. The large lowering in the thresholds in the presence of a discharge was seen to be due to sufficiently high uv preionization such that the main loss mechanism in the breakdown process was ambipolar diffusion. The transition from free to ambipolar diffusion loss typically occurred around $n \simeq 10^{11} cm^{-3}$.

The breakdown thresholds were determined both inside and outside the discharge. Thresholds were also measured without preionization. In fact the results of the measurements without preionization were used to check the validity of the cascade model discussed above. The gas was first conditioned to ensure that the measured thresholds were true avalanche thresholds. A comparison of the measured thresholds with preionization and shock compression with theoretical predictions was made and there was generally reasonable agreement. This further supports the cascade theory of laser induced gas breakdown.

When the laser was focused in the discharge, a discrepancy between theoretical and experimental thresholds was observed. This was attributed

to difficulty in experimentally determining the occurrence of breakdown when there is strong light emission from the plasma being studied. If other ways of determining breakdown can be used this difficulty may be overcome.

The possibility of using breakdown to measure the electron or neutral density of a plasma was explored. The threshold was not very sensitive to changes in the initial electron density which implies that the uncertainty in the densities derived from the threshold is large. It appears to be applicable only for order of magnitude estimates.

On the other hand, as long as n is known and there is no difficulty in observing the spark, the breakdown threshold yields neutral densities in good agreement with well established techniques. There seems to be enough reason for further study of the breakdown process. As a probe it will offer a high degree of space and time resolution and the convenience of minimum optics and very little or no detecting instruments. The disadvantage seems to be the need for many "shots" before the threshold is determined, the dependence of the threshold on numerous parameters such as lens focal length, laser divergence and most of all the dependence of the threshold on the properties of the gas or plasma being studied. Interpretation in terms of a cascade model will be more difficult because of these factors. For example, the calculations done on this work which seem to agree quite well with experimental results may be good only for the particular laser, gas, and optical system used.

The technique seems to be limited also to low electron densities, gas densities, and low plasma temperature. Only further work will tell whether these problems can be overcome.

It would be interesting to study the breakdown process in the presence of weaker discharges such as glow discharges. Here the light emission from the plasma may be weak enough so that the problem of seeing the spark will be non-existent. The study of the distribution of the photons causing ionization emitted by the discharge should be pursued further.

REFERENCES

CHAPTER II

1. P.D. Maker, R.W. Terhune, and C.M. Savage, "Quantum Electronics, Proceedings of the Third International Congress", P. Grivet and N. Blumberger, eds. (Columbia University Press, New York, 1964).
2. Yu. P. Raizer, Sov. Phys. Uspekhi 8, 650 (1966).
3. C. DeMichelis, IEEE J. Quantum Electron. QE-5, 188 (1969).
4. G.V. Ostrovskaya and A.N. Zaidel', Sov. Phys. Uspekhi 16, 834 (1974).
5. E. Panarella, Found. of Phys. 4, 227 (1974).
6. R. Papoular, "Laser Interaction and Related Plasma Phenomena", Vol. 2, H. Schwarz and H. Hora, eds. (Plenum Press, New York, 1972).
7. R.G. Meyerand and A.F. Haught, Phys. Rev. Lett. 13, 7 (1964).
8. L.V. Keldysh, Sov. Phys. JETP 20, 1307 (1965).
9. A. Gold and H.B. Bebb, Phys. Rev. Lett. 14, 60 (1965).
10. H.B. Bebb and A. Gold, "Physics of Quantum Electronics", P.L. Kelly, B. Lax, and P.E. Tannenwald, eds. (McGraw-Hill, New York, 1966).
11. H.B. Bebb and A. Gold, Phys. Rev. 143, 1 (1966).
12. D.C. Smith, J. Appl. Phys. 41, 4501 (1970).
13. D.R. Cohn, M.P. Hacker, B. Lax, and W. Halverson, J. Appl. Phys. 46, 668 (1975).
14. C.H. Chan, C.D. Moody, and W.B. McKnight, J. App. Phys. 44, 1179 (1973).
15. F. Morgan, L.R. Evans, and C.G. Morgan, J. Phys. D. 4, 225 (1975).
16. M.P. Hacker, D.R. Cohn, and R.L. Brooks, Appl. Phys. Lett. 24, 173 (1974).
17. G.A. Hill, D.J. James, and S.A. Ramsden, J. Phys. D. 5, L97 (1972).

18. N. Kroll and K.M. Watson, Phys. Rev. A 5, 1883 (1972).

19. C.H. Chan, and C.D. Moody, J. Appl. Phys. 45, 1105 (1974).

20. R.G. Meyerand, Jr. and A.F. Haught, Phys. Rev. 11, 401 (1973).

21. M.P. Hacker, D.R. Cohn, and B. Lax, Appl. Phys. Lett. 23, 392 (1973).

22. W. Holzer, P. Ranson, and P. Peretti, IEEE J. Quantum Electron. QE-7, 204 (1971).

23. R.G. Tomlinson,E.K. Damon, and H.T. Buscher, "Physics of Quantum Electronics", P. Kelley, B. Lax, P. Tannenwald, eds. (McGraw-Hill, New York, 1966).

24. H.T. Buscher, R.G. Tomlinson and E.K. Damon, Phys. Rev. Lett. 15, 847 (1965).

25. S.A. Akhmanov, A.I. Kovrigin, M.M. Strukov, and R.V. Khoklivov, JETP Lett. 1, 25 (1965).

26. D. Smith and R.G. Tomlinson, Appl. Phys. Lett. 11, 73 (1967).

27. A.J. Alcock, C. DeMichelis, and M.C. Richardson, IEEE J. Quantum Electron. QE-6, 622 (1970).

28. D.C. Smith and A.F. Haught, Phys. Rev. Lett. 16, 1085 (1966).

29. D.C. Smith, Appl. Phys. Lett. 19, 405 (1971).

30. G. Canavan and P.E. Nielsen, Appl. Phys. Lett. 22, 409 (1973).

31. A.J. Alcock, C. DeMichelis, and M.C. Richardson, Phys. Lett. A 28, 356 (1968).

32. A.J. Alcock and C. DeMichelis, Phys. Rev. Lett. 21, 667 (1968).

33. A.M. Robinson, Appl. Phys. Lett. 22, 33 (1973).

34. J. Santiago and A.M. Robinson, Phys. Lett. A 51, 229 (1975).

35. V.S. Letokhov, E.A. Ryabov, and O.A. Tumanov, Phys. Lett. A 40, 55 (1972).

36. R.T. Brown and D.C. Smith, Appl. Phys. Lett. 22, 245 (1973).

37. M. Young, M. Herscher, and C.Y. Wu, J. Appl. Phys. 37, 4938 (1966).

38. E.V. George, G. Bekefi, and B. Ya'akobi, Phys. Fluids 14, 2708 (1971).

CHAPTER III

1. F. Morgan, L.R. Evans, and C.G. Morgan, J. Phys. D 4, 225 (1971).

2. D.C. Smith, Appl. Phys. Lett. 19, 405 (1971).

3. C.H. Chan, C.D. Moody and W.B. McKnight, J. Appl. Phys. 44, 1179 (1973).

4. G.A. Hill, D.J. James, and S.A. Ramsden, J. Phys. D 5, L97 (1972)

5. A.M. Robinson, Appl. Phys. Lett. 22, 33(1973).

6. I.K. Krasyuk, P.P. Pashinin, and A.M. Prokhorov, Sov. Phys. JETP 9, 354 (1969).

7. R.G. Tomlinson and E.K. Damon, Experimental Data in the Breakdown of Air and Argon by a Ruby Laser Pulse", Ohio State University Res. Found. Rep. AD 443 (June, 1964).

8. Y.L. Pan, J.R. Simpson, and A.E. Bernhardt, Appl. Phys. Lett. 24, 87 (1974).

9. M.P. Hacker, D.R. Cohn, and B. Lax, Appl. Phys. Lett. 23, 372 (1973).

10. D.R. Cohn, M.P. Hacker, B. Lax, and W. Halverson, J. Appl. Phys. 46, 668 (1975).

CHAPTER IV

1. R.W. MacPherson, Defense Research Establishment Valcartier: Report DREV R 701/13, 1973.

2. T.G. Roberts, Rev. Sci. Instrum. 47, 257 (1976).

3. A.W. Pasternak, Ph.D. Thesis, University of Alberta, 1976.

4. I.S. Abramshon and N.M. Gegeckhori, Zhur. Eksptl. i Teoret. Fiz. 21, 484 (1951).

CHAPTER V

1. H. Seguin, J. Tulip and D. McKen, Appl. Phys. Lett. 23, 344 (1973).
2. R. Babcock, I. Liberman, and W.D. Partlow, IEEE J. Quantum Electron. QE-12, 29 (1976).
3. P.R. Smy and A. Noor, J. Appl. Phys. 47, 1372 (1976).
4. P.R. Smy, Advances in Physics, 25, 517 (1976).
5. R.M. Clements and P.R. Smy, J. Appl. Phys. 40, 4553 (1969).
6. R.M. Clements and P.R. Smy, J. Appl. Phys. 41, 3745 (1970).
7. G. Schulz and S.C. Brown, Phys. Rev. 98, 1642 (1955).
8. R.M. Clements, R.D. Kerr, A.A. Offenberger, and P.R. Smy, Electron. Lett. 8, 361 (1972).
9. S.H. Lam, AIAA, J. 2, 256 (1964).
10. C.H. Su and R.E. Kiel, J. Appl. Phys. 37, 4907 (1966).
11. C.H. Su and S.H. Lam, Phys. Fluids, 6, 1479 (1963).
12. R.M. Clements, B.M. Oliver, A.I. Noor, and P.R. Smy, Electron. Lett. 12, 274 (1976).
13. P.R. Smy, Can. J. Phys. 54, 1627 (1976).
14. D.L. Thomas, Electron. Lett. 5, 341 (1969).
15. E.W. McDaniel, "Collision Phenomena in Ionized Gases", (John Wiley and Sons, Inc., New York, 1964).
16. D. McKen, Ph.D. Thesis, University of Alberta, 1976.
17. D. McKen, H.J. Seguin, and J. Tulip, IEEE J. Quantum Electron. QE-12, 470 (1976).

18. E. Nasser, "Fundamentals of Gaseous Ionization and Plasma Electronics", (John Wiley and Sons, Inc., New York, 1971).

19. P. Warneck, Z. Naturforsch. 27, 1127 (1972).

20. D.R. Bates, Case Studies in Atomic Physics, 4, 57 (1976).

21. G.L. Weissler, "Handbuch der Physik", Vol. 21, (Springer Verlag, Berlin, 1965).

22. A.N. Zaidel and E. Ya. Shreider, "Vacuum Ultraviolet Spectroscopy", (Ann Arbor Humphrey Science Publishers, Ann Arbor, 1970).

23. Y. Tanaka, R.E. Huffman, and J.C. Larrabee, J. Quant. Spectrosc. Radiat. Transfer, 2, 451 (1962).

24. R.E. Huffman, Y. Tanaka, and J.C. Larrabee, Compt. Rend. V/ Conf. Int. Phen. D'dionisation dans les Gaz, (Paris, 1963).

25. O.P. Judd, App. Phys. Lett. 22, 95 (1973).

26. R.D. Kerr, Ph.D. Thesis, University of Alberta, 1975.

27. Ya B. Zel'dovich and Yu. P. Raizer, "Physics of Shock Waves and High Temperature Hydrodynamic Phenomena", Vol. 1 (Academic Press, New York, 1967).

28. H.L. Brode, J. Appl. Phys. 26, 766 (1955).

29. M.N. Plooster, Phys. Fluids, 13, 2665 (1970).

CHAPTER VI

1. R.H. Huddlestone and S.L. Leonard, eds. "Plasma Diagnostic Tecniques", (Academic Press, New York, 1965).

2. T.K. Cheng and L.W. Casperson, J. Appl. Phys. 46, 1961 (1975).

3. H. Margenau and G.M. Murphy, "The Mathematics of Physics and Chemistry", (D. Van Nostrand Company, Inc., Princeton, 1967).

4. A.A. Offenberger and R.D. Kerr, J. Appl. Phys. 41, 354 (1972).

5. R.M. Clements and P.R. Smy, J. Appl. Phys. 41, 3745 (1970).
6. R.M. Clements, R.D. Kerr, A.A. Offenberger, and P.R. Smy, Electron. Lett. 8, 361 (1972).
7. P.R. Smy, J. Phys. D 9, 2403 (1976).
8. M.A. Gusinow, J.B. Gerardo, and J.T. Verdeyen, Phys. Rev. 149, 91 (1966).
9. S.V. Desai and W.H. Corcoran, J. Quant. Spectrosc. Radiat. Transfer 9, 1371 (1969).

CHAPTER VII

1. Y.B. Zel'dovich and Yu. P. Raizer, Sov. Phys. JETP 20, 772 (1965).
2. L. Friedland, Phys. Rev. A 12, 2024 (1975).
3. Ya. B. Zel'dovich and Yu. P. Raizer, "Physics of Shock Waves and High Temperature Hydrodynamic Phenomena" (Academic Press, New York, 1966).
4. M.P. Hacker, D.R. Cohn, and B. Lax, Appl. Phys. Lett. 23, 392 (1973).
5. D.R. Cohn, M.P. Hacker, B. Lax, and W. Halverson, J. Appl. Phys. 46, 668 (1975).
6. C.H. Chan, C.D. Moody, and W.B. McKnight, J. Appl. Phys. 44, 1179 (1973).
7. C.H. Chan and C.D. Moody, J. Appl. Phys. 45, 1105 (1974).
8. N. Kroll and K.M. Watson, Phys. Rev. A 5, 1883 (1972).
9. F. Morgan, L.R. Evans, and C.G. Morgan, J. Phys. D 4, 225 (1971).
10. H. Raether, "Electron Avalanches and Breakdown in Gases", (Butterworth, London, 1964).
11. A. Von Engel, "Encyclopedia of Physics", S. Flugge, ed. (Springer Verlag, Berlin, 1956). Vol. XXI.

12. J. Tulip and H. Seguin, Phys. Lett. A 44, 469 (1963).

13. W.P. Allis, "Encyclopedia of Physics", S. Flugge, ed. (Springer Verlag, Berlin, 1956). Vol. XXI.

14. A.G. Engelhardt and A.V. Phelps, Phys. Rev. 133, A375 (1964).

15. J. Fletcher and D.S. Burch, J. Phys. D 5, 2037 (1972).

16. S.C. Brown, "Basic Data of Plasma Physics", (MIT Press, Cambridge, Mass., 1966).

17. L.C. Van Atta, Phys. Rev. 38, 876 (1931).

18. W.P. Allis and D.J. Rose, Phys. Rev. 93, 84 (1954).

CHAPTER VIII

1. R.T. Brown and D.C. Smith, Appl. Phys. Lett. 22, 245 (1973).

2. J. Santiago and A.M. Robinson, Phys. Lett. A 51, 229 (1975).

APPENDIX

```
C       THIS PROGRAM SOLVES THE RATE EQUATIONS FOR THE ELECTRON DENSITY
C       AND THE ELECTRON TEMPERATURE WHICH DESCRIBE THE BUILDUP IN
C       THE FOCUS OF A LENS DUE TO A LASER BEAM.  ENERGY IS GAINED FROM
C       THE RADIATION FIELD VIA ELECTRON-NEUTRAL INVERSE BREMSSTRAHLUNG.
C       PARTICLE LOSS MECHANISM IS DIFFUSION OF ELECTRONS OUT OF THE
C       FOCAL VOLUME.  ENERGY IS LOST DUE TO DIFFUSION, ELASTIC COLLISION
C       AND INELASTIC COLLISIONS.  RECOMBINATION,RADIATION, HYDRODYNAMIC
C       EFFECTS,COLLISIONS OF THE SECOND KIND, AND IONIZATION OF EXCITED
C       STATES ARE NEGLECTED IN THE CALCULATION.  BREAKDOWN IS DEFINED AS
C       THE ATTAINMENT OF AN ELECTRON DENSITY IN THE FOCUS EQUAL TO
C       NB=9.4E13*PR WHERE PR IS THE GAS PRESSURE IN TORR.
C
C       NT = ELECTRON-ION DENSITY
C       NB = DENSITY AT BREAKDOWN
C       DB = BACKGROUND ELECTRON DENSITY
C       DL = DIFFUSION LENGTH
C       PR = GAS PRESSURE IN TORR
C       EI  IONIZATION POTENTIAL IN EV
C       EX = EXCITATION ENERGY IN EV
C       PMAX = PEAK LASER POWER IN W/CM**2
C       DIV = CONSTANT
C       TPRES = PRESENT TIME
C       TT = ELECTRON TEMPERATURE IN EV
C       ICOUNT = COUNTER
C       R = RADIUS OF FOCAL SPOT
C       A = FOCAL AREA
C       ENERGY = LASER PULSE ENERGY
        EXTERNAL GAIN, SINK, ELOSS, HEAT, POWR
        REAL NT, NB
        COMMON DB,DL,PR,EI,EX,PMAX,DIV
        PR=4000.
        PMAX=1.46E8
        NT=1.E5
        TT=.025
        TPRES=0.0
        DIV=1.
        ICOUNT=1
        NB=9.4E13*PR
        DL=6.7E-3
        EX=11.5
        EI=15.8
        R=.01
        A=1.57E-4
        ENERGY=1.16E-7*PMAX*A
        PRINT 101, PMAX, ENERGY
        PRINT 100, DL,NT,TT,NB,DIV
        NT=NT/DIV
        DB=NT
        NB=NB/DIV
     65 CALL FD(TT,NT,TPRES,HEAT,ELOSS,GAIN,SINK,POWR,NB)
        STOP
    100 FORMAT('0',5X,E14.7,E14.7,E14.7,E14.7,E14.7,E14.7,E14.7)
    101 FORMAT('0','PMAX=',E14.7,'ENERGY=',E14.7)
        END
```

```
      SUBROUTINE FD(TT,NT,TPRES,HEAT,ELOSS,GAIN,SINK,POWR,BD)
C     SUBROUTINE FD SOLVES THE SET OF DIFFERENTIAL EQUATIONS FOR THE
C     ELECTRON DENSITY AND TEMPERATURE.   TIME STEP SIZE IS EQUAL TO W
C     CONTROL IS RETURNED TO MAIN PROGRAM IF THE ELECTRON DENSITY
C     EQUALS OR EXCEEDS NB OR WHEN THE PARTICLE LOSS TERM EXCEEDS
C     THE PARTICLE GAIN TERM.  FUNCTIONS GAIN(PARTICLE GAIN), SINK
C     (PARTICLE LOSS), HEAT(ENERGY GAIN), AND ELOSS(ENERGY LOSS) ARE
C     CALLED IN THE CALCULATIONS.
      REAL NT
      COMMON DB,DL,PR,EI,EX,PMAX,DIV
      W=1.E-11
      I=0
      PRINT100
      TPRES=TPRES+W
      DTEMP=NT
      TTEMP=TT
    1 POW=POWR(TPRES,PMAX)
      I=I+1
      DO 10 L=1,2
      D1=GAIN(TTEMP,PR)-SINK(DL,DTEMP,TTEMP,PR)
      C1=HEAT(PR,TTEMP,POW)-ELOSS(TTEMP,DL,PR,EI,EX,DTEMP)-TTEMP*D1
      IF(D1.LT.0.) RETURN
      TTEMP=TT+W*C1
      DTEMP=NT/(1.-W*D1)
   10 CONTINUE
      NT=DTEMP
      TT=TTEMP
      TPRES=TPRES+W
      IF(NT.GT.BD) GO TO 11
      IF(TPRES.GT.3.E-7) RETURN
      IF(I.LT.100) GO TO 1
      I=0
      NT=NT*DIV
      PRINT101, TPRES,NT,TT,C1,D1
      NT=NT/DIV
      GO TO 1
   11 PRINT102, TPRES
      RETURN
  100 FORMAT('1',5X,'TIME',9X,'DENSITY',5X,'TEMPERATURE',6X,'EGAIN',
     15X,'PGAIN')
  101 FORMAT('0',5E14.7)
  102 FORMAT('1','BREAKDOWN BEFORE THE END OF LASER PULSE',5X,
     1'TIME=',E14.7)
      END
      FUNCTION ELOSS(TT,DL,P,EI,EX,DE)
C     FUNCTION ELOSS COMPUTES THE ENERGY LOSSES DUE TO IONIZATION,
C     EXCITATION, DIFFUSION AND ELASTIC COLLISIONS.  THERE IS A GRADUAL
C     TRANSITION FROM FREE DIFFUSION TO AMBIPOLAR DIFFUSION SIMILAR
C     TO THE THAT DONE BY ALLIS AND ROSE.
C     S = RATIO OF ELECTRON MOBILITY TO ION MOBILITY
C     THE RATES HAVE BEEN OBTAINED BY BY AVERAGING THE PROPER EXPRESSIONS
C     OVER A MEXWELLIAN DISTRIBUTION.  A N EIGHT ORDER POLYNOMIAL
C     HAS BEEN FITTED INTO THESE NUMERICALLY OBTAINED RATES AND USED
C     BELOW (E1,E2,E3,E4)
      COMMON Q,A,B,C,D,PMAX,DIV
      DOUBLE PRECISION E1,E2,E3,E4,T ,Z,S,S1,ZZ,DL
      DB=Q
      DE=DE*DIV
    7 T=TT
      S=270.
```

```
      X=DE*DL**2/T
      IF(X.LT.1.E6) GO TO 30
      IF(X.LT.5.E10) GO TO 40
      X1=ALOG(X)
      F =.0194+1./(X1+37.26)
      GO IO 50
   30 F =1.0693069*(X**(-.0291024))
      GO TO 50
   40 X1=ALOG(X)
      F =-22.40979119+4.059998075*X1-.2354787146*X1*X1+.0041446379З*X1
     1**3
      F=EXP(F)
   50 CONTINUE
      DE=DE/DIV
    4 IF(T.CT..09) GO TO 2
    1 E1=-90504.62565+18710134.96*T*(1.-62.09561313*T*(1.-8.290271858
     1*T*(1.+145.0273445*T*(1.-31.97124387*T*(1.-13.26317363*T*(1.-
     26.413112570*T*(1.-2.554797329*T)))))))
      E1=E1*(1.-DB/DE)
      E2=159.5485745-34866.1747*T*(1.-70.85201168*T*(1.-25.84540384*T*
     1(1.-10.67633897*T*(1.+1.022064823*T*(1.-125.9607123*T*(1.-
     28.966764848*T*(1.-2.963647535*T)))))))-90.3438225
   13 E3=6.69E7*((4.42F-4*T+11.4*I*T+1.05*T**3-.074*T**4)*DFXP(-15.8/T)
     1+(-407.2*T-15.1*T*T+.738*T**3+.074*T**4)*DEXP(-40./T))/(T**1.5)
      E4=3.39E10*DEXP(1.-11.5/T)/((T**1.5)*((1.+11.5/T)**2))
      GO TO 3
    2 E1=61936.47815+27525706.66*T*(1.-1.908401863*T*(1.-1.036365552*
     1T*(1.-.617184294*T*(1.-.391568672*1*(1.-.254244796*T*(1.-
     2.164416326*T*(1.-.102455896*T*(1.-.057971726*T*(1.-.025022737*T
     3)))))))))
      E1=E1*(1.-DB/DE)
      E2=4.97P5*(T**1.5)*(1./((1.+.045*T)**3)-1./((1.+.115*T)**3))
     1-90.3438225
   16 E3=6.69E7*((4.42P-4*T+11.4*T*T+1.05*T**3-.074*T**4)*DEXP(-15.8/T)
     1+(-407.2*T-15.1*T*T+.738*T**3+.074*T**4)*DEXP(-40./T))/(T**1.5)
      E4=3.39E10*DEXP(1.-11.5/T)/((T**1.5)*((1.+11.5/T)**2))
    3 ELOSS=F*E1/(P*DL**2)+E2*P+E3*EI*P+E4*P*EX
      ELOSS=ELOSS*2./3.
      RETURN
      END
      FUNCTION HEAT(P,TT,PW)
      DOUBLF PRECISION G,T
      COMMON DB
      T=TT
      IF(T.GT..09) GO TO 2
    1 G   =.005262611632-1.376274564*T*(1.-94.70036758*T*(1.-
     143.87836987*T*(1.-24.99144824*T*(1.-15.21324399*T*(1.-9.201797018
     2*T*(1.-5.128126403*T*(1.-2.196435630*T)))))))
      HEAT=G
      GO TO 3
    2 G   =.255*(T**.5) *(1./((1.+.045*T)**3)-1./((1.+.115*T)**3))
      HEAT=G
    3 HEAT=HEAT*P*PW*2./3.
      RETURN
      END
      FUNCTION SINK(DL,DE,TT,P)
      COMMON Q,A,B,C,D,PMAX,DIV
      DOUBLF PRECISION A1,Z,S,S1,ZZ,T,DL
      DB=Q
      DE=DE*DIV
```

```
    9 T=TT
      S=270.
      X=DE*DL**2/T
      IF(X.LT.1.E6) GO TO 30
      IF(X.LT.5.E10) GO TO 40
      X1=ALOG(X)
      F =.0194+1./(X1+37.26)
      GO TO 50
   30 F =1.0693069*(X**(-.0291024))
      GO TO 50
   40 X1=ALOG(X)
      F =-22.40979119+4.059998075*X1-.2354787146*X1*X1+.0041446379З*X1
     1**3
      F=EXP(F)
   50 CONTINUE
      DE=DE/DIV
    4 IF(T.GT..09) GO TO 2
    1 A1=-440449.2602+93887505.5*T*(1.-67.8196688*T*(1.-16.56933631*T*
     1(1.+48.10972895*T*(1.-38.32996662*T*(1.-14.03782813*T*(1.-
     26.602210808*T*(1.-2.600287366*T)))))))
      A1=A1*(1.-DB/DE)
      GO TO 3
    2 A1=6071192.958+43257636.95*T*(1.-2.623880189*T*(1.-1.133838983*T*
     1(1.-.6454695O2*T*(1.-.401601116*T*(1.-.258344115*T*(1.-.166187809
     2*T*(1.-.103223899*T*(1.-.058284988*T*(1.-.025123406*T)))))))))
      A1=A1*(1.-DB/DE)
    3 SINK=A1*F/(P*(DL**2))
      RETURN
      END
      FUNCTION GAIN(TT,P)
      COMMON DB
      DOUBLE PRECISION G ,T
      T=TT
      G=P*6.69E7*((4.42E-4*T+11.4*T*T+1.05*T**3-.074*T**4)*DEXP(-15.8/
     1T)+(-407.2*T-15.1*T**2+.738*T**3+.074*T**4)*DEXP(-40./T))/(T**1.5)
      GAIN=G
      P=0.
      G=P*3.39E10*DEXP(1.-11.5/T)/((T**1.5)*((1.+11.5/T)**2))
      GAIN=GAIN+F*G
      RETURN
      END
      FUNCTION POWR(T1,PMAX)
      COMMON DB
      T=T1
      IF(T-6.E-8) 1,1,2
    1 POWR=PMAX*T/6.E-8
      RETURN
    2 IF(T-1.2E-7) 3,3,4
    3 POWR=PMAX*(-0.6*T/6.E-8+1.6)
      RETURN
    4 IF(T-1.6E-7) 5,5,6
    5 POWR=0.4*PMAX
      RETURN
    6 POWR=PMAX*(-0.4*T/1.4E-7+6./7.)
      RETURN
      END
```

B30210